Optoelectronic and thermoelectric applications of Pr and Nb doped $SrTiO_3$ nanostructures

Thesis submitted to the University of Calicut for the partial fulfillment of the requirements for the award of the degree of

DOCTOR OF PHILOSOPHY IN PHYSICS
Under the Faculty of Science

By

Midhun Shah

Under the guidance of
Prof.Dr.P.P.PRADYUMNAN
DEPARTMENT OF PHYSICS
UNIVERSITY OF CALICUT
KERALA 673635, INDIA
April 2025

Optoelectronic and Thermoelectric Applications of Pr and Nb Doped $SrTiO_3$ Nanostructures

Thesis submitted to the University of Calicut for the partial fulfillment of the requirements for the award of the degree of

DOCTOR OF PHILOSOPHY IN PHYSICS

Under the Faculty of Science

By

Midhun Shah

Under the guidance of
Prof.Dr.P.P.PRADYUMNAN

DEPARTMENT OF PHYSICS
UNIVERSITY OF CALICUT
KERALA 673635, INDIA

April 2025

Optoelectronic and Thermoelectric Applications of Pr and Nb Doped $SrTiO_3$ Nanostructures

Ph.D. thesis in Physics

AUTHOR:

Midhun Shah
Department of Physics,
University of Calicut.
Calicut University (PO) - 673635, Kerala, India.
Email: midhunshah@farookcollege.ac.in

Under the guidance of

Prof.(Dr).P.P.Pradyumnan
Senior Professor
Department of Physics
University of Calicut
Calicut University (PO) - 673635,
Kerala, India.
Email : ppp@uoc.ac.in
April 2025

UNIVERSITY OF CALICUT

CERTIFICATE ON PLAGIARISM CHECK

1.	Name of the research scholar	Midhun Shah	
2.	Title of thesis/dissertation	Optoelectronic and Thermoelectric Applications of Pr and Nb Doped $SrTiO_3$ Nanostructures	
3.	Name of the supervisor	Dr.P.P.Pradyumnan	
4.	Department/Institution	Department of Physics, University of Calicut	
5.	Similar content (%) identified	Non-Core	Core
		Introduction/ Theoretical Overview/Review of literature/Materials & Methods/Methodology	Analysis/ Result/Discussion/ Summary/Conclusions/ Recommendations
		5	5
	Acceptable maximum limit (%)	10	10
6.	Software used	iThenticate	
7.	Date of verification	9.04.2025	

**Report on plagiarism check, specifying included/excluded items with % of similarity to be attached.*

JAMSHEER N. P.
Assistant Librarian
University of Calicut
Malappuram - 673 635

Checked by (with name, designation & signature)

Name & Signature of the Researcher Midhun Shah

Name & Signature of the Supervisor

Prof.(Dr.) P.P. PRADYUMNAN
Senior Professor
Department of Physics
University of Calicut
Kerala - 673 635, India

The Doctoral Committee* has verified the report on plagiarism check with the contents of the thesis, as summarized above and appropriate measures have been taken to ensure originality of the Research accomplished herein.

Prof. M.M.MUSTHAFA

HEAD OF THE DEPARTMENT
DEPARTMENT OF PHYSICS
UNIVERSITY OF CALICUT

Name & Signature of the HoD/HoI (Chairperson of the Doctoral Committee)

** In case of languages like Malayalam, Tamil, etc. on which no software is available for plagiarism check, a manual check shall be made by the Doctoral Committee, for which an additional certificate has to be attached*

DEPARTMENT OF PHYSICS

UNIVERSITY OF CALICUT, KERALA 673635 - INDIA

Dr. P.P. Pradyumnan
Senior Professor

Calicut University P.O
Kerala, India 673 635
Tel: +919895961751
Fax: 0494-2400269
E-mail: ppp@uoc.ac.in

CERTIFICATE

Certified that the work presented in this thesis entitled "***Optoelectronic and Thermoelectric Applications of Pr and Nb Doped $SrTiO_3$ Nanostructures***" is submitted to the University of Calicut in partial fulfillment of the requirements for the award of degree of Doctor of Philosophy in Physics is a record of original research work done by Mr. MIDHUN SHAH under my guidance in the Department of Physics, University of Calicut. The thesis has not formed the basis for the award of any Degree/Diploma and has undergone plagiarism check using iThenticate software at CHMK Library, University of Calicut and the similarity index is found within the permissible limit.

Calicut University
10th April 2025

Dr. P.P.Pradyumnan

DEPARTMENT OF PHYSICS

UNIVERSITY OF CALICUT, KERALA 673635 - INDIA

Dr. P.P. Pradyumnan
Senior Professor

Calicut University P.O
Kerala, India 673 635
Tel: +919895961751
Fax: 0494-2400269
E-mail: ppp@uoc.ac.in

CERTIFICATE

Certified that all the corrections/suggestions recommended by the adjudicators have been incorporated in the thesis entitled "***Optoelectronic and Thermoelectric Applications of Pr and Nb Doped $SrTiO_3$ Nanostructures*** " submitted to the University of Calicut for the award of the degree of Doctor of Philosophy in Physics by Mr. Midhun Shah, Department of Physics, University of Calicut, and content in this thesis and the soft copy are one and same.

Calicut University
22nd October 2025

Dr. P.P.Pradyumnan

DECLARATION

Certified that the work presented in this thesis entitled "***Optoelectronic and Thermoelectric Applications of Pr and Nb Doped $SrTiO_3$ Nanostructures*** "submitted to the University of Calicut for the award of the degree of Doctor of Philosophy is based on the original research work done by me under the supervision and guidance of Dr. P.P.Pradyumnan, Senior Professor, Department of Physics, University of Calicut, Calicut University P.O, Kerala- 673635 and has not been included in any other thesis submitted previously for the award of any degree. I declare that the thesis has undergone plagiarism check using iThenticate software at CHMK Library, University of Calicut and the similarity index is found within the permissible limit. I also declare that the thesis is free from AI generated contents.

Calicut University

10^{th} April 2025

Midhun Shah

Dr. P.P.Pradyumnan
Senior Professor
Department of Physics
University of Calicut

ACKNOWLEDGEMENT

I would like to express my sincere gratitude to all of the people whose assistance and encouragement made this thesis possible. I would like to express my heartfelt gratitude to Prof. Dr. P.P. Pradyumnan, Professor, Department of Physics, University of Calicut, for his invaluable guidance, unwavering support, and insightful suggestions throughout the course of my Ph.D. His expertise and encouragement have been pivotal in shaping both my research and academic growth. I am deeply indebted to him for his mentorship, which has significantly contributed to the successful completion of this thesis.

I would like to extend my sincere thanks to Prof. Dr. Mohamed Shahin Thayyil, Head of the Department of Physics, University of Calicut, for his constant support and encouragement during my PhD journey. I am also deeply grateful to the former Heads of the Department, Prof. Dr. C.D. Ravikumar and Prof. Dr. A.M. Vinod kumar, for their valuable guidance during the early stages of my research. I am deeply grateful to Dr. Antony Joseph, Prof. Dr. M.M. Musthafa, Professors, Department of Physics, University of Calicut, for their motivation throughout my PhD journey. I would like to express my heartfelt gratitude to Dr. Libu K Alexander, Dr. Zuhail K.P, and Dr. K. Drisya for their friendly advice & constant encouragement. Their insights and camaraderie have been a source of motivation and inspiration.

I am deeply grateful to Dr. K.A. Aysha Swapna, Principal of Farook College, Kozhikode, for her encouragement. I would also like to express my heartfelt thanks to Prof. E.P. Imbichi Koya and Dr. K.A. Naseer, former Principals of Farook College, for their valuable support during my research. My sincere thanks go to Dr. P.A. Subha and Dr. K.K. Abdulla, former Heads of the Department of Physics at Farook College, for their guidance throughout my work. I am equally grateful to the faculty members of the Department of Physics, Farook College, for their unwavering encouragement and assistance during my PhD journey.

I would like to express my sincere thanks to the Central Sophisticated Instrumentation Facility (CSIF) at Calicut University for their invaluable technical

assistance in the characterization of my samples. Their support has been instrumental in the progress and success of my research work. I would like to extend my sincere gratitude to the Central Instrumentation Facility (CIF), IISER Trivandrum, the Sophisticated Analytical Instrument Facility (SAIF), IIT Madras, and the Center for Nano Science and Engineering (CeNSE), IISc Bangalore, for providing technical assistance with various characterization facilities. I would like to thank RUSA for the financial assistance via Ref: letter No: G3/RUSA/FRP (4)/2019, Farook College, Calicut.

I would like to sincerely thank Mr. Jamshihas A.P, Assistant Professor , AKNM Govt Polytechnic, Malappuram, for his invaluable technical support in implementing few experimental setups. I would like to express my heartfelt gratitude to my seniors in the lab, Dr. Muhammed Sabeer, Dr. Shyni P., Dr. Soumya, Dr. Anju Paulson, and Dr. Vineetha, for their constant support. I would like to extend my sincere thanks to my lab mates Nabeela, Parvathy, Hashir, and Hisna for their support throughout my PhD journey.

I am deeply grateful to Ms. Jamshina Sanam P.K, my co-researcher in the lab, for her invaluable academic and mental support throughout my Ph.D. journey. Her constant encouragement and collaborative spirit have made a significant impact on the progress of my work. I sincerely appreciate her insightful suggestions and her willingness to assist in overcoming various challenges along the way. Her contributions have been instrumental in shaping both my research and personal growth. I would like to sincerely thank Dr. Biju K.P, Associate Professor at Govt. Arts and Science College, Kozhikode, for his valuable research discussions and guidance, as well as Dr. Reji Thomas, Assistant Professor at Farook College, for his support during the early stages of my PhD journey.

I am deeply grateful to my parents Prof.A. Shavudeen and S.Sebinnisa for their unconditional love and support, which have been the foundation of my journey. A special thanks to my wife, Jaseera.C.P, and my daughters, Jahnara and Ahana, for their patience, understanding, and constant encouragement, which have given me the strength to complete this work.

Midhun shah

"If I have seen further, it is by standing on the shoulders of giants"- Isaac Newton

Dedicated to

Family, Friends, Teachers & Students

PREFACE

Thermoelectricity and optoelectronics are emerging as pivotal technologies in addressing global energy challenges by enabling the direct interconversion of heat and electricity, as well as facilitating light-matter interactions for energy harvesting and emission. This thesis, titled **"*Optoelectronic and Thermoelectric Applications of Pr and Nb Doped $SrTiO_3$ Nanostructures*"**, presents a comprehensive investigation into the synthesis, characterization, and functional tuning of Praseodymium (Pr) and Niobium (Nb) doped Strontium Titanate in both bulk and thin film forms. The work explores how controlled doping, defect engineering, and nanostructuring influence key properties such as electrical conductivity, Seebeck coefficient, bandgap, photoluminescence, and carrier mobility. By employing techniques such as graphite burial sintering and oxygen-deficient sputtering, the study achieves significant improvements in both thermoelectric performance including high power factors and enhanced infrared absorption—and optoelectronic behavior, such as visible-range transparency and tunable emission. This dual-functional approach positions Pr and Nb doped $SrTiO_3$ as a promising material platform for next-generation energy and electronic devices. The thesis is divided in to nine chapters,

An overview of optoelectronic and thermoelectric materials is given in Chapter 1. The fundamentals of thermoelectricity, optoelectronic materials, and thermoelectric materials are covered in this chapter. The fundamentals of the thermoelectric phenomena are briefly explained, along with standard criteria that indicate the effectiveness of thermoelectric materials and techniques for enhancing waste heat conversion capabilities. This chapter also elucidates the motivation and objective of the work, which is to modify the optoelectronic and thermoelectric properties of materials through doping, band engineering, defect modulation and carrier optimization in order to alter functional capabilities for potential applications in optoelectronic and thermoelectric devices.

Chapter 2 deals with the synthesis and characterization of polycrystalline bulk materials as well as monocrystalline thin films. The chapter explains the high temperature

solid-state reaction and graphite sintering approach to synthesis bulk materials and it also illustrates the optimal settings for Radio frequency sputtering to prepare thin films. A brief overview on different structural, compositional, morphological characterization methods along with optical, electrical, thermal and thermoelectrical studies employed in this work is presented in this chapter.

Chapter 3 deals with the synthesis of $Sr_{1-x}Pr_xTiO_3$ bulk ceramics series of samples with x=0.05, 0.075, 0.10, 0.125, 0.15, 0.20 via high temperature solid state reaction and subsequent graphite burial sintering. The detailed structural and compositional analysis before and after burial sintering were investigated by XRD, Raman spectroscopy. The morphological features were analyzed using FE-SEM. The analysis reveals a structural transformation from cubic to tetragonal system for doping concentrations $x \geq 0.1$, which was verified by Rietveld refinement. The proper concentration and distribution of the dopant in the host matrix is verified using XRF and EDS analysis. The presence of oxygen vacancies in the system which plays a vital role in determining optoelectronic properties of the system was validated through XPS analysis. Graphite sintered samples analyzed using UV-Vis-NIR spectroscopy showed a significant reduction in optical bandgap and substantial NIR absorption. The role of excess Pr doping and generated oxygen vacancies in the photoluminescence emission mechanism was also examined in the samples.

Chapter 4 focuses on the thermoelectric properties of $Sr_{1-x}Pr_xTiO_3$ bulk ceramics. A two-step graphite burial reduction technique was employed to reduce the double Schottky barrier (DSB), which is formed by strontium and oxygen vacancies at the grain boundaries, by adjusting the carrier concentration through point defects. The oxygen deficiency in the system was analyzed using a combination of XPS and TGA. The thermoelectric performance was assessed through temperature-dependent studies of electrical and thermal conductivity. The thermoelectric figure of merit was found to be enhanced by the two-step burial sintering combined with Pr doping. The increased infrared absorption, along with a high thermoelectric power factor, suggests that the sample is a promising candidate for both optoelectronic and thermoelectric applications.

The size confinement effect of Pr doped $SrTiO_3$ on its thermoelectric and optoelectronic properties is covered in Chapter 5. Oxygen-deficient RF magnetron sputtering was used to create transparent and conducting Pr-STO thin films deposited on quartz substrates. Intriguing structural characteristics such as Stranski–Krastanov (SK) growth and cation segregation were observed which have adverse effect on their chemical stability and optoelectronic performance. The structural parameters, analyzed via XRD and Raman spectroscopy, were correlated with the temperature-dependent electrical transport properties obtained from Hall Effect measurements. Morphological features, investigated through FESEM and AFM, were further examined to elucidate the conduction mechanism in the films. The optical studies unveiled significant transparency in the visible spectrum, which could be adjusted through Pr doping. Additionally, the analysis of photoluminescence emissions at specific wavelengths shed light on the involvement of oxygen vacancies in the emission process. Controlled sputtering and post deposition annealing resulted in formation of Sr cluster free thin films with high electron mobility and conductivity. Deposition on Silicon substrates resulted in formation of thin films with three to four order higher carrier concentration and enhanced TE performance.

Chapter 6 examines the impact of B-site doping and the size confinement effect on STO thin films. In this study, titanium (Ti) sites in the $SrTiO_3$ (STO) system were substituted with niobium (Nb) ions to assess their electrical and thermoelectric properties. The $SrTi_{0.9}Nb_{0.1}O_3$ powder was synthesized using a high-temperature solid-state reaction and subsequently cold-pressed to create a sputtering target. Oxygen-free sputtering, followed by high-temperature vacuum annealing, produced a high carrier concentration in the range of 10^{20} - 10^{21} cm^{-3}. The structural, compositional, and morphological characteristics of the film were analyzed using XRD, SEM, EDS, and AFM techniques. The influence of sputtering power and argon gas pressure on the electrical and thermoelectric properties of the films was systematically examined. By optimizing the sputtering parameters, a record-breaking thermoelectric power factor of 1.85 W/mK^2 Watts achieved.

Chapter 7 explores the impact of external magnetic fields and magnetic ion inclusions on the thermoelectric performance of thin films. External magnetic fields can significantly influence the thermoelectric properties of materials, especially in magnetic thin films and nanostructures. To test this concept, thin films of nickel were deposited using the RF magnetron sputtering technique. Magnetic force microscopy (MFM) imaging revealed the formation of magnetic domains, while XRD patterns indicated a preferred orientation of nickel films along the (111) plane. The thermoelectric and magneto-thermoelectric properties of the sputtered thin films were investigated using a custom-built experimental setup. This setup included Peltier elements, thermostats, and PID controllers to regulate the sample's temperature, allowing for the examination of variations in the Seebeck coefficient under an applied magnetic field. Saturation behavior of thermoelectricity was also observed, providing insights into the magnetic nature of the materials.

Chapter 8, presents a general conclusion and summary, in the field of optoelectronic and thermoelectric (TE) materials. It highlights that doping, controlling oxygen vacancies, removing double Schottky barriers (DSB) via graphite sintering, and exploiting size confinement effects can be strategically employed to optimize the optoelectronic and thermoelectric properties of strontium titanate (STO). Analyzing defect chemistry provides a clear pathway to engineer the band structure and enhance the intrinsic features of STO.

Chapter 9, the concluding chapter, outlines future research possibilities aimed at further improving the optoelectronic and thermoelectric performance of $SrTiO_3$-based materials. It emphasizes approaches like vacancy manipulation, incorporation of metallic and magnetic nano-inclusions, and the design of superlattice structures to enhance charge transport, energy filtering, and reduce thermal conductivity. The chapter also explores the development of oxide-based p–n junction thermoelectric generators for efficient energy conversion, along with the promising application of these materials in temperature sensing due to their strong response to thermal and electrical variations.

ABBREVIATIONS

- XRD : X-ray Diffraction
- ICDD : International Centre for Diffraction Data
- AFM : Atomic Force Microscopy
- FE-SEM : Field Emission Scanning Electron Microscopy
- EDX : Energy Dispersive X-ray Spectroscopy
- XRF : X- Ray fluorescence
- PL : Photoluminescence
- UV-Vis : Ultraviolet-Visible Spectroscopy
- XPS : X-ray Photoelectron Spectroscopy
- TEG : Thermoelectric Generator
- ZT : Figure of Merit (thermoelectric performance)
- MR : Magnetoresistance
- TGA : Thermogravimetric Analysis
- RF : Radio Frequency
- TE : Thermoelectricity
- DSB : Double Schottky Barrier
- SK growth : Stranski-Krastanov growth
- MFM : Magnetic Force Microscopy

JOURNAL PUBLICATIONS

1. **Midhun Shah**, Sanam P.K. Jamshina, P.P. Pradyumnan, Optimization of carrier mobility in Pr-doped $SrTiO_3$ thin films through controlled Sr-segregation for optoelectronic applications, Surfaces and Interfaces, Volume 55, 2024, 105331, ISSN 2468-0230, https://doi.org/10.1016/j.surfin.2024.105331
2. **Midhun Shah**, Jamshina Sanam P.K, P.P. Pradyumnan, Graphite sintered strontium praseodymium titanate perovskite for thermoelectric applications, Materials Chemistry and Physics, Volume 327, 2024, 129866, ISSN 0254-0584, https://doi.org/10.1016/j.matchemphys.2024.129866.
3. **Midhun Shah**, P.K. Jamshina Sanam, P.P. Pradyumnan, Tuning of photoluminescence properties: Impact of Pr-doping in $SrTiO_3$ crystallites, Materials Today Communications, Volume 39, 2024, 109323,ISSN 2352-4928, https://doi.org/10.1016/j.mtcomm.2024.109323.
4. **Midhun Shah**, P.K. Jamshina Sanam, P.P. Pradyumnan, Defect-induced $Sr_{1-x}Pr_xTiO_3$ crystallites by burial sintering and its optoelectronic applications, Journal of Physics and Chemistry of Solids, Volume 181, 2023, 111516, ISSN 0022-3697, https://doi.org/10.1016/j.jpcs.2023.111516.
5. **Midhun Shah**, A.P. Jemshihas, P.K. Jamshina Sanam, P.P. Pradyumnan, Magneto thermoelectric effect of nickel thin film synthesized by RF magnetron sputtering, Physica E: Low-dimensional Systems and Nanostructures, Volume 147,2023,115591,ISSN,1386-9477,https://doi.org/10.1016/j.physe.2022.115591.
6. P.K. Jamshina Sanam , **Midhun Shah** , P.P. Pradyumnan , 'Structure induced modification on thermoelectric and optical properties by Mg doping in $CuCrO_2$ nanocrystals', Solid State Communications 353 (2022) 114855
7. Sanam, P.K.J., **Shah, M**. & Pradyumnan, P.P. Raman spectroscopic investigation and thermoelectric studies of defect-induced Mg-doped delafossite thin film. J Mater Sci: Mater Electron 33, 22346–22360 (2022). https://doi.org/10.1007/s10854-022-09013-y

8. P.K. Jamshina Sanam, **Midhun Shah**, P.P. Pradyumnan,The enhancement of NIR transparency due to annealing and Mg-doping in $CuCrO_2$ thin films, Materials Letters, Volume 330,2023,133295,ISSN 0167-577X, https://doi.org/10.1016/j.matlet.2022.133295.
9. P.K. Jamshina Sanam, **Midhun Shah**, P.P. Pradyumnan, Enhanced thermoelectric properties in dual cation doped CuCrO2 nanocrystals mediated by magnon-carrier drag, Materials Research Bulletin, Volume164,2023,112244, ISSN00255408,https://doi.org/10.1016/j.materresbull.2023.112244.
10. Jamshina Sanam P.K., **Midhun Shah**, P.P. Pradyumnan, Magnetoelectric coupling and thermoelectric behaviors in Ni-doped $CuCrO_2$ crystallites,Chemical Engineering Journal, Volume 476,2023,146568, ISSN 1385-8947, https://doi.org/10.1016/j.cej.2023.146568.
11. Jamshina Sanam P.K., **Midhun Shah**, P.P. Pradyumnan, Tailoring structure and nanoscale surface topography in Mg–N doped $CuCrO_2$ thin films via post deposition annealing for optothermoelectric application, Optical Materials, Volume 147, 2024, 114703, ISSN 0925-3467, https://doi.org/10.1016/j.optmat.2023.114703.
12. Jamshina Sanam P.K., **Midhun Shah**, P.P. Pradyumnan, Intense narrow band blue emission in $CuCrO_2$ delafossite by Ni^{2+}-Mg^{2+} dual cation doping, Spectrochimica Acta Part A: Molecular and Biomolecular Spectroscopy, Volume 305, 2024, 123442, ISSN 1386-1425, https://doi.org/10.1016/j.saa.2023.123442.
13. Jamshina Sanam P.K., **Midhun Shah**, P.P. Pradyumnan, Multi-cation doped CuCrO2 crystallite matrix: Exploring bandgap tunability through Ni-Zn and Ni-Zn-Mg doping for optoelectronic application, Optical Materials, 2024, 116283, ISSN 0925-3467, https://doi.org/10.1016/j.optmat.2024.116283.
14. P.K, J.S., **Shah, M.** & Pradyumnan, P. Structural and magnetic modifications in Ni–Mg dual-doped $CuCrO_2$: Insights into carrier filtering and thermoelectric enhancement. J Mater Sci: Mater Electron 36, 1458 (2025). https://doi.org/10.1007/s10854-025-15526-z.

PAPER PRESENTATIONS

1. Enhanced power factor in Nb doped $SrTiO_3$ thin films via strain induced band degeneracy and energy filtering, 21st European Conference on Thermoelectrics, September 8-12, Nancy, France.
2. Graphite Sintered Strontium Praseodymium Titanate Perovskite for Thermoelectric Applications at 68th DAE Solid state Physics Symposium at BARC, Bombay, December 18-22, 2024.
3. Graphite sintered $Sr_{1-x}Pr_xTiO_3$ for thermoelectric applications at Asian Symposium on Materials and Processing 2024 (ASMP2024), IIT Madras, December 5-7, 2024.organised by IIT Madras and Nagoka University, Japan
4. Presented paper titled Defect induced $Sr_{1-x}Pr_xTiO_3$ crystallites by burial sintering for optoelectronic applications, at International Conference on Photo physics and Photochemistry (14-16 October, 2024, IIT Bombay).
5. Presented a paper titled 'Improved electrical and optoelectronic properties of Pr doped $SrTiO_3$ thin films' at International Conference on Materials for Energy & Sustainable Development 27-29 October 2023, JNU, New Delhi.
6. Presented a paper titled 'Structural and Thermoelectric properties of burial sintered Pr doped $SrTiO_3$ crystallites' at World conference on thermoelectrics (WCT 2023), Jaipur National University, Jaipur, Rajasthan, March 14th~18th, 2023.
7. Presented a paper titled 'Structural and Photo luminescence studies of Pr doped $SrTiO_3$ Ceramics' in CMPA 2022 held at Manipal university, From 02/12/2022 To 03/12/2022 organized by Manipal Institute of Technology, Karnataka.
8. Presented paper 'An Experimental Setup to Study Magneto Thermoelectric Effect and Spin Seebeck Effect of Thin Films and Nanostructures, International Conference on Advanced Materials Mechanical Characterization (ICAMMC 2021), SRM IST, Chennai, Tamil Nadu Dec 2-4 2021.
9. Presented paper titled 'Effect of annealing on growth of RF magnetron sputtered YIG thin films at ITAM 2021 (Interdisciplinary Topics in Advanced Materials

(ITAM-2021) organized by JNCASR, IISc, Bangalore, Karnataka- July 27-30, 2021.

10. Presented a paper titled 'Thermoelectric studies of Magnetic tunnel Junctions' in National Symposium on Nanoscience and nanotechnology, IISc, Bangalore.20-22 June, 2018.

AWARDS

1. Best oral presentation Award for the paper titled "An Experimental Setup to Study Magneto Thermoelectric Effect and Spin Seebeck Effect of Thin Films and Nanostructures, International Conference on Advanced Materials Mechanical Characterization', (ICAMMC 2021), SRM IST, Chennai. Dec 2-4 2021.
2. Best Poster award for 'Structural and Photo luminescence studies of Pr-Doped $SrTiO_3$ Ceramics' in National conference, CMPA 2022 held at Manipal University, organized by Manipal Institute of Technology-Supported by DST, Dec 2-3, 2022.
3. Best oral presentation Award for the paper titled 'Structural and Thermoelectric properties of burial sintered Pr doped $SrTiO_3$ crystallites' at World conference on thermoelectrics (WCT 2023), Jaipur National University, Jaipur March 14-18, 2023.

CONTENTS

LIST OF FIGURES

LIST OF TABLES

Chapter 1

Introduction to optoelectronics and thermoelectricity

Objectives

The objective of this chapter is to provide a comprehensive overview of the fundamental principles and significance of optoelectronic and thermoelectric materials relevant to this research. It highlights the interplay between electronic structure, defect engineering, and carrier dynamics in functional materials, particularly transparent conducting oxides (TCOs). The chapter also explores the mechanisms by which materials convert temperature gradients into electrical energy and vice versa, emphasizing their technological importance. The investigated materials exhibit excellent optical properties, making them promising for optoelectronic applications while also demonstrating strong thermoelectric performance. This dual nature necessitates a combined study of optical and thermoelectric characteristics to maximize their potential in energy and sensing applications. Understanding these properties is essential for optimizing their roles in energy conversion, sensor technologies, and multifunctional material applications.

1.1 Introduction

The study of optoelectronic and thermoelectric properties in materials is crucial for advancing energy conversion, sensing, and display technologies. Optoelectronic materials, particularly transparent conducting oxides (TCOs) like indium tin oxide (ITO), fluorine-doped tin oxide (FTO), and doped $SrTiO_3$, exhibit high optical transmittance (~85–90% in the visible range) and electrical conductivity (>10^3 S/cm), making them essential for applications such as photovoltaics, LEDs, and photodetectors. Similarly, thermoelectric materials, including $SrTiO_3$-based perovskites, Bi_2Te_3, and emerging double perovskites like Ca_2NaIO_6 and Sr_2NaIO_6, enable direct heat-to-electricity conversion. Notably, these double perovskites have demonstrated direct band gaps of 2.64 eV and 2.48 eV, respectively, alongside high Seebeck coefficients and low thermal conductivities, resulting in promising thermoelectric figures of merit (ZT values) at elevated temperatures. This intrinsic relationship between optoelectronic and thermoelectric properties stems from shared factors such as band structure, carrier dynamics, and defect engineering. For instance, optimizing carrier concentration in $SrTiO_3$-based systems enhances both electrical conductivity and optical transparency, while controlled defect introduction, such as oxygen vacancies, improves infrared absorption and thermoelectric efficiency. This interplay suggests that optimizing one property can positively influence the other, as materials with strong light absorption often exhibit favorable electronic structures that enhance charge carrier mobility, benefiting thermoelectric performance. Understanding these correlations enables the design of multifunctional materials capable of efficiently managing both electronic and thermal energies, thereby contributing to sustainable energy solutions and next-generation optoelectronic and thermoelectric applications. Furthermore, advancements in defect engineering, doping strategies, and nanostructuring have demonstrated the potential to tailor these properties, offering new avenues for developing high-performance materials for energy harvesting, electronics, and environmental applications [1–5].

1.2 Optoelectronics

Optoelectronics combines the fundamental principles of optics and electronics to develop devices capable of emitting, detecting, and controlling light. These devices leverage the quantum mechanical properties of photons and electrons to perform a wide range of functions, including signal processing, communication, and energy conversion [6,7]. Key components in optoelectronics include light-emitting diodes (LEDs), laser diodes, photodetectors, and solar cells. Transparent conducting oxides (TCOs) play a critical role in this domain, serving as essential materials that combine high electrical conductivity with optical transparency, making them ideal for applications in displays, photovoltaics, and touch screens. LEDs and laser diodes generate light through the recombination of electron-hole pairs in semiconductor materials, while photodetectors and solar cells convert light into electrical signals or power through the photoelectric and photovoltaic effect. Advances in materials science, particularly with the development of new direct bandgap semiconductor materials significantly enhanced the efficiency and capabilities of optoelectronic devices. These innovations have profound implications for numerous applications, from fiber optic communications and medical imaging to renewable energy and consumer electronics, driving the ongoing miniaturization and performance enhancement of modern technology [8,9].

The development of improved semiconductor materials and theoretical models has significantly impacted the modern electronic device industry. Novel experimental characterization techniques have also played a crucial role, providing sensitive and diverse physical-chemical information. The optical properties of materials, including transmission, absorption, and emission, arise from their interaction with electromagnetic radiation, particularly in semiconductors. These optical properties, observed in the ultraviolet, visible, and infrared ranges, are closely tied to the materials' electronic band characteristics and atomic structures. Historical studies, particularly those on Si, Ge, and GaAs from the 1950s to 1960s, not only detailed their optical properties but also advanced our understanding of modern solid-state physics. The optical absorption edges of semiconductors reveal information about the energy separation between valence and

conduction bands, which is crucial for determining their suitability for future applications. Optical methods of measuring bandgaps are advantageous as they are non-destructive, require minimal sample preparation, and provide valuable atomic-structural information, making them versatile tools for various experimental conditions [10].

Nitrides and phosphide materials find widespread use in LED technology, while tellurides and perovskites are commonly utilized in solar cell applications. Metal oxides, perovskites, and delafossite oxides are employed as transparent conducting oxides, offering both high electrical conductivity and optical transparency. An increasing variety of 2D non-layered materials, such as metal chalcogenides (PbS, CdS/Se), topological crystalline insulators and organic–inorganic hybrid perovskites are being utilized in optoelectronic advances [6,11]. Oxide-based optoelectronics and perovskite oxide-based optoelectronics represent two significant branches of research in the field of advanced materials for electronic and photonic devices.

Oxide perovskite optoelectronics are critically important due to their unique combination of properties that span electronic, optical, and structural domains. Perovskite oxides, such as strontium titanate ($SrTiO_3$) and barium titanate ($BaTiO_3$), exhibit high dielectric constants, ferroelectricity, piezoelectricity, and other functional characteristics that are crucial for various optoelectronic applications. These materials offer opportunities for developing high-performance photovoltaics, capacitors with enhanced energy storage capabilities, and sensors with sensitive response characteristics. Their tunable properties through doping, strain engineering, and interface engineering further expand their utility across different devices. Moreover, oxide perovskites provide a platform for exploring novel phenomena and pushing the boundaries of materials science, driving innovation in optoelectronic world [12–14].

Several theoretical frameworks addressed this key concepts to provide a solid foundation for understanding the principles governing the materials and devices involved. These frameworks link the optical and electronic properties of materials, providing

explanations for phenomena like light absorption, emission, and charge transport. The following theoretical frameworks are crucial.

Semiconductor band theory forms the basis for understanding the electronic and optical properties critical to optoelectronic device performance. In a semiconductor, electrons occupy energy levels within the valence band at low energies, while the conduction band contains higher energy states that are typically unoccupied at absolute zero temperature. The energy difference between these two bands, termed the bandgap (E_g), is a key parameter that governs electrical conductivity and optical absorption. Semiconductors with direct bandgaps, like GaAs ($E_g \approx 1.42$ eV), allow for efficient electron transitions between the conduction and valence bands, making them ideal for optoelectronic applications such as LEDs and solar cells. Conversely, materials with indirect bandgaps, such as Si ($E_g \approx 1.1$ eV), require phonon interactions to facilitate these transitions, making them less efficient for light emission but suitable for photovoltaic devices. Band theory also provides the framework to understand the effects of doping, where introducing impurities into the semiconductor lattice creates localized energy states that influence carrier concentration and transport. This manipulation of the band structure enables the design of various devices like photodetectors and laser diodes, emphasizing the versatile role of band theory in modern semiconductor research [15,16].

Optical phenomena in materials science involve the interaction of light (electromagnetic radiation) with materials, leading to various behaviors like absorption, reflection, refraction, and emission of light. These phenomena are governed by the electronic, structural, and compositional properties of materials, which can be manipulated to tailor optical properties for specific applications in photonics, optoelectronics, sensors, and energy systems.

The development of high-performance optoelectronic oxides has increasingly relied on the coordinated modulation of band structure, defect chemistry, and carrier transport to reconcile optical transparency, photonic response, and conductive functionality. In $SrTiO_3$-based perovskites, substitutional doping at both the A-site (Sr^{2+}) and B-site (Ti^{4+}) serves to tailor the electronic density of states, modify lattice distortions,

and adjust phonon scattering pathways, thereby influencing key optical parameters such as absorption edge, refractive index, and photoluminescent emission [17]. Rare-earth dopants (Pr, Nd, La and Sm) occupying the Sr^{2+} site introduce localized 4f-states which hybridize with Ti 3d–O 2p orbitals, effectively reducing the bandgap, red-shifting the absorption into the visible/NIR region and activating new emission centers [18]. Concurrently, B-site substitution of Ti^{4+} with transition metals such as Nb, Ta, Cr, or Mn modifies the electronic structure by introducing additional d-electrons or defect states, thereby increasing carrier concentration and electrical conductivity; however, excessive doping can induce free-carrier absorption and plasmonic shifts, compromising optical transparency and necessitating careful control of dopant levels [19]. At the nanoscale regime, further tuning emerges via quantum-confinement, enhanced grain boundary scattering, and engineered oxygen deficiency: oxygen vacancies create Ti^{3+} donor states, boost free-carrier mobility, increase sub-band absorption (especially in IR), and alter recombination kinetics of photo generated carriers [20] . These phenomena point to a deeply interconnected relationship: strong light–matter interaction (via dopant/defect triggered absorption or emission) frequently correlates with favorable charge–carrier dynamics, which in turn underpin transparent conductive behavior and photonic-device functionality. Comparative investigations show that oxide perovskites, compared to chalcogenides, offer superior chemical and thermal stability alongside optical transparency, yet they are often limited by lower carrier mobility and higher lattice thermal conductivity. Advanced synthesis strategies including graphite-burial sintering, oxygen-deficient sputter growth and epitaxial strain engineering have demonstrated success in mitigating these limitations by controlling microstructure, interface states and defect distribution. Nonetheless, a comprehensive, quantitative mapping between defect concentration, band-edge realignment, carrier scattering lifetime and optical/transport behaviour is still lacking. This gap forms the core motivation for the present work, which systematically explores Pr and Nb doping, coupled defect engineering and nanostructuring of $SrTiO_3$ to derive design rules for multifunctional optoelectronic oxides.

1.2.1 Optical absorption, emission & band gap

Optical absorption and emission are properties that govern the interaction of light with materials, which are central to optoelectronic devices. Optical absorption occurs when photons with energy greater than or equal to the material's bandgap excite electrons from the valence band (VB) to the conduction band (CB), creating electron-hole pairs. The efficiency of absorption is influenced by the material's band structure and the absorption coefficient, which is higher for direct bandgap materials due to the ease of electron transitions without phonon assistance. Photon emission or radiative

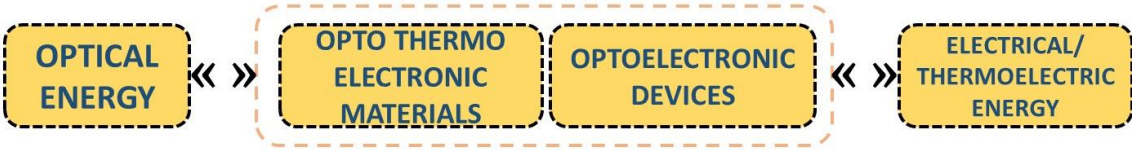

Figure 1- 1 Function representation of opto thermoelectronic materials and devices.

recombination occurs when electrons in the CB relax back to the VB, emitting a photon with energy corresponding to the bandgap. This emission process is crucial in devices like LEDs and lasers, where light is generated through electron-hole recombination [21].

Fundamental principle of optoelectronics lies in the quantum mechanical interactions between light and electronic materials. Optoelectronics encompasses both the study and practical applications of electronic devices involving generating, sensing, and controlling photons. These devices facilitate the conversion of electrical signals, such as current or voltage, into optical signals (photons) and vice versa, through complex interactions between electrons and light in nanoscale semiconductor structures. Light-emitting devices harness voltage and current to generate electromagnetic radiation, commonly used for illumination purposes. Conversely, light-detecting devices, including photodiodes, phototransistors, and photodetectors, convert incoming electromagnetic energy into electric current or voltage, making them suitable for light sensing and communication. Generally, these light-detecting devices operate by using photons to free bound electrons within semiconductor materials [22–24]. Fig. 1-1 illustrates the various electronic functions within semiconductors when subjected to excitations in the form of light and electricity.

Materials with different bandgaps absorb different wavelengths of light, with larger bandgaps typically absorbing in the ultraviolet range, and smaller bandgaps absorbing visible or infrared light. This characteristic makes optical bandgaps key in designing devices such as solar cells, light-emitting diodes (LEDs), and photodetectors, where precise control over the absorption and emission of light is necessary. The nature of the bandgap - whether direct or indirect-also affects the efficiency of light absorption and emission [25,26].

1.2.2 Direct & indirect band gap semiconductors

A direct band gap semiconductor is characterized by a similarity in both the magnitude and direction of the wave vector, *k* for the highest energy states in the valence band and the lowest energy states in the conduction band. This relationship is crucial for optical transitions, which involve minimal changes in the wave vector since the optical wavelengths are significantly longer than interatomic distances or the lattice constant. In direct band gap semiconductors, optical transitions can occur as soon as the energy of the incoming photons exceeds the band gap energy, leading to the excitation of an electron from the valence band to the conduction band, while simultaneously creating a hole in the valence band. The density of states available for these transitions is typically low at the band gap energy, resulting in a steep increase in the absorption coefficient as photon energy rises, following a square root dependence on the difference between the photon energy and the band gap energy. Beyond the band gap energy, the absorption length can diminish to the scale of micrometers, indicating a significant imaginary component in the refractive index. Likewise, emission transitions from the conduction band to the valence band are readily achievable, as each electron in the conduction band can pair with a corresponding hole in the valence band, which tends to exist at higher energy states. Consequently, the carrier lifetime in direct band gap materials is generally short, often lasting only a few nanoseconds, even in crystals with low defect densities [27,28].

The ease of transition in direct bandgap materials typically results in shorter carrier lifetimes, often on the order of nanoseconds, even in high-quality crystal structures with

low defect densities. Prominent examples of direct bandgap semiconductors include gallium arsenide (GaAs), indium gallium arsenide (InGaAs), gallium nitride (GaN),

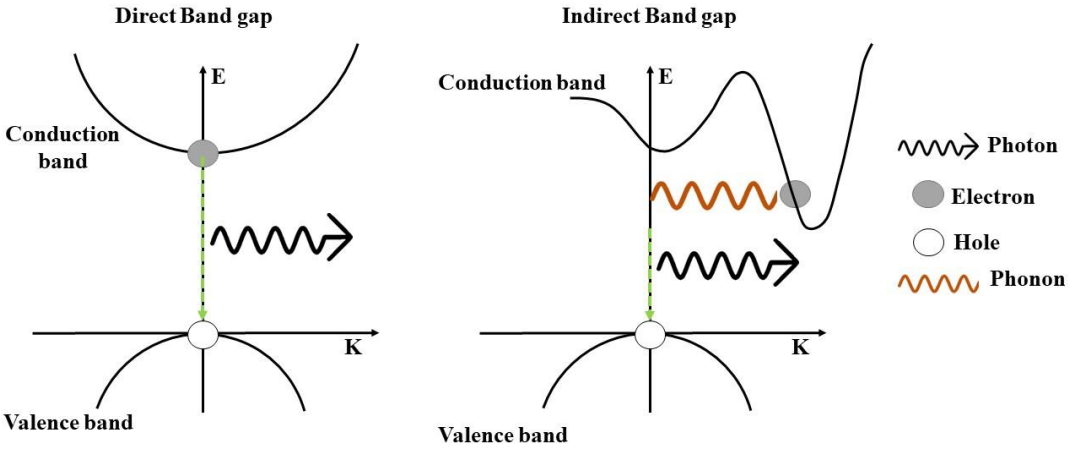

Figure 1- 2 Direct and indirect band gap transitions.

aluminum nitride (AlN), cadmium sulfide (CdS), cadmium selenide (CdSe), cadmium telluride (CdTe), zinc sulfide (ZnS), lead sulfide (PbS), lead selenide (PbSe), Strontium titanate ($SrTiO_3$), and Calcium titanate ($CaTiO_3$) [29–31].

In an indirect band gap semiconductor, the wave vector, *k* of the lowest energy states in the conduction band significantly differs from that of the highest energy states in the valence band. This disparity complicates absorption processes for photons with energies just above the band gap, as suitable target states in the conduction band are lacking in both energy and wave vector. Consequently, energy and momentum conservation cannot be simultaneously satisfied unless a phonon is emitted, which can facilitate the necessary momentum change without significantly affecting the energy balance. While such processes are feasible, they occur at significantly lower rates, resulting in a reduced absorption coefficient [32]. Furthermore, the wavelength dependence of the absorption coefficient near the band gap is less pronounced, and temperature plays a crucial role, as it influences the population of phonons. At much higher photon energies, direct excitation of carriers into the conduction band becomes possible without the involvement of phonons, leading to a substantial increase in the

absorption coefficient-often several orders of magnitude greater than that observed near the band gap. Emission, often necessitates the emission of a phonon, further diminishing the rates of recombination and emission. This can adversely affect the quantum efficiency of fluorescence, particularly as non-radiative recombination processes, such as those caused by crystal defects, may dominate without exhibiting high rates. Examples of indirect band gap semiconductors include silicon (Si), germanium (Ge), aluminum arsenide (AlAs), and gallium phosphide (GaP) [29,33–35]. The difference is depicted in Fig 1-2.

1.2.3 Tuning of optical bandgap - Strategies

Bandgap engineering can be achieved through various strategies, each influencing electronic structure and charge transport. Doping introduces impurity atoms that create localized states within the bandgap, shifting conduction or valence bands and effectively tuning the bandgap depending on donor or acceptor states. Quantum confinement, observed when material dimensions approach the exciton Bohr radius, increases discrete energy levels, leading to a widened bandgap due to spatial confinement effects. Strain engineering alters interatomic spacing through compressive or tensile strain, modifying orbital interactions and band dispersion, resulting in either bandgap narrowing or widening. Surface and interface engineering induces charge redistribution, dipole formation, and interfacial states, significantly affecting band alignment and enhancing electronic and optical properties. Oxygen vacancy regulation introduces defect states near the conduction band, reducing the bandgap by creating mid-gap states that enhance carrier concentration and influence charge transport. The ability to tune the optical bandgap of materials is crucial for optimizing their performance in various optoelectronic applications such as photovoltaics, transparent conducting oxides (TCO's), LEDs, and photocatalysis. The optical bandgap determines how a material absorbs light and how efficiently it can convert light into electrical energy or catalyze reactions. Several strategies have been developed to modulate the bandgap, each with specific advantages depending on the target application.

Bandgap engineering strategies such as doping, quantum confinement, and strain engineering simultaneously optimize carrier concentration, band dispersion, and density of states, enhancing both optoelectronic and thermoelectric performance. Surface and interface modifications, along with oxygen vacancy regulation, improve charge transport while reducing thermal conductivity, making materials like oxide perovskites efficient for both TE and optical applications. These approaches enable multifunctional materials with tunable electrical and thermal properties, bridging the gap between thermoelectric energy conversion and optoelectronic technologies.

1.2.3.1 Doping

Doping involves introducing foreign atoms (dopants) into the host material to alter its electronic structure. By choosing dopants with different valence electrons, one can either create new electronic states within the bandgap or shift the energy levels of the conduction and valence bands. This is widely used in materials to improve performance for solar cells or photocatalysts, as dopants can also affect carrier concentrations and recombination rates. Transition metals like Ni, Co, Fe, Cr, Sc, Cu, Ti, V and Mn, rare earth elements like La, Pr, Ce, Nd, Sm, Gd and Eu, group III and V elements like Al,Ga and N, P are commonly used dopants to alter optical properties of materials. Transition metal doping mainly introduces electrons to the CBM and VBM, which causes the change of band structure. The band-gap gradually decreases with the atomic number [36–40]. Rare earth elements can introduce localized states within the band gap of the host material, which are often derived from the 4f electronic states. These states can act as intermediate energy levels between the CBM and VBM, effectively narrowing the bandgap. The presence of these dopants can also affect the density of free carriers in the conduction band. By introducing additional charge carriers or trap states, the overall carrier concentration can be modified, impacting the effective mass of charge carriers and consequently the mobility, which can lead to improved performance in optoelectronic applications [41–45] .

The quantitative impact of doping on bandgap engineering can be understood through:

- **Bandgap narrowing:** In heavily doped semiconductors, increased carrier concentration leads to many-body interactions such as band tailing and bandgap shrinkage. The empirical relation for bandgap narrowing (ΔEg) is given by:

$$\Delta Eg = -\gamma \cdot N^{1/3} \tag{1.1}$$

  γ is a material-dependent constant, and N is the dopant concentration.

- **Burstein-Moss shift:** In n-type degenerate semiconductors, excess electrons fill the conduction band states, shifting the Fermi level and increasing the apparent bandgap as in eqn (1.2)

$$Eg^* = Eg + \frac{\hbar^2}{2m^*}(3\pi^2 N)^{2/3} \tag{1.2}$$

  m^* is the effective mass of charge carriers, N is the electron concentration, and Eg^* is the shifted bandgap.

- **Effective mass and density of states (DOS) esngineering:** Doping modifies band curvature and density of states effective mass m_d^* influencing electrical and thermoelectric properties. The Seebeck coefficient (S) depends on the DOS effective mass as:

$$S = \frac{8\pi^2 k_B^2}{3eh^2} m_d^* T \left(\frac{\pi}{3n}\right)^{2/3} \tag{1.3}$$

  where n is the carrier concentration, showing that doping can optimize both band structure and thermoelectric efficiency.

1.2.3.2 Quantum confinement

Quantum confinement occurs when the material size is reduced to the nanoscale, confining the motion of charge carriers (electrons and holes) in one or more dimensions.

In bulk materials, electrons occupy continuous energy bands, but as the dimensions shrink, these bands become discretized into quantized energy levels. This is due to the spatial confinement of the wave functions of charge carriers. In smaller structures, the effective bandgap becomes larger than that in bulk materials, making quantum confinement particularly useful in tunable light-emitting devices and next-generation photovoltaics. Quantum confinement typically results in an increase in the optical band gap of the material. For instance, the band gap energy (E_g) can be approximated by the equation:

$$E_g = E_g^{Bulk} + \frac{\hbar^2 \pi^2}{2m^* d^2} \tag{1.4}$$

Where E_g^{Bulk} , the band gap energy of the bulk material is, m^* is the effective mass of the charge carriers, and d is the dimension of the nanostructure [46].

1.2.3.3 Strain engineering

Strain can be applied to materials by altering their lattice constants through mechanical deformation or by growing them on substrates with mismatched lattice parameters. Tensile or compressive strain modifies the atomic spacing, thereby shifting the energy levels of the conduction and valence bands. For example, in thin films, tensile strain usually reduces the bandgap, making the material more efficient for infrared applications, while compressive strain tends to increase the bandgap. This method is particularly useful in heterostructures and multilayered devices [47,48].

The key effect of strain on materials is the deformation of the conduction and valence bands. Strain affects these bands by altering the effective mass of charge carriers (electrons and holes) and changing the curvature of the bands, leading to either band gap widening or narrowing. In certain materials, tensile strain can shift the CBM and VBM positions, transforming an indirect band gap material into one with a direct band gap. This is highly beneficial in optoelectronic devices where efficient light absorption or emission is critical [49,50]. Tensile strain generally causes a reduction in the optical band gap. This is because it elongates the bonds between atoms, thereby reducing the overlap

between atomic orbitals. Compressive strain typically increases the band gap by increasing the overlap of atomic orbitals, which enhances the bonding interaction between atoms. This often leads to more tightly bound electron-hole pairs (excitons), increasing the optical band gap and enhancing the material's stability. Perovskite oxides, such as $SrTiO_3$ (STO) and $BaTiO_3$ (BTO), are highly sensitive to strain, making them ideal candidates for optical band gap tuning through strain engineering. $SrTiO_3$, when subjected to tensile strain, undergoes a significant reduction in its optical band gap, which can improve its performance in visible-light photocatalysis and photovoltaic applications. For example, tensile strain has been shown to reduce the band gap from ~3.2 eV to values closer to ~2.5 eV, enabling enhanced absorption in the visible range [51,52].

1.2.3.4 Surface, interface engineering & oxygen vacancy regulation

Surface and interface engineering are pivotal in tailoring the optical band gap and energy levels of materials, especially in semiconductor technologies. By modifying the surface or interface properties, one can influence the electronic structure and, consequently, the optical behavior of materials. Surface states are electronic energy levels localized at the surface of a material, distinct from the bulk states. These states arise due to the disruption of the periodic potential at the surface, leading to localized energy levels within the band gap. They can significantly influence the optical properties by introducing additional pathways for electron transitions. In nanostructures, surface states can facilitate charge carrier recombination or enhance conductivity near the surface, thereby affecting the optical band gap and overall optical performances [53,54].

Interface states occur at the junction between two materials, such as in semiconductor heterojunctions. These states can lead to the formation of interface dipoles and affect the alignment of energy bands between materials. The energy level alignment at interfaces is crucial for the performance of electronic and optoelectronic devices, as it influences charge transfer and recombination processes. Understanding and controlling interface states enable the engineering of desired energy level alignments, thereby optimizing device performance. Various surface treatment techniques, such as laser

surface treatment, chemical passivation, or coating, can alter the surface morphology and chemistry, leading to changes in optical properties. For example, laser surface treatment can modify the microstructure of the surface, resulting in enhanced optical absorption or reduced reflectivity. Similarly, applying anti-reflective coatings can minimize surface reflections and improve the transmission of optical components. By strategically engineering surface and interface states, and employing appropriate surface treatments, it is possible to tailor the optical band gap and energy levels of materials, leading to enhanced optical properties for specific applications [55,56].

Using oxygen vacancies to tune the band gap is another widely adopted strategy in materials science, particularly for oxide materials like $SrTiO_3$, ZnO, and TiO_2. Oxygen vacancies introduce localized states within the bandgap, modifying the electronic structure and optical properties of the material. Oxygen vacancies lead to the removal of oxygen atoms from the lattice, creating unfilled spaces. These vacancies introduce defect states within the bandgap, typically near the conduction band. This narrows the effective bandgap, allowing for lower energy photon absorption and making the material more responsive to visible light. By controlling the concentration of oxygen vacancies, the bandgap can be tailored [57–59]. High concentrations of oxygen vacancies can significantly reduce the bandgap, enhancing the optical absorption in the visible spectrum, which is beneficial for photocatalytic and photovoltaic applications. Oxygen vacancies often act as electron donors, increasing the free carrier concentration. This not only affects the optical properties but also improves the electrical conductivity of the material. In materials like $SrTiO_3$, oxygen-deficient films exhibit increased conductivity due to the presence of free electrons from the vacancies [60].

1.2.4 Luminescence

Luminescence refers to the emission of light from a material when electrons, excited by external stimuli, release energy as they return to their ground state. This phenomenon occurs without the significant generation of heat, distinguishing it from incandescence, where light is produced due to thermal excitation. Luminescence can be

triggered through various mechanisms, such as exposure to light, electric fields, or chemical reactions, making it a versatile area of study in both fundamental and applied science. The key types of luminescence are based on the excitation source are photoluminescence, electroluminescence, chemiluminescence, bioluminescence, cathodoluminescence, thermoluminescence, radio luminescence and sono luminescence [61–64]. Among these various class part of this thesis work focus on photoluminescence.

1.2.4.1 Photoluminescence

Photoluminescence (PL) is a crucial tool for investigating the electronic and optical properties of materials, providing insights into their band structure, defects, and recombination mechanisms. When a material absorbs photons, it excites electrons from the valence band to the conduction band, creating electron-hole pairs. As these charge carriers recombine, they emit photons, which can be analyzed to reveal the energy gap, defect states, and impurity levels in the material [65]. The PL spectrum is influenced by factors such as temperature, excitation wavelength, and the quality of the crystal lattice, making it a versatile tool in material science. For semiconductors and nanostructures, PL is indispensable in characterizing the band gap and excitonic features, which are critical for applications in optoelectronic devices such as light-emitting diodes (LEDs), lasers, and solar cells.

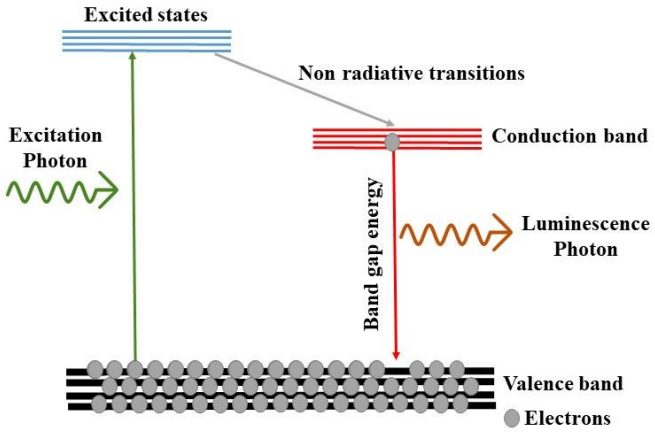

Figure 1- 3 Mechanism of PL emission.

In addition to studying intrinsic properties, PL can also help optimize material performance by identifying defects and impurities that affect efficiency. For example, oxygen vacancies or transition metal impurities often introduce localized states in the band gap, resulting in characteristic emission peaks in the PL spectrum. These defect-related emissions provide a non-destructive way to detect and quantify defects, which is vital for improving material quality in electronic and optoelectronic applications [66–68]. The mechanism of PL emission is represented in Fig 1-3.

PL plays a significant role in the study of emerging materials like perovskites and 2D materials, where it aids in tuning optical bandgaps for specific applications like photovoltaics and photodetectors. PL studies on oxide perovskites like $SrTiO_3$ often focus on understanding the material's band gap, defect-induced emissions, and how doping or surface engineering affects its optical behavior. Photoluminescence of $SrTiO_3$ has been extensively investigated since the 1960s as a valuable method for extracting information regarding the band gap, impurities, dopants, and defect-related energy levels. However, interpreting the PL spectra of STO can be challenging due to the variety of specimens studied, which differ in growth methods, doping levels (doped vs. undoped), stoichiometry, and processing states, as well as the diverse excitation conditions employed. Carrier dynamics in $SrTiO_3$ remain poorly understood due to the influence of both intrinsic factors, such as strong electron–phonon interactions, and extrinsic factors, including impurities and defects, on the optical responses and carrier recombination dynamics [69–71]. Under intense photoexcitation, it is observed that defect and impurity photoluminescence (PL) saturates, allowing intrinsic carrier recombination processes to emerge. Specifically, PL spectrum was detected in the blue spectral region at room temperature and under intense photoexcitation. Spectroscopic data of undoped, La-doped, Nb-doped, and Ar^+-irradiated STO crystals also reveal intrinsic properties of the system [72]. In undoped STO, a broad green PL appears at around 2.5 eV at low temperatures under weak continuous wave laser excitation, influenced by extrinsic defects and impurities. With intense pulse laser excitation, a blue PL band appears in undoped STO at both low and room temperatures. Time-resolved PL spectra at low

temperatures reveal three components: a sharp peak at 3.2 eV and a broad band around 2.9 eV, while the room temperature spectrum shows a broad blue PL band at approximately 2.9 eV. This blue PL does not depend on excitation intensity or delay time, suggesting it is not due to electron-hole plasmas (EHPs). Both undoped and electron-doped STO samples exhibit complex temperature-dependent PL spectra, with the green PL displaying a long decay time attributed to impurity centers or self-trapped excitons. Ultimately, the observed blue PL is a critical probe for investigating intrinsic carrier recombination processes in STO crystals [73–75].

Oxygen vacancies in STO play a significant role in influencing its photoluminescence (PL) properties. Studies have shown that the presence of oxygen vacancies results in a broad emission band in the visible region, often centered on 2.5–2.9 eV, which is attributed to defect-related transitions. The intensity and energy of this emission can vary depending on the concentration of oxygen vacancies, excitation conditions, and temperature. PL characteristics associated with oxygen vacancies can be tuned through various techniques such as doping with transition metals or rare earth elements, adjusting the stoichiometry during synthesis and employing thermal treatments [76].

1.2.5 Transparent conducting oxides & applications

Transparent conducting oxides (TCOs) are materials that uniquely combine optical transparency with electrical conductivity, making them critical for advanced optoelectronic applications. Their functionality arises from a wide band gap, typically above 3 eV, which allows visible light to pass through while still permitting electron conduction via doped or intrinsic defects. The fine balance between transparency and conductivity is a critical area of research, with doping strategies and defect engineering significantly altering their electronic structure. TCO materials such as indium tin oxide (ITO) and doped zinc oxide (ZnO) are widely used in photovoltaic cells, displays, and smart windows [77,78]. TCOs play a crucial role in solar cells, where they function as front electrodes in thin-film technologies. Their dual capability of transmitting light

while conducting electricity is essential for efficient charge collection. Fluorine-doped tin oxide (FTO) is particularly favored in dye-sensitized solar cells (DSSCs) due to its stability under high-temperature processing and exposure to electrolytes. In the realm of displays and touch panels, indium tin oxide (ITO) dominates as a transparent conductive layer, facilitating capacitive sensing and current flow without compromising visual clarity. These properties are indispensable for modern interactive devices such as smartphones, tablets, and monitors [79,80].

Beyond these applications, TCOs enable innovative technologies such as smart windows, where electrochromic layers dynamically regulate light and heat transmittance to improve energy efficiency in buildings and vehicles. In thin-film transistors (TFTs), TCOs like indium gallium zinc oxide (IGZO) serve as channel materials, offering high carrier mobility and faster response times, crucial for advanced displays. Transparent heaters based on TCOs find applications in sectors like automotive and aerospace for defogging and de-icing, showcasing their versatility in combining optical transparency with functional conductivity.

The properties are a result of their electronic structure, where doping introduces shallow donor states near the conduction band. The dual functionality stems from wide bandgaps (>3 eV) that permit visible light transmission while preventing significant absorption, and high free carrier concentrations ($\sim 10^{20}$-10^{21} cm^{-3}), achieved through doping or intrinsic defects like oxygen vacancies. This enables TCOs to behave as degenerate semiconductors, where the Fermi level lies within the conduction band [81]. Key optical characteristics include a transmission window spanning 0.4-1.5 μm, where shorter wavelengths are absorbed due to the bandgap, and longer wavelengths are reflected at the plasma edge. The Burstein-Moss effect, caused by band filling at high carrier concentrations, shifts the absorption edge to higher energies, effectively widening the optical bandgap. Classical and quantum models, such as the Drude theory and Lorentz oscillator model, describe these phenomena, linking optical and electronic properties to carrier dynamics, effective mass, and scattering mechanisms [78,82].

The electrical conductivity of TCOs is governed by the factors like carrier concentration, mobility, and scattering. Mobility is influenced by parameters such as concentration of ionized impurities, lattice vibrations, and grain boundaries. Higher carrier concentrations enhance electrical conductivity but also intensify free-carrier absorption in the infrared region, necessitating an optimal trade-off between carrier density and mobility. The plasma frequency, governed by carrier concentration and effective mass, defines the onset of reflectivity in the infrared spectrum, influencing optical transparency. Additionally, at elevated doping levels, band parabolicity alters the effective mass and carrier scattering mechanisms, thereby affecting both charge transport dynamics and optical response [83].

The evolution of TCO technologies hinges on systematic advancements in material science, integrating innovative synthesis methodologies with rigorous structural and optoelectronic characterization. Key optimization parameters include defect engineering, crystallographic refinement, and the development of low-effective-mass semiconductors to maximize carrier mobility. Advanced optical metrology techniques—such as variable-angle spectroscopic ellipsometry and broadband reflectance spectroscopy—quantify critical optoelectronic properties, including wavelength-dependent complex refractive indices and absorption coefficients. Concurrently, electrical transport analyses employing Hall effect measurements, thermoelectric characterization (Seebeck coefficient), and magnetotransport studies (Nernst effect) elucidate intrinsic charge transport phenomena, scattering mechanisms, and band structure modifications. These empirical correlations between structural/electronic properties and performance metrics directly inform iterative material design paradigms, prioritizing synergistic enhancements in conductivity and optical transparency. Emerging strategies, such as combinatorial high-throughput screening and codoping schemes to modulate defect chemistry, are accelerating the discovery of novel TCO compositions. Continued progress in these domains is expected to enable next-generation optoelectronic applications, including high-efficiency tandem photovoltaics and ultrathin transparent transistors, by leveraging

tailored charge transport and broadband transparency at reduced interfacial losses [84,85].

1.2.5.1 Transparent conducting oxides-classification

TCO's are broadly categorized into n-type and p-type TCOs, based on the dominant charge carriers responsible for conductivity. In n-type TCOs, the conduction band is primarily derived from the s-orbitals of metal cations such as Sn in SnO_2, In in In_2O_3, or Zn in ZnO. These s-orbitals contribute to a parabolic conduction band structure, characterized by a low effective mass of electrons. This low effective mass facilitates higher carrier mobility, which is essential for applications requiring efficient charge transport, such as solar cells and transparent electrodes. The wide bandgap of n-type TCOs, typically greater than 3 eV, ensures that the materials remain optically transparent in the visible spectrum while allowing conduction in the higher energy range, making them ideal for optoelectronic devices. Furthermore, doping with donor elements such as F (in FTO), Al (in AZO), or Sn (in ITO) increases free carrier concentration, enhancing conductivity without significantly affecting transparency [86].

The electrical conductivity in n-TCOs arises from the presence of free electrons, typically introduced through doping with aliovalent elements or intrinsic defects like oxygen vacancies. Common examples of n-TCOs include indium tin oxide (ITO), aluminum-doped zinc oxide (AZO), fluorine-doped tin oxide (FTO), and gallium-doped zinc oxide (GZO). These materials are characterized by high carrier mobility, low resistivity, and tunable work functions, enabling their seamless integration into optoelectronic systems [87,88].

In addition to these widely recognized n-TCOs, emerging materials such as perovskite-based transparent conductors are garnering significant interest. Perovskite oxides, such as $SrTiO_3$, $BaSnO_3$, and La doped $SrTiO_3$ offer a unique advantage due to their remarkable electron mobility and stability under extreme conditions. For example, $BaSnO_3$, doped with elements like lanthanum, exhibits exceptionally high room-temperature mobility, making it a promising candidate for high-performance TCOs.

Other noteworthy materials include cadmium oxide (CdO), hafnium-doped indium oxide (Hf), and cerium-doped tin oxide (Ce), which expand the range of applications due to their tailored properties such as high-temperature stability and enhanced optical transparency. These advancements, particularly in perovskite-based TCOs, represent a significant step toward sustainable and efficient optoelectronic devices, with ongoing research focused on optimizing synthesis methods and exploring earth-abundant alternatives for scalable production [86].

The p-type TCOs face inherent challenges due to the nature of their valence band structure. The valence band is largely composed of oxygen 2p orbitals or hybridized d-orbitals of transition metals such as Cu, Ni, or Co. These orbitals lead to a flatter band structure, resulting in a higher effective mass for holes. The higher effective mass limits the hole mobility, making it challenging to achieve high conductivity. Moreover, the tendency for oxygen vacancies in these materials to act as donors often suppresses the intrinsic p-type behavior. Despite these challenges, materials like Cu_2O, NiO, and delafossites (e.g., $CuAlO_2$) have emerged as promising candidates for p-type TCOs. Innovations in material design, such as co-doping and band structure engineering, aim to address the mobility and conductivity limitations, broadening the scope for applications like p-n junction diodes and transparent electronics [89–91].

The fundamental differences in band structure and mobility between n-type and p-type TCOs underline their distinct functionalities and challenges, driving ongoing research to enhance their performance and applicability.

1.2.5.2 n-type perovskite TCOs

Perovskite TCOs have emerged as a transformative alternative to conventional TCOs. These materials, with the general formula ABO_3, offer unique advantages derived from their structural flexibility and tunable electronic properties. The perovskite crystal structure, consisting of a large cation (A-site), a transition or post-transition metal (B-site), and oxygen atoms, enables remarkable chemical and structural stability while

allowing for extensive doping and defect engineering. These features provide unparalleled opportunities to design TCOs with optimized performance.

The most promising perovskite TCOs include n-type materials like strontium vanadate ($SrVO_3$), barium stannate ($BaSnO_3$), and strontium titanate ($SrTiO_3$), each of which exhibits unique properties tailored for specific applications. For instance, $SrVO_3$ boasts high carrier concentrations and conductivity, $BaSnO_3$ delivers exceptional electron mobility, and $SrTiO_3$ offers a balance of transparency and chemical stability. The wide bandgap of these materials (>3.0 eV) ensures minimal absorption of visible light, while their electronic configurations enable robust charge transport. These characteristics make perovskite TCOs ideal candidates for advanced optoelectronic devices, offering potential solutions to the limitations of traditional TCOs. Research into perovskite TCOs focuses on understanding and optimizing their properties through doping strategies, defect engineering, and innovative fabrication methods. These efforts aim to harness the full potential of perovskite oxides, paving the way for next-generation sustainable and high-performance optoelectronic technologies [92].

Strontium titanate is a perovskite oxide with a wide bandgap (~3.2 eV), offering excellent optical transparency in the visible spectrum and high chemical and structural stability. As an n-type transparent conducting oxide (TCO), it can achieve notable electrical conductivity and carrier concentrations through aliovalent doping with elements such as niobium (Nb), lanthanum (La), or antimony (Sb). Nb-doped STO (Nb) and La-doped STO (La) are particularly prominent, achieving carrier concentrations of $\sim 10^{20}$ cm^{-3} and moderate mobilities ($\sim 10\ cm^2 \cdot V^{-1} \cdot s^{-1}$). The conduction band minimum (CBM) is derived from Ti 3d orbitals, enabling reasonable electron transport properties, although the effective mass and scattering mechanisms limit mobility compared to other TCOs like $BaSnO_3$ (BSO). Despite these limitations, STO's ability to combine high transparency, chemical resilience, and tunable electronic properties makes it a versatile material for optoelectronic applications. The fabrication of high-quality STO films involves techniques such as pulsed laser deposition (PLD) and molecular beam epitaxy (MBE),

which allow precise control of stoichiometry and defect concentrations [93,94]. Oxygen vacancies (VO), which play a critical role in n-type conductivity, require careful management during growth to avoid excessive scattering and optical losses. Lattice-matching substrates, including $SrTiO_3$ itself or $(LaAlO_3)_{0.3}(Sr_2AlTaO_6)_{0.7}$ (LSAT), are often employed to enhance film properties by minimizing strain and dislocations. These efforts yield films with stable performance across varying environmental conditions, making STO particularly suitable for applications as a transparent electrode, a substrate for heterostructures, or an interface material in multilayer devices [95].

Strontium titanate exhibits a variety of intriguing optical properties, both in its pure form and when doped with different elements. Pure $SrTiO_3$ is transparent to visible light while absorbing ultraviolet (UV) light. This characteristic makes pure $SrTiO_3$ an excellent candidate for UV filtering and transparent optical components.

The high refractive index of $SrTiO_3$, typically around 2.4 in the visible spectrum, allows it to be used in applications requiring materials with significant light-bending capabilities. Its transparency, coupled with a high dielectric permittivity, makes it useful in optoelectronic devices and capacitors, where stable optical properties are crucial. When doped, $SrTiO_3$ exhibits significantly modified optical properties. Doping with elements like lanthanum (La), niobium (Nb), or rare earth elements introduces new electronic states within the band gap, thereby affecting the material's absorption and emission characteristics. For instance, doping with europium (Eu) or cerium (Ce) can induce photoluminescence, resulting in characteristic emission spectra that are valuable in lighting and display technologies [96,97].

Doping $SrTiO_3$ with lanthanum, praseodymium or niobium can also increase its electrical conductivity without compromising its optical transparency, making it a potential candidate for transparent conducting oxides. Additionally, the introduction of dopants can enhance nonlinear optical properties, such as second-harmonic generation (SHG), which are important for applications in frequency conversion and laser technologies. The optical absorption edge of $SrTiO_3$, which is around 3.2 eV, can be

shifted by doping, allowing for the tuning of its absorption properties for specific applications. This tunability makes doped $SrTiO_3$ suitable for use in UV detectors, where precise control over the absorption spectrum is required. Doped STO has shown enhanced photocatalytic activity under UV light, which is beneficial for environmental applications like water purification and air cleaning. The presence of dopants can also improve the photoelectric properties of $SrTiO_3$, enhancing its efficiency in photovoltaic devices and potentially leading to better-performing solar cells.

Praseodymium doped $SrTiO_3$, after being subjected to reduced atmosphere sintering, exhibits a unique combination of properties due to the generation of oxygen vacancies V_o. These vacancies enhance the material's electrical conductivity by providing additional charge carriers while simultaneously modifying the electronic band structure. This results in a high degree of tunability for the material's optical and thermoelectric performance. The presence of Pr ions and oxygen vacancies also increases infrared (IR) absorption, which can be precisely controlled by adjusting the Pr dopant level. This tunability of IR absorption is crucial in optoelectronic applications, where selective light absorption and emission are essential. The ability to modify both electrical conductivity and IR absorption through doping and sintering conditions makes Pr-doped $SrTiO_3$ an excellent candidate for opto-thermoelectric devices, which require materials capable of efficiently converting thermal and optical energy into electrical energy. The combination of good electrical conductivity and enhanced IR absorption suggests that Pr-doped $SrTiO_3$ could be integrated into solar photovoltaic (PV)-thermoelectric (TE) hybrid modules. In such systems, the material would not only convert solar energy into electricity via photovoltaic processes but also harvest waste heat through thermoelectric conversion. This dual functionality would improve the overall efficiency of solar energy systems by capturing both photon energy and thermal energy that would otherwise be lost.

In addition to these functional properties, the grain size and morphology of $SrTiO_3$ can influence its optical behavior. For example, smaller crystallite sizes can lead to increased grain boundary areas, which affect the material's scattering and absorption

characteristics. The ability to modify the optical properties of $SrTiO_3$ through doping makes it a highly versatile material for a wide range of technological applications. From UV filtering and transparent conductive oxides to advanced photonic and photovoltaic devices, both pure and doped STO offer promising potential. This versatility, combined with its inherent high refractive index and transparency, underscores the significant impact of $SrTiO_3$ in the field of material science and optoelectronics.

1.3 Thermoelectricity

The ever-growing demand for energy to support large-scale industrial operations and daily activities has led to greater fossil fuel consumption and higher greenhouse gas emissions. The depletion of fossil fuel reserves and the impact of global climate change have driven the search for alternative green energy sources, prompting extensive research efforts worldwide. Unlike fossil fuels, green energy sources such as solar, wind, hydro, and geothermal power produce minimal to no greenhouse gas emissions, significantly reducing carbon footprint [98]. Green energy sources are vital for a sustainable future as they offer a solution to the pressing challenges of environmental degradation and climate change. The efficient utilization of existing resources is just as important as the search for new energy sources. Recent statistics indicate that over 60% of the energy generated

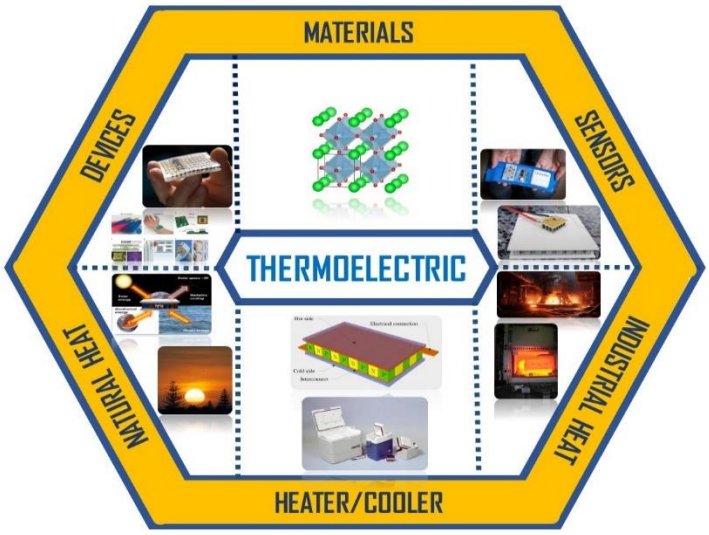

Figure 1- 4 Applications of thermoelectricity from materials to devices.

from primary sources is lost in the form of waste heat [99]. From an environment sustainability view point, scavenging this unused potential can make the usage of existing resources efficient.

Thermoelectricity (TE), the phenomenon of converting temperature gradient directly into electrical voltage and vice versa, offers a promising pathway for sustainable and efficient energy solutions. As the global demand for energy continues to escalate and environmental concerns intensify, the development of advanced thermoelectric materials becomes increasingly vital. Thermoelectric devices have the potential to harness waste heat from industrial processes, automobiles, and electronic devices, and converting it into useful electrical power as represented in Fig 1-4 [100]. This capability not only enhances energy efficiency but also contributes to reducing greenhouse gas emissions and dependence on fossil fuels. Since TE materials can convert the temperature differences between a hot end and ambient temperature directly in to electricity, they can be employed to harvest heat energy from natural sources like sun, geothermal and human body [101]. TE conversion relies on solid-state devices with no moving parts, resulting in robust, reliable, and low-maintenance operation. Thermoelectric systems are versatile and can function in diverse and extreme environments, making them suitable for a wide range of applications, from industrial processes to space missions.

Due to their low efficiency and high cost, TE materials are mainly used in highly specified areas, where reliability is more important than cost. Thermoelectric generators (TEGs) in automobiles use heat from the engine-exhaust systems, breaking systems to generate electricity, which can power vehicle electronics and increase the efficiency [102,103]. In space missions, thermoelectric generators are utilized to supply consistent power for spacecraft and rovers by converting heat from radioactive decay into electricity in conditions where solar power is unfeasible [104,105]. Portable coolers and heaters for food and beverages use thermoelectric modules to control temperature in an effective and compact manner. Thermoelectric technology is directly used in cryotherapy and serves as a power source for medical implants [106,107]. It also offers accurate temperature

control in medical applications, such as in portable insulin coolers and temperature-regulated surgical tools. Thermoelectric coolers help manage heat in consumer electronics, such as cooling computer processors, thereby enhancing performance and extending the lifespan of the devices [108]. Thermoelectric materials are integrated into renewable energy systems to improve efficiency, such as in hybrid solar-thermal panels. Hybrid thermoelectric-photovoltaic (HTEPV) panels can improve solar harvesting efficiency by recovering the heat dissipated by the PV stage via a thermoelectric (TE) stage [109].

Bismuth telluride (Bi_2Te_3) and its derivatives are the best-known commercially viable thermoelectric material in the bulk form for cooling and power generation in near room temperature region. However, their thermoelectric figure of merit (ZT) is not high enough to achieve macroscale practical applications. Moreover, thermal stability (with T_{max} around 600 °C) poses a challenge when used in high-temperature applications. Alloys based on bismuth telluride could not be appropriate for large-scale conversion due to the cost and scarcity of tellurium [110,111]. Over the years, numerous classes of materials have been developed and tested for their thermoelectric conversion efficiency, including tellurides, selenides, silicides, sulfides, clathrates, chalcogenides, oxides, half-Heusler compounds, and skutterudites. The performance of these diverse materials varies across different temperature ranges. Certain materials, such as Mg_3Sb_2, MgAgSb, Cu_2Se, and Bi_2Te_3-based compounds, perform particularly well at room temperature (Up to 250-300 °C). Whereas other class of materials like PbTe, SnSe, GeTe, BiCuSeO, Half-Heusler, SnTe, and Skutterudite perform well in mid temperature ranges (300-800 °C). Further research is essential to explore and develop thermoelectric materials capable of operating efficiently at high temperatures above 800 °C. This involves exploring highly stable compounds in forms of oxides, with particular emphasis on various forms of perovskite and delafossite materials [112–117].

Oxide-based thermoelectric materials deserve significant attention for several compelling reasons. They exhibit exceptional thermal and chemical stability, making

them ideal for high-temperature applications where other materials may degrade or lose efficiency. Additionally, oxides are often composed of abundant elements, alleviating concerns about resource scarcity compared to exotic thermoelectric materials. Their ability to be synthesized in various forms, such as perovskites and delafossites, allows for customized properties and optimized thermoelectric performance. Moreover, oxides typically have low toxicity and minimal environmental impact, aligning well with sustainability objectives. Recent advancements have demonstrated that certain oxide-based materials like $CaMnO_3$ and $SrTiO_3$ derivatives can achieve competitive thermoelectric efficiencies, particularly at elevated temperatures, further bolstering their suitability for practical applications [118–120].

The integration of optoelectronics and thermoelectricity presents exciting opportunities for advanced energy solutions. For example, hybrid devices can combine photovoltaic and thermoelectric technologies to maximize the conversion of solar energy into electricity. These integrated systems can significantly enhance the overall efficiency and reliability of renewable energy technologies, contributing to a more sustainable and energy-efficient future. The pursuit of optimizing both optoelectronic and thermoelectric materials involves a deep understanding of material science, solid-state physics, and engineering principles. This dual functionality of certain class of materials, especially perovskites offers opportunities for integrated devices that can harvest energy from both light and heat sources, providing enhanced energy efficiency and flexibility in diverse technological applications, from energy harvesting to advance sensing systems.

In its current form, thermoelectric devices have significant potential to complement and enhance current primary energy sources rather than outright replacing them. They excel in niche applications such as waste heat recovery and remote power generation where conventional sources are impractical or inefficient. However, for widespread adoption as a primary energy source, thermoelectric technology would need substantial advancements in efficiency and cost-effectiveness to compete with traditional energy sources like fossil fuels and renewable sources such as solar and wind. At the outset, the

thesis focuses on tuning the optoelectronic properties and improving the thermoelectric efficiency of $SrTiO_3$-based perovskite oxides using the following methods.

I. **Doping:** Introducing donor or acceptor impurities alters the band structure of host materials to achieve the desired density of states near the Fermi level, thereby regulating both optical bandgap, electrical and thermal conductivity.

II. **Regulation of oxygen vacancies:** Oxygen vacancies can alter the optical properties of materials by introducing localized electronic states within the bandgap, affecting absorption and emission spectra. These vacancies can also influence the material's transparency, luminescence behavior, and charge carrier dynamics, crucially impacting the performance of optoelectronic devices. They can introduce additional scattering centers for charge carriers, influencing electrical conductivity and the Seebeck coefficient. Moreover, they can modify the thermal conductivity by affecting phonon scattering mechanisms. Therefore, understanding and controlling the defect chemistry of oxygen vacancies is crucial for optimizing the thermoelectric performance of oxide materials.

III. **Quantum confinement:** Quantum confinement in thin film perovskites enhances thermoelectric properties by altering the electronic and phononic behavior at the nanoscale. In these thin films, reduced dimensions restrict the motion of charge carriers, leading to discrete energy levels and an increased density of states near the Fermi level leading to bandgap modification. Quantum confinement can also reduce thermal conductivity by increasing phonon scattering at the film boundaries, thereby minimizing heat transfer. This combination of enhanced electrical properties and reduced thermal conductivity boosts the thermoelectric figure of merit (ZT) in perovskite thin films.

1.4 Thermoelectric effects

The dynamics of charge carriers significantly influence the transport characteristics in materials. The interdependence of thermal and electrical conductivity is crucial in optimization of thermoelectric properties. The complex interplay between electrical and thermal gradients with charge carriers within materials results in a set of phenomena known collectively as thermoelectric effects.

1.4.1 Seebeck effect

A temperature gradient can be efficiently converted into a charge gradient, a phenomenon first observed by Seebeck in 1821 and known as the Seebeck effect. Seebeck demonstrated that heating the junction between two conductors can generate an electromotive force (EMF). This EMF can be monitored with a galvanometer or voltmeter, and the voltage generated is proportional to the temperature gradient at the thermocouple junction as represented in Fig 1-5 [121]. This temperature difference causes charge carriers to move from the hot end to the cold end, creating a charge imbalance known as thermoelectric potential. Eventually, the accumulation of carriers ceases, and the system reaches a steady state. However, further drifting of charge carriers and an increase in thermoelectric voltage can still occur with a greater temperature gradient.

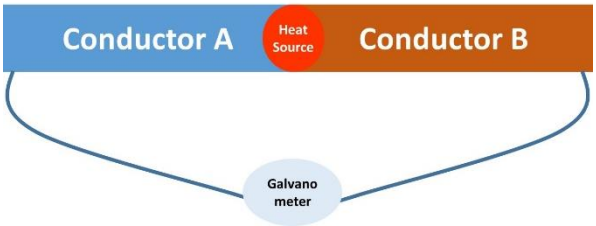

Figure 1- 5 Schematic representation of Seebeck effect.

The Seebeck coefficient (S), also known as thermopower, describes how a voltage gradient (ΔV) develops in response to a temperature difference (ΔT) across a material and represented as,

$$S = \frac{V_{Hot} - V_{cold}}{T_{Hot} - T_{cold}} = -\frac{\Delta V}{\Delta T} = -\frac{dV}{dT} \tag{1.5}$$

For a thermocouple made of two different materials A and B, with Seebeck coefficients S_A and S_B the Seebeck coefficient of the thermocouple junction is given by,

$$S = S_A - S_B \tag{1.6}$$

The voltage developed across the junction V_{AB} can be represented by eqn (1.6)

$$V_{AB} = \int_{T_1}^{T_2} (S_A - S_B)\, dT \tag{1.7}$$

Where T_1 and T_2 are the temperature at the hot and cold end. The Seebeck coefficient for semiconductors can be more complex to analyze compared to metals due to the presence of both electrons and holes as charge carriers and their temperature-dependent behavior. The Seebeck coefficient is negative when electrons are the dominant charge carriers, as they diffuse from the hot region to the cold region, making the hot side negative relative to the cold side and this behavior is observed for n type semiconductors. Conversely, for p type semiconductors the Seebeck coefficient is positive when holes are the primary carriers, as they move from the hot region to the cold region, making the hot side positive relative to the cold side. Thus, the sign of the Seebeck coefficient directly reflects the type of charge carrier and their direction of diffusion under a temperature gradient [122–124].

The Seebeck effect arises from the interplay between entropy and Fermi energy in carrier transport. The difference in entropy between the hot and cold regions drives the diffusion of charge carriers, creating a voltage that reflects this entropy difference. At the same time the position of the Fermi level influences the energy distribution and density of states of the carriers, affecting their response to a temperature gradient and thereby determining the sign and magnitude of the Seebeck coefficient. At the hot end, there will be a higher concentration of charge carriers above the Fermi level, while at the cold end, the population of carriers above the Fermi level will be lower, resulting in an imbalance as indicated in Fig. 1-6. On a microscopic point of view all thermoelectric

effects are connected with the transport of electrons and phonons and their mutual interactions.

These microscopic dynamics can be analyzed using Boltzmann transport equations (BTE). In this analysis, electrons can be treated using Fermi-Dirac statistics and phonons can be treated as quasi-particles using Bose-Einstein statistics using the following equations.

$$electron\ distribution\ function, f_0 = \frac{1}{e^{\left(\frac{\varepsilon(k)-\mu}{K_B T}\right)} + 1} \tag{1.8}$$

Where $\varepsilon(k)$ is the electron energy, μ is the chemical potential K_B is the Boltzmann constant and T is the absolute temperature.

$$Phonon\ distribution\ function\ f_0 = \frac{1}{e^{\left(\frac{\hbar\omega(q)}{K_B T}\right)} - 1} \tag{1.9}$$

Where $\hbar\omega(q)$ is the phonon energy. These distribution functions are temperature-dependent, and variations in population are anticipated as the temperature changes.

These equations together with scattering integral, thermal conductivity and relaxation time considerations eventually leads to the Seebeck Coefficient in a Semiconductor [125].

$$S = \frac{\pi^2}{2} \frac{{K_B}^2 T}{} \frac{\partial \ln \sigma(E)}{\partial} \Big| \tag{1.10}$$

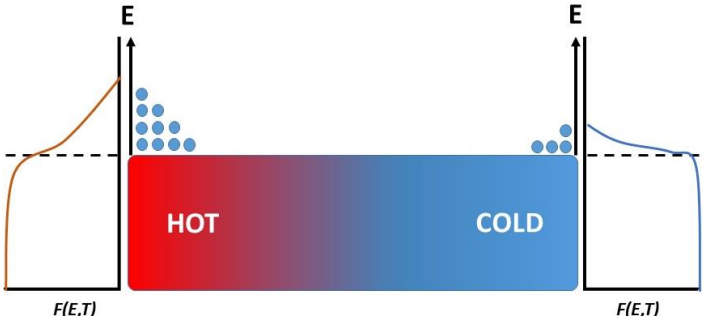

Figure 1- 6 Schematic representation of charge carrier imbalance near fermi level.

For a degenerated semiconductor with parabolic band dispersion, assuming that dopant does not change the scattering or band structure significantly eqn (1.10) become

$$S = \frac{8\pi^2 {K_B}^2}{3eh^2} m^* T \left(\frac{\pi}{3n}\right)^{2/3} \tag{1.11}$$

Where h, is the Planck's constant, m^* is the effective mass of carriers and n is the carrier concentration. Carefully modulating these parameters is needed to ensure efficiency of TE materials [126,127].

1.4.2 Peltier effect

The Peltier effect, discovered by Jean Charles Athanase Peltier in 1834, is a thermoelectric phenomenon wherein an electric current passing through a junction of two different conductors or semiconductors causes heat to be absorbed or released at the junction. This is mathematically described by the equation

$$Q = \pi I \tag{1.12}$$

Where Q represents the heat transfer, π is the Peltier coefficient, and I denotes the electric current. The Peltier coefficient π is related to the Seebeck coefficient (S) by the relationship with T being the absolute temperature. The schematic representation of Peltier effect along thermocouple AB is given in Fig 1-7.

$$\pi = ST \tag{1.13}$$

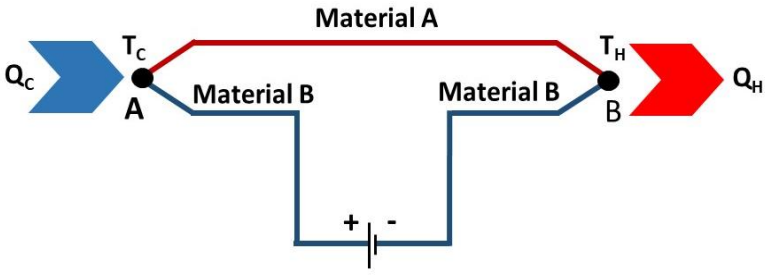

Figure 1- 7 Schematic representation of Peltier effect.

When a current flows through the junction, electrons and holes transport energy, leading to a cooling effect at one junction A and a heating effect at the other junction B. This makes the Peltier effect particularly useful in thermoelectric cooling devices, such as Peltier coolers, which are employed for precise temperature control in electronics, medical devices, and portable refrigerators. The efficiency of the Peltier effect depends on the material properties, including the Seebeck coefficient and thermal conductivity, which affect the magnitude of heat transfer and overall device performance. High-efficiency thermoelectric materials, like bismuth telluride (Bi_2Te_3) are commonly used to optimize these effects.

1.4.3 Thomson effect

The relationship between the Seebeck and Peltier effects was first identified and mathematically described by William Thomson, later known as Lord Kelvin, using principles of classical thermodynamics. He demonstrated a third thermoelectric effect that occurs within a single conductor rather than a thermocouple. When an electric current flows through a material with a temperature gradient as represented in Fig. 1-8, reversible heating or cooling occurs and is known as Thomson effect. Thomson demonstrated that a thermocouple operates as a heat engine, capable of using a temperature gradient to generate electricity, and conversely, using electrical energy to create a temperature gradient, similar to the function of a heat pump or refrigerator [128].

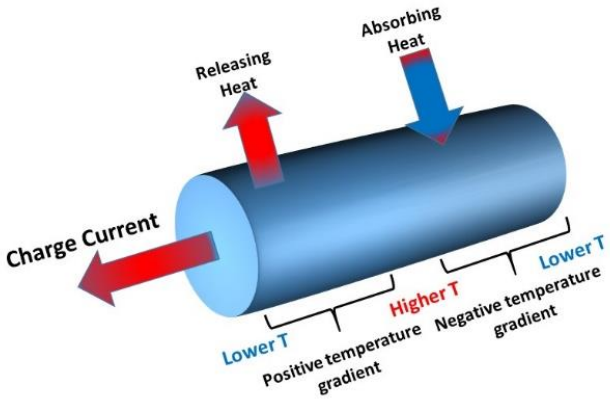

Figure 1- 8 Schematic representation of Thomson effect.

The two important kelvin relations are expressed in eqn 1.13 and 1.14. First equation connect seebeck coefficient S and Peltier coefficient π, whereas the second connects Seebeck and Thomson coefficient,τ.

$$\tau_A - \tau_B = T\frac{dS}{dT} \tag{1.14}$$

The rate of heating per unit length that occurs when a unit current passes through a conductor having a unit temperature gradient is known as the Thomson coefficient. Unlike the Seebeck and Peltier coefficients, which require a second material for calculation, the Thomson coefficient can be determined within a single material.

1.5 Magnetic field and thermoelectricity

Thermoelectric properties are determined by the transport of charge carriers, which can be influenced by external interactions such as magnetic fields. These interactions can significantly impact the performance of thermoelectric materials, leading to the emergence of new phenomena like the spin Seebeck effect, spin Peltier effect, Umkehr effect, Nernst effect, and Ettingshausen effect.

1.5.1 Magneto thermoelectric effect

Thermovoltage varies with the magnitude and direction of an applied external magnetic field, and in most of the cases, it increases. Studies on indium antimonide (InSb), thermovoltage shows a monotonic increase with magnetic field. The application of magnetic field along different crystallographic axes produces interesting results. The magneto-thermoelectric effect involves the influence of a magnetic field on the thermoelectric properties of a material, such as the Seebeck and Peltier effects. This phenomenon can lead to changes in electrical conductivity, thermal conductivity, and thermoelectric power when a magnetic field is applied. It is particularly significant in materials with high mobility of charge carriers, where the Lorentz force can alter the trajectory of electrons or holes, affecting heat and charge transport. Studying this effect is crucial for developing advanced thermoelectric devices that operate efficiently in

magnetic environments. The magneto-thermoelectric effect also has potential applications in magnetic sensors, energy harvesting, and cooling systems.

Topological Dirac and Weyl semimetals are an interesting class of materials where the applied field has a very strong effect on thermal and electronic transport properties. As an example, Cd_3As_2 is expected to be great potential for high thermoelectric performance because of the ultrahigh electron mobility (10^4– 10^6 cm^2 V^{-1} s^{-1}) leading to a large value of power factor [129]. Applying an external field in an appropriate direction can significantly enhance thermoelectric performance. It allows for the coupling of magnetic and thermoelectric parameters to measure the magneto-thermoelectric figure of merit for these materials. The magnetic field substantially decreases the electronic thermal conductivity and increases thermoelectric power, this combined action ultimately boosts the thermoelectric figure of merit.

1.5.2 Spin seebeck effect

A novel approach to thermoelectric generation, termed the spin Seebeck effect (SSE), was identified approximately two decades ago within the field of spintronics. Although thermoelectric generation based on spin properties remains in its early stages of development, it presents distinct advantages over traditional thermoelectric mechanisms. Over the past decade, this research direction have made significant advancements in terms of TE performance [130].

There are two measurement modes for SSE.

i. Transverse mode (Transverse spin Seebeck effect-TSSE)
ii. Longitudinal mode (Longitudinal spin Seebeck effect-LSSE)

The transverse spin Seebeck effect describes the spin current generation perpendicular to the temperature gradient, while the longitudinal spin Seebeck effect defined the spin current generation parallel to the temperature gradient.

The first reported results on SSE were obtained in transverse mode by Uchida et al., in 2008. A temperature difference ΔT was created across the plane of the ferromagnetic permalloy (NiFe) layer to generate a spin voltage [131]. Employing the

phenomenon of ISHE, this was measured at the ends of a platinum strip attached to the film perpendicular to the direction of temperature gradient as indicated in the Fig. 1-9.

The Pt detector transforms it to an electric field in y-direction according to the eqn (1.15) of the inverse spin Hall effect, ISHE,

$$\bar{E}_{ISHE=}\,\theta_{ISHE}\,\bar{J}_s \times \bar{\sigma} \tag{1.15}$$

Here, $\bar{J}_s$ carries a polarization $\bar{\sigma}$ parallel to the magnetization vector $\bar{M}$ of the ferromagnetic layer along temperature gradient ΔT applied in the x-direction. The spin current propagates in a plane perpendicular to the sample surface, which is aligned in the X-direction. An electric field generates an electrical voltage V_y, which is subsequently detected by a platinum strip deposited on the sample. The strength of the detected signal varies with the position of the platinum strip.

Additionally, the spin Seebeck effect (SSE) signal shows angular dependence on the direction of the applied magnetic field [130,132].

The alternative approach to SSE is the application of out-plane temperature gradient in magnetic-nonmagnetic bilayer structure known as the longitudinal mode represented in the Fig. 1-9.

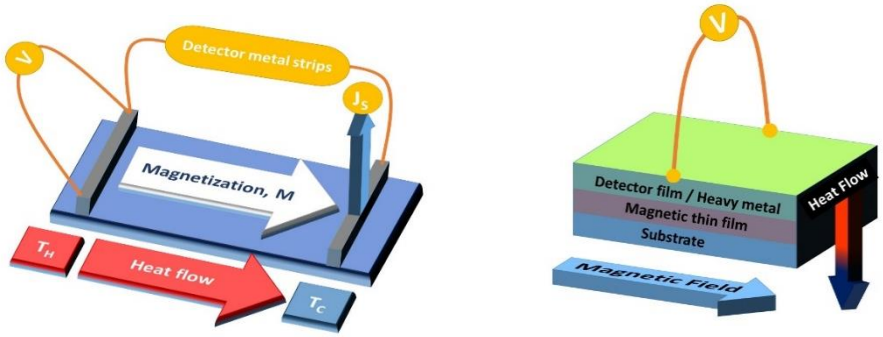

Figure 1- 9 Schematic diagram representing TSSE and LSSE.

It was first reported by Uchida et al., in a Pt/YIG bilayer on a GGG (Gadolinium Gallium Garnet) substrate. As the field becomes parallel to the temperature gradient, that signal decreases to zero. LSSE has been measured in several other materials as well signal are

screened by anomalous Nernst effect (ANE) signals. Even though the transverse spin Seebeck effect was first reported research groups across the world are more focussed on the longitudinal spin Seebeck effect since the former may accommodate parasitic effects like planar and anomalous Nernst effect [131,133] . The terms "transverse" and "longitudinal" in the context of the spin Seebeck effect (SSE) refer to the geometry of the temperature gradient and the resulting spin current, not the nature of the effect itself. Transverse SSE has a temperature gradient applied perpendicular to the spin current, while longitudinal SSE has the gradient and current aligned.

1.6 Efficiency of thermoelectric material

We can create devices for either power generation or refrigeration, utilizing fundamental thermoelectric effects. In practice, a thermoelectric generator (TEG) can be constructed using p-type and n-type materials maintained at a temperature gradient, with a load resistance connected across them, as illustrated in Fig. 1-10.

A TEG converts heat energy (Q) to electric power (P) with an efficiency η as per the eqn (1.16)

$$P = \eta Q \tag{1.16}$$

Efficiency of a generator can be expressed as

$$\eta = \frac{Work\ done\ by\ the\ engine}{Heat\ supplied\ to\ the\ engine} = \frac{W}{dQ/dt} = \frac{P_{electrical}}{Q_H} \tag{1.17}$$

With the assumptions that electrical and thermal conductivities, Seebeck coefficients of both p-type and n-type material are constant in a given leg of TE generator. The contact resistances are assumed to be negligible when compared to the material resistance of generator. The ends are connected to a load using ideal conductors with negligible Seebeck coefficient, ensuring that thermoelectric effects in the leads are disregarded.

The work done by the generator is accounted only after subtracting the joule heating term from Seebeck contribution,

$$W = P_{electrical} = S\Delta TI - \frac{I}{A}^{2} L\rho = S\Delta TI - I^2R \tag{1.18}$$

$$\frac{dQ}{dt} = IS\Delta T - \frac{\kappa A\Delta T}{L} - \frac{I^2\rho L}{2A} \tag{1.19}$$

$$\eta = \frac{IS\Delta T - I^2R}{\kappa\Delta T + IST - I^2R} \tag{1.20}$$

Here, κ represents the thermal conductivity, ρ is the material's resistivity, and L denotes the length. During TEG operation, the electrical conductivity, thermal conductivity, and Seebeck coefficient vary with temperature. To determine the maximum load current, I_{max} one can set the first derivative of the efficiency η in equation 1.20 to zero, leading to the result expressed in equation 1.21.

$$I_{max} = \frac{S\Delta T}{R\left(\sqrt{1 + \left(\frac{S^2}{R\kappa}\right)T + 1}\right)} \tag{1.21}$$

The term $\left(\frac{S^2}{R\kappa}\right)$ in the denominator is known as the figure of merit, $Z = \left(\frac{S^2}{R\kappa}\right)$. The term $\left(\frac{S^2}{R\kappa}\right)$ will have a maximum value when the product, Rk will have a minimum value. Substituting eqn (1.20) in (1.21), we will get the efficiency of a TEG

$$Efficiency\ of\ TEG, \eta = \frac{T_H - T_C}{T_H}\frac{\sqrt{(1 + ZT)} - 1}{\sqrt{(1 + ZT)} + {T_C}/{T_H}} \tag{1.22}$$

$$ZT = \frac{S^2\sigma}{\kappa}T \tag{1.23}$$

Here, ZT is known as the figure of merit of the thermoelectric material. The dimensionless figure of merit, ZT is the most significant parameter in the thermoelectric community as it directly determines the efficiency of converting heat to electricity. To maximize ZT, we need to optimize the following parameters: increase the Seebeck coefficient and electrical conductivity while minimizing thermal conductivity. This optimization frequently includes complex trade-offs, as improving one characteristic can adversely affect another. Materials with strong electrical conductivity may also have high electronic thermal conductivity, thereby reducing ZT. Nanostructuring and doping are adopted in advanced materials engineering to alter properties to attain high ZT values. [124,128].

Another useful parameter in defining the performance of thermoelectric materials is the thermoelectric power factor. It is a measure of a material's efficiency in converting heat to electrical energy and is given by the product of the square of the Seebeck coefficient (S^2) and the electrical conductivity(σ). We may rewrite the thermoelectric figure of merit as

$$ZT = \frac{Power\ factor}{\kappa}T = \frac{PF}{\kappa}T \tag{1.24}$$

A high power factor indicates that the material can produce a large voltage with minimal resistance, making it desirable for thermoelectric applications. Optimizing the power factor is crucial for enhancing the overall performance of thermoelectric devices. The defining terms in power factor, both S and σ are strongly dependent on carrier concentration. Another parameter that influences the figure of merit is the thermal conductivity, κ, but it is significantly affected by the lattice contribution than the carrier concentration.

1.7 Factors affecting thermoelectric efficiency

Thermoelectric efficiency is primarily determined by the material's electrical and thermal conductivities. For practical applications, the strategy is to maintain a reasonably high *ZT* across the operating temperature range rather than achieving a peak *ZT* at a specific temperature. This ensures consistent performance and efficiency over a wider range of conditions. One of the main objectives of thermoelectric research is the optimization of the Seebeck coefficient, thermal, and electrical conductivities to attain a maximum power factor. These interlinked parameters depend on carrier concentration and the material nature and the optimization strategy is represented in Fig. 1-10.

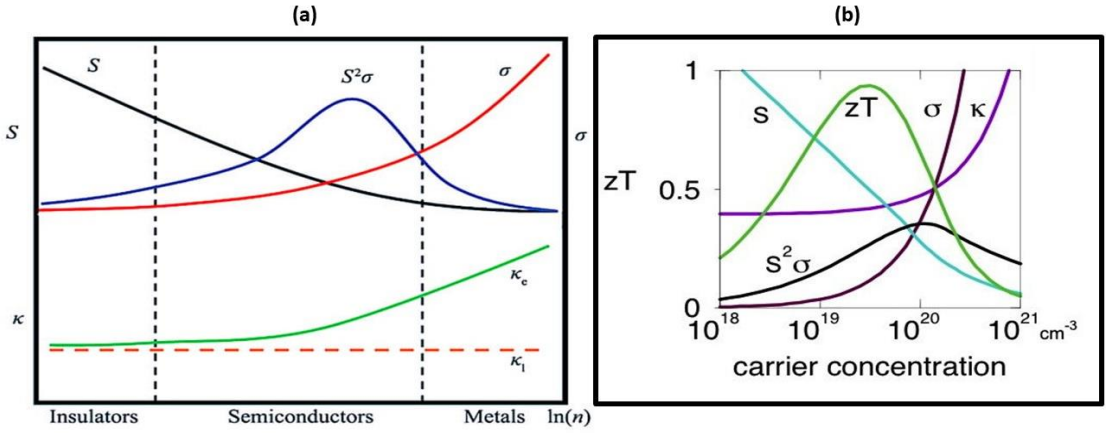

Figure 1- 10 (a) Power factor and **(b)** figure of merit dependence on carrier concentration for optimization strategy.

A metallic conducting material has a high carrier concentration, which results in good electrical and thermal conductivity, but the seebeck coefficient is too low to create a significant power factor. Insulators, on the other hand have low the carrier concentration, resulting in poor electrical conductivity. Even though the Seebeck coefficient is high, it is insufficient to achieve a reasonably high power factor. So semiconductors are the class of materials that maintains equilibrium across all of these characteristics, and they are the focus of TE research. Most of the promising thermoelectric materials are extensively doped semiconductors, which sufficient number of free electrons mimicking the behavior of metals. The concentration of charge carriers

is determined by both intrinsic defects including vacancies and the extrinsic defects due to the insertion of dopants in host lattice. Optimizing charge carrier concentration is a significant challenge in thermoelectric research. Achieving high ZT in a material requires balancing the interdependent and often conflicting relationships between the Seebeck coefficient, electrical resistivity, and thermal conductivity. This delicate optimization is essential for enhancing thermoelectric performance [134–136].

We may also define another performance indicator known as thermoelectric quality factor B, defined using the weighted mobility of charge carriers and lattice thermal conductivity.

$$B = \frac{8\pi k_B (2m_e)^{\frac{3}{2}}}{3eh^3}(k_B T)^{5/2}\frac{\mu_w}{\kappa_L} = \frac{B_E T}{\kappa_L} \tag{1.25}$$

As per eqn (1.25), the quality factor has an electronic contribution indicated by B_E and a thermal counterpart determined by lattice thermal conductivity.

1.7.1 Thermal conductivity

Thermal conductivity describes a material's ability to conduct heat. It is quantified by the amount of heat that passes through a material per unit time, per unit area, and per unit temperature gradient schematically represented in Fig 1-11. This transport coefficient κ is connected to the temperature gradient ΔT and heat flux q by the Fourier law as in eqn (1.26)

$$q = \kappa \Delta T \tag{1.26}$$

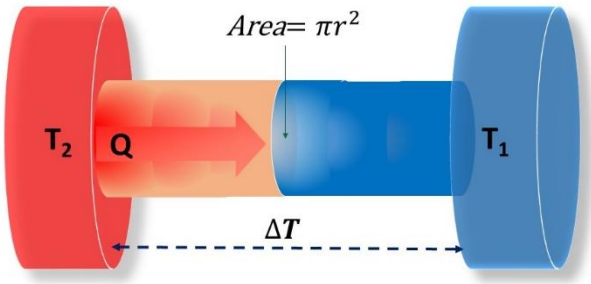

Figure 1- 11 Schematic representation of heat flow and concept of thermal conductivity.

In conduction, heat is transferred between particles through molecular vibrations and the movement of free electrons, facilitating energy exchange [137]. In the heat transport in metals and semiconductors, the role of charge carriers and lattice are assumed to be independent, and are represented by their own unperturbed wave functions.

Then, the total thermal conductivity κ will be,

$$\kappa = \kappa_e + \kappa_l \tag{1.27}$$

There are still other terms like spin current contributing to the thermal conductivity, but it is fractionally too low to be accounted. When an external electric potential is applied, it causes a current to flow through the medium, allowing us to define the electric current density. Similarly, when a thermal gradient is applied across a material, it generates a heat current density J_Q. It is represented as a vector aligned with the direction of heat flow, with a magnitude representing the average thermal energy per unit time crossing a unit area perpendicular to the flow. Based on the kinetic theory, the heat current density will be,

$$J_Q = \frac{1}{3} l_e \bar{v} C_v (-\Delta T) \tag{1.28}$$

l_e, represents the electron mean free path and C_v is the electron specific heat per unit volume, and $\bar{v}$ represents the average velocity of the particles. Eqn (1.28) is a statement of Fourier law with thermal conductivity k_e is represented as,

$$\kappa_e = \frac{1}{3} l_e \bar{v} C_v \tag{1.29}$$

According to Drude model the specific heat of electrons is represented as

$$c_v = C_m \frac{n}{N_A} = \frac{3}{2} N_A k_B \frac{n}{N_A} = \frac{3}{2} k_B n \tag{1.30}$$

On substitution we will get classical expression for electron thermal conductivity

$$\kappa_e = \frac{k_B n l_e \bar{v}}{2} \tag{1.31}$$

From eqn (1.31) we may deduce the well-established Wiedemann-Franz law.

Lattice vibrations play a major role in the thermal conductivity of all solids, regardless of their state. In-depth analysis of thermal conductivity requires investigating electron-phonon interactions. In this interaction, electrons are regarded as Bloch waves and follow Fermi-Dirac statistics while, vibrating metal ions show minor displacements from their equilibrium positions, and they are modelled as harmonic oscillators that obey Bose-Einstein statistics. We may proceed to find the coupling constant of this interaction as

$$C_q = \frac{ie^2 z}{\left(1 + \frac{k_{TF}^2}{q^2}\right)\varepsilon_0 q^2 V_0}\sqrt{\frac{N\hbar}{2M\omega_q}\left(q.\widehat{e_q}\right)} \tag{1.32}$$

Here polarization is assumed to be either longitudinal or transverse to the phonon wave vector q, and z is charge state of an ion, ε_0 permittivity of free space k_{TF} Thomas-Fermi wave vector, N is the number of modes or particles (could refer to atoms or phonon modes), ω_q Phonon frequency associated with the wave vector q, $\widehat{e_q}$ is unit vector representing the direction of the wave vector or polarization of the phonon. Finding, square of the coupling constant in long wavelength limit we get,

$$\left|C_q\right|^2_{q\to 0} = \frac{2\pi^2}{3}\frac{zE_F^2\hbar\omega_q}{v_s^2 k_F^3 V_0 M} = \lambda\frac{\hbar\omega_q}{2N(0)V_0} \tag{1.33}$$

With $N(0)$ being the density of states per spin at the Fermi level and λ is a dimensionless parameter. With this coupling constant we may proceed to find the collision integral as,

$$\begin{aligned}\left(\frac{\partial f}{\partial t}\right)_{coll} = -\frac{2\pi}{\hbar}\sum_{k'\alpha}|C|^2\Big\{&\left[f_k\left(1-f_{k'}\right)\left(1+N_{-q}\right) - f_{k'}(1-f_k)N_{-q}\right]\delta\left(E_{k'}\right.\\ &\left.- E_k + \hbar\omega_{-q}\right)\\ &+\left[f_k\left(1-f_{k'}\right)N_q - f_{k'}(1-f_k)\left(1+f_k\left(1-f_{k'}\right)\right)\right]\delta\left(E_{k'}\right.\\ &\left.- E_k - \hbar\omega_q\right)\Big\}\end{aligned} \tag{1.34}$$

The functions such as $f_k(1-f_{k'})$ is included here as a result of Pauli Exclusion Principle. N_q and N_{-q} represent phonon distribution functions in emission and absorption. In equation (1.34) the influence of electron-phonon interactions on electron distribution function is represented. The interaction also affect the phonon distribution function and is described as,

$$\left(\frac{\partial N_q}{\partial t}\right)_{coll} = -\frac{2\pi}{\hbar}|C_q|^2 \sum_{k\sigma}\left[(1-f_{k+q})f_k N_q - (1-f_k)f_{k+q}(N_q+1)\right]\delta(E_{k+q} - E_k - \hbar\omega_q) \tag{1.35}$$

Just like the summation for electron wave function represented in equation (1.34) done over all possible phonon states, in equation (1.35) summation is done over all possible electron states. After linearizing the terms, we get,

$$\left(\frac{\partial N_q}{\partial t}\right)_{coll} = -\frac{2\pi}{\hbar}|C_q|^2 \sum_{k\sigma} f^0(E_k)\left[1-f^0(E_{k+q})\right]N_0(\omega_q)\delta(E_{k+q} - E_k - \hbar\omega_q)(\varphi_k - \varphi_{k+q} + \emptyset_q) \tag{1.36}$$

Introducing the term relaxation time τ_{p-e} and substituting for coupling constant from equation (1.32) we get,

$$k_{p-e}(T) = G\left(\frac{T}{\theta_D}\right)^2 J_3\left(\frac{\theta}{T}\right) \tag{1.37}$$

The coefficient G is,

$$G = \frac{{K_B}^3 h\theta_D^2 M}{2\pi^2 m_e^2 a^3}\sum_{J=1}^{3}\frac{1}{c_j^2} \tag{1.38}$$

Where the mass of ions are represented by M, coupling constant of electron-phonon interaction is represented by c_j^2 and j represents one longitudinal and two transverse branches [137].

At high temperatures

$$k_{p-e}(T) \cong \frac{G}{2} \quad for\ T \geq \theta_D \tag{1.39}$$

At low temperatures

$$k_{p-e}(T) \cong 7.18G\left(\frac{T}{\theta_D}\right)^2 \quad for\ T \ll \theta_D \tag{1.40}$$

Here θ_D refers to the Debye temperature. At high temperatures, phonon thermal conductivity, affected by electron scattering, becomes temperature-independent, but it rapidly declines at low temperatures due to increased electron scattering, showing that electrons effectively regulate heat flow by phonons. High temperatures cause the total lattice thermal conductivity to never approach the levels shown in equation (1.32) because the phonon-phonon Umklapp processes are significantly more effective than electrons in scattering phonons. However, one significant limiting factor for the lattice thermal conductivity of metals at low temperatures is phonon-electron scattering.

The phonon-phonon interactions in lattice is divided to two

1. Normal process (N- Process)
2. Umklapp process (U-Process)

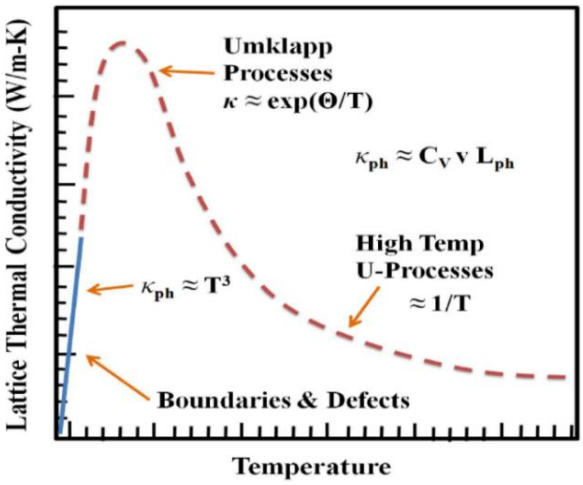

Figure 1- 12 Possible phonon scattering mechanisms and thermal conductivity.

The U-process generates a third phonon, altering the phonon momentum and contributing to thermal conductivity. In contrast, the N-process does not change the net phonon momentum. At moderately high temperatures, the U-process is the main phonon scattering mechanism, significantly impacting lattice thermal conductivity as $k_{ph} \propto {}^{1}/_{T}$ At low temperature, phonon contribution is relatively small and the phonon scattering at the grain boundaries will be prominent and $k_{ph} \propto T^3$. In the mid temperature range both these effects have competitive role as represented in Fig. 1-12.

1.7.2 Electrical conductivity

Electrical conductivity is the measure of a material's ability to allow the flow of an electric current, quantified by the inverse of electrical resistivity. Materials with high electrical conductivity, such as metals facilitate the efficient transmission of electric signals, making them essential for various electrical and electronic applications. Based on the classical free electron theory by Drude and Lorentz, electrical conductivity is expressed as equation (1.41). Where n, the number of charge carriers/unit volume is, τ_e is the relaxation time, e and m are the electron charge and mass respectively.

$$\sigma = \frac{ne^2\tau_e}{m} \tag{1.41}$$

However, the theory was unable to differentiate between metallic conductors and insulators in terms of the conduction process. This problem is addressed by the quantum picture of electron interaction with periodic potentials in a crystal lattice, which suggests the creation of energy bands. While each atom has a distinct energy level, the energy levels of solid materials are too close together to create an energy band. The band diagrams differentiating metals, semiconductor and insulator are represented in Fig. 1-13. In metals, the valence band and conduction band overlap, allowing free movement of electrons and resulting in high electrical conductivity. In semiconductors, a small band gap exists between the valence band and the conduction band, which can be overcome by thermal energy or doping, enabling controlled conductivity. In insulators, the band gap

is large, preventing electrons from easily moving to the conduction band, thus resulting in very low electrical conductivity.

For an intrinsic semiconductor at temperatures above 0 K, there will be enough thermal agitation to shift electrons to conduction band. The total conduction in that case will be sum of electron and hole conduction and represented as,

$$\sigma = n_e q_e \mu_e + n_h q_h \mu_h \tag{1.42}$$

Where n_e, q_e, μ_e are electron concentration, electron charge and mobility, n_h, q_h, μ_h are hole concentration, charge and mobility. In intrinsic region number of holes will be same as number of electrons. So eqn (1.27) becomes,

$$\sigma = n_e q_e (\mu_e + \mu_h) = nq\mu \tag{1.43}$$

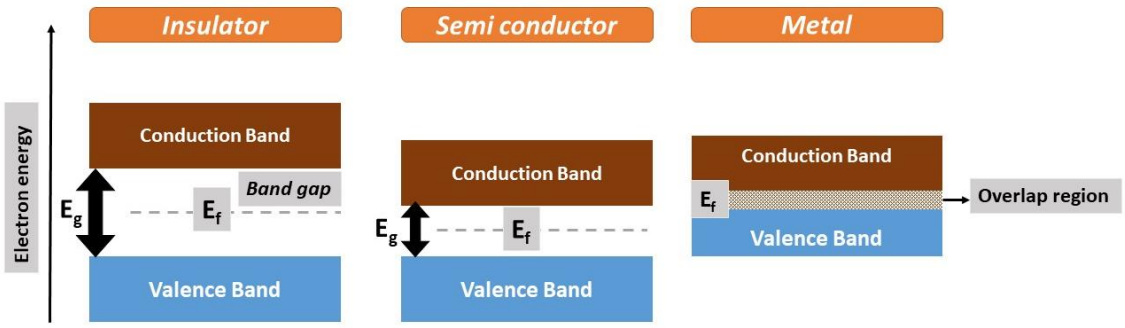

Figure 1- 13 Energy band diagrams of metals, semiconductors and insulator.

1.7.3 Transport properties and thermoelectricity in metals and semiconductors

The fermi distribution function of electron to be occupied in energy E is given by,

$$f_0(E) = \frac{1}{exp\left(\frac{E - E_F}{K_B T}\right) + 1} \tag{1.44}$$

The distribution function can be approximated to unity if $(E - E_F) \ll 1$ and the function will be zero for $(E - E_F) \gg 1$. Representing the number of states within the energy level E and $E + \Delta E$ as $g(E)dE$, number of electrons n is,

$$n = \int_0^\infty f_0(E)g(E)dE \tag{1.45}$$

The conduction process is governed by partially filled states where electrons are free to flow; it cannot occur for empty or completely filled states. In metals, the Fermi level is well within the conduction band, hence there will be a large number of electrons available for conduction. In insulators, the Fermi level is within the band gap, which indicates no free electrons are available. For semiconductors, the fermi level is near to the conduction band, and only a few electrons can contribute to conduction

Electron density of states is represented as,

$$g(E)dE = \frac{4\pi e(2m^*)^{3/2}\tau}{h^3}dE \tag{1.46}$$

Here m^* is the effective mass. The same kind of transport equations will govern hole conduction where the energy is measured downward with respect to Fermi level. In terms of relaxation time τ_e , the change in distribution function is expressed as,

$$\frac{df(E)}{dt} = -\frac{f(E) - f_0(E)}{\tau_e} \tag{1.47}$$

We may express the relaxation time as $\tau_0 E^r$. In most of the TE materials the scattering mechanism is governed by acoustic phonons, for which $r = -1/2$. Based on Boltzmann transport equations, taking the variations in FD distribution function as small,

$$\frac{f(E) - f_0(E)}{\tau_e} = u\frac{df_0(E)}{dE}\left(\frac{dE_f}{dx} + \frac{(E - E_f)}{T}\frac{dT}{dx}\right) \tag{1.48}$$

u is the velocity of charge carriers. Based on eqn (1.46) the current density may be expressed as in eqn (1.49).

$$i = \mp\int_0^\infty euf(E)\ g(E)dE \tag{1.49}$$

The heat flux density may be represented as,

$$j = \int_0^\infty u\left(E - E_f\right)\ F(E)g(E)dE \tag{1.50}$$

Here $\left(E - E_f\right)$ can be treated as the amount of energy carried over by the electrons or holes. There isn't any form of flow when $f = f_0$, and drift velocity has little contribution to total velocity, Replacing f by $f - f_0$ and u by $\frac{2E}{3m^*}$ we will write eqn (1.49) and (1.50) as,

$$i = \mp\frac{2E}{3m^*}\int_0^\infty g(E)\tau_e\, E\,\frac{df_0(E)}{dE}\left(\frac{dE_f}{dx} + \frac{\left(E - E_f\right)}{T}\frac{dT}{dx}\right)\, dE \tag{1.51}$$

$$j = \pm\frac{E_F}{e}i + \frac{2}{3m^*}\int_0^\infty g(E)\tau_e\, E^2\,\frac{df_0(E)}{dE}\left(\frac{dE_f}{dx} + \frac{\left(E - E_f\right)}{T}\frac{dT}{dx}\right)\, dE \tag{1.52}$$

Applying the proper boundary conditions,

$$Electrical\ conductivity, \sigma = |Ratio\ of\ i\ to\ the\ electric\ field|_{\frac{dT}{dX}=0}$$

$$thermal\ conductivity_{Electronic}, \kappa_e = |Ratio\ of\ j\ to\ (-dT/dx)|_{i=0}$$

The three quantities entering in TE figure of merit may be expressed as,

$$\sigma = \frac{1}{\rho} = \frac{-2e^2}{3m^*}\int_0^\infty g(E)\tau_e\ \frac{df_0(E)}{dE}\,dE \tag{1.53}$$

$$k_e = \frac{2}{3m^*T}\left\langle\left\{\frac{\left[\int_0^\infty g(E)\tau_e E^2\ \frac{df_0(E)}{dE}dE\right]^2}{\int_0^\infty g(E)\tau_e\ \frac{df_0(E)}{dE}dE}\right\} - \int_0^\infty g(E)\tau_e E^3\ \frac{df_0(E)}{dE}dE\right\rangle \tag{1.54}$$

Finally the Seebeck coefficient S may be represented as,

$$S = Ratio\ of\ i\ to\ the\ electric\ field\ to\ temperature\ gradient$$

$$S = \frac{\pm 1}{eT}\left[E_f - \frac{\left[\int_0^\infty g(E)\tau_e E^2 \frac{df_0(E)}{dE} dE\right]^2}{\int_0^\infty g(E)\tau_e E \frac{df_0(E)}{dE} dE}\right] \tag{1.55}$$

Expressing the transport coefficients as an integral,

$$K_s = \frac{-2T}{3m^*}\int_0^\infty g(E)\tau_e E^{s+1}\frac{df_0(E)}{dE} dE \tag{1.56}$$

Eliminating g and τ_e in favor of m^*, r and τ_0

$$K_s = \frac{8\pi}{3}\left(\frac{2}{h^2}\right)^{\frac{3}{2}} (m^*)^{\frac{1}{2}} T\tau_0 \left(s + r + \frac{3}{2}\right)(kT)^{s+r+\frac{3}{2}} F_{s+r+\frac{1}{2}} \tag{1.57}$$

Where the integral $F_n$is known as Fermi-Dirac integral. In terms of the integral K_s

$$\sigma = \frac{e^2}{T} K_1 \tag{1.58}$$

$$\kappa_e = \frac{1}{T^2}\left(K_2 - \frac{K_1^2}{K_0}\right) \tag{1.59}$$

$$S = \frac{\pm 1}{eT}\left(E_F - \frac{K_1}{K_0}\right) \tag{1.60}$$

These set of equations are of prime importance in determining TE figure of merit.

In analyzing the thermoelectric properties of materials, the position of Fermi energy with respect to thermal energy $k_B T$ plays an important role. If $E_F \gg k_B T$, degenerate approximation is valid taking the material as a conductor. FD integrals in this situation may be expressed as,

$$f_n(\eta) = \frac{\eta^{n+1}}{n+1} + n\eta^{n-1}\frac{\pi^2}{6} + n(n-1)(n-2)\eta^{n-3}\frac{7\pi^4}{360} + \cdots \tag{1.61}$$

The series is converging rapidly and to calculate electrical conductivity the first term is sufficient.

$$\sigma = \frac{8\pi}{3}\left(\frac{2}{h^2}\right)^{3/2} e^2 (m^*)^{1/2} \tau_0 E_F^{r+3/2} \tag{1.62}$$

First two terms are needed to determine electronic thermal conductivity, where we can directly employ Wiedemann-Franz law and concept of Lorentz number.

$$L = \frac{\pi^2}{3}\left(\frac{\kappa}{e}\right)^2 \tag{1.63}$$

The seebeck coefficient calculation in metals requires first two terms in the series

$$S = \mp \frac{\pi^2}{3}\frac{\kappa}{e}\frac{(r+3/2)}{\eta} \tag{1.64}$$

As η will become large, Seebeck coefficient will be considerably small and metals in general end up with very low S of the order of few microvolts.

For semiconductors we need to go with non-degenerate approximation where $\eta < -2k_BT$ and FD integral become,

$$f_n(\eta) = exp(\eta)\int_0^\infty \xi^n \exp(-\xi) d\xi = exp(\eta)\Gamma(n+1) \tag{1.65}$$

And the FD integral can be expressed as,

$$K_s = \frac{8\pi}{3}\left(\frac{2}{h^2}\right)^{\frac{3}{2}} (m^*)^{\frac{1}{2}} T\tau_0 (k_BT)^{s+r+3/2}\, \Gamma(s+r+5/2) exp(\eta) \tag{1.66}$$

And the electrical conductivity become

$$\sigma = \frac{8\pi}{3}\left(\frac{2}{h^2}\right)^{3/2} e^2 (m^*)^{1/2} T\tau_0 (k_BT)^{(r+3/2)} \Gamma(r+5/2) exp(\eta) \tag{1.67}$$

Comparing with equation (1.43) $\sigma = ne\mu$, we may write

$$n = 2\left(\frac{2\pi m^* k_B T}{h^2}\right)^{3/2} exp(\eta) \tag{1.68}$$

n Can be treated as effective density of states, and the mobility μ will be,

$$\mu = \frac{4}{3\pi^{1/2}}\,\Gamma\left(r+\frac{5}{2}\right)\frac{e\tau_0(k_BT)^r}{m^*} \tag{1.69}$$

The Seebeck coefficient in non-degenerate case is represented as

$$S = \mp\frac{\kappa}{e}\left[\eta-\left(r+\frac{5}{2}\right)\right] \tag{1.70}$$

The Peltier coefficient is equal to ST, indicating that the energy carried by each electron or hole consists of a potential component $-\frac{\eta k_BT}{e}$, and a kinetic component $(r+5/2)\frac{k_BT}{e}$. In a typical extrinsic semiconductor, ˙ may be significantly greater than unity, resulting in the Seebeck coefficient reaching several hundred microvolts per degree. For a nondegenerate conductor, the Lorenz number is

$$L = \left(\frac{\kappa}{e}\right)^2\left(r+\frac{5}{2}\right) \tag{1.71}$$

The intrinsic relationship between the thermal and electrical conductive properties of metals, arising from the behavior of free electrons is established by Wiedemann-Franz law. It is particularly useful in understanding and predicting the conductive properties of metals under varying thermal conditions, where the electrons are treated based on a semi-classical treatment of the electron gas.

$$\frac{\kappa}{\sigma} = LT \tag{1.72}$$

L is the proportionality constant, and it is called the Lorenz number. The Wiedemann-Franz law is primarily applicable to metals, where free electrons are the dominant carriers of both heat and electrical current. However, in semiconductors, the situation is more complex due to the involvement of both electrons and holes as charge carriers, and the presence of significant lattice vibrations (phonons) contributing to thermal conductivity. While the law can sometimes offer insights into the relationship between thermal and electrical conductivities in semiconductors.

1.8 Strategies for optimizing thermoelectric figure of merit

Tuning the thermoelectric power factor, is challenging in many aspects. Optimizing one parameter has a negative impact on the others; for example, boosting electrical conductivity typically reduces the Seebeck coefficient due to their interdependence on carrier concentration. Furthermore, improving the power factor while keeping low thermal conductivity is difficult since advances in electrical conductivity might result in greater thermal conductivity. Material selection and doping schemes require precise control to attain the required balance. Intrinsic material features such as carrier mobility and effective mass limit the ability to tune the thermoelectric power factor effectively. These complications need cutting-edge material engineering and fabrication approaches to improve thermoelectric performance [138].

1.8.1 Phonon glass electron crystal (PGEC) concept

For a semiconducting material to be an ideal thermoelectric material, the required qualities are,

1. High crystal symmetry with electronic bands near the Fermi level and multiple valleys.
2. Compounds composed of heavy elements with minimal electronegativity differences between their constituent elements.
3. Energy gap of the order of 10 $k_B T$.

But in most of the cases the thermal conductivity of material will be too high to make use of them in practical TE devices. In order to meet the criteria for a good TE material Slack proposed the idea of Phonon glass electron crystal (PGEC) [139]. PGEC materials exhibit thermal conductivity similar to that of amorphous materials, resembling glass, while simultaneously possessing the superior electronic properties of a semiconductor. In PGEC materials very low thermal conductivity without compromising electron mobility may be achieved. One strategy to achieve this behavior is alloying with elements having similar electronic configuration. Alloying preserves the crystalline

nature while act like point scattering centers for phonons and reduce thermal conductivity. Increasing the complexity of unit cell is also a desired quality for PGEC materials.

Phonon-Phonon interaction is the chief mechanism of thermal transport in materials. At moderately high temperatures lattice thermal conductivity $\kappa_{lattice}$ is represented as,

$$\kappa_{lattice} \propto \frac{mV^{1/3}\theta_D^3}{\gamma^2 T} \tag{1.73}$$

Here γ is the GrÜneisen parameter which is the measure of anharmonicity of lattice vibrations. High value of γ is obtained for materials with large thermal expansion, isothermal bulk modulus and low density which eventually results in low thermal conductivity. Since thermal conductivity is proportional to specific heat, lowering C_v is another strategy to reduce $k_{lattice}$. Introducing the unique structural characteristics of ionic conductors can increase complexity in the crystal and reduce C_v. The phonon mean free path can be reduced in nanostructured semiconductor super lattices and low-dimensional systems due to increased layer scattering effects. This combined strategies will reduce thermal conductivity.

1.8.2 Optimizing power factor

Early efforts to optimize the figure of merit primarily focused on reducing thermal conductivity. However, there is significant potential for enhancing the power factor. The thermoelectric power factor integrates two critical material properties: the Seebeck coefficient and electrical conductivity via $PF = S^2\sigma$. Various methods exist to improve these aspects.

1.8.2.1 Stabilizing Carrier concentration & Mobility

To maximize the figure of merit by increasing the carrier concentration, we need to have an optimum doping level that correspond to reduced fermi level $\xi = {}^{E_F}/_{k_B T}$ approaches value close to zero. . The optimal carrier concentration n^* estimated by Ioffe is proportional to $(m^*T)^{3/2}$, where m^* is the effective mass. Most of the TE materials

usually have an electron concentration (n) that is much higher than the optimal concentration (n^*) required for low temperatures, but lower than what is needed for high temperatures [140]. This discrepancy presents a fundamental challenge in achieving the maximum possible ZT across all temperatures. This is dealt with a strategy known as functional doping [136]. We may also adopt gradient doping to optimize carrier concentration by integrating two or more different segments. Another strategy is to increase the dopant solubility with temperature. The most effective way to stabilize carrier concentration is through band engineering, which adjusts the temperature-dependent density of states by tuning the effective mass. This can be achieved by alloying, which decreases the effective number of available states as the temperature increases.

Carrier mobility is another aspect to be taken care of while doping. An effective way to stabilize mobility is to have modulation doping other than uniform doping. Ionized impurity scattering can cause a decrease in carrier mobility in semiconductors

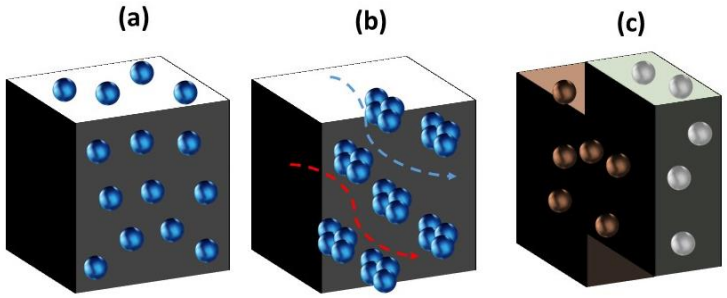

Figure 1- 14 Different strategies of doping **(a)** Uniform doping **(b)** Modulated doping **(c)** Graded doping.

that are evenly doped. Modulation doping, on the other hand, reduces the effect of ionized dopants on carriers and increases carrier mobility by adding dopants to just one phase as indicated in Fig.1-14 [141]. In addition to these techniques modification in synthesis parameters like synthesis / annealing / calcination temperature, can also be used as an effective method to optimize carrier concentration and mobility. Modulation doping involves spatially separating dopant atoms from the region where charge carriers

(electrons/holes) reside. Graded doping gradually varies the doping concentration across a material (e.g., from high to low). It creates built-in electric fields or bandgap gradients to control carrier movement, improve efficiency in devices like solar cells or photodetectors. Besides modulation doping, utilizing the texture or structure of the material represents another effective method to enhance carrier mobility, particularly in materials with anisotropic structures.

1.8.2.2 Modulating Seebeck coefficient

Seebeck coefficient is usually expressed using the Pisarenko relationship.

$$S = \frac{8\pi^2 k_B^2 T}{3qh^2} m^* \left(\frac{\pi}{3p}\right)^{3/2} \tag{1.74}$$

Where q is the carrier charge, m^* is the density of states (DOS) effective mass, p is the hole concentration, h is the Planck's constant. Since Seebeck coefficient is directly connected tom^*, tuning effective mass is one of the most widely used strategy to increase . As the density of states increases, the bands distorted and there occurs an enhancement in the effective mass. The effect of local changes in density of states significantly affect Seebeck coefficient and is given by the Mott relation [142].

$$S = \frac{\pi^2}{3}\frac{K_B}{q} K_B T \left\{\frac{1}{n}\frac{dn(E)}{dE} + \frac{1}{\mu}\frac{d\mu(E)}{dE}\right\}_{E=E_F} \tag{1.75}$$

To increase the Seebeck coefficient(S), two strategies can be employed. First strategy involves increasing the energy dependence of $\mu(E)$ through a scattering mechanism that heavily relies on the energy of charge carriers. Multivalley semiconductors with small inertial mass exhibit high mobility, despite having moderately high effective mass in certain valleys, due to the availability of multiple conduction pathways. The second strategy involves increasing the dependence of $n(E)$. Introducing resonant impurity levels via dopants is an effective method for enhancing the Seebeck coefficient. An effective way to implement the first strategy is size confinement where

the density of states play crucial role as indicated in Fig 1-15. At nanometer scales, the energy levels of electrons and holes become quantized. This quantization can increase the density of states near the Fermi level, potentially enhancing the Seebeck coefficient. As the system size decreases to the nanometer scale, it becomes possible to vary the Seebeck coefficient (S) quasi-independently.

Energy Filtering is another effective strategy to attain high Seebeck coefficient. Nano structuring can introduce barriers or interfaces that preferentially scatter low-energy carriers while allowing high-energy carriers to pass. This energy filtering effect can increase the average energy of the carriers, thereby boosting the Seebeck coefficient.

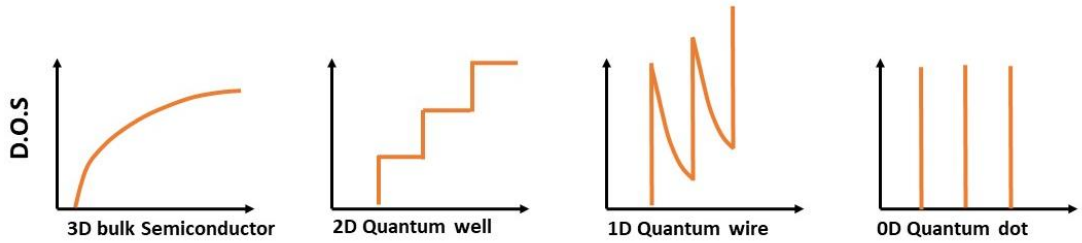

Figure 1- 15 Electronic density of states for a bulk semiconductor, 2D quantum well, 1D nanowire or nanotube and a 0D quantum dot.

1.8.2.3 Regulation of oxygen vacancies (V_o) to optimize power factor

Annealing in reduced atmospheres, doping, formation of layered structures, fine-tuned synthesis conditions can induce oxygen vacancies in oxide based TE materials. Regulating this vacancies can significantly impact the TE performance.

Oxygen vacancies can significantly affect the electrical and thermal properties of a material, thereby influencing its thermoelectric performance. It can act as electron donors in oxide materials, increasing the carrier concentration. An optimal carrier concentration is crucial for maximizing the electrical conductivity (σ) while maintaining a high Seebeck coefficient (S). Precise control of oxygen vacancies can help achieve this balance. V_o can scatter charge carriers, affecting their mobility. While excessive vacancies reduce mobility due to increased scattering, a controlled introduction of vacancies can optimize defect density, enhancing mobility and improving electrical

conductivity. Additionally, vacancies can modify the electronic band structure, increasing the density of states near the Fermi level, which enhances the Seebeck coefficient by amplifying the energy dependence of the electronic states. V_o can create localized states that act as energy filters, preferentially scattering low-energy carriers and allowing high-energy carriers to contribute to the electrical transport. This energy filtering effect can increase the average energy of the carriers, thus enhancing the Seebeck coefficient [143–147].

1.8.2.4 Super lattice structures to optimize figure of merit

Super lattices, composed of alternating nanometer-thick layers of different materials, can significantly enhance thermoelectric performance by reducing thermal conductivity through increased phonon scattering at interfaces. The quantum confinement effect in super lattices can increase the density of states near the Fermi level, thereby improving the Seebeck coefficient. Super lattices can be engineered to selectively scatter low-energy carriers, enhancing the average energy of charge carriers and boosting the thermoelectric power factor.

The confinement effects may be used to create conduction valleys in nanostructures and further confinement lead to formation of carrier pockets. The thickness of each layer in super lattices may be reduced, to form a completely different shaped carrier pockets as in Fig. 1-16.

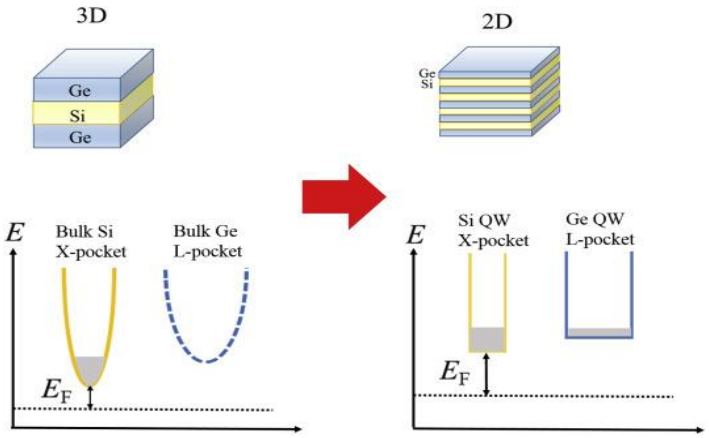

Figure 1- 16 Carrier pocket formation in bulk and nano dimensional super lattice structures.

Materials for super lattices are chosen based on their ability to form high-quality interfaces, optimal carrier concentration, and favorable electronic and thermal properties that contribute to high thermoelectric performance. Super lattices reduce thermal conductivity by introducing numerous interfaces that scatter phonons more effectively than electrons, lowering lattice thermal conductivity while preserving electrical conductivity. The periodic structure of super lattices can create phonon bandgaps, limiting the propagation of heat-carrying phonons. Reduced dimensionality in super lattices alters phonon dispersion, decreasing phonon group velocity and further reducing thermal conductivity. Differences in atomic masses and induced strain fields in create mass fluctuation and strain scattering, which impede phonon transport and enhance thermoelectric performance. Several combinations have been successfully tried and implemented by various researches including tin telluride (SnTe), lead telluride (PbTe), Silicon-Germanium (SiGe), lead selenide (PbSe) and Nb-STO/ Pr-STO [148–152].

1.8.2.5 Magnetic inclusions to optimize figure of merit

Magnetic nano inclusions in thermoelectric materials offer a promising route to enhance thermoelectric performance by influencing both electronic and phononic properties. Magnetic nano inclusions affect thermoelectric properties through drag effects, where interactions with localized magnetic moments alter the mobility of charge carriers. This phenomenon modifies the Seebeck coefficient by introducing spin-dependent scattering mechanisms that influence electron transport. The presence of magnetic nanoparticles can increase carrier concentration by acting as dopants, thereby enhancing electrical conductivity. In terms of phonon transport, magnetic inclusions create interfaces that scatter phonons, reducing thermal conductivity by disrupting their propagation. The presence of magnetic fields around these inclusions can also induce strain fields in the host material, further enhancing phonon scattering and lowering thermal conductivity [153–155].

Oxide and ferrite based nano inclusions like iron oxide (Fe_3O_4), manganese oxide (MnO), $NiFe_2O_4$, cobalt ferrite ($CoFe_2O_4$) and elemental forms of magnetic materials like

iron (Fe), nickel (Ni), dysprosium (Dy) and gadolinium (Gd) are widely explored in this aspect.

1.9 Thermoelectric materials

Seebeck effect and Peltier effect discovered during the early period of 18th century paved the way for thermoelectric research, but practical applications remained limited until the mid-twentieth century. Significant breakthroughs occurred in the 1950s with the introduction of bismuth telluride (Bi_2Te_3) and related alloys, which became the standard materials for thermoelectric devices due to their high efficiency at ambient temperature. Skutterudites, Oxide perovskites, half-Heusler compounds, delaffosites, clathrates, zintl phases, selenides, Silicides, silicon-germanium alloys (Si-Ge), organic and hybrid materials, and chalcogenides are among the various classes of thermoelectric (TE) materials. These materials can also be classified based on temperature ranges. The class of materials with promising TE performances used as n and p type legs is represented in Fig. 1-17 [156]. In recent decades, the emphasis has switched towards nanostructured materials and complex compounds like skutterudites and clathrates, which offer higher thermoelectric performance through greater phonon scattering and reduced heat conductivity. Few major class of TE materials are as follows.

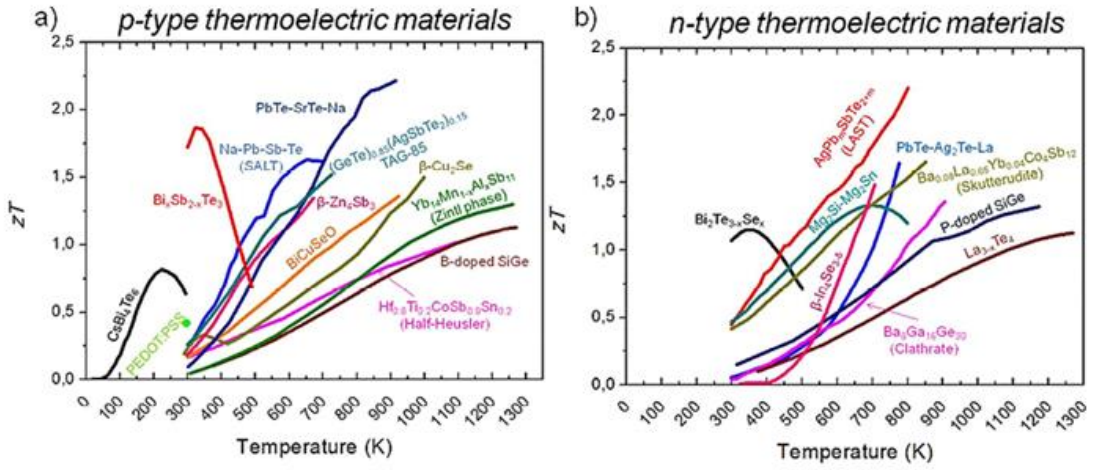

Figure 1- 17 Class of thermoelectric materials with maximum values of figure of merit.

In recent decades, the emphasis has switched towards nanostructured materials and complex compounds like skutterudites and clathrates, which offer higher thermoelectric performance through greater phonon scattering and reduced heat conductivity. Few major class of TE materials are as follows.

1.9.1 Skutterudites

The mineral skutterudite ($CoAs_3$) is the source of skutterudite thermoelectric materials, which are renowned for their promising thermoelectric qualities, especially at intermediate to high temperatures. Due to the presence of voids in their crystal structure, which can be filled with guest atoms like alkali metals or rare earth elements, these materials substantially reduce heat conductivity by phonon scattering. "Filled skutterudites," as a result of this filling process, show noticeably better thermoelectric performance than their unfilled equivalents. These class of compounds have a general formula TPn_3, where T is transition metal (T=Co, Rh or Ir) and Pn is a pnictogen (Pn=Sb, As or P) represented by the structure in Fig. 1-18 [156].

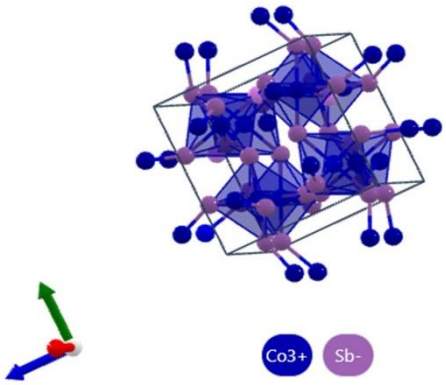

Figure 1- 18 Unit cell of skutterudite ($CoSb_3$) ($Im\bar{3}$).

Traditional $CoSb_3$ skutterudites, when optimally doped and filled with rare earth elements like barium (Ba), have shown ZT values in the range of 1.5 to 1.6 at high temperatures (around 800 K). Specific advanced formulations and approaches have occasionally reported even higher ZT values, with some reports indicating values up to 1.7 under optimal conditions, though these are often under specific experimental setups and may vary with practical applications [157,158].

1.9.2 Half-Heusler compounds

Half-Heusler compounds are a promising class of thermoelectric materials characterized by their ternary alloy structure, typically composed of elements from groups 14, 15, and 16 of the periodic table. These compounds, such as TiNiSn and ZrNiSn, exhibit excellent mechanical stability and can operate efficiently at high temperatures, making them suitable for applications in waste heat recovery and automotive thermoelectric generators. (HH) compounds typically have the formula XYZ, where Z is a main group element and X and Y are typically transition metals as represented in Fig. 1-19 [159].

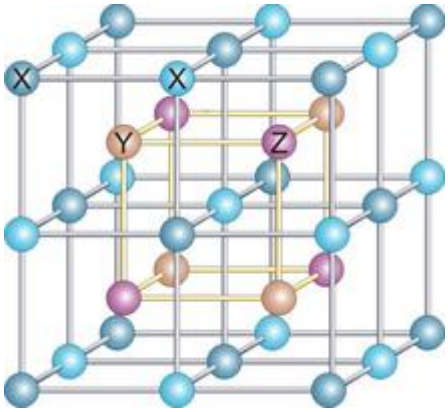

Figure 1- 19 Crystal structure of a Half-Heusler compounds (F-43 m): blue, gray, and purple spheres represent the X, Y, and Z atoms.

One of the key advantages of half-Heusler compounds is their relatively high power factor, which arises from a combination of good electrical conductivity and a moderate Seebeck coefficient. However, their inherent high thermal conductivity poses a challenge for achieving high thermoelectric performance. Advances in material synthesis and doping techniques have led to significant improvements in the thermoelectric figure of merit (ZT) of Half-Heusler compounds, with values reaching around 1.0 to 1.5 at high temperatures [160,161]. One of the highest figures of merit (ZT = 1.5 at 700 K) for Heusler compounds was reported by Sakurada and Shutoh for Sb-doped $NiTi_{0.50}Zr_{0.25}Hf_{0.25}Sn$ [162]. The versatility of Half-Heusler compounds allows for a wide range of compositional tuning, enabling the optimization of both n-type and p-type thermoelectric materials.

1.9.3 Clathrates

Clathrate-based thermoelectric materials are characterized by their unique cage-like crystal structure, which consists of a framework of atoms enclosing guest atoms or molecules. Due to their weak interaction with the host lattice, guest atoms are relatively free to move or "rattle" within the framework. This localized rattling causes resonant scattering of acoustic phonon modes in the lattice, which reduces thermal conductivity while still preserving good electrical conductivity. Clathrates are frequently classed as host-guest or inclusion compounds because they contain numerous sub lattices. Type I clathrates, such as $Ba_8Ga_{16}Ge_{30}$, are among the most studied, offering a balance of low thermal conductivity and high electrical conductivity. The guest atoms within the cages disrupt the lattice vibrations, reducing the material's overall thermal conductivity and enhancing the thermoelectric figure of merit (ZT) [163]. The structure of I and II clathrates are represented in Fig 1-20 [163].

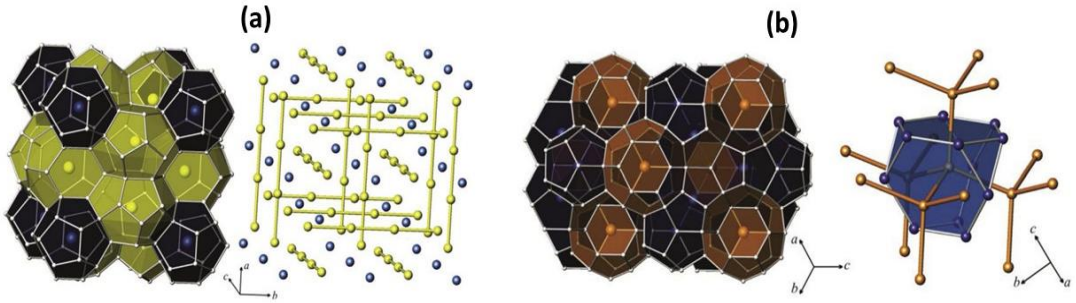

Figure 1- 20 Crystal structure of **(a)** clathrate-I **(b)** clathrate-I.

Traditional clathrates accommodate group 13 and 14 elements in the framework, with alkali, alkaline-earth, or rare-earth cations as guests. Group 14 elements fit very nicely with the tetrahedral coordinated clathrate structure. To keep charge balance when guest ions are added to the clathrate cages, aliovalent substitution in the framework is necessary. Water hydrates crystallize into seven primary structural types, denoted by Roman numbers I–VII. Inorganic clathrates have been classified into clathrate-VIII, clathrate-IX, and twisted clathrate. Many clathrate phases have showcased for their good

TE characteristics. The highest thermoelectric figure of merit, ZT is 1.35 for $Ba_{16}Ga_{16}Ge_{30}$ at 823 K [164,165].

1.9.4 Chalcogenides

Chalcogenide-based thermoelectrics leverage the unique properties of group 16 elements to efficiently convert thermal energy into electrical energy. These materials typically include compounds such as bismuth telluride (Bi_2Te_3) and lead telluride (PbTe), which exhibit high thermoelectric performance. The structure of PbTe is highly symmetric and is contrary to the concept structure of ideal thermoelectrics. With very low values of thermal conductivities of the range 2 to 3 $Wm^{-1}K^{-1}$, n type PbTe has attained maximum figure of merit 1.4 at temperatures 700-800 K. Nano structuring with Ag and Sb inclusions have reported a highest power factor of 2.2 for the composition $AgPb_{18}SbTe_{20}$ [166,167]. Another conventional materials in this family is Bismuth telluride and its derivatives. Its alloys with antimony telluride (Sb_2Te_3) and bismuth selenide (Bi_2Se_3) are the most significant thermoelectric materials due to their unparalleled efficiency near room temperature.

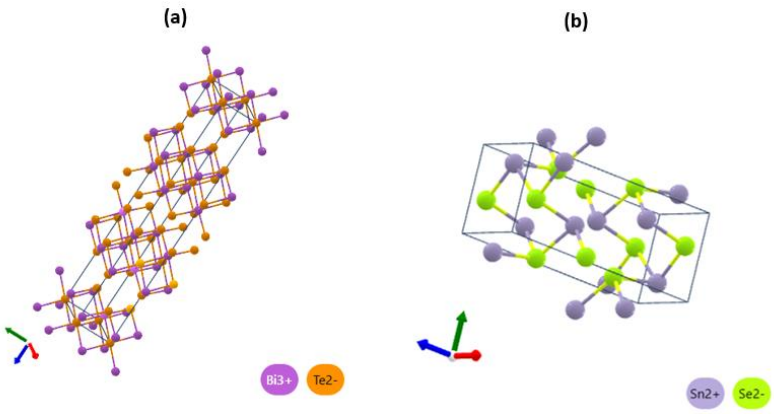

Figure 1- 21 structure of **(a)** bismuth telluride with Bi atoms in violet and Te atoms in orange (R-3m) **(b)** SnSe in (Pnma) at room temperature with Sn atoms in blue and Se atoms in green.

For many of practical applications involving TE cooling, TE refrigeration and TE wearable devices these materials are explored since they can be modified to induce n type and p type semiconducting materials with suitable dopants. P type derivatives have been

made with highest figure of merit 1.6 and n type figure of merit value has reached 1.5. Recent research has concentrated on improving the thermoelectric performance of n-type Bi_2Te_3-based alloys using techniques such as Ag doping, hot deformation, low-angle grain boundaries, and the inclusion of materials like Ag_9AlSe_6. Investigations have also delved into innovative fabrication methods, including selective laser sintering and melt-spinning, to enhance the microstructure and properties of n-type Bi_2Te_3-based thermoelectric materials, with the goal of achieving superior efficiency and performance [168,169]. The crystal structures of these class of compounds is represented in Fig. 1-21.

Tin selenide (SnSe) exhibits remarkable thermoelectric properties due to its exceptionally low thermal conductivity and favorable electronic characteristics, leading to a high figure of merit (ZT). SnSe is a binary compound demonstrates strong an harmonic and anisotropic bonding, and when doped with holes, it exhibits an exceptionally high power factor due to its high electrical conductivity and significantly increased Seebeck coefficient. This enhancement is facilitated by the contribution of multiple electronic valence bands. Advances in doping and nanostructuring techniques have further optimized its thermoelectric performance, making it a highly promising material for energy conversion applications. Even after doping it is able to maintain ultra-low thermal conductivities in range 0.4-0.5 $Wm^{-1}K^{-1}$ to attain figure of merit reaching values greater than 2 [170].

1.9.5 Oxide thermoelectric materials

Oxide-based thermoelectric materials have garnered significant interest due to their stability, abundance, and environmental friendliness compared to traditional thermoelectric materials. These materials, including oxides of elements such as cobalt, zinc, and titanium, exhibit promising thermoelectric properties at high temperatures, making them suitable for applications in harsh environments. Doping and nanostructuring are common strategies employed to enhance the thermoelectric performance of oxide materials, aiming to reduce thermal conductivity while maintaining

or improving electrical properties. Complex oxides, such as perovskites and layered structures, offer tunable electronic and thermal properties, making them versatile candidates for thermoelectric applications.

Oxides were not considered as good TE materials till 1990's because of their low electrical conductivity and optimum thermal conductivity. Works done on transition metal oxides like $NaCo_2O_4$ and ZnO paved the oxide way of thermoelectrics. They possess strong electronic correlations and narrow d bands, which result in significant spin and orbital fluctuations, as well as high degeneracy. These characteristics in d-electron systems are beneficial for enhancing thermoelectric performance. In recent years several other oxide materials like Zinc oxide (ZnO), Calcium cobaltate ($Ca_3Co_4O_9$), Calcium Manganate ($CaMnO_3$), Strontium titanate ($SrTiO_3$) and delafossite $CuCrO_2$ has emerged as promising TE materials. Single crystals of Calcium cobaltate and its derivatives has reached a maximum ZT value of 0.90, whereas polycrystalline samples has reached up to ZT=0.40. Different doping strategies has been incorporated in calcium cobaltate materials to improve the figure of merit to reach values in the range 1 for practical applications.

ZnO-based thermoelectric materials are appealing due to their excellent thermal stability, non-toxicity, and abundance. They show promising thermoelectric properties, when doped with elements like aluminum or gallium, which improve their electrical conductivity and Seebeck coefficient. N-type ZnO can be achieved by adding donors like Al or Ni. ZnO-based materials have been synthesized in bulk, nanostructured, thin film, and layered forms, with the thermoelectric figure of merit at room temperature reaching up to ZT ~ 0.98 for ZnO (1120) monolayers and ZT ~ 1.49 for ZnO (0001) monolayers. Interfacing low-oxidized graphene quantum dots has been adopted as a strategy to improve ZT of zinc oxide to get maximum value of 0.486 [171,172].

1.9.6 Strontium Titanate ($SrTiO_3$)

Strontium titanate ($SrTiO_3$) is a promising thermoelectric material due to its high thermal stability and non-toxicity. When doped with elements such as lanthanum,

praseodymium or niobium, $SrTiO_3$ exhibits enhanced electrical conductivity and Seebeck coefficient, improving its thermoelectric performance. Advanced synthesis techniques, such as nanostructuring and defect engineering, have been employed to optimize the properties of the material.

1.9.6.1 Crystal structure

Strontium titanate ($SrTiO_3$) has a perovskite crystal structure, characterized by a cubic lattice where strontium (Sr) ions occupy the corners of the cube. Titanium (Ti) ions are located at the center of the cube, while oxygen (O) ions are positioned at the face centers, forming an octahedral coordination around the titanium ions. This structure contributes to its high dielectric constant and favorable electronic properties. $SrTiO_3$ can undergo structural transitions under varying temperature and pressure conditions, influencing its physical and electronic behavior.

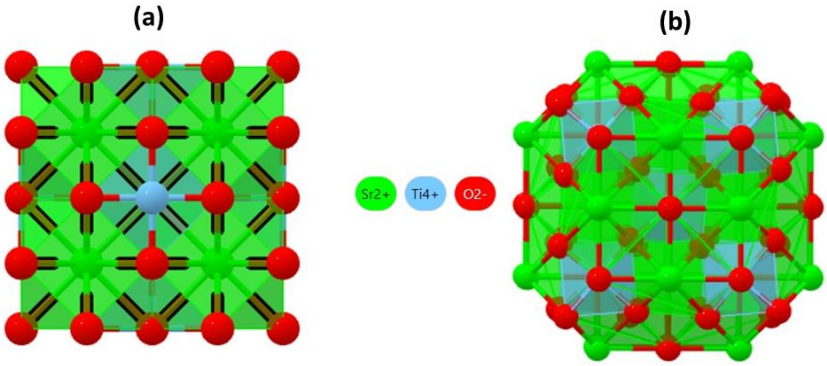

Figure 1- 22 Crystal structure of **(a)** Cubic strontium titanate (Pm3m) **(b)** Tetragonal strontium titanate (I4/mcm).

At room temperature, $SrTiO_3$ crystallizes in the ABO_3 cubic perovskite structure (Pm3m) with a lattice parameter of 0.3905 nm. The cubic structure of $SrTiO_3$ can change to tetrahedral, octahedral, or even rhombohedral forms due to crystal distortions caused by factors like size effects, deviations from the ideal composition, and the Jahn-Teller effect induced by doping or temperature variations as represented in Fig.1-22. $SrTiO_3$ transitions to a tetrahedral structure (I4/mcm space group) at temperatures below 105 K

and further transforms to octahedral and rhombohedral structures at temperatures below 50 K and 10 K, respectively [173,174].

The structure stability of perovskites is often represented by Goldschmidt tolerance factor (t), calculated using the ionic radii of the constituent ions. It is represented using the equation (1.76).

$$t = \frac{[r_A + r_O]}{\sqrt{2}(r_B + r_O)} \tag{1.76}$$

Where r_A and r_B are the radii of the A and B cations, and r_O is the radius of the oxygen anion. A tolerance factor close to 1 indicates a stable cubic perovskite structure, while deviations from this value suggest potential distortions or different crystal symmetries. The introduction of a dopant at either the A or B site, or the creation of oxygen vacancies, distorts the structure and leads to deviations from the ideal tolerance factor value [175,176].

1.9.6.2 Electronic structure and transport properties

The electronic structure of strontium titanate is complex and can be understood by examining its band structure, density of states, and the contributions from its constituent atoms. STO has an indirect band gap of approximately 3.2 eV, with the conduction band minimum (CBM) located at the Γ point and the valence band maximum (VBM) at the R point in the Brillouin zone. The conduction band is primarily composed of the Ti 3d states, which are split into t_{2g} and e_g levels due to the octahedral crystal field created by the surrounding oxygen atoms. The valence band is mainly derived from the O 2p states, which form bonding states with the Ti 3d states. The total DOS shows a clear separation between the valence and conduction bands, with the valence band edge dominated by O 2p states and the conduction band edge by Ti 3d states. The contributions from Sr 4d states are found at higher energies in the conduction band and do not significantly contribute to the electronic properties near the band edges [176,177].

The electronic transport properties of $SrTiO_3$ are crucial for its applications in electronics and thermoelectrics. Pure $SrTiO_3$ is an insulator with low intrinsic electrical conductivity due to its wide band gap, whereas doping with donor elements like lanthanum (La) or niobium (Nb) introduces extra electrons into the conduction band, significantly enhancing its electrical conductivity. La^{3+} substitutes for Sr^{2+}, providing one additional electron per dopant atom, and Nb^{5+} substitutes for Ti^{4+}, similarly adding an extra electron. At cryogenic temperatures, STO exhibits exceptionally high electron mobility, reaching values as high as 10^4 cm^2/Vs due to reduced phonon scattering [178].

1.9.6.3 Thermal transport properties

Pure $SrTiO_3$ exhibits relatively high thermal conductivity due to its strong ionic bonding and efficient phonon transport. At room temperature, the thermal conductivity is typically in the range of 10-12 $Wm^{-1}K^{-1}$. Thermal conductivity of STO decreases with increasing temperature. This is mainly due to enhanced phonon-phonon scattering at higher temperatures. At temperatures above 1000 K, the thermal conductivity can drop significantly, to around 2-3 $Wm^{-1}K^{-1}$. The introduction of dopants typically reduces thermal conductivity by introducing additional phonon scattering mechanisms. La^{3+}, Pr^{3+} Sm^{3+}, Dy^{3+}, Y^{3+}, Yb^{3+} -doped $SrTiO_3$ can exhibit thermal conductivities as low as 2-4 W/mK at room temperature, depending on the doping concentration. Similar to La doping, Nb doping (substituting Ti^{4+} with Nb^{5+}) also reduces the thermal conductivity of $SrTiO_3$. Nb-doped $SrTiO_3$ can have thermal conductivities in the range of 3-5 $Wm^{-1}K^{-1}$ at room temperature. In the Dy^{3+} doped samples, a thermal conductivity of 2.1 $Wm^{-1}K^{-1}$ at 1073 K was achieved, marking the lowest value ever reported. Creating oxygen vacancies can introduce additional phonon scattering sites, drastically reducing thermal conductivity. $SrTiO_3$ with a high concentration of oxygen vacancies can have thermal conductivities as low as 2-3 $Wm^{-1}K^{-1}$ at room temperature. Oxygen vacancies cause local lattice distortions and strain fields, which enhance phonon scattering. Through careful control of composite doping strategies, the thermal conductivity of $SrTiO_3$ can be reduced to values in the range 1 to 1.5 $Wm^{-1}K^{-1}$ in some cases, especially at high doping concentrations and with additional defect engineering [179,180].

1.9.6.4 Thermoelectric properties of $SrTiO_3$

STO has emerged as a promising material for thermoelectric applications due to its exceptional ability to convert heat into electricity, driven by its unique electronic and thermal transport properties. The high value of Seebeck coefficient, electrical conductivity, and thermal stability makes STO unique among other $ATiO_3$ perovskites. The carrier concentration in pure STO is in 10^{15} cm^{-3} range which is far below the value required for a reasonable power factor. Donor doping using La, Pr, Sm, Dy and Y for Sr and Nb, Ta for Ti are the best strategies to improve the carrier density to desired level. Intrinsic defects like oxygen vacancies will aid the electrical conductivity. Large effective mass and conductive band degeneracy enhance Seebeck coefficient. Single crystal STO have very high thermal conductivity due to the lack of scattering centres. For practical purposes this should be reduced. In general, introducing defects across multiple dimensions in the lattice effectively reduces thermal conductivity by scattering phonons of various wavelengths. These defects encompass zero-dimensional (0D) point defects, one-dimensional (1D) dislocations, two-dimensional (2D) interfaces, and three-dimensional (3D) inclusions. The introduction of defects across dimensional scales not only suppresses thermal conductivity by scattering a broad spectrum of phonons but also modifies opto-thermoelectric properties by altering light-matter interactions. For instance, 0D point defects and 2D interfaces can create mid-gap states or strain fields that enhance sub-bandgap photon absorption, improving photothermal carrier generation, while 1D dislocations and 3D inclusions may tailor charge carrier mobility and recombination dynamics, synergistically boosting both thermoelectric and light-harvesting efficiency [181].

In comparison with single doping co-doping on both Sr-site and Ti-site is commonly used to boost TE performance of STO. Computational results indicate that an estimated high *ZT* of 0.7 can be realized by La/Nb co-doping. After co-doping with 10% La and 10% Nb, a *ZT* of 0.31 at 1050 K was observed. Similarly, a competitively high *ZT* of 0.43 at 1009 K was achieved in polycrystalline $Sr_{0.93}La_{0.07}Ti_{0.93}Nb_{0.07}O_3$ fabricated by a similar method [182]. Partial doping was also developed to improve the

thermoelectric performance of STO. Partial doping, nano compositing with TiO_2, nano inclusions of metallic species, graphene/graphene oxide inclusions were used to enhance TE characteristics of STO in bulk form [183–187].

Like their 3D bulk counterparts in single-crystal or polycrystalline forms, 2D $SrTiO_3$ is increasingly gaining interest for use in thermoelectric devices, particularly miniature ones. This interest stems from their strong mechanical properties and excellent thermal stability, especially at elevated temperatures. Doping and vacancy tuning has been found as effective strategy to enhance TE characteristics of STO in thin film forms. ZT values in the range 0.3 has been achieved in Nb doped STO films prepared by PLD method [188]. A variety of synthesis routes like MBE, RF sputtering, ALD, other physical deposition methods may be adopted to fine tune the figure of merit.

Thin film super lattices of $SrTiO_3$ have shown promising thermoelectric properties due to enhanced phonon scattering at interfaces, which reduces thermal conductivity. These structures can be engineered to optimize electronic transport while maintaining low thermal conductivity, thus improving the thermoelectric figure of merit (ZT). For $SrTiO_3$-based super lattices, a maximum ZT value of around 2.4 at high temperatures has been reported, highlighting their potential for high-efficiency thermoelectric applications. The precise control of layer thickness and interface quality in these super lattices is crucial for achieving such high ZT values. Most widely prepared super lattices include alternating layers of Pr^{3+} doped $SrTiO_{3-\delta}$ (SPTO) and Nb^{5+} doped $SrTiO_{3-\delta}$ (STNO) prepared by various thin film deposition techniques [189–191].

1.10 Motivation and objectives

Recent progress in thermoelectric materials has focused on enhancing TE performance through nanostructuring, which improves phonon scattering and reduces thermal conductivity. Advanced synthesis and fabrication techniques, such as doping and alloying, have been developed to optimize the electrical and thermal transport properties of these materials. Despite these advancements, challenges remain in achieving high

efficiency and scalability for practical applications. Ensuring long-term stability and cost-effectiveness of thermoelectric materials also continues to be a significant hurdle in their widespread adoption.

The objective of this study is to synthesize $SrTiO_3$-based materials with a high thermoelectric figure of merit (ZT) by strategically engineering electronic and lattice structures to synergistically enhance thermoelectric and optical performance. $SrTiO_3$ was selected as the base material due to its exceptional thermal/chemical stability, low toxicity, and dual-site (A/B) dopability. Praseodymium (Pr^{3+}) was introduced at the A-site to induce mid-gap electronic states within $SrTiO_3$'s band structure, which not only optimizes thermoelectric parameters (e.g., elevating the Seebeck coefficient and modulating carrier concentration) but also tailors its optical properties. These mid-gap states enhance photoluminescence and sub-bandgap photon absorption, enabling broadband light harvesting and emission tuning—critical for optoelectronic applications such as transparent conductive oxides (TCOs) and photodetectors. Concurrently, niobium (Nb^{5+}) doping at the B-site boosts electrical conductivity by increasing carrier density, while graphite burial sintering generates oxygen vacancies, further enhancing electronic transport and introducing defect-mediated optical transitions (e.g., visible-light absorption via vacancy states).

The confinement effects in Pr/Nb-doped thin films, fabricated via oxygen-free sputtering, amplify these dual functionalities: reduced dimensionality suppresses thermal conductivity through phonon boundary scattering, while quantum confinement sharpens electronic states, improving both thermoelectric efficiency and optoelectronic performance. This dual engineering of electronic and defect structures enables $SrTiO_3$ to operate as a multifunctional material, bridging optoelectronic and thermoelectric applications. For instance, the tailored optical absorption (via Pr-induced mid-gap states and oxygen vacancies) synergizes with enhanced electrical transport, making these materials ideal for solar PV-integrated thermoelectric modules, smart windows with energy-harvesting capabilities, or photothermally driven sensors. The interplay of defect-

mediated light-matter interactions and thermoelectric optimization positions Pr/Nb-doped $SrTiO_3$ as a platform for next-generation opto-thermoelectric devices, where tunable optical properties and energy conversion efficiency are co-engineered at the atomic scale.

References:

[1] M. Shah, P.K.J. Sanam, P.P. Pradyumnan, Tuning of photoluminescence properties: Impact of Pr-doping in $SrTiO_3$ crystallites, Mater Today Commun 39 (2024) 109323. https://doi.org/10.1016/j.mtcomm.2024.109323.

[2] M. Shah, P.K. Jamshina Sanam, P.P. Pradyumnan, Defect-induced $Sr_{1-x}Pr_xTiO_3$ crystallites by burial sintering and its optoelectronic applications, Journal of Physics and Chemistry of Solids 181 (2023) 111516. https://doi.org/10.1016/j.jpcs.2023.111516.

[3] H.A. Rahnamaye Aliabad, A. Asadpour Arzefooni, S.Z. Sadati, E.G. Özdemir, P. Khosrojerdi, High-performance optoelectronic and thermoelectric properties of transparent conductors based on Tl2O3 under pressure, Sci Rep 14 (2024) 9237. https://doi.org/10.1038/s41598-024-58657-9.

[4] H. Abu-Farsakh, B. Gul, M. Salman Khan, Investigating the Optoelectronic and Thermoelectric Properties of CdTe Systems in Different Phases: A First-Principles Study, ACS Omega 8 (2023) 14742–14751. https://doi.org/10.1021/acsomega.3c00757.

[5] M.A. Ali, A.A. Alothman, M. Mushab, M. Faizan, Optoelectronic and thermoelectric properties of novel stable lead-free cubic double perovskites A_2NaIO_6 (A = Ca, Sr) for renewable energy applications, Physical Chemistry Chemical Physics 26 (2024) 3614–3622. https://doi.org/10.1039/D3CP04919A.

[6] M.M.H. Khalil, A.M. Ishmael, I.M. El-Sewify, Chapter Three - 2D non-layered metal dichalcogenides, in: I.H. Abidi (Ed.), Semiconductors and Semimetals, Elsevier, 2023: pp. 63–100. https://doi.org/10.1016/bs.semsem.2023.09.010.

[7] F. Gao, E. Reichmanis, Introduction: Emerging Materials for Optoelectronics, Chem Rev 123 (2023) 10835–10837. https://doi.org/10.1021/acs.chemrev.3c00349.

[8] A. Bibi, I. Lee, Y. Nah, O. Allam, H. Kim, L.N. Quan, J. Tang, A. Walsh, S.S. Jang, E.H. Sargent, D.H. Kim, Lead-free halide double perovskites: Toward stable and sustainable optoelectronic devices, Materials Today 49 (2021) 123–144. https://doi.org/10.1016/j.mattod.2020.11.026.

[9] Y. Wang, P. Liu, F. Vogelbacher, M. Li, Bioinspired multiscale optical structures towards efficient light management in optoelectronic devices, Mater Today Nano 19 (2022) 100225. https://doi.org/https://doi.org/10.1016/j.mtnano.2022.100225.

[10] A.R. Zanatta, Revisiting the optical bandgap of semiconductors and the proposal of a unified methodology to its determination, Sci Rep 9 (2019) 11225. https://doi.org/10.1038/s41598-019-47670-y.

[11] X. Yu, T.J. Marks, A. Facchetti, Metal oxides for optoelectronic applications, Nat Mater 15 (2016) 383–396. https://doi.org/10.1038/nmat4599.

[12] L.L. Rusevich, M. Tyunina, E.A. Kotomin, N. Nepomniashchaia, A. Dejneka, The electronic properties of $SrTiO_{3-\delta}$ with oxygen vacancies or substitutions, Sci Rep 11 (2021) 23341. https://doi.org/10.1038/s41598-021-02751-9.

[13] T. Hasegawa, M. Shirai, K. Tanaka, Localizing nature of photo-excited states in $SrTiO_3$, J Lumin 87–89 (2000) 1217–1219. https://doi.org/10.1016/S0022-2313(99)00520-7.

[14] J. Zhu, H. Li, L. Zhong, P. Xiao, X. Xu, X. Yang, Z. Zhao, J. Li, Perovskite Oxides: Preparation, Characterizations, and Applications in Heterogeneous Catalysis, ACS Catal 4 (2014) 2917–2940. https://doi.org/10.1021/cs500606g.

[15] P.Y. Yu, M. Cardona, Electronic Band Structures, in: P.Y. Yu, M. Cardona (Eds.), Fundamentals of Semiconductors: Physics and Materials Properties, Springer Berlin Heidelberg, Berlin, Heidelberg, 2010: pp. 17–106. https://doi.org/10.1007/978-3-642-00710-1_2.

[16] Charles Kittel, Introduction to Solid State Physics, 8th ed., Wiley, 2004.

[17] M. RaeisianAsl, S. Jouybar, S. Sarabadani Tafreshi, L. Naji, Exploring the key features for enhanced $SrTiO_3$ functionality: A comprehensive overview, Materials Today Sustainability 29 (2025) 101072. https://doi.org/10.1016/j.mtsust.2025.101072.

[18] E. Zhou, J.-M. Raulot, H. Xu, H. Hao, Z. Shen, H. Liu, Structural, electronic, and optical properties of rare-earth-doped $SrTiO_3$ perovskite: A first-principles study, Physica B Condens Matter 643 (2022) 414160. https://doi.org/10.1016/j.physb.2022.414160.

[19] T. Nakagawa, M. Menelaou, M. Vrankić, Showcasing the Structure and Properties of Lanthanide-Doped $BaTiO_3$, Advanced Physics Research 4 (2025) 2500006. https://doi.org/10.1002/apxr.202500006.

[20] X. Pan, M.-Q. Yang, X. Fu, N. Zhang, Y.-J. Xu, Defective TiO_2 with oxygen vacancies: synthesis, properties and photocatalytic applications, Nanoscale 5 (2013) 3601–3614. https://doi.org/10.1039/C3NR00476G.

[21] H. Dong, C. Ran, W. Gao, M. Li, Y. Xia, W. Huang, Metal Halide Perovskite for next-generation optoelectronics: progresses and prospects, ELight 3 (2023) 3. https://doi.org/10.1186/s43593-022-00033-z.

[22] O. Ostroverkhova, Organic Optoelectronic Materials: Mechanisms and Applications, Chem Rev 116 (2016) 13279–13412. https://doi.org/10.1021/acs.chemrev.6b00127.

[23] M. Leskelä, M. Mattinen, M. Ritala, Review Article: Atomic layer deposition of optoelectronic materials, Journal of Vacuum Science & Technology B 37 (2019) 030801. https://doi.org/10.1116/1.5083692.

[24] B. Saleh, M. Teich, Fundamentals of Photonics, 3rd Edition, 2019.

[25] Physics and Properties of Semiconductors—A Review, in: Physics of Semiconductor Devices, 2006: pp. 5–75. https://doi.org/https://doi.org/10.1002/9780470068328.ch1.

[26] P.Y. Yu, M. Cardona, Fundamentals of semiconductors, 4th ed., Springer, Berlin, Germany, 2010. https://doi.org/10.1007/978-3-642-00710-1.

[27] D. Stange, S. Wirths, N. von den Driesch, G. Mussler, T. Stoica, Z. Ikonic, J.M. Hartmann, S. Mantl, D. Grützmacher, D. Buca, Optical Transitions in Direct-Bandgap $Ge_{1-x}Sn_x$ Alloys, ACS Photonics 2 (2015) 1539–1545. https://doi.org/10.1021/acsphotonics.5b00372.

[28] B.S. Holinsworth, D. Mazumdar, C.M. Brooks, J.A. Mundy, H. Das, J.G. Cherian, S.A. McGill, C.J. Fennie, D.G. Schlom, J.L. Musfeldt, Direct band gaps in multiferroic h-$LuFeO_3$, Appl Phys Lett 106 (2015) 082902. https://doi.org/10.1063/1.4908246.

[29] D. Rainko, Z. Ikonic, N. Vukmirović, D. Stange, N. von den Driesch, D. Grützmacher, D. Buca, Investigation of carrier confinement in direct bandgap GeSn/SiGeSn 2D and 0D heterostructures, Sci Rep 8 (2018) 15557. https://doi.org/10.1038/s41598-018-33820-1.

[30] M.K. Hudait, S.W. Johnston, Probing crystallographic orientation-specific carrier lifetimes in epitaxial Ge/AlAs and InGaAs/InP heterostructures, Mater Adv 3 (2022) 5034–5042. https://doi.org/10.1039/D2MA00260D.

[31] E.M.T. Fadaly, A. Dijkstra, Direct Bandgap Emission from Hexagonal Ge and SiGe Alloys, ArXiv Preprint (2019). https://arxiv.org/abs/1911.00726.

[32] J. Kangsabanik, M.K. Svendsen, A. Taghizadeh, A. Crovetto, K.S. Thygesen, Indirect Band Gap Semiconductors for Thin-Film Photovoltaics: High-Throughput Calculation of Phonon-Assisted Absorption, J Am Chem Soc 144 (2022) 19872–19883. https://doi.org/10.1021/jacs.2c07567.

[33] T. Torimoto, T. Kameyama, T. Uematsu, S. Kuwabata, Controlling optical properties and electronic energy structure of I–III–VI semiconductor quantum dots for improving their photofunctions, Journal of Photochemistry and Photobiology C: Photochemistry Reviews 54 (2023) 100569. https://doi.org/https://doi.org/10.1016/j.jphotochemrev.2022.100569.

[34] M. Noda, K. Iida, M. Yamaguchi, T. Yatsui, K. Nobusada, Direct Wave-Vector Excitation in an Indirect-Band-Gap Semiconductor of Silicon with an Optical Near-field, Phys Rev Appl 11 (2019) 44053. https://doi.org/10.1103/PhysRevApplied.11.044053.

[35] R. Shi, A.-V. Mudring, Phonon-Mediated Nonradiative Relaxation in Ln^{3+}-Doped Luminescent Nanocrystals, ACS Mater Lett 4 (2022) 1882–1903. https://doi.org/10.1021/acsmaterialslett.2c00595.

[36] Z. Suo, J. Dai, S. Gao, H. Gao, Effect of transition metals (Sc, Ti, V, Cr and Mn) doping on electronic structure and optical properties of CdS, Results Phys 17 (2020) 103058. https://doi.org/10.1016/j.rinp.2020.103058.

[37] L. Soussi, T. Garmim, O. Karzazi, A. Rmili, A. El Bachiri, A. Louardi, H. Erguig, Effect of (Co, Fe, Ni) doping on structural, optical and electrical properties of sprayed SnO_2 thin film, Surfaces and Interfaces 19 (2020) 100467. https://doi.org/10.1016/j.surfin.2020.100467.

[38] S.B. Sharma, I.A. Qattan, M.A. Jaoude, S. Abedrabbo, First-principles DFT study of structural, electronic and optical properties of Cu-doped TiO_2 (112) surface for enhanced visible-light photocatalysis, Comput Mater Sci 218 (2023) 111952. https://doi.org/10.1016/j.commatsci.2022.111952.

[39] C.M. Tian, W.-W. Li, Y.M. Lin, Z.Z. Yang, L. Wang, Y.G. Du, H.Y. Xiao, L. Qiao, J.Y. Zhang, L. Chen, D.-C. Qi, J.L. MacManus-Driscoll, K.H.L. Zhang, Electronic Structure, Optical Properties, and Photoelectrochemical Activity of Sn-Doped Fe_2O_3 Thin Films, The Journal of Physical Chemistry C 124 (2020) 12548–12558. https://doi.org/10.1021/acs.jpcc.0c02875.

[40] S. Chowdhury, P. Venkateswaran, D. Somvanshi, A systematic study on the electronic structure of 3d, 4d, and 5d transition metal-doped WSe2 monolayer, Superlattices Microstruct 148 (2020) 106746. https://doi.org/10.1016/j.spmi.2020.106746.

[41] S.K. Gupta, K. Sudarshan, R.M. Kadam, Optical nanomaterials with focus on rare earth doped oxide: A Review, Mater Today Commun 27 (2021) 102277. https://doi.org/https://doi.org/10.1016/j.mtcomm.2021.102277.

[42] I. Gupta, S. Singh, S. Bhagwan, D. Singh, Rare earth (RE) doped phosphors and their emerging applications: A review, Ceram Int 47 (2021) 19282–19303. https://doi.org/10.1016/j.ceramint.2021.03.308.

[43] M. Mjahed, H. Bouda, E. Salmani, H.E. Zahraouy, A. Benyoussef, Impact of rare earth (La, Pr, Eu) impurities on the perovskite $SrTiO_3$ for efficient photocatalytic activity, Phys Scr 99 (2024) 025916. https://doi.org/10.1088/1402-4896/ad13de.

[44] M.K. Hossain, S. Hossain, M.H. Ahmed, M.I. Khan, N. Haque, G.A. Raihan, A Review on Optical Applications, Prospects, and Challenges of Rare-Earth Oxides, ACS Appl Electron Mater 3 (2021) 3715–3746. https://doi.org/10.1021/acsaelm.1c00682.

[45] R. Sun, D. Zhou, H. Song, Rare earth doping in perovskite luminescent nanocrystals and photoelectric devices, Nano Select 3 (2022) 531–554. https://doi.org/10.1002/nano.202100187.

[46] S. V Gaponenko, H.V. Demir, eds., Quantum confinement effects in semiconductors, in: Applied Nanophotonics, Cambridge University Press, Cambridge, 2018: pp. 52–91. https://doi.org/DOI: 10.1017/9781316535868.004.

[47] Y. Sun, S.E. Thompson, T. Nishida, Physics of strain effects in semiconductors and metal-oxide-semiconductor field-effect transistors, J Appl Phys 101 (2007) 104503. https://doi.org/10.1063/1.2730561.

[48] H. Peelaers, C.G. Van de Walle, Effects of strain on band structure and effective masses in MoS_2, Phys Rev B 86 (2012) 241401. https://doi.org/10.1103/PhysRevB.86.241401.

[49] M. Wang, Z. Ni, X. Xiao, Y. Zhou, J. Huang, Strain engineering in metal halide perovskite materials and devices: Influence on stability and optoelectronic properties, Chemical Physics Reviews 2 (2021) 031302. https://doi.org/10.1063/5.0044588.

[50] Y. Miao, Y. Zhao, S. Zhang, R. Shi, T. Zhang, Strain Engineering: A Boosting Strategy for Photocatalysis, Advanced Materials 34 (2022) 2200868. https://doi.org/10.1002/adma.202200868.

[51] A.B. Posadas, C. Lin, A.A. Demkov, S. Zollner, Bandgap engineering in perovskite oxides: Al-doped $SrTiO_3$, Appl Phys Lett 103 (2013) 142906. https://doi.org/10.1063/1.4824023.

[52] M. Tahir, et.al, Recent development in band engineering of binary semiconductor materials for solar driven photocatalytic hydrogen production, Int J Hydrogen Energy 45 (2020) 15985–16038. https://doi.org/10.1016/j.ijhydene.2020.04.071.

[53] S. Wang, D. Song, L. Liao, M. Li, Z. Li, W. Zhou, Surface and interface engineering of BiOCl nanomaterials and their photocatalytic applications, Adv Colloid Interface Sci 324 (2024) 103088. https://doi.org/10.1016/j.cis.2024.103088.

[54] D. Kim, W. Zu, C. Lam Kwok, L.Y.S. Lee, Interface Engineering of Electrocatalysts for Efficient and Selective Oxygen Evolution in Alkaline/Seawater, ChemCatChem 16 (2024) e202400125. https://doi.org/10.1002/cctc.202400125.

[55] S. Guan, Et.al, Oxygen vacancies induced band gap narrowing for efficient visible-light response in carbon-doped TiO_2, Sci Rep 13 (2023) 14105. https://doi.org/10.1038/s41598-023-39523-6.

[56] Md.H. Miah, M.U. Khandaker, Md.B. Rahman, M. Nur-E-Alam, M.A. Islam, Band gap tuning of perovskite solar cells for enhancing the efficiency and stability: issues and prospects, RSC Adv 14 (2024) 15876–15906. https://doi.org/10.1039/D4RA01640H.

[57] A. El Mesoudy, D. Machon, A. Ruediger, A. Jaouad, F. Alibart, S. Ecoffey, D. Drouin, Band gap narrowing induced by oxygen vacancies in reactively sputtered TiO_2 thin films, Thin Solid Films 769 (2023) 139737. https://doi.org/10.1016/j.tsf.2023.139737.

[58] X. Bi, G. Du, A. Kalam, D. Sun, Y. Yu, Q. Su, B. Xu, A.G. Al-Sehemi, Tuning oxygen vacancy content in TiO_2 nanoparticles to enhance the photocatalytic performance, Chem Eng Sci 234 (2021) 116440. https://doi.org/https://doi.org/10.1016/j.ces.2021.116440.

[59] S.A. Ansari, M.M. Khan, S. Kalathil, A. Nisar, J. Lee, M.H. Cho, Oxygen vacancy induced band gap narrowing of ZnO nanostructures by an electrochemically active biofilm, Nanoscale 5 (2013) 9238–9246. https://doi.org/10.1039/C3NR02678G.

[60] I. Fareed, M. ul H. Farooq, M.D. Khan, Z. Ali, F.K. Butt, Band gap engineering of Strontium Titanate (SrTiO3) for improved photocatalytic activity and excellent bio-sensing aptitude, Mater Sci Semicond Process 177 (2024) 108327. https://doi.org/10.1016/j.mssp.2024.108327.

[61] N.T. Kalyani, H. Swart, S.J. Dhoble, Chapter 1 - Luminescence: Basic Principles and Applications, in: N.T. Kalyani, H. Swart, S.J. Dhoble (Eds.), Principles and Applications of Organic Light Emitting Diodes (OLEDs), Woodhead Publishing, 2017: pp. 1–37. https://doi.org/10.1016/B978-0-08-101213-0.00001-1.

[62] G.B. Nair, S.J. Dhoble, 1 - Introduction to luminescence, in: G.B. Nair, S.J. Dhoble (Eds.), The Fundamentals and Applications of Light-Emitting Diodes, Woodhead Publishing, 2021: pp. 3–33. https://doi.org/10.1016/B978-0-12-819605-2.00001-X.

[63] A. Edgar, Luminescent Materials, in: S. Kasap, P. Capper (Eds.), Springer Handbook of Electronic and Photonic Materials, Springer US, Boston, MA, 2007: pp. 983–996. https://doi.org/10.1007/978-0-387-29185-7_40.

[64] X. Zhou, Z. Xia, 15 - Fundamentals of ceramics for photonics applications, in: P. Cao, Z.-G. Chen, Z. Xia (Eds.), Advanced Ceramics for Energy Storage, Thermoelectrics and Photonics, Elsevier, 2023: pp. 365–394. https://doi.org/10.1016/B978-0-323-90761-3.00003-6.

[65] M. Yoshikawa, Photoluminescence (PL) Spectroscopy, in: M. Yoshikawa (Ed.), Advanced Optical Spectroscopy Techniques for Semiconductors: Raman, Infrared, and Cathodoluminescence Spectroscopy, Springer International Publishing, Cham, 2023: pp. 27–32. https://doi.org/10.1007/978-3-031-19722-2_3.

[66] J. Liqiang, Q. Yichun, W. Baiqi, L. Shudan, J. Baojiang, Y. Libin, F. Wei, F. Honggang, S. Jiazhong, Review of photoluminescence performance of nano-sized semiconductor materials and its relationships with photocatalytic activity, Solar Energy Materials and Solar Cells 90 (2006) 1773–1787. https://doi.org/10.1016/j.solmat.2005.11.007.

[67] G. Pettinari, A. Polimeni, M. Capizzi, Photoluminescence: A Tool for Investigating Optical, Electronic, and Structural Properties of Semiconductors, in: A. Patane, N. Balkan (Eds.), Semiconductor Research: Experimental Techniques, Springer Berlin Heidelberg, Berlin, Heidelberg, 2012: pp. 125–170. https://doi.org/10.1007/978-3-642-23351-7_5.

[68] Y. Jin, M. Govoni, G. Wolfowicz, S.E. Sullivan, F.J. Heremans, D.D. Awschalom, G. Galli, Photoluminescence spectra of point defects in semiconductors: Validation of first-principles calculations, Phys Rev Mater 5 (2021) 84603. https://doi.org/10.1103/PhysRevMaterials.5.084603.

[69] J. Zhang, Y. Hao, Q. Wang, J. Xu, L. Guo, K. Bi, Enhanced photoluminescence properties of $SrTiO_3$:Pr^{3+} nanocrystals by the "TEG-sol" method, APL Mater 6 (2018) 086102. https://doi.org/10.1063/1.5041821.

[70] A. Rubano, D. Paparo, F.M. Granozio, U. Scotti di Uccio, L. Marrucci, Blue luminescence of $SrTiO_3$ under intense optical excitation, J Appl Phys 106 (2009) 103515. https://doi.org/10.1063/1.3256140.

[71] Y.T. Sihvonen, Photoluminescence, Photocurrent, and Phase-Transition Correlations in $SrTiO_3$, J Appl Phys 38 (1967) 4431–4435. https://doi.org/10.1063/1.1709142.

[72] D. Kan, T. Terashima, R. Kanda, A. Masuno, K. Tanaka, S. Chu, H. Kan, A. Ishizumi, Y. Kanemitsu, Y. Shimakawa, M. Takano, Blue-light emission at room temperature from Ar^+-irradiated $SrTiO_3$, Nat Mater 4 (2005) 816–819. https://doi.org/10.1038/nmat1498.

[73] D. Kan, R. Kanda, Y. Kanemitsu, Y. Shimakawa, M. Takano, T. Terashima, A. Ishizumi, Blue luminescence from electron-doped $SrTiO_3$, Appl Phys Lett 88 (2006) 191916. https://doi.org/10.1063/1.2202750.

[74] A. Rubano, D. Paparo, F.M. Granozio, U. Scotti di Uccio, L. Marrucci, Blue luminescence of $SrTiO_3$ under intense optical excitation, J Appl Phys 106 (2009) 103515. https://doi.org/10.1063/1.3256140.

[75] Y. Yamada, H. Yasuda, T. Tayagaki, Y. Kanemitsu, Photocarrier recombination dynamics in highly excited $SrTiO_3$ studied by transient absorption and photoluminescence spectroscopy, Appl Phys Lett 95 (2009) 121112. https://doi.org/10.1063/1.3238269.

[76] W. Xu, J. Yang, W. Bai, K. Tang, Y. Zhang, X. Tang, Oxygen vacancy induced photoluminescence and ferromagnetism in SrTiO3 thin films by molecular beam epitaxy, J Appl Phys 114 (2013) 154106. https://doi.org/10.1063/1.4825257.

[77] C. Bundesmann, R. Schmidt-Grund, M. Schubert, Optical Properties of ZnO and Related Compounds, in: K. Ellmer, A. Klein, B. Rech (Eds.), Transparent Conductive Zinc Oxide: Basics and Applications in Thin Film Solar Cells, Springer Berlin Heidelberg, Berlin, Heidelberg, 2008: pp. 79–124. https://doi.org/10.1007/978-3-540-73612-7_3.

[78] R.A. Afre, N. Sharma, M. Sharon, M. Sharon, Transparent Conducting Oxide Films for Various Applications: A Review, 53 (2018) 79–89. https://doi.org/doi:10.1515/rams-2018-0006.

[79] B.G. Lewis, D.C. Paine, Applications and Processing of Transparent Conducting Oxides, MRS Bull 25 (2000) 22–27. https://doi.org/DOI: 10.1557/mrs2000.147.

[80] J.A. Spencer, A.L. Mock, A.G. Jacobs, M. Schubert, Y. Zhang, M.J. Tadjer, A review of band structure and material properties of transparent conducting and semiconducting oxides: Ga_2O_3, Al_2O_3, In_2O_3, ZnO, SnO_2, CdO, NiO, CuO, and Sc_2O_3, Appl Phys Rev 9 (2022) 011315. https://doi.org/10.1063/5.0078037.

[81] T.J. Coutts, D.L. Young, T.A. Gessert, Modeling, Characterization, and Properties of Transparent Conducting Oxides, in: D.S. Ginley (Ed.), Handbook of Transparent Conductors, Springer US, Boston, MA, 2011: pp. 51–110. https://doi.org/10.1007/978-1-4419-1638-9_3.

[82] J. Robertson, B. Falabretti, Electronic Structure of Transparent Conducting Oxides, in: D.S. Ginley (Ed.), Handbook of Transparent Conductors, Springer US, Boston, MA, 2011: pp. 27–50. https://doi.org/10.1007/978-1-4419-1638-9_2.

[83] B.A.D. Williamson, T.J. Featherstone, S.S. Sathasivam, J.E.N. Swallow, H. Shiel, L.A.H. Jones, M.J. Smiles, A. Regoutz, T.-L. Lee, X. Xia, C. Blackman, P.K. Thakur, C.J. Carmalt, I.P. Parkin, T.D. Veal, D.O. Scanlon, Resonant Ta Doping for Enhanced Mobility in Transparent Conducting SnO_2, Chemistry of Materials 32 (2020) 1964–1973. https://doi.org/10.1021/acs.chemmater.9b04845.

[84] L. Hu, R.H. Wei, X.W. Tang, W.J. Lu, X.B. Zhu, Y.P. Sun, Design strategy for p-type transparent conducting oxides, J Appl Phys 128 (2020) 140902. https://doi.org/10.1063/5.0023656.

[85] J. Singh, P. Bhardwaj, R. Kumar, V. Verma, Progress in Developing Highly Efficient p-type TCOs for Transparent Electronics: A Comprehensive Review, J Electron Mater (2024). https://doi.org/10.1007/s11664-024-11445-7.

[86] J. Robertson, B. Falabretti, Electronic Structure of Transparent Conducting Oxides, in: D.S. Ginley (Ed.), Handbook of Transparent Conductors, Springer US, Boston, MA, 2011: pp. 27–50. https://doi.org/10.1007/978-1-4419-1638-9_2.

[87] L. Hu, R.H. Wei, X.W. Tang, W.J. Lu, X.B. Zhu, Y.P. Sun, Design strategy for p-type transparent conducting oxides, J Appl Phys 128 (2020) 140902. https://doi.org/10.1063/5.0023656.

[88] S.C. Dixon, D.O. Scanlon, C.J. Carmalt, I.P. Parkin, n-Type doped transparent conducting binary oxides: an overview, J Mater Chem C Mater 4 (2016) 6946–6961. https://doi.org/10.1039/C6TC01881E.

[89] G. Hautier, A. Miglio, G. Ceder, G.-M. Rignanese, X. Gonze, Identification and design principles of low hole effective mass p-type transparent conducting oxides, Nat Commun 4 (2013) 2292. https://doi.org/10.1038/ncomms3292.

[90] J. Robertson, P.W. Peacock, M.D. Towler, R. Needs, Electronic structure of p-type conducting transparent oxides, Thin Solid Films 411 (2002) 96–100. https://doi.org/10.1016/S0040-6090(02)00195-5.

[91] Y. Kumagai, Computational Screening of p-Type Transparent Conducting Oxides Using the Optical Absorption Spectra and Oxygen-Vacancy Formation Energies, Phys Rev Appl 19 (2023) 34063. https://doi.org/10.1103/PhysRevApplied.19.034063.

[92] H. He, Z. Yang, Y. Xu, A.T. Smith, G. Yang, L. Sun, Perovskite oxides as transparent semiconductors: a review, Nano Converg 7 (2020) 32. https://doi.org/10.1186/s40580-020-00242-7.

[93] A. Biswas, N. Li, M.H. Jung, Y.W. Lee, J.S. Kim, Y.H. Jeong, La doped $SrTiO_3$ thin films on $SrLaAlO_4$ (001) as transparent conductor, J Appl Phys 113 (2013) 183711. https://doi.org/10.1063/1.4804664.

[94] Y.S. Lee, D. Djukic, R.M. Roth, R. Laibowitz, T. Izuhara, R.M. Osgood Jr., S. Bakhru, H. Bakhru, W. Si, D. Welch, Fabrication of patterned single-crystal $SrTiO_3$ thin films by ion slicing and anodic bonding, Appl Phys Lett 89 (2006) 122902. https://doi.org/10.1063/1.2355457.

[95] H.J. Kim, U. Kim, T.H. Kim, J. Kim, H.M. Kim, B.-G. Jeon, W.-J. Lee, H.S. Mun, K.T. Hong, J. Yu, K. Char, K.H. Kim, Physical properties of transparent perovskite oxides (Ba,La)$SnO_3$with high electrical mobility at room temperature, Phys Rev B 86 (2012) 165205. https://doi.org/10.1103/PhysRevB.86.165205.

[96] Sonali Saha, T P Sinha, Abhijit Mookerjee, Structural and optical properties of paraelectric $SrTiO_3$, Journal of Physics: Condensed Matter 12 (2000) 3325. https://doi.org/10.1088/0953-8984/12/14/309.

[97] D. Xu, Y. Yuan, H. Zhu, L. Cheng, C. Liu, J. Su, X. Zhang, H. Zhang, X. Zhang, J. Li, Nanostructure and Optical Property Investigations of $SrTiO_3$ Films Deposited by Magnetron Sputtering, Materials 12 (2019). https://doi.org/10.3390/ma12010138.

[98] X.F. Zheng, C.X. Liu, Y.Y. Yan, Q. Wang, A review of thermoelectrics research – Recent developments and potentials for sustainable and renewable energy applications, Renewable and Sustainable Energy Reviews 32 (2014) 486–503. https://doi.org/10.1016/j.rser.2013.12.053.

[99] L. Wang, Z. Zhang, Y. Liu, B. Wang, L. Fang, J. Qiu, K. Zhang, S. Wang, Exceptional thermoelectric properties of flexible organic−inorganic hybrids with monodispersed and periodic nanophase, Nat Commun 9 (2018) 3817. https://doi.org/10.1038/s41467-018-06251-9.

[100] Z. Wu, S. Zhang, Z. Liu, E. Mu, Z. Hu, Thermoelectric converter: Strategies from materials to device application, Nano Energy 91 (2022) 106692. https://doi.org/10.1016/j.nanoen.2021.106692.

[101] P. Ren, Y. Liu, J. He, T. Lv, J. Gao, G. Xu, Recent advances in inorganic material thermoelectrics, Inorg Chem Front 5 (2018) 2380–2398. https://doi.org/10.1039/C8QI00366A.

[102] S. Bhakta, B. Kundu, A Review of Thermoelectric Generators in Automobile Waste Heat Recovery Systems for Improving Energy Utilization, Energies (Basel) 17 (2024). https://doi.org/10.3390/en17051016.

[103] F.P. Brito, N. Pacheco, R. Vieira, J. Martins, L. Martins, J. Teixeira, L.M. Goncalves, J. Oliveira, M.J. Hall, Efficiency improvement of vehicles using temperature controlled exhaust thermoelectric generators, Energy Convers Manag 203 (2020) 112255. https://doi.org/https://doi.org/10.1016/j.enconman.2019.112255.

[104] Ö.F. Keser, B. İdare, B. Bulat, A. Okan, The Usability of PV-TEG Hybrid Systems on Space Platforms, in: 2019 9th International Conference on Recent Advances in Space Technologies (RAST), 2019: pp. 109–115. https://doi.org/10.1109/RAST.2019.8767785.

[105] M. Von Lukowicz, E. Abbe, T. Schmiel, M. Tajmar, Thermoelectric Generators on Satellites—An Approach for Waste Heat Recovery in Space, Energies (Basel) 9 (2016). https://doi.org/10.3390/en9070541.

[106] Y. Rao, C. Xu, M. Voss, P. Ying, H. Reith, K. Nielsch, T. Bechtold, D. Hohlfeld, Fabrication and Characterization of a Thermoelectric Generator with High Aspect Ratio Thermolegs for Electrically Active Implants, Adv Mater Technol 9 (2024) 2301157. https://doi.org/https://doi.org/10.1002/admt.202301157.

[107] B. Hu, X.-L. Shi, J. Zou, Z.-G. Chen, Thermoelectrics for medical applications: Progress, challenges, and perspectives, Chemical Engineering Journal 437 (2022) 135268. https://doi.org/https://doi.org/10.1016/j.cej.2022.135268.

[108] W.-Y. Chen, X.-L. Shi, J. Zou, Z.-G. Chen, Thermoelectric coolers for on-chip thermal management: Materials, design, and optimization, Materials Science and Engineering: R: Reports 151 (2022) 100700. https://doi.org/https://doi.org/10.1016/j.mser.2022.100700.

[109] D. Narducci, B. Lorenzi, Economic Convenience of Hybrid Thermoelectric-Photovoltaic Solar Harvesters, ACS Appl Energy Mater 4 (2021) 4029–4037. https://doi.org/10.1021/acsaem.1c00394.

[110] H.J. Goldsmid, Bismuth Telluride and Its Alloys as Materials for Thermoelectric Generation, Materials (Basel) 7 (2014) 2577–2592. https://doi.org/10.3390/ma7042577.

[111] T. Cao, X.-L. Shi, M. Li, B. Hu, W. Chen, W.-D. Liu, W. Lyu, J. MacLeod, Z.-G. Chen, Advances in bismuth-telluride-based thermoelectric devices: Progress and challenges, EScience 3 (2023) 100122. https://doi.org/https://doi.org/10.1016/j.esci.2023.100122.

[112] D. Van Hoang, A. Tuan Thanh Pham, T. Baba, T. Huu Nguyen, T. Bao Nguyen Le, T. Dieu Thi Ung, J. Hong, J.-S. Bae, H. Park, S. Park, I. Ohkubo, T. Mori, V. Cao Tran, T. Bach Phan, New record high thermoelectric ZT of delafossite-based $CuCrO_2$ thin films obtained by simultaneously reducing electrical resistivity and thermal conductivity via heavy doping with controlled residual stress, Appl Surf Sci 583 (2022) 152526. https://doi.org/10.1016/j.apsusc.2022.152526.

[113] T. Wu, P. Gao, Development of Perovskite-Type Materials for Thermoelectric Application, Materials 11 (2018). https://doi.org/10.3390/ma11060999.

[114] Z. Han, J.-W. Li, F. Jiang, J. Xia, B.-P. Zhang, J.-F. Li, W. Liu, Room-temperature thermoelectric materials: Challenges and a new paradigm, Journal of Materiomics 8 (2022) 427–436. https://doi.org/https://doi.org/10.1016/j.jmat.2021.07.004.

[115] G. Schierning, R. Chavez, R. Schmechel, B. Balke, G. Rogl, P. Rogl, Concepts for medium-high to high temperature thermoelectric heat-to-electricity conversion: a review of selected materials and basic considerations of module design, Translational Materials Research 2 (2015) 025001. https://doi.org/10.1088/2053-1613/2/2/025001.

[116] B. Li, R. Zhai, T. Fang, K. Xia, Y. Wu, T. Zhu, Mid-temperature thermoelectric performance of zone-melted Sb2(Te,Se)3 alloys near phase transition boundary, Journal of Materiomics 5 (2019) 590–596. https://doi.org/10.1016/j.jmat.2019.08.001.

[117] Z. Han, J.-W. Li, F. Jiang, J. Xia, B.-P. Zhang, J.-F. Li, W. Liu, Room-temperature thermoelectric materials: Challenges and a new paradigm, Journal of Materiomics 8 (2022) 427–436. https://doi.org/10.1016/j.jmat.2021.07.004.

[118] D. Van Hoang, A. Tuan Thanh Pham, T. Baba, T. Huu Nguyen, T. Bao Nguyen Le, T. Dieu Thi Ung, J. Hong, J.-S. Bae, H. Park, S. Park, I. Ohkubo, T. Mori, V. Cao Tran, T. Bach Phan, New record high thermoelectric ZT of delafossite-based $CuCrO_2$ thin films obtained by simultaneously reducing electrical resistivity and thermal conductivity via heavy doping with controlled residual stress, Appl Surf Sci 583 (2022) 152526. https://doi.org/10.1016/j.apsusc.2022.152526.

[119] Y. Yin, B. Tudu, A. Tiwari, Recent advances in oxide thermoelectric materials and modules, Vacuum 146 (2017) 356–374. https://doi.org/10.1016/j.vacuum.2017.04.015.

[120] M. Acharya, S.S. Jana, M. Ranjan, T. Maiti, High performance (ZT>1) n-type oxide thermoelectric composites from earth abundant materials, Nano Energy 84 (2021) 105905. https://doi.org/10.1016/j.nanoen.2021.105905.

[121] T.J. Seebeck, Über den Magnetismus der galvanischen Kette". Abhadlungen der physikalischen Klasse der Königlisch-Preußsischen. Akademie der Wissenschaftten aus den Jahren, (1822).

[122] G. Prunet, F. Pawula, G. Fleury, E. Cloutet, A.J. Robinson, G. Hadziioannou, A. Pakdel, A review on conductive polymers and their hybrids for flexible and wearable thermoelectric applications, Materials Today Physics 18 (2021) 100402. https://doi.org/10.1016/j.mtphys.2021.100402.

[123] L. Qiu, Y. Ouyang, F. Li, Chapter 2 - Experimental techniques overview, in: L. Qiu, Y. Feng (Eds.), Micro and Nano Thermal Transport, Academic Press, 2022: pp. 19–45. https://doi.org/10.1016/B978-0-12-823539-3.00006-4.

[124] H.J. Goldsmid, The Physics of Thermoelectric Energy Conversion, Morgan & Claypool Publishers, 2017. https://doi.org/10.1088/978-1-6817-4641-8.

[125] A. Cantarero, F.X. Àlvarez, Thermoelectric Effects: Semiclassical and Quantum Approaches from the Boltzmann Transport Equation, in: X. Wang, Z.M. Wang (Eds.),

Nanoscale Thermoelectrics, Springer International Publishing, Cham, 2014: pp. 1–39. https://doi.org/10.1007/978-3-319-02012-9_1.

[126] PhysRev.133.A1143, (n.d.).

[127] G. Tan, L.-D. Zhao, M.G. Kanatzidis, Rationally Designing High-Performance Bulk Thermoelectric Materials, Chem Rev 116 (2016) 12123–12149. https://doi.org/10.1021/acs.chemrev.6b00255.

[128] H.J. Goldsmid, Introduction to Thermoelectricity, Springer Berlin Heidelberg, Berlin, Heidelberg, 2016. https://doi.org/10.1007/978-3-662-49256-7.

[129] H. Wang, X. Luo, K. Peng, Z. Sun, M. Shi, D. Ma, N. Wang, T. Wu, J. Ying, Z. Wang, X. Chen, Magnetic Field-Enhanced Thermoelectric Performance in Dirac Semimetal Cd_3As_2 Crystals with Different Carrier Concentrations, Adv Funct Mater 29 (2019) 1902437. https://doi.org/10.1002/adfm.201902437.

[130] K. Uchida, T. Ota, K. Harii, K. Ando, H. Nakayama, E. Saitoh, Electric detection of the spin-Seebeck effect in ferromagnetic metals (invited), J Appl Phys 107 (2010) 09A951. https://doi.org/10.1063/1.3357413.

[131] K. Uchida, S. Takahashi, K. Harii, J. Ieda, W. Koshibae, K. Ando, S. Maekawa, E. Saitoh, Observation of the spin Seebeck effect, Nature 455 (2008) 778–781. https://doi.org/10.1038/nature07321.

[132] M. Schmid, S. Srichandan, D. Meier, T. Kuschel, J.-M. Schmalhorst, M. Vogel, G. Reiss, C. Strunk, C.H. Back, Transverse Spin Seebeck Effect versus Anomalous and Planar Nernst Effects in Permalloy Thin Films, Phys Rev Lett 111 (2013) 187201. https://doi.org/10.1103/PhysRevLett.111.187201.

[133] K. Uchida, T. Nonaka, T. Kikkawa, Y. Kajiwara, E. Saitoh, Longitudinal spin Seebeck effect in various garnet ferrites, Phys Rev B 87 (2013) 104412. https://doi.org/10.1103/PhysRevB.87.104412.

[134] Y. Pei, H. Wang, G.J. Snyder, Band Engineering of Thermoelectric Materials, Advanced Materials 24 (2012) 6125–6135. https://doi.org/https://doi.org/10.1002/adma.201202919.

[135] W. Dong, Z. Zhou, L. Zhang, M. Zhang, P.K. Liaw, G. Li, R. Liu, Effects of Y, GdCu, and Al Addition on the Thermoelectric Behavior of CoCrFeNi High Entropy Alloys, Metals (Basel) 8 (2018). https://doi.org/10.3390/met8100781.

[136] D.M. Rowe, Thermoelectrics and its Energy Harvesting, 2-Volume Set, CRC Press, 2018. https://doi.org/10.1201/b11869.

[137] Terry M. Tritt, Thermal Conductivity, Springer US, 2004. https://doi.org/10.1007/b136496.

[138] 10.3389-fchem.2022.865281-citation, (n.d.).

[139] G.A. Slack, V.G. Tsoukala, Some properties of semiconducting $IrSb_3$, J Appl Phys 76 (1994) 1665–1671. https://doi.org/10.1063/1.357750.

[140] A.F. Ioffe, L.S. Stil'bans, E.K. Iordanishvili, T.S. Stavitskaya, A. Gelbtuch, G. Vineyard, Semiconductor Thermoelements and Thermoelectric Cooling, Phys Today 12 (1959) 42. https://doi.org/10.1063/1.3060810.

[141] B. Yu, M. Zebarjadi, H. Wang, K. Lukas, H. Wang, D. Wang, C. Opeil, M. Dresselhaus, G. Chen, Z. Ren, Enhancement of Thermoelectric Properties by Modulation-Doping in Silicon Germanium Alloy Nanocomposites, Nano Lett 12 (2012) 2077–2082. https://doi.org/10.1021/nl3003045.

[142] 18653890, (n.d.).

[143] O. V Merkulov, I. V Shamsutov, M.A. Ryzhkov, B. V Politov, I. V Baklanova, E. V Chulkov, V.P. Zhukov, Impact of oxygen vacancies on thermal and electronic transport of donor-doped $CaMnO_{3-\delta}$, J Solid State Chem 326 (2023) 124231. https://doi.org/10.1016/j.jssc.2023.124231.

[144] B. Duan, Y. Li, J. Li, Y. Gao, P. Zhai, J. Yang, Z. Lu, H. Yang, H. Wang, G. Li, Regulation of oxygen vacancy and reduction of lattice thermal conductivity in ZnO ceramic by high temperature and high pressure method, Ceram Int 46 (2020) 26176–26181. https://doi.org/10.1016/j.ceramint.2020.07.115.

[145] S.R.S. Kumar, A.Z. Barasheed, H.N. Alshareef, High Temperature Thermoelectric Properties of Strontium Titanate Thin Films with Oxygen Vacancy and Niobium Doping, ACS Appl Mater Interfaces 5 (2013) 7268–7273. https://doi.org/10.1021/am4015956.

[146] U. Ijaz, M. Siyar, C. Park, The power of pores: review on porous thermoelectric materials, RSC Sustainability 2 (2024) 852–870. https://doi.org/10.1039/D3SU00451A.

[147] H. Wang, W. Su, J. Liu, C. Wang, Recent development of n-type perovskite thermoelectrics, Journal of Materiomics 2 (2016) 225–236. https://doi.org/10.1016/j.jmat.2016.06.005.

[148] X. Chen, Z. Zhou, Y.-H. Lin, C. Nan, Thermoelectric thin films: Promising strategies and related mechanism on boosting energy conversion performance, Journal of Materiomics 6 (2020) 494–512. https://doi.org/10.1016/j.jmat.2020.02.008.

[149] L.D. Hicks, T.C. Harman, X. Sun, M.S. Dresselhaus, Experimental study of the effect of quantum-well structures on the thermoelectric figure of merit, Phys Rev B 53 (1996) R10493–R10496. https://doi.org/10.1103/PhysRevB.53.R10493.

[150] A. Ishida, D. Cao, S. Morioka, M. Veis, Y. Inoue, T. Kita, Enhanced Seebeck coefficient in EuTe/PbTe [100] short-period superlattices, Appl Phys Lett 92 (2008) 182105. https://doi.org/10.1063/1.2917482.

[151] H. Ohta, Two-dimensional thermoelectric Seebeck coefficient of $SrTiO_3$-based superlattices, Physica Status Solidi (b) 245 (2008) 2363–2368. https://doi.org/https://doi.org/10.1002/pssb.200844248.

[152] H. Ohta, Y. Mune, K. Koumoto, T. Mizoguchi, Y. Ikuhara, Critical thickness for giant thermoelectric Seebeck coefficient of 2DEG confined in $SrTiO_3/SrTi_{0.8}Nb_{0.2}O_3$ superlattices, Thin Solid Films 516 (2008) 5916–5920. https://doi.org/10.1016/j.tsf.2007.10.034.

[153] C. Zhu, J. Wang, X. Zhu, S. Zhang, F. Xu, F. Luo, J. Wang, Y. Zhang, H. Liu, Z. Sun, Effects of magnetism and size of nano-oxide inclusions on the thermoelectric properties of $Ge_{0.96}Bi_{0.06}Te$, J Mater Chem A Mater 11 (2023) 1268–1280. https://doi.org/10.1039/D2TA08403A.

[154] V.C.S. Theja, V. Karthikeyan, D.S. Assi, V.A.L. Roy, Insights into the Classification of Nanoinclusions of Composites for Thermoelectric Applications, ACS Appl Electron Mater 4 (2022) 4781–4796. https://doi.org/10.1021/acsaelm.2c00617.

[155] R. Lu, J.S. Lopez, Y. Liu, T.P. Bailey, A.A. Page, S. Wang, C. Uher, P.F.P. Poudeu, Coherent magnetic nanoinclusions induce charge localization in half-Heusler alloys leading to high-Tc ferromagnetism and enhanced thermoelectric performance, J Mater Chem A Mater 7 (2019) 11095–11103. https://doi.org/10.1039/C9TA01156K.

[156] M. Rull-Bravo, A. Moure, J.F. Fernández, M. Martín-González, Skutterudites as thermoelectric materials: revisited, RSC Adv 5 (2015) 41653–41667. https://doi.org/10.1039/C5RA03942H.

[157] C. Zhu, J. Wang, X. Zhu, S. Zhang, F. Xu, F. Luo, J. Wang, Y. Zhang, H. Liu, Z. Sun, Effects of magnetism and size of nano-oxide inclusions on the thermoelectric properties of $Ge_{0.96}Bi_{0.06}Te$, J Mater Chem A Mater 11 (2023) 1268–1280. https://doi.org/10.1039/D2TA08403A.

[158] X. Shi, J. Yang, J.R. Salvador, M. Chi, J.Y. Cho, H. Wang, S. Bai, J. Yang, W. Zhang, L. Chen, Multiple-Filled Skutterudites: High Thermoelectric Figure of Merit through Separately Optimizing Electrical and Thermal Transports, J Am Chem Soc 133 (2011) 7837–7846. https://doi.org/10.1021/ja111199y.

[159] G. Li, Q. An, U. Aydemir, W.A. Goddard III, M. Wood, P. Zhai, Q. Zhang, G.J. Snyder, Enhanced ideal strength of thermoelectric half-Heusler TiNiSn by sub-structure engineering, J Mater Chem A Mater 4 (2016) 14625–14636. https://doi.org/10.1039/C6TA04123J.

[160] C. Fu, S. Bai, Y. Liu, Y. Tang, L. Chen, X. Zhao, T. Zhu, Realizing high figure of merit in heavy-band p-type half-Heusler thermoelectric materials, Nat Commun 6 (2015) 8144. https://doi.org/10.1038/ncomms9144.

[161] H. Zhu, W. Li, A. Nozariasbmarz, N. Liu, Y. Zhang, S. Priya, B. Poudel, Half-Heusler alloys as emerging high power density thermoelectric cooling materials, Nat Commun 14 (2023) 3300. https://doi.org/10.1038/s41467-023-38446-0.

[162] C. Yu, T.-J. Zhu, R.-Z. Shi, Y. Zhang, X.-B. Zhao, J. He, High-performance half-Heusler thermoelectric materials Hf_{1-x} $Zr_xNiSn_{1-y}Sb_y$ prepared by levitation melting and spark plasma sintering, Acta Mater 57 (2009) 2757–2764. https://doi.org/10.1016/j.actamat.2009.02.026.

[163] J.-A. Dolyniuk, B. Owens-Baird, J. Wang, J. V Zaikina, K. Kovnir, Clathrate thermoelectrics, Materials Science and Engineering: R: Reports 108 (2016) 1–46. https://doi.org/https://doi.org/10.1016/j.mser.2016.08.001.

[164] V. Pecunia, Et.al, Roadmap on energy harvesting materials, Journal of Physics: Materials 6 (2023) 042501. https://doi.org/10.1088/2515-7639/acc550.

[165] L.-H. Wang, L.-S. Chang, Thermoelectric properties of p-type $Ba_8Ga_{16}Ge_{30}$ type-I clathrate compounds prepared by the vertical Bridgman method, J Alloys Compd 722 (2017) 644–650. https://doi.org/https://doi.org/10.1016/j.jallcom.2017.06.110.

[166] K. Biswas, J. He, I.D. Blum, C.-I. Wu, T.P. Hogan, D.N. Seidman, V.P. Dravid, M.G. Kanatzidis, High-performance bulk thermoelectrics with all-scale hierarchical architectures, Nature 489 (2012) 414–418. https://doi.org/10.1038/nature11439.

[167] K.F. Hsu, S. Loo, F. Guo, W. Chen, J.S. Dyck, C. Uher, T. Hogan, E.K. Polychroniadis, M.G. Kanatzidis, Cubic $AgPbmSbTe^{2+m}$: Bulk Thermoelectric Materials with High Figure of Merit, Science (1979) 303 (2004) 818–821. https://doi.org/10.1126/science.1092963.

[168] I.T. Witting, T.C. Chasapis, F. Ricci, M. Peters, N.A. Heinz, G. Hautier, G.J. Snyder, The Thermoelectric Properties of Bismuth Telluride, Adv Electron Mater 5 (2019) 1800904. https://doi.org/10.1002/aelm.201800904.

[169] T. Cao, X.-L. Shi, M. Li, B. Hu, W. Chen, W.-D. Liu, W. Lyu, J. MacLeod, Z.-G. Chen, Advances in bismuth-telluride-based thermoelectric devices: Progress and challenges, EScience 3 (2023) 100122. https://doi.org/10.1016/j.esci.2023.100122.

[170] L.-D. Zhao, C. Chang, G. Tan, M.G. Kanatzidis, SnSe: a remarkable new thermoelectric material, Energy Environ Sci 9 (2016) 3044–3060. https://doi.org/10.1039/C6EE01755J.

[171] Y. Zhang, H. Ohta, Recent progress in thermoelectric layered cobalt oxide thin films, NPG Asia Mater 15 (2023) 67. https://doi.org/10.1038/s41427-023-00520-w.

[172] M. Choi ,Et.al, High figure-of-merit for ZnO nanostructures by interfacing lowly-oxidized graphene quantum dots, Nat Commun 15 (2024) 1996. https://doi.org/10.1038/s41467-024-46182-2.

[173] B. Rahmati Kalkhoran, Microstructural studies on the reoxidation behavior of Nb-doped $SrTiO_3$ ceramics, 2004. http://inis.iaea.org/search/search.aspx?orig_q=RN:36065906.

[174] F.W. Lytle, X-Ray Diffractometry of Low-Temperature Phase Transformations in Strontium Titanate, J Appl Phys 35 (1964) 2212–2215. https://doi.org/10.1063/1.1702820.

[175] The ABX3 Perovskite Structure, in: Perovskites, 2016: pp. 1–41. https://doi.org/10.1002/9781118935651.ch1.

[176] ABX_3–Related Structures, in: Perovskites, 2016: pp. 42–78. https://doi.org/10.1002/9781118935651.ch2.

[177] L.D. Hicks, M.S. Dresselhaus, Thermoelectric figure of merit of a one-dimensional conductor, Phys Rev B 47 (1993) 16631–16634. https://doi.org/10.1103/PhysRevB.47.16631.

[178] A. Tsukazaki, Et.al , High Electron Mobility Exceeding 104 $cm^2 V^{-1} s^{-1}$ in $Mg_xZn_{1-x}O$/ZnO Single Heterostructures Grown by Molecular Beam Epitaxy, Applied Physics Express 1 (2008) 055004. https://doi.org/10.1143/APEX.1.055004.

[179] F. Gao, S. Yang, J. Li, M. Qin, Y. Zhang, H. Sun, Fabrication, dielectric, and thermoelectric properties of textured $SrTiO_3$ ceramics prepared by RTGG method, Ceram Int 41 (2015) 127–135. https://doi.org/10.1016/j.ceramint.2014.08.045.

[180] H. Bakhshi, R. Sarraf-Mamoory, A. Yourdkhani, S. Song, Y.-C. Tseng, Y. Mozharivskyj, Improvements in the thermoelectric efficiency of $SrTiO_3$ through donor doping, Ceram Int 48 (2022) 5831–5839. https://doi.org/10.1016/j.ceramint.2021.11.131.

[181] G.J. Snyder, E.S. Toberer, Complex thermoelectric materials, Nat Mater 7 (2008) 105–114. https://doi.org/10.1038/nmat2090.

[182] D. Liu, Y. Et al., Ultrahigh electrical conductivities and low lattice thermal conductivities of La, Dy, and Nb Co-doped SrTiO3 thermoelectric materials with complex structures, J Mater Sci Technol 52 (2020) 172–179. https://doi.org/10.1016/j.jmst.2020.02.065.

[183] J.-B. Li, J. Wang, J.-F. Li, Y. Li, H. Yang, H.-Y. Yu, X.-B. Ma, X. Yaer, L. Liu, L. Miao, Broadening the temperature range for high thermoelectric performance of bulk polycrystalline strontium titanate by controlling the electronic transport properties, J Mater Chem C Mater 6 (2018) 7594–7603. https://doi.org/10.1039/C8TC02130A.

[184] S. Ohta, T. Nomura, H. Ohta, K. Koumoto, High-temperature carrier transport and thermoelectric properties of heavily La- or Nb-doped $SrTiO_3$ single crystals, J Appl Phys 97 (2005) 034106. https://doi.org/10.1063/1.1847723.

[185] C. Mallada, J.L. Menéndez, O.J. Dura, M.A. López de la Torre, R. Menéndez, R. Santamaría, Spark plasma sintered $BaTiO_3$/graphene composites for thermoelectric applications, J Eur Ceram Soc 37 (2017) 3741–3746. https://doi.org/10.1016/j.jeurceramsoc.2017.02.027.

[186] Y. Lin, C. Norman, D. Srivastava, F. Azough, L. Wang, M. Robbins, K. Simpson, R. Freer, I.A. Kinloch, Thermoelectric Power Generation from Lanthanum Strontium

Titanium Oxide at Room Temperature through the Addition of Graphene, ACS Appl Mater Interfaces 7 (2015) 15898–15908. https://doi.org/10.1021/acsami.5b03522.

[187] D. Srivastava, C. Norman, F. Azough, M.C. Schäfer, E. Guilmeau, R. Freer, Improving the thermoelectric properties of $SrTiO_3$-based ceramics with metallic inclusions, J Alloys Compd 731 (2018) 723–730. https://doi.org/10.1016/j.jallcom.2017.10.033.

[188] S.R.S. Kumar, A.Z. Barasheed, H.N. Alshareef, High Temperature Thermoelectric Properties of Strontium Titanate Thin Films with Oxygen Vacancy and Niobium Doping, ACS Appl Mater Interfaces 5 (2013) 7268–7273. https://doi.org/10.1021/am4015956.

[189] A.I. Abutaha, S.R.S. Kumar, K. Li, A.M. Dehkordi, T.M. Tritt, H.N. Alshareef, Enhanced Thermoelectric Figure-of-Merit in Thermally Robust, Nanostructured Superlattices Based on $SrTiO_3$, Chemistry of Materials 27 (2015) 2165–2171. https://doi.org/10.1021/acs.chemmater.5b00144.

[190] H. Ohta, Two-dimensional thermoelectric Seebeck coefficient of SrTiO3-based superlattices, Physica Status Solidi (b) 245 (2008) 2363–2368. https://doi.org/10.1002/pssb.200844248.

[191] H. Ohta, Y. Mune, K. Koumoto, T. Mizoguchi, Y. Ikuhara, Critical thickness for giant thermoelectric Seebeck coefficient of 2DEG confined in $SrTiO_3/SrTi_{0.8}Nb_{0.2}O_3$ superlattices, Thin Solid Films 516 (2008) 5916–5920. https://doi.org/10.1016/j.tsf.2007.10.034.

Chapter 2

Experimental methods and characterization techniques

Objectives

The objective of this chapter is to detail the experimental methods and characterization techniques used in the synthesis and analysis of materials. It aims to provide a comprehensive description of the techniques employed to synthesize the materials, as well as the methodologies for investigating their structural, spectroscopic, optical, and thermoelectric properties. This chapter seeks to highlight the importance of these characterization tools in understanding the relationship between the materials' microstructure and their optoelectronic and thermoelectric performances.

2.1 Introduction

This chapter investigates synthesis approaches tailored for both optical and thermoelectric applications: bulk synthesis via solid-state reaction with subsequent graphite sintering, and thin film fabrication using RF sputtering. Solid-state reaction methods are employed to ensure material homogeneity and optimal thermoelectric properties, enhanced further by graphite sintering to improve density and electrical conductivity. Meanwhile, RF sputtering offers precise control over thin film deposition, crucial for tailoring optical and thermoelectric properties at the nanoscale level, making these materials suitable for advanced optical and thermoelectric device applications.

2.2 Solid state reaction (SSR)

The solid-state reaction method is one of the most widely used techniques for the synthesis of a variety of materials, including ceramics, oxides, and composite materials. This method involves the reaction of solid reactants to form a new solid product through diffusion processes. It is particularly valued for its simplicity, versatility, and the ability to produce high-purity and homogeneously mixed materials [1,2].

The mechanisms of solid-state reactions can be complex and are influenced by factors such as temperature, particle size, and the nature of the reactants. Common mechanisms include:

- **Diffusion-controlled reactions**: The rate of the reaction is controlled by the rate at which reactant species diffuse through the solid lattice.
- **Nucleation and growth**: New phases form at specific sites (nuclei) and grow until the reaction is complete.
- **Topo chemical reactions**: These involve structural rearrangements within the solid reactant, often preserving the overall morphology.

2.2.1 Mixing the raw materials

Combining the raw materials for solid-state reactions involves mixing solid powders of the reactants in stoichiometric ratios. The homogeneity of the mixture is crucial for ensuring a uniform reaction and consistent final product quality. To achieve this, the reactant powders are often ground together using a mortar and pestle or a ball mill. Ball milling is particularly effective as it not only mixes the powders but also reduces particle size, increasing the surface area for the reaction as indicated in Fig. 2-1. Proper mixing helps to enhance the contact between reactant particles, facilitating efficient diffusion during the high-temperature reaction process. Additives, such as binders or dispersants, may be used to improve the mixing and prevent agglomeration of particles. Once the mixing is complete, the homogenous powder is ready for the subsequent calcination step, where the solid-state reaction will occur.

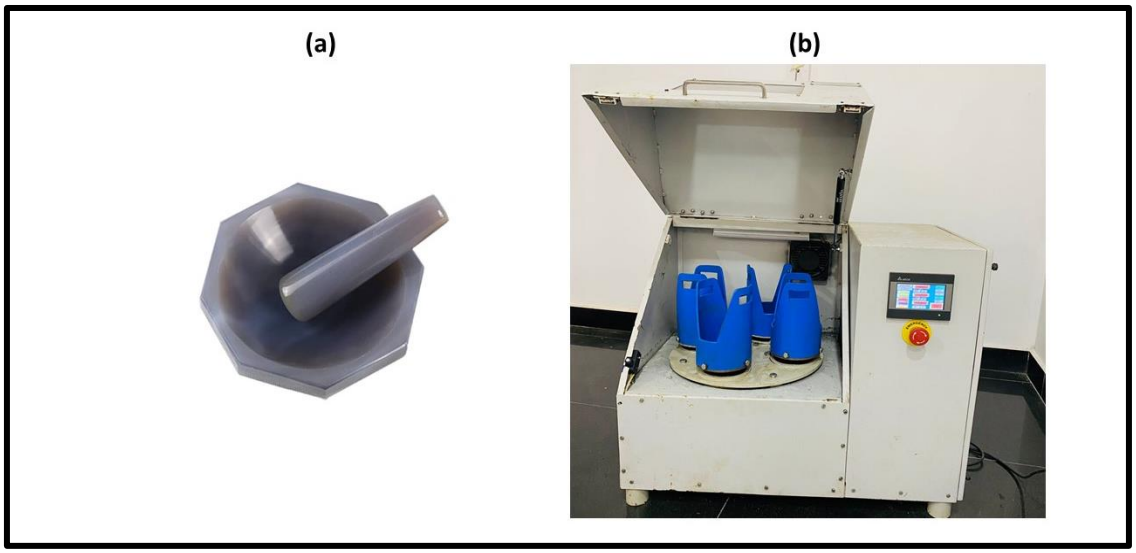

Figure 2- 1 (a) Mortar and pestle used for manual mixing and grinding **(b)** automated planetary ball mill using steel jars and agate balls.

2.2.2 Calcination

Calcination is a thermal treatment process used in solid-state reactions to induce phase changes, decomposition, or removal of volatile components from the reactants. It involves heating the reactant mixture to high temperatures, typically between 500 °C and 1500 °C using a programmable high temperature furnace, in an oxidizing or inert

atmosphere as indicated in Fig. 2-2. The primary goal of calcination is to facilitate the diffusion of reactant species, promoting the formation of a homogeneous solid product. During calcination, chemical bonds in the reactants break and reform, leading to the development of new crystalline phases. This process eliminates water, carbon dioxide, and other volatile impurities, enhancing the purity of the final product. The calcined material is then cooled and characterized to ensure the desired properties and composition.

Figure 2- 2 High temperature furnace (T_{max}=1700 °C) with PID programmable controller and molybdenum disilicide ($MoSi_2$) heating elements.

2.2.3 Re-grinding and pelletization

Re-grinding the calcined powder in solid-state reactions is essential to achieve finer particle size and increase the surface area, which enhances the uniformity and reactivity of the material. This step ensures that any unreacted regions are broken down, facilitating further diffusion and reaction in subsequent thermal treatments. Using a binder like Poly vinyl alcohol (PVA) to pelletize ceramic powder involves mixing the powder with a binder solution, which acts as a temporary adhesive to hold the particles together.

2-5 % PVA solution in distilled water is usually prepared and 3 ml is added to calcined powder. The mixture is then shaped into pellets using a hydraulic pelletizer with 5-10

Figure 2- 3 Dye and hydraulic pelletizer.

tonne pressure as indicated in Fig. 2-3. The pellets are dried at very slow heating rates (2-3 °C/ Min) to remove excess moisture and binder, ensuring they maintain their shape. The use of binders helps to improve the handling and transport of the powder by reducing dust and preventing segregation of the different particle sizes.

Pelletizing enhances the packing density and uniformity of the material, leading to better sintering and mechanical properties in the final ceramic product. Pellets are easier to feed into furnaces or other processing equipment, resulting in more efficient and consistent fabrication processes.

2.2.4 Sintering

Sintering is a crucial thermal process in solid-state reactions that compacts and densifies powdered materials into a solid mass by heating them below their melting point. This process promotes particle adhesion through diffusion and mass transport, resulting in a reduction of porosity and enhancement of mechanical properties. Sintering is vital for achieving desired material characteristics such as increased hardness, strength, and thermal conductivity. It also enables precise control over the microstructure, which is

essential for tailoring the performance of materials for specific applications. By promoting phase transformations and chemical reactions, sintering helps in the formation of desired crystalline structures.

2.2.4.1 Graphite burial sintering

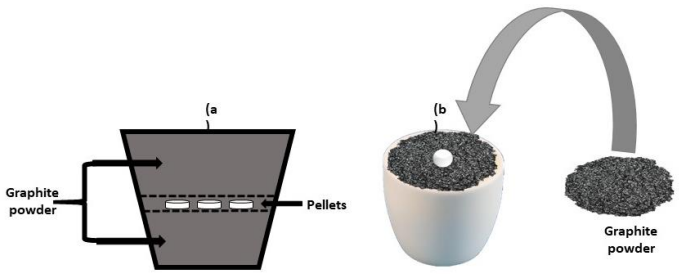

Figure 2- 4 (a) Schematic and **(b)** real representation of graphite burial sintering.

Graphite burial sintering as depicted in Fig. 2-4 is a process where powdered materials are sintered within a bed of graphite to enhance the sintering environment. The graphite acts as a reducing agent releasing reducing gas carbon monoxide, CO at high temperatures above 1200 °C, helping to prevent oxidation of the material during high-temperature treatment. This method is particularly useful for sintering metals and ceramics that are sensitive to oxidation. The graphite also provides a uniform thermal environment, improving the consistency and quality of the sintered product.

The reducing atmosphere can help in the removal of impurities from the material, leading to higher purity in the final product. Graphite burial sintering is widely used in the production of advanced ceramics and high-performance materials due to its effectiveness in enhancing material properties [3,4].

2.2.4.2 Polishing and impurity removal

Polishing using SiC (silicon carbide) papers of different grit sizes ranging from 400 to 3000, after graphite sintering is essential for achieving a smooth, even surface by removing residual roughness and irregularities. This process enhances the surface quality, which is crucial for applications requiring precise mechanical or aesthetic properties.

Polishing prepares the material for further processing steps like coating or bonding by providing a clean and smooth surface.

Steps for synthesis of Pr and Nb doped bulk samples: For the synthesis of Sr_{1-x} Pr_x TiO_3 (x=0.05, 0.075, 0.10, 0.125, 0.15, 0.20 ceramics, stoichiometricic amounts of $SrCO_3$ (Sigma-Aldrich 99.9%), TiO_2 (Sigma-Aldrich 99.9%), and Pr_6O_{11} (Sigma-Aldrich 99.9%) were mixed and ground for 2 hours in ethanol medium. TiO_2 and Pr_6O_{11} were initially dried at 900 ^oC in a clean chamber furnace for 8 hours. $SrCO_3$ was dried at 180 ^oC for 16 hrs. Ground powders were calcined at 1250 ^oC for eight hours and obtained powders were ground again. For the pure sample calcination temperature was optimized to 1200 ^oC. The powders were mixed with PVA binder and uniaxially pressed into pellets of 13 mm in diameter and 2 mm in thickness. The binder was eliminated by annealing the pellets at 600 ^oC for 4 hours at a slow heating rate. Prepared pellets were then transferred to a crucible densely filled with graphite powder for the burial sintering process at 1450 ^oC for 4 hrs with optimized dwell cycles. For Nb doped $SrTiO_3$, precursors $SrCO_3$ (Sigma-Aldrich 99.9%), TiO_2 (Sigma-Aldrich 99.9%), and Nb_2O_5 (Sigma-Aldrich 99.9%) were used. High temperature calcination and sintering were done at PID controlled furnace with optimal dwell cycles.

2.3 Sputtering

Sputtering is a physical vapor deposition (PVD) technique used to deposit thin films of material onto a substrate. In this process, a target material is bombarded with high-energy ions from a plasma, causing atoms or molecules to be ejected from the target. These ejected particles then travel through a vacuum or low-pressure usually 1 to 2 mbar gas environment and condense onto the substrate, forming a thin film. Sputtering technique is widely used in the semiconductor, display, and optical industries due to its ability to create high-quality, uniform coatings with precise thickness control.

One of the main advantages of sputtering is its ability to deposit a wide variety of materials, including metals, alloys, insulators, and polymers. The process allows for

excellent adhesion of the thin film to the substrate, which is critical for applications such as electronic components and wear-resistant coatings. Sputtering can be used to create multilayer films and complex material structures by sequentially or simultaneously sputtering different target materials. The technique also enables the deposition of films with specific properties, such as high electrical conductivity, optical transparency, or chemical resistance, by adjusting parameters like the quality of target material, gas composition, gas pressure, substrate temperature and power of RF supply. It is often preferred over other deposition methods for its ability to achieve high deposition rates and large-area coatings. The process can also be performed at relatively low temperatures, making it suitable for heat-sensitive substrates. Advanced sputtering techniques, such as magnetron sputtering, use magnetic fields to enhance the plasma density and increase the deposition rate and film quality.

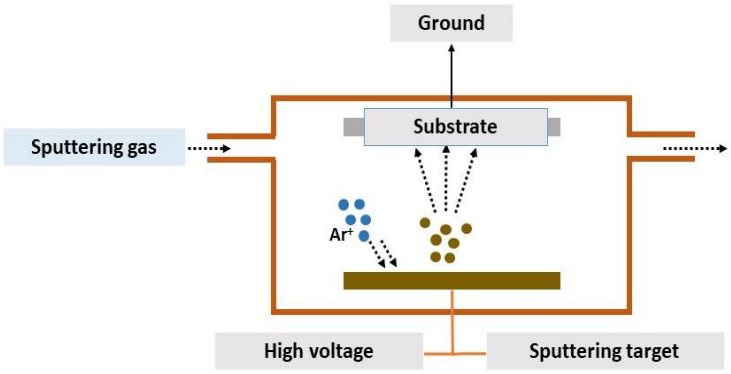

Figure 2- 5 Schematic representation of sputtering system.

The principle of sputtering involves high-energy argon ions generated in a plasma, which are accelerated towards the target material. When these argon ions collide with the target, they transfer energy, causing atoms or molecules from the target to be ejected. These ejected particles then travel and deposit onto the substrate, forming a thin film as indicated in Fig. 2-5.

2.3.1 RF magnetron sputtering

Radio frequency (RF) magnetron sputtering is a sophisticated and versatile technique for thin-film deposition that has garnered significant attention in materials

science and engineering schematically indicated in Fig. 2-6. RF sputtering allows for the effective deposition of both conductive and insulating materials, overcoming the charge buildup issues faced in DC sputtering. The fundamental mechanism of sputtering involves the ejection of atoms from target material due to bombardment by high-energy ions. In RF magnetron sputtering, the process is further refined by the application of radio frequency power, enabling the effective sputtering of non-conductive targets and enhancing film uniformity and quality. The principle of RF magnetron sputtering involves the deposition of thin films facilitated by RF generated plasma.

The entire sputtering process takes place within a vacuum chamber to minimize contamination and ensure a controlled environment for thin-film deposition. It provides the low-pressure conditions needed for stable plasma formation, which is critical for consistent ionization of the inert gas. This environment increases the mean free path of argon ions, allowing them to reach the target material with sufficient energy to achieve effective sputtering. By minimizing collisions with other gas molecules, low pressure environment improves the efficiency of material deposition onto the substrate. Inert gas such as argon is introduced into the vacuum chamber to facilitate plasma formation. Inert gas environment ensures that the gas itself does not chemically react with the target or substrate, maintaining the purity of the deposited thin film. The RF power supply in sputtering generates an oscillating electric field that ionizes the inert gas, creating a stable plasma essential for the sputtering process. It allows for the sputtering of both conductive and insulating materials by preventing charge buildup on the target surface. High-frequency oscillations of the RF power supply, enhance the efficiency and uniformity of the sputtering process, ensuring consistent ejection of target atoms from the target [5].

RF power supply for sputtering is designed to generate high-frequency alternating current, typically in the range of 13.56 MHz, to ionize the gas in the sputtering chamber and sustain the plasma. It provides precise control over power output, ensuring stable and consistent deposition rates of the target material onto the substrate. These power supplies

are equipped with advanced features such as automatic matching networks to optimize power transfer efficiency and minimize reflected power [6].

It provides excellent control over film thickness, composition, and microstructure, ensuring high-quality and uniform thin films. This proves to be a versatile, capable of depositing a wide range of materials, including metals, oxides, and complex compounds, making it suitable for diverse applications in electronics, optics, and advanced materials.

Sputtering yield is one key parameter in the sputtering process that describes the number of atoms ejected from a target material per incident ion [7,8]. It is a measure of the efficiency of the sputtering process and is influenced by several factors, including the energy of the incident ions, the type of ions, and the properties of the target material.

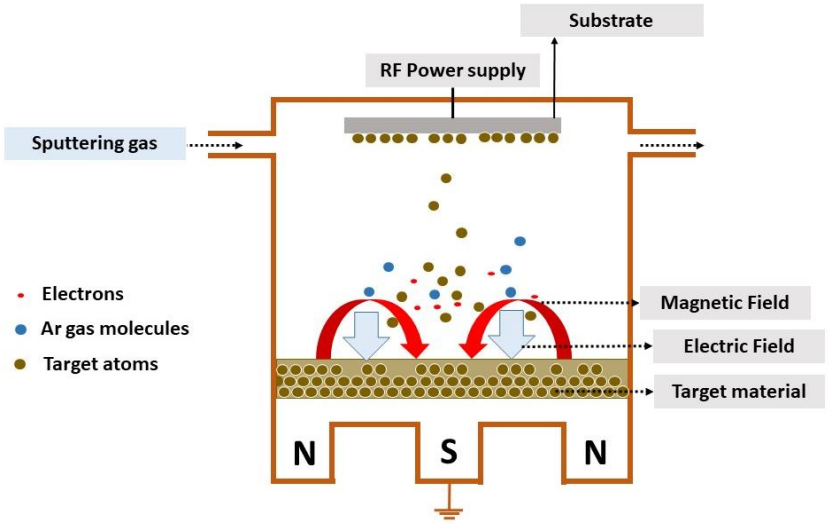

Figure 2- 6 Schematic representation of working of RF magnetron sputtering system.

The sputtering yield $'Y'$ can be expressed by the following empirical equation:

$$Y = \alpha\left(\frac{E_i - E_{th}}{E_b}\right) \tag{2.1}$$

Where α is a material-specific constant that varies depending on the target material and the type of ion used for sputtering. It encompasses factors like the atomic mass and the surface binding energy of the target material.

E_i is the energy of the ions bombarding the target significantly impacts the sputtering yield. Higher energy ions have a greater capacity to dislodge atoms from the target surface, increasing the sputtering yield.

E_{th} is the threshold Energy. This is the minimum energy required to overcome the binding forces holding an atom in the target lattice. If the ion energy is below this threshold, sputtering will not occur.

E_b is the binding energy, the energy required to remove an atom from the surface of the target material. Materials with lower binding energies typically have higher sputtering yield [9].

2.3.1.1 Stages of thin film formation in RF magnetron sputtering

The growth of thin films in RF magnetron sputtering involves several stages, each critical for achieving the desired film properties [9,10].

- **Nucleation**:
    - Atoms or molecules from the target material are ejected and travel through the plasma to reach the substrate surface. These adatoms adsorb onto the substrate, forming nucleation sites where clusters of atoms begin to form. Initially, small islands or clusters of atoms are created. The density and size of these islands depend on factors like substrate temperature, deposition rate, and surface energy.
- **Coalescence**:
    - As more adatoms arrive at the substrate, the islands grow larger and start to coalesce. The merging of islands results in the formation of grain boundaries, which are regions where the crystal orientation changes.
- **Continuous film formation**:
    - A continuous film forms when the growing islands connect and cover the substrate entirely, reaching the percolation threshold. Once a continuous film is formed, and further deposition leads to the growth of the film's

thickness. This stage involves the filling in of any remaining gaps and the development of a uniform layer.

- **Post-growth processes**:
    - In some cases, post-deposition annealing is performed to improve film properties like crystallinity, adhesion, and stress relief. Ensuring a high-quality interface and surface is crucial for the film's performance in its intended application. This can involve processes like surface passivation or chemical treatments.

2.3.1.2 Different film growth modes

Thin film growth in RF sputtering can follow different modes, depending on factors like the substrate material, deposition conditions, and the interactions between the film and substrate [11,12] . The primary growth modes include:

- **Volmer-Weber (Island) growth**: In this mode, atoms or molecules deposited on the substrate initially form small clusters or islands that grow independently. This occurs when the atoms are more strongly bound to each other than to the substrate. This mode is typically seen in the growth of metals on insulators or materials with low wettability.
- **Frank-van der Merwe (Layer-by-layer) growth**: Atoms or molecules form a uniform monolayer before starting to form the next layer. This mode occurs when the interaction between the film and substrate is stronger than the interaction among film atoms. This is common in the epitaxial growth of semiconductors and thin metal films.
- **Stranski-Krastanov (Layer-plus-island) growth**: Initially, atoms form one or more complete monolayers (like in Frank-van der Merwe growth), followed by the formation of three-dimensional islands. This mode occurs when there is a strain due to lattice mismatch between the film and substrate that builds up after the formation of a few monolayers, leading to island formation. This is common

in the growth of strained-layer epitaxy and certain semiconductor heterostructures.

- **Ostwald ripening**: Over time, smaller islands or clusters dissolve and reorient onto larger islands, leading to the growth of larger grains at the expense of smaller ones. This process is driven by the reduction of the total surface energy of the system.

2.3.1.3 Factors influencing growth modes

Achieving high-quality thin films in RF sputtering involves carefully tuning various factors and parameters.

- **RF power**: High RF power Increases the ionization rate and the number of sputtered atoms, leading to higher deposition rates. However, it can also increase substrate heating and potential damage. Whereas a lower power reduces the deposition rate but can improve film uniformity and reduce defects.
- **Substrate temperature**: High substrate temperature enhances adatom mobility, promoting better crystalline quality and larger grain sizes. It can also reduce stress and improve adhesion. Whereas a lower temperature may be necessary for substrates sensitive to heat but can lead to amorphous or nanocrystalline films depending on the formation energy of the material.
- **Gas pressure**: High gas pressure increases the collision frequency of sputtered atoms, leading to a more isotropic deposition and potential increase in film density. However, it can reduce the mean free path, affecting the energy of the arriving atoms. Whereas a lower pressure leads to a more directional flux of sputtered atoms, which can improve step coverage in certain applications but may reduce film density.
- **Sputtering gas:** Argon is commonly used due to its inertness and effective sputtering yield. But we may introduce reactive gases like oxygen or nitrogen for reactive sputtering to form compounds (e.g., oxides or nitrides).

- **Target-to-substrate distance**: Shorter distances increases deposition rate and can lead to higher energy impact of sputtered atoms, improving film density. Wheras longer distances provides better uniformity over larger substrates but may reduce deposition rate and film density.

By carefully optimizing these parameters, it is possible to tailor the properties of the thin films for specific applications, such as electronic devices, thermoelectrical modules, optical coatings, and protective layers, ensuring high-quality and reliable performance.

Steps for synthesis of Pr and Nb doped thin films: In this work, the sputtering target was prepared via high-temperature solid-state reaction method with stoichiometric amounts of $SrCO_3$ (Sigma-Aldrich 99.9%), TiO_2 (Sigma-Aldrich 99.9%), Pr_6O_{11} (For Pr doped films) (Sigma-Aldrich 99.9%) and Nb_2O_5 (For Nb doped films) (Sigma-Aldrich 99.9%). The obtained powder was sintered and formed into a 2-inch disk-shaped target. To ensure compositional uniformity, the disk was crushed, pulverized, repressed, and re-sintered. Ultrasonically cleaned quartz and Si substrates were then placed in the sputtering chamber, which was evacuated to 5×10^{-6} mbar prior to deposition. Pr, Nb-doped films were grown on the quartz, Si substrates at a temperature of 500 °C with a sputtering power of 120 W and 150 W for 90 minutes. For Nb doped film, sputtering occurred in a pure argon atmosphere with chamber pressures ranging from 1×10^{-2} to 3×10^{-2} mbar. The deposited Nb doped films were then annealed in tubular a vacuum furnace at 700 °C for 1 hour.

Pr doped films were grown on quartz substrates with substrate temperature of 500 °C, sputtering power of 150 W for a duration of 90 mins. Sputtering was done in pure argon atmosphere with chamber pressures between 1×10^{-2} to 3×10^{-2} mbar. As deposited films were annealed in tubular furnace for 4 Hrs at 600, 700 and 800 °C.

2.4 Materials characterization

Materials characterization entails examining and analyzing properties of materials to gain insight into its structure, composition, and physical attributes, including electrical, optical, thermoelectric, and magnetic properties. In this work we used various techniques, such as microscopy, spectroscopy, and diffraction to reveal detailed information about materials at different scales. Accurate characterization is crucial in developing new materials, enhancing existing ones, and ensuring quality control in synthesis and fabrication processes.

2.4.1 Structural analysis

Structural characterization of materials focuses on determining the arrangement of atoms and molecules within a material. Techniques such as X-ray diffraction (XRD), electron microscopy, and neutron diffraction are commonly used to reveal the crystal structure, phase composition, and defects. Understanding the structure is essential for correlating material properties with their performance and guiding the development of advanced materials.

2.4.1.1 X-ray diffraction

X-ray diffraction is a powerful analytical technique used to study the atomic and molecular structure of materials. By directing X-rays at a material and analyzing the diffraction patterns produced as depicted in Fig. 2-7. XRD can reveal detailed information about the crystal structure, phase composition, and lattice parameters. It is essential in identifying unknown materials, determining crystallinity, and detecting structural defects.

According to Bragg's Law, constructive interference occurs when the path difference between scattered X-rays from successive lattice planes is equal to an integer multiple of the wavelength [13]. This condition is mathematically expressed as:

$$n\lambda = 2d \sin\theta \tag{2.2}$$

Where n is the order of reflection, λ is the wavelength of the incident X-rays, d is the distance between lattice planes, θ is the angle of incidence.

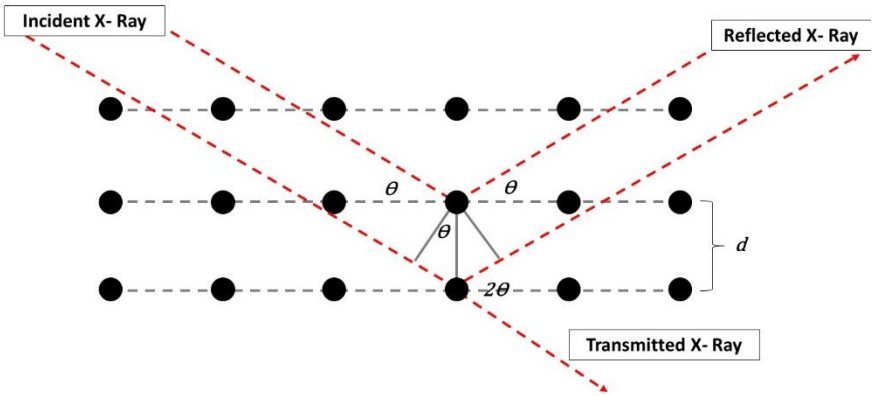

Figure 2- 7 Diagram representing Bragg's diffraction on crystal planes.

The analysis of XRD patterns relies heavily on Miller indices. The interplanar spacing d can be related to the Miller indices (h, k, l) and the lattice parameters of the crystal [14,15]. Depending on the structure of unit cell we obtain different formula connecting these parameters. The relationships relevant to this research is indicated in Table.2-1.

The Miller indices help in determining which planes are responsible for the observed diffraction peaks. Each set of (h, k, l) indices corresponds to a specific set of crystal planes and thus a specific diffraction angle θ. By indexing the diffraction peaks using Miller indices, one can identify the crystal structure and phase of the material.

Table 2- 1 Crystal systems and corresponding interplanar spacing relevant to the work

Crystal system	Axial translation	Axial angles	Planar spacing $(1/d^2)$
Cubic	$a = b = c$	$\alpha = \beta = \gamma = 90^\circ$	$\frac{h^2 + k^2 + l^2}{a^2}$
Tetragonal	$a = b \neq c$	$\alpha = \beta = \gamma = 90^\circ$	$\frac{h^2 + k^2}{a^2} + \frac{l^2}{c^2}$

As the crystal is gradually rotated, different lattice planes come into orientation to satisfy Bragg's condition, producing a series of diffraction peaks at specific angles. These diffraction patterns are recorded and analyzed to determine the crystal structure, phase

identification, and other structural parameters of the material. The intensity and position of the diffraction peaks provide information about the atomic arrangement, crystallite size, and possible lattice distortions

In XRD, the diffraction condition is satisfied when the difference between the incident wave vector $\overrightarrow{K_i}$ and the diffracted wave vector $\overrightarrow{K_f}$ is equal to a reciprocal lattice vector $\vec{G}$

$$\overrightarrow{K_f} - \overrightarrow{K_i} = \vec{G} \tag{2.3}$$

This relationship is known as the Laue condition for diffraction. For a given set of crystal planes with Miller indices (h, k, l), the corresponding reciprocal lattice vector $\vec{G}_{hkl}$ is represented as

$$\vec{G}_{hkl} = h\overrightarrow{a^*} + k\overrightarrow{b^*} + l\overrightarrow{c^*} \tag{2.4}$$

When this condition is met, constructive interference occurs, resulting in a diffraction peak. Bragg's law, can also be interpreted using the reciprocal lattice [16]. In reciprocal space, Bragg's law corresponds to the condition that the end points of the incident and diffracted wave vectors form reciprocal lattice vector with magnitude $|G|$ as indicated in eqn (2.5).

$$|G| = \frac{2\pi}{d_{hkl}} \tag{2.5}$$

X-ray diffraction commonly uses several types of X-ray sources, each suited to different applications. Copper (Cu) K_α radiation, with a wavelength of 1.5406 Å, is the most widely used due to its balance of intensity and versatility for a range of materials. Molybdenum (Mo) K_α radiation, with a shorter wavelength of 0.7107 Å, is preferred for studying materials with smaller unit cells and for reducing fluorescence in samples with heavier elements. Cobalt (Co) K_α radiation, with a wavelength of 1.7889 Å, is used to minimize fluorescence in iron-containing samples, making it ideal for analyzing steel and similar materials.

2.4.1.1.1 Analysis of XRD spectrum

From the XRD obtained we may calculate a wide variety of structural parameters. The Scherrer equation is used to estimate the size of crystallites in a sample based on the broadening of diffraction peaks. The equation is given by

$$D = \frac{k\lambda}{\beta \cos\theta} \tag{2.6}$$

Where D is the crystallite size, k is the shape factor (typically around 0.9), λ is the X-ray wavelength, β is the full width at half maximum (FWHM) of the peak in radians, and θ is the Bragg angle. This equation assumes that the broadening is solely due to the small size of the crystallites and not due to other factors like strain or instrumental effects. Another useful structural analysis is by using Williamson-Hall equation and plot expressed as

$$\beta \cos\theta = \frac{k\lambda}{D} + 4\epsilon \sin\theta \tag{2.7}$$

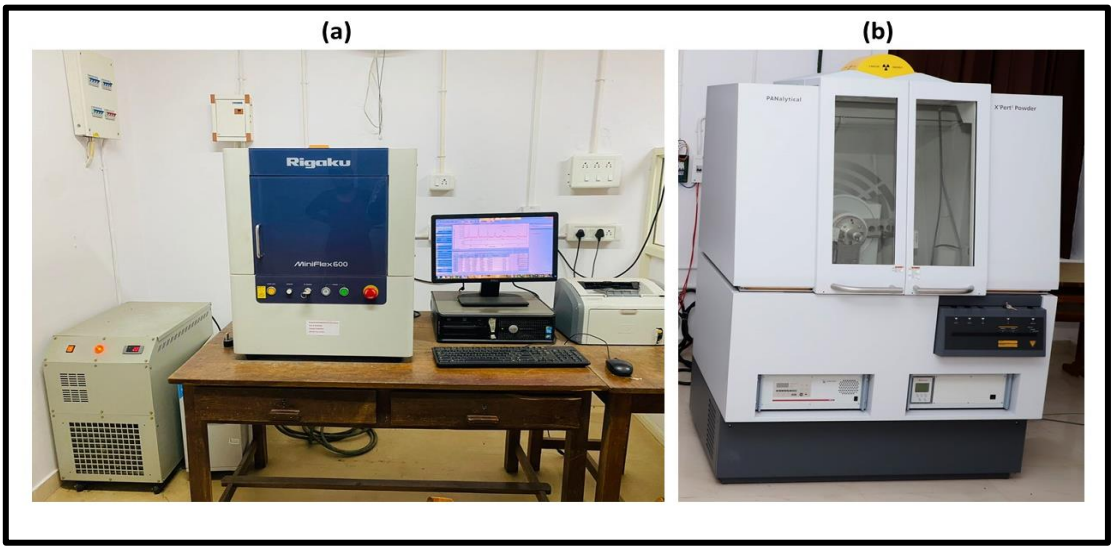

Figure 2- 8 (a) Rigaku Miniex 600 X-ray diffractometer **(b)** PANalytical X'pert 3 diffractometer.

It is a graphical method used in X-ray diffraction (XRD) analysis to separate size-induced broadening and strain-induced broadening of diffraction peaks. It plots the quantity $\beta \cos\theta$ against $4 \sin\theta$. From the linear fit of this plot, the y-intercept provides the

crystallite size, and the slope gives information about the microstrain within the material. This method allows for a more comprehensive understanding of the factors contributing to peak broadening compared to using the Scherrer equation alone[13,16–18].

In this work, XRD analysis were performed using PANalytical X'pert 3 and Rigaku Minfiex 600 X-ray diffractometer as represented in Fig. 2-8. Both the equipment use X-Ray source with (Cu) K_α radiation, with a wavelength of 1.5406 Å. The diffraction patterns obtained between 20 and 90^o were analyzed using PDXL software and are compared with the ICDD (International Centre for Diffraction Data) data base. PDXL offers user-friendly features and advanced algorithms to streamline the process of analyzing XRD data, making it suitable for both routine and complex research applications. Rietveld refinement and profile matching of patterns were employed using FullProf Suite software.

2.4.1.1.2 Structural refinement using FullProf Suite

Rietveld refinement using the FullProf Suite is a sophisticated method for analyzing and refining crystal structures based on X-ray and neutron diffraction data. This technique involves the adjustment of a theoretical model to fit the observed diffraction pattern by refining various structural parameters, such as atomic positions, lattice constants, and thermal displacement factors. FullProf is a powerful and flexible software tool for this process, allowing for the refinement of both simple and complex structures, including those with magnetic ordering.

One of the significant advantages of FullProf is its ability to handle multiple phases simultaneously, making it possible to refine mixed-phase materials accurately. The software also supports the use of constraints and restraints, which help maintain chemically and physically realistic models during refinement. This ensures that the refined structure is not only mathematically accurate but also physically meaningful. FullProf includes tools for visualizing and assessing the quality of the fit, such as difference plots that show the residuals between the observed and calculated patterns. The

software's graphical interface, WinPLOTR, enhances user interaction by providing easy-to-use options for data manipulation and visualization. FullProf also supports the refinement of anisotropic displacement parameters, providing detailed insights into atomic vibrations within the crystal lattice.

In addition to structural parameters, FullProf allows for the refinement of profile parameters, such as peak shapes and background, ensuring a comprehensive fit to the entire diffraction pattern. This software can integrate with other tools for pre-processing and post-processing, enhancing its utility in detailed structural studies [19].

The refinement process involves collecting high-quality X-ray or neutron diffraction data, followed by preparing an initial crystallographic model in a CIF file, including atomic positions, lattice parameters, and space group. Instrumental parameters such as wavelength and detector geometry are gathered, and a *.pcr file is created for FullProf, containing model parameters, refinement settings, and observed data. The initial refinement is executed in FullProf, generating output files with refined parameters and fit quality indicators. The results are analyzed, and adjustments are made to parameters like atomic positions, peak shapes, and background. This iterative process continues until the fit converges to acceptable values. The final model is validated by checking physical and chemical consistency, including bond lengths and angles and least chi square values. Finally, results are documented with refinement details and quality indicators. By iteratively refining model parameters to best fit the observed data, this method ensures accurate and reliable structural analysis essential for advanced research and development [19].

2.4.1.2 Raman spectroscopy

Raman spectroscopy is an analytical technique used to study vibrational, rotational, and other low-frequency modes in molecules. It relies on inelastic scattering of monochromatic light, typically from a laser, where the frequency of scattered light shifts due to interactions with molecular vibrations as indicated in Fig. 2-9. This shift

provides a unique molecular fingerprint, making Raman spectroscopy useful for chemical identification and characterization. Unlike infrared spectroscopy, Raman spectroscopy can analyze samples in various states, including solids, liquids, and gases, with minimal preparation. It is particularly advantageous for studying inorganic compounds, carbon-based materials, and biological samples. Enhanced techniques like Surface-Enhanced Raman Spectroscopy (SERS) significantly amplify the Raman signal, allowing for the detection of trace amounts of substances [20].

When incident photons from a laser source interact with a sample, most scatter elastically (Rayleigh scattering) without a change in energy. However, a small fraction of photons scatter inelastically, resulting in either a gain (anti-Stokes shift) or loss (Stokes shift) of energy, corresponding to the vibrational energy levels of the molecules in the sample with frequencies$(\vartheta_0 - \vartheta_m)$ and $(\vartheta_0 + \vartheta_m)$ respectively.

The Raman scattering intensity is linked to changes in the polarizability tensor of the molecule. The polarizability describes how the electron cloud around a molecule is distorted by the electric field $\vec{\boldsymbol{E}}$ of the incident light.

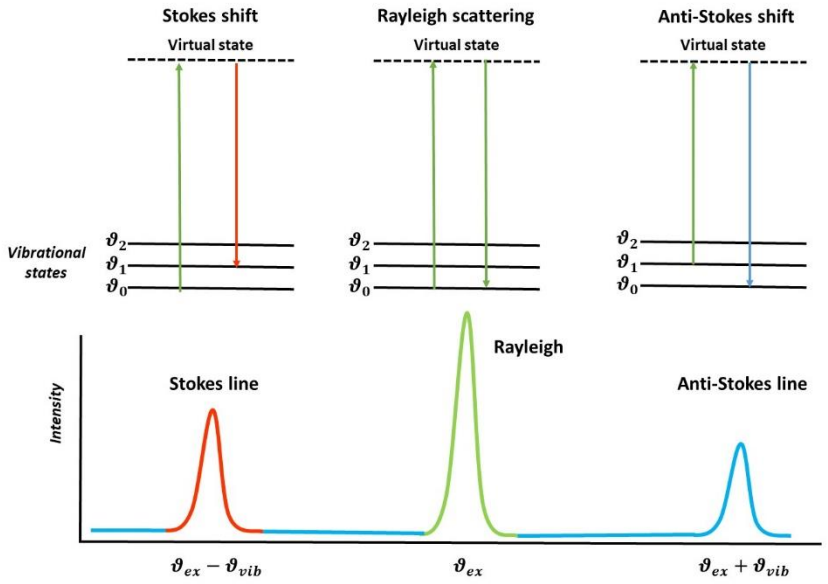

Figure 2- 9 Schematic representation of Raman scattering.

The induced dipole moment Pcan be expressed as

$$P = \alpha \vec{\boldsymbol{E}} \tag{2.8}$$

For a vibrational mode to be Raman active, the polarizability must change during the vibration. Mathematically, this is described as

$$\alpha = \alpha_0 + \frac{\partial \alpha}{\partial Q} \tag{2.9}$$

Where α_0 is the equilibrium polarizability, Q is the normal coordinate of the vibration, and $\frac{\partial \alpha}{\partial Q}$ is the rate of change of polarizability with respect to the vibrational coordinate [21,22].

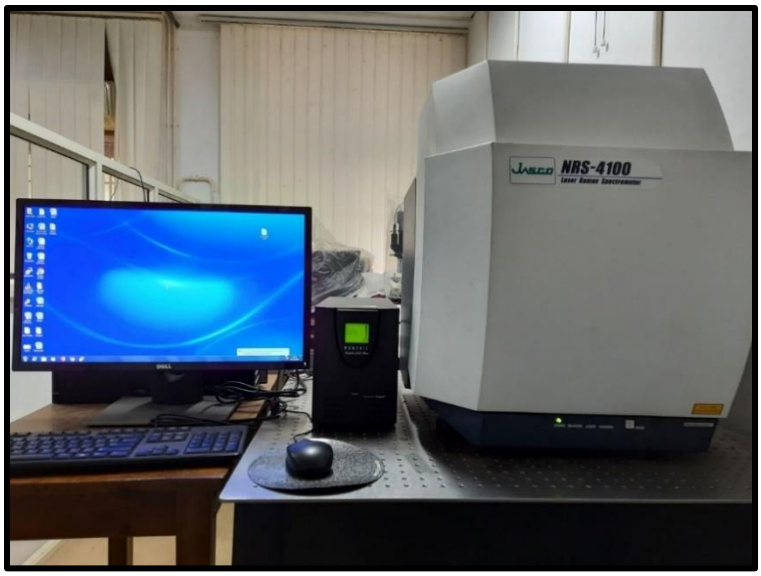

Figure 2- 10 JASCO NRS 4100 micro Raman spectrophotometer.

The vibrational modes of a molecule can be classified according to their symmetry properties, described by the irreducible representations of the molecule's point group. These modes often involve bond stretching or compressions that symmetrically alter the polarizability of the molecule. Modes that are not totally symmetric can also be Raman active if they induce changes in the polarizability tensor. The specific selection rules depend on the symmetry properties of the vibrational mode and the molecule. Group

theory provides a systematic way to determine the symmetry properties of molecules, which in turn helps predict which vibrational modes will be Raman active [23] .

In this work, Raman measurements were performed on powder samples and thin film samples using JASCO NRS 4100 having Nd-YAG laser of wavelength 532 nm as represented in Fig. 2-10. The measured resolution of the spectrometer is 2 cm^{-1}.

2.4.2 Morphological analysis

Morphological analysis involves studying the physical structure and shape of materials to understand their properties and behavior. This analysis includes examining features such as grain size, porosity, surface roughness, and the arrangement of phases within a material. Techniques such as electron microscopy, atomic force microscopy are commonly used to visualize and quantify these morphological characteristics. By correlating morphology with material performance, we can tailor materials for specific applications in fields like thermoelectricity, optoelectronics, energy conversion and storage etc.

2.4.2.1 Scanning electron microscopy

Scanning electron microscopy (SEM) analysis is a powerful technique used to observe the surface morphology and composition of materials at high resolution. It employs a focused beam of electrons to generate detailed images of the sample. The principle of SEM revolves around the interaction of electrons with the atoms of a sample, resulting in the production of various signals that provide detailed information about the surface of the sample and composition.

An electron gun generates a focused beam of high-energy electrons. The electron gun can be of different types, such as thermionic, field emission, or Schottky. It is then accelerated to high velocities using an electric field, and their energy typically ranges from 0.1 to 30 keV. The electron beam is focused into a fine spot using a series of electromagnetic lenses, including condenser lenses and objective lenses. These lenses control the convergence of the electron beam and adjust the spot size to achieve high-resolution imaging. The focused electron beam is scanned across the surface of the sample

in a raster pattern by deflection coils or scanning coils. This systematic scanning allows for the collection of data point-by-point over the sample's surface [24,25].

The working principle of SEM is illustrated in Fig. 2-11 [26]. As the electron beam interacts with the sample, it penetrates the surface and interacts with the atoms, causing various types of emissions. Primary interactions include elastic scattering, inelastic scattering, and the generation of secondary electrons, backscattered electrons, and X-rays. Secondary electrons are emitted from the sample surface due to inelastic collisions between the incident electrons and the sample's atoms. They have low energy (typically less than 50 eV) and provide high-resolution images with good surface detail. Backscattered electrons are high-energy electrons that are reflected back from the sample due to elastic scattering. BSEs provide compositional contrast in images because their yield depends on the atomic number of the elements in the sample [27].

When the incident electron beam displaces inner-shell electrons of the sample's atoms, it causes the emission of characteristic X-rays as outer-shell electrons fill the vacancies. This forms the basis for Energy dispersive X-ray spectroscopy (EDS), which is used to determine the elemental composition of the sample. Various detectors are used to collect the emitted secondary electrons, backscattered electrons, and X-rays. Secondary

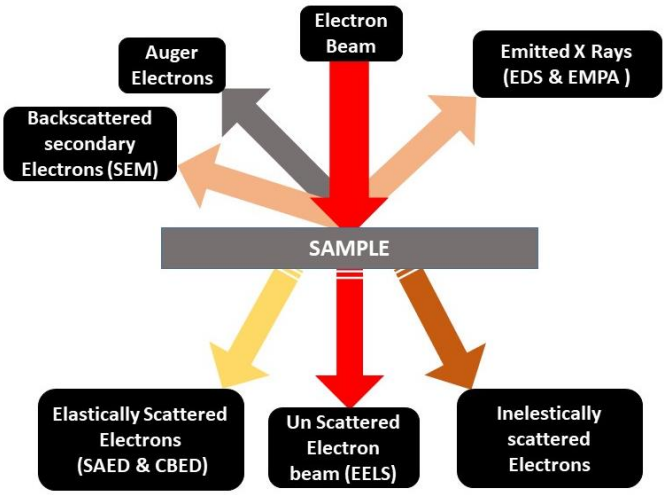

Figure 2- 11 Schematic of electron beam interaction with sample.

electron detectors (Everhart-Thornley detectors) provide topographical information, while backscattered electron detectors give compositional data [24].

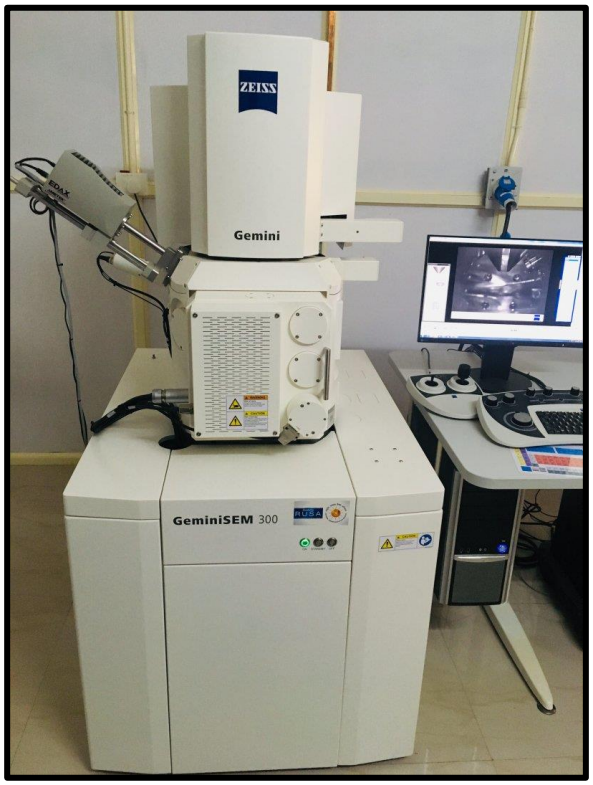

Figure 2- 12 ZEISS Gemini SEM 300 FE SEM with Octane plus EDAX detector.

The signals collected by the detectors are amplified and converted into an image displayed on a monitor. The intensity of the detected signals corresponds to the brightness in the SEM image, revealing detailed surface morphology and composition. Proper sample preparation is essential for accurate SEM analysis. Non-conductive samples are often coated with a thin layer of conductive material (e.g., gold or carbon) to prevent charging under the electron beam. The sample must be stable under high vacuum and electron beam exposure.

In this work, the surface morphology of the prepared samples was analyzed using a field emission gun scanning electron microscope (FE-SEM), ZEISS Gemini SEM 300 working at an accelerated voltage between 0.02 - 30 kV as indicated in Fig. 2-12.

2.4.2.2 Atomic force microscopy (AFM)

AFM is a high-resolution imaging technique used to map the surface topography of materials at the nanoscale. It operates by scanning a sharp tip attached to a cantilever across a sample surface, measuring the forces between the tip and the surface. These forces cause the cantilever to deflect, and this deflection is detected using a laser beam reflected off the top of the cantilever into a photodetector. AFM can operate in various modes, such as contact, tapping, and non-contact, each providing different types of information about the sample.

The main parts of AFM are cantilever tip, laser and photodetector and piezoelectric scanner. AFM uses a cantilever with a sharp tip (usually made of silicon or silicon nitride) at its end. The radius of the tip is typically in the range 10–20 nm. A laser beam is focused onto the back of the cantilever, and the reflected beam is detected by a position-sensitive photodetector. The photodetector is usually a quadrant photodiode that measures the deflection of the cantilever. The sample is mounted on a piezoelectric scanner that can precisely move in the x, y, and z directions, allowing for controlled scanning of the sample surface [28].

AFM can operate in different modes depending on the interaction between the tip and the sample [29–33]:

- **Contact mode:** The contact mode also known as repulsive mode, the tip actually makes physical contact with the surface, and have forces in the range of 10^{-6} to 10^{-8} N are typically generated. As the cantilever scans the surface, it bends due to the repulsive forces between the tip and the sample atoms. The deflection ($\Delta \boldsymbol{Z}$) of the cantilever is proportional to the force exerted by the surface according to Hooke's law. The cantilever deflection is kept constant using a feedback loop that adjusts the height of the scanner (z-direction). The adjustments made by the feedback loop generate the topographical image. Contact mode AFM is widely used in materials science for studying surface roughness, grain boundaries, and defects.

- **Tapping mode (Intermittent contact):** In tapping mode, the cantilever oscillates near its resonance frequency and lightly taps the sample surface during scanning. This mode reduces lateral forces that could damage soft samples and provides high-resolution images. The amplitude of oscillation changes as the tip interacts with the surface, and these changes are used to form the image.
- **Non-contact mode:** To prevent surface contacts a stiff cantilever is used resulting in low-tip specimen forces of 10^{-12} N. Since it is difficult to detect small forces the cantilever is vibrated, typically at 100 to 400 kHz. The tip oscillates at a distance just above the sample surface, where attractive van der Waals forces act. Changes in the oscillation amplitude or frequency due to these forces are monitored and used to generate the image. This mode is useful for imaging delicate samples without physical contact.

In this work we used Multimode 8 high performance AFM with high speed ScanAsyst mode.

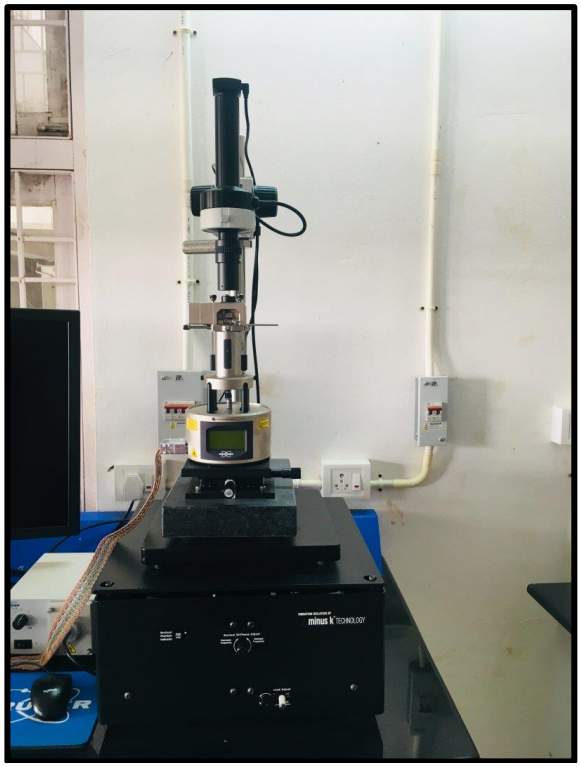

Figure 2- 13 BRUKER- Multimode 8 high performance AFM.

2.4.3 Chemical analysis

Chemical analysis techniques like X-ray photoelectron spectroscopy (XPS) and X-ray fluorescence (XRF) are crucial in material science for determining the elemental composition and chemical states of materials. These techniques provide detailed surface and bulk chemical information, which is essential for understanding material properties, performance, and behavior. Accurate chemical characterization helps in the development of new materials, quality control, and failure analysis.

2.4.3.1 X-ray photoelectron spectroscopy (XPS)

X-ray photoelectron spectroscopy is a surface-sensitive analytical technique used to determine the elemental composition and chemical states of surface of a material. It works by irradiating a material with X-rays, causing the emission of photoelectrons whose kinetic energy is measured to identify the elements and their electronic states. XPS provides information about the chemical environment of atoms, including oxidation states and chemical bonding [34].

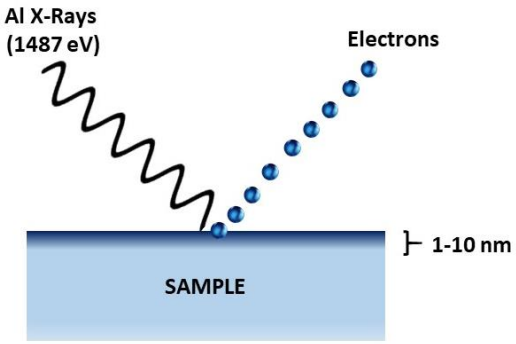

Figure 2- 14 Schematic representation of principle of XPS.

XPS is based on the photoelectric effect, where X-ray photons irradiate a material, causing the emission of core-level electrons as indicated in Fig.2-14. The energy of these emitted electrons provides information about the binding energies of the electrons within the atoms, which is characteristic of each element and its chemical state. When X-rays strike a material, they can transfer energy to an electron, ejecting it from the atom. This process is governed by the Einstein photoelectric equation. Where E_k is the kinetic

energy of the emitted photoelectron, $h\vartheta$ is the energy of the incident X-ray photon, E_b is the binding energy of the electron within the atom, relative to the Fermi level, ϕ is the work function of the spectrometer, which accounts for the energy required to bring an electron from the sample to the detector [35]. The emitted photoelectrons pass through an energy analyzer, which measures their kinetic energy. The analyzer is typically a hemispherical energy analyzer that sorts electrons based on their kinetic energy. The detector measures the number of electrons (intensity) at each kinetic energy, producing a spectrum according to eqn. (2.10).

$$E_k = h\vartheta - E_b - \phi \tag{2.10}$$

Figure 2- 15 Omicron Nanotechnology XPS system.

The peaks in the spectrum correspond to electrons from specific atomic orbitals and elements. The binding energy E_b of the electrons is calculated using the photoelectric

equation. The binding energies are characteristic of specific elements and their chemical states, allowing for qualitative and quantitative analysis. The intensity of the peaks can be used to determine the relative concentration of elements. The chemical shift, which is a slight change in the binding energy, can provide information about the chemical environment and oxidation state of the elements [36,37]. In our work we employed Omicron Nanotechnology XPS system represented in Fig. 2-15. The samples are exposed to X-rays (typically Al K_α with 1487 eV photon energy, respectively under ultra-high vacuum (UHV) conditions.

2.4.3.2 X-ray fluorescence spectroscopy (XRF)

X-ray fluorescence is an analytical technique used to determine the elemental composition of materials. It operates on the principle that when a material is exposed to high-energy X-rays or gamma rays, it emits secondary (or fluorescent) X-rays that are characteristic of the elements present in the sample. XRF is a non-destructive technique, allowing for the analysis of a wide variety of samples, including solids, liquids, and powders [38].

XRF is based on the interaction between incident X-rays and the atoms in a sample. This interaction can cause the ejection of inner-shell electrons, resulting in a vacancy. An electron from a higher energy level then fills this vacancy, and the difference in energy between these two levels is released in the form of an X-ray photon, known as fluorescence. The incident X-rays have sufficient energy to eject an inner-shell electron (often from the K or L shell), creating a vacancy. An electron from a higher energy level (such as L or M shell) fills the vacancy, emitting an X-ray photon in the process. The energy of this photon $E_{Fluorescence}$ is characteristic of the difference in energy levels between the two shells and is unique for each element as per eqn. (2.11).

$$E_{Fluorescence} = E_i - E_j \tag{2.11}$$

E_i and E_j are the energy levels of the electrons involved in the transition, with $E_i > E_j$.

As electrons from higher energy levels drop down to fill these vacancies, characteristic X-ray photons are emitted. Since most atoms have several electron orbitals

(such as the K, L, and M shells), multiple fluorescent transitions can occur. As an example, when X-rays interact with an atom containing K, L, and M shells, a vacancy might form in the K shell, which can then be filled by an electron from either the L or M shell, resulting in what is known as K transitions. Consequently, a single element can produce several XRF peaks, typically all appearing in the spectrum with varying intensities. This element's fingerprint is distinct due to these peaks. Not every X-ray encounter produces fluorescence. The ratio of fluorescence X-rays to incident X-rays is known as the fluorescence yield [39–41].

The emitted X-ray photons are detected by an energy-dispersive detector (such as a silicon drift detector) or a wavelength-dispersive detector. These detectors measure the energy (and sometimes the intensity) of the incoming X-ray photons. The energy spectrum generated by the detector displays peaks corresponding to the characteristic X-rays of different elements in the sample. Each peak's position (energy) indicates the element, and its intensity is proportional to the concentration of that element. The intensity of the characteristic X-rays is used to quantify the concentration of each element in the sample. Calibration with standards or fundamental parameters can correct for matrix effects and enhance accuracy.

In this work we used SPECTRO XEPOS spectrometer with X-ray tube with thick binary Pd/Co alloy anode with air-cooling.

Figure 2- 16 SPECTRO XEPOS XRF spectrometer.

2.4.3.3 Energy dispersive X-ray spectroscopy (EDAX)

Energy dispersive X-ray analysis (EDAX), also known as energy dispersive spectroscopy (EDS or EDX), is a widely used analytical technique for determining the elemental composition of a material. It operates by detecting characteristic X-rays emitted from a sample when it is irradiated with an electron beam, typically within a scanning electron microscope (SEM) or transmission electron microscope (TEM). The energies of these emitted X-rays are unique to each element, allowing for precise identification and quantification. EDAX provides spatially resolved chemical information.

The sample is placed in an electron microscope, and an electron beam is directed at the sample surface. The beam can be scanned across the sample to analyze different regions. As the electron beam interacts with the atoms in the sample, it causes the ejection of inner-shell electrons, leading to the emission of characteristic X-rays as electrons from higher energy levels fill the resulting vacancies [42].

The emitted X-rays are collected by an energy-dispersive detector, usually a semiconductor detector like a silicon drift detector (SDD) or a lithium drifted silicon detector (Si (Li)). These detectors measure the energy of the X-rays with high precision. The detector generates an energy spectrum, with peaks corresponding to the characteristic X-ray energies of the elements present in the sample. The position of these peaks identifies the elements, while the intensity of the peaks provides quantitative information about the concentration of each element. The energy spectrum is analyzed using specialized software to identify the elements and their relative abundances in the sample. Corrections for background noise, overlap of peaks, and other factors are applied to ensure accurate results. EDX detect elements with atomic number $Z > 4$(Be) to $Z<92$ (U), not all instruments are equipped with detection of light elements ($Z<11$). The detection limit of EDX ranging from 0.1 to 1atomic % and the lateral resolution lies $\sim 1\ \mu m$ [43,44].

In this work we used Octane plus EDAX attached to Gemini 300/EDS with an active area of 30 mm^2 as indicated in Fig. 2-12.

2.4.4 Optical properties

In material science, studying optical properties involves examining how materials interact with light, including absorption, reflection, refraction, and emission. These properties are critical for understanding and designing materials for applications such as optics, photonics, and optoelectronics. Optical properties are influenced by a material's electronic structure, band gap, and the arrangement of atoms, which determine how it absorbs and transmits light. Techniques such as diffused reflection spectroscopy (DRS), Transmission spectroscopy, and photoluminescence are commonly used to analyze these properties. Understanding optical behavior is essential for developing advanced materials for optoelectronic and thermoelectric applications.

2.4.4.1 UV-Visible-NIR spectroscopy

UV-Visible-NIR Spectroscopy is an analytical technique used to measure the absorption and reflectance of ultraviolet, visible, and near-infrared light by a sample. This method provides information about the electronic transitions and molecular structure of compounds, making it useful for identifying and characterizing materials. In the UV-visible range, electronic transitions of molecules, especially involving pi-electrons and non-bonding electrons, are typically observed. In the NIR region, overtones and combinations of vibrational modes are often detected. When a beam of light passes through the sample, it undergoes absorption, transmittance and reflection (A+T+R =1) in the ultraviolet, visible and NIR region of the electromagnetic spectrum.

2.4.4.1.1 Diffused Reflectance Spectroscopy (DRS)

Diffuse reflectance spectroscopy (DRS) is a technique used to analyze the scattering and absorption properties of powdered or solid samples. It measures the intensity of light scattered by the sample, providing information about its composition and structure. DRS is particularly useful for studying samples that are opaque or difficult to dissolve, making it a valuable tool in material science. When light strikes a sample, it can be absorbed, transmitted, or reflected. In DRS, the focus is on the diffuse reflectance, which occurs when light is scattered in many directions due to the sample's surface

roughness or particulate nature. Diffuse reflectance refers to the light that is scattered from a sample surface in various directions. This scattered light carries information about the material's surface and bulk properties, including its composition and morphology. A common approach to interpret DRS data is the Kubelka-Munk theory, which relates the reflectance of a material to its absorption and scattering coefficients. The Kubelka-Munk function (K-M function) is used to quantify the reflectance data and is defined as:

$$F(R_\infty) = \frac{(1 - R_\infty^2)}{2R_\infty} \tag{2.12}$$

Where R_∞ is the reflectance of the sample layer that is thick enough so that no light passes through it (infinite thickness), $F(R_\infty)$ is proportional to the absorption coefficient K and scattering coefficient S of the material, given by,

$$F(R_\infty) = \frac{K}{S} \tag{2.13}$$

The Kubelka-Munk function allows for the determination of the concentration of absorbing species in a sample by relating the reflectance to the sample's absorption characteristics [45].

In DRS, a spectrophotometer equipped with an integrating sphere is typically used to collect the scattered light. The integrating sphere captures light reflected in all directions, allowing for an accurate measurement of diffuse reflectance. The sample is placed in front of the sphere's entrance port, and light is directed onto it. The reflected light is then detected, and its intensity is measured across different wavelengths. The physical state of the sample (particle size, surface roughness, etc.) can significantly affect the diffuse reflectance measurements. Samples are often ground into fine powders or pressed into pellets to standardize the measurements.

In order to determine bandgap of a material we need to measure the reflectance R_∞ over a range of wavelengths using a spectrophotometer equipped with an integrating sphere. To calculate band gap, we need to convert the reflectance data to $F(R_\infty)$ using the Kubelka-Munk function. This conversion relates the optical absorption to the

reflectance data, allowing for the analysis of electronic transitions. A graph between $[F(R_\infty) \times h\vartheta]^n$ and the photon energy $h\vartheta$ is plotted and E_g is determined by extrapolating the linear portion of the plot to the x-axis. Here h Planck's constant is and ϑ is the frequency of the incident light. The exponent n depends on the nature of the electronic transition: n=2 for direct allowed transitions, $n = \frac{1}{2}$ for indirect allowed transitions [45,46].

2.4.4.1.2 Transmission spectroscopy

Transmission spectroscopy is an analytical technique used to study the properties of materials by measuring the amount of light that passes through a sample. It provides information about the material's composition, structure, and optical properties based on the wavelengths of light that are absorbed, transmitted, or reflected. Transmission spectroscopy is a valuable tool for studying thin films, particularly for determining their optical properties, such as the band gap and absorption edge.

In this technique, a beam of light is passed through a thin film sample, and the intensity of the transmitted light is measured across a range of wavelengths. The amount of light absorbed by the sample provides information about the material's optical properties. Key properties like transmittance, absorbance and bandgap can be derived from transmission spectroscopy [47]. Transmittance (T) is the fraction of incident light that passes through the film indicated by

$$T = \frac{I}{I_0} \tag{2.14}$$

Where I is the transmitted intensity and I_0 is the incident intensity. Absorbance (A), is a measure of the amount of light absorbed by the film, represented by

$$A = -\log T = \log \frac{I_0}{I} \tag{2.15}$$

Absorption coefficient (α) quantifies how much light is absorbed per unit distance as it travels through the material. The relationship between the absorption coefficient and transmittance is given by the Beer-Lambert law:

$$T = e^{-\alpha d} \tag{2.16}$$

Where d is the thickness of the thin film. The absorption coefficient can be determined using

$$\alpha = -\frac{\ln T}{d} \tag{2.17}$$

The band gap of material of thin film can be estimated using the Tauc plot method. For direct allowed transitions, the Tauc plot is generated by plotting $(\alpha h\vartheta)^2$ against the photon energy $h\vartheta$. The band gap energy is obtained by extrapolating the linear portion of the plot to the x-axis.

$$(\alpha h\vartheta)^2 = A\left(h\vartheta - E_g\right) \tag{2.18}$$

For indirect allowed transitions, the equation modifies to

$$(\alpha h\vartheta)^{\frac{1}{2}} = A\left(h\vartheta - E_g\right) \tag{2.19}$$

Where A is constant related to the material and E_g is the band gap energy [48,49].

In our work we used Cary 5000 high performance UV-Vis-NIR spectrophotometer with photometric performance in the 175-3300 nm range as indicated in Fig.2-17.

Figure 2- 17 Cary 5000 high performance UV-Vis-NIR spectrophotometer.

2.4.4.2 Photoluminescence spectroscopy

Photoluminescence spectroscopy is a non-destructive analytical technique used to study the electronic structure and optical properties of materials. It involves the excitation of a sample with light, leading to the emission of photons as the material returns to a lower energy state. This emitted light, or photoluminescence, is analyzed to provide insights into the electronic band structure, defect levels, and impurities in the material. When the light is directed to the sample, it will be absorbed and transfers additional energy into the material through a process known as photo-excitation. The material can then release this excess energy by emitting light, a phenomenon referred to as luminescence. When this emitted light results from photo-excitation, it is specifically termed photoluminescence.

The basic steps involved in photoluminescence are:

1. **Excitation**: Absorption of photons by the material, promoting electrons from the valence band to the conduction band (in semiconductors) or to higher energy states (in molecules).
2. **Non-radiative relaxation**: The excited electrons lose some energy through interactions with phonons (vibrational energy states) and relax to lower energy levels.
3. **Radiative recombination**: The electrons eventually recombine with holes, releasing energy as photons. The energy of these emitted photons corresponds to the energy difference between the excited state and the ground state.

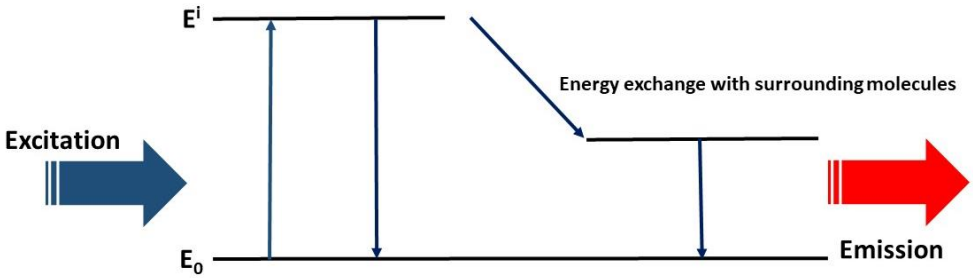

Figure 2- 18 Excitation emission mechanism of photoluminescence.

The information that can be deduced from PL spectra includes band gap energy, Impurity and defect States, excitonic effects, quantum efficiency, carrier dynamics and lifetime etc. [50].

The energy difference between the conduction band and the valence band in semiconductors, can be determined from the wavelength or energy position of the main PL peak. The emitted photon energy corresponds to the band gap energy, which is crucial for understanding and designing semiconductor devices. The band gap energy can be calculated using the formula $E = \frac{hc}{\lambda}$. Peaks at energies lower than the band gap can indicate the presence of impurity states or defect levels within the band gap. These states can trap electrons or holes, which recombine radiatively, resulting in characteristic emissions. The analysis of these sub-band-gap emissions provides insights into the types and concentrations of impurities or defects, which can affect the material's electronic properties and device performance. In some materials, particularly at low temperatures, excitons (bound states of electrons and holes) can form. These excitons emit light at slightly lower energies than the band gap. PL spectra can reveal excitonic transitions, which are important for understanding optical properties in low-dimensional systems like quantum wells, wires, and dots. The binding energy of excitons can be inferred from the difference between the free exciton peak and the band gap energy [51].

Figure 2- 19 Horiba FluoroMax -4 series spectrofluorometer.

The intensity of the PL emission can provide information about the quantum efficiency of radiative recombination. High-intensity PL indicates efficient radiative recombination, which is desirable in light-emitting applications like LEDs and lasers. Comparing PL intensities under different conditions (e.g., temperature, excitation power) can also provide information about non-radiative recombination processes and carrier dynamics. Time-resolved PL spectroscopy can be used to study the dynamics of carriers (electrons and holes) in the material. By measuring the decay time of the PL signal, one can determine the carrier lifetime, which is important for understanding the recombination processes and the quality of the material

Photoluminescence (PL) spectroscopy instrumentation typically consists of a light source, such as a laser or a lamp, to excite the sample. The emitted light from the sample is collected and directed into a spectrometer, which disperses the light based on its wavelength. A detector, such as a photomultiplier tube (PMT) or a charge-coupled device (CCD), measures the intensity of the emitted light across different wavelengths. The resulting data is processed to produce a PL spectrum, which reveals information about the electronic and optical properties of the material. In our work we used Horiba FluoroMax - 4 series spectrofluorometer indicated in Fig. 2-18.

2.4.5 Electrical properties

The electrical properties of materials are fundamental to a wide range of technologies, from semiconductors in electronics to insulators in electrical systems. These properties includes electrical conductivity, resistivity, carrier mobility, carrier concentration and dielectric constant, are determined by the material's composition, structure, and measuring temperature. Gaining insight into these characteristics facilitates the design and optimization of materials for applications, such as efficient energy conversion and storage, advanced computing, and communication technologies. This field of study is critical for advancing technology and enhancing the functionality and efficiency of modern electronic devices.

2.4.5.1 Hall measurements

Hall measurements are a crucial technique in characterizing the electrical properties of materials, particularly semiconductors. This method involves applying a magnetic field perpendicular to a current-carrying sample and measuring the resulting transverse voltage, known as the Hall voltage. The Hall effect allows for the determination of key parameters such as carrier concentration, carrier type (electrons or holes), and carrier mobility, which are essential for understanding a material's electronic behavior.

Figure 2- 20 Schematic representation of Hall effect.

The Hall effect occurs when an electric current flows through a conductor or semiconductor in the presence of a perpendicular magnetic field, resulting in a voltage difference across the material. This voltage, known as the Hall voltage, arises due to the Lorentz force acting on the charge carriers (electrons or holes), which causes them to accumulate on one side of the material as indicated in Fig.2-20 [52]. From the Hall voltage measurements carrier mobility, concentration, resistivity, Hall coefficient and the type of conductivity (n or p type) can be determined.

Hall current is affected by several factors. The carrier concentration, carrier mobility, applied voltage, and cross-sectional area all directly relate to the current, but the sample length has an inverse relationship with the current as indicated in the equation.

$$I = \frac{V}{R} = \frac{V}{\left(\rho L/_A\right)} = \frac{qn\mu VA}{L} \tag{2.20}$$

Where I is the current, V is the voltage, R and ρ is the resistance and resistivity of the sample, L and A is the length and area of cross section of the sample, n and μ are the carrier concentration and mobility of carriers[53,54].

Measuring the Hall voltage (V_H) by applying a magnetic field perpendicular to the sample and passing current through it is the first step in figuring out carrier mobility. A transverse current is produced when the magnetic field (B) and current flow (I) combine. Across the device, the resultant potential (V_H) is measured. Precise assessments of the sample's resistivity (ρ) and thickness (t) are also necessary. Van der Pauw measuring method or a four-point probe can be used to find the resistivity. This formula may be used to get the Hall mobility with just these five parameters (B, I, V_H, t, and resistivity)

$$\mu_H = \frac{|V_H t|}{Bl\rho} \tag{2.21}$$

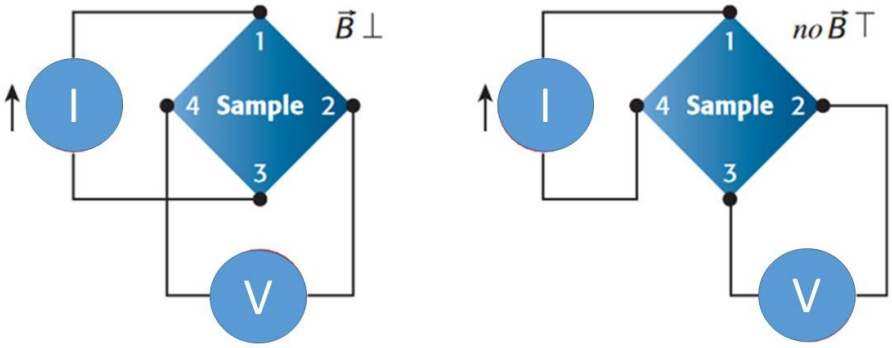

Figure 2- 21 Hall effect voltage Vs van der Pauw resistance measurement.

Figure 2-21 shows the setups for measuring Hall effect voltage and van der Pauw resistivity. Both configurations are quite similar in that they use four contacts and involve

applying a current and measuring a voltage. However, in the Hall effect measurement, the current is applied between two opposite nodes of the sample, and the voltage is measured between the other two opposite nodes, with the points of current application and voltage measurement interlaced. For semiconductors, the Hall voltage typically measures around kT/q, which is roughly 25 millivolts.

Reversing the polarity of the source current, sourcing on additional terminals, and reversing the magnetic field direction are also done to get reliable results. Hall voltages are found with both forward and reverse current and magnetic field and average all the values [52,53].

$$R_A = \frac{\left(R_{21,34} + R_{12,43} + R_{43,12} + R_{34,21}\right)}{4} \tag{2.22}$$

$$R_B = \frac{\left(R_{32,41} + R_{23,14} + R_{14,23} + R_{41,32}\right)}{4} \tag{2.23}$$

$$e^{-\left(\frac{\pi R_A}{R_s}\right)} + e^{-\left(\frac{\pi R_B}{R_s}\right)} = 1 \tag{2.24}$$

And from this values resistivity can be calculated using the eqn. (2.25).

$$\rho = R_s t \tag{2.25}$$

where R_s is the sheet resistance.

The Hall coefficient for electron,

$$R_H = \frac{V_H t}{IB} \tag{2.26}$$

From the Hall coefficient, the carrier concentration can be determined as

$$R_H = \frac{-1}{ne} \tag{2.27}$$

And the mobility can be expressed as,

$$\mu = \frac{-\sigma_n V_H T}{IB} \tag{2.28}$$

Hall mobility is significantly influenced by the sample's temperature, making it important to monitor temperature, especially in applications where measurements are repeated after adjusting the sample's temperature. Many test setups include a temperature-measuring probe, and for high-accuracy measurements, the probe should have a resolution of approximately 0.1°C. Temperature-dependent Hall effect measurements are crucial for understanding how a material's electrical properties change with temperature. By varying the temperature during these measurements, one can gain insights into carrier

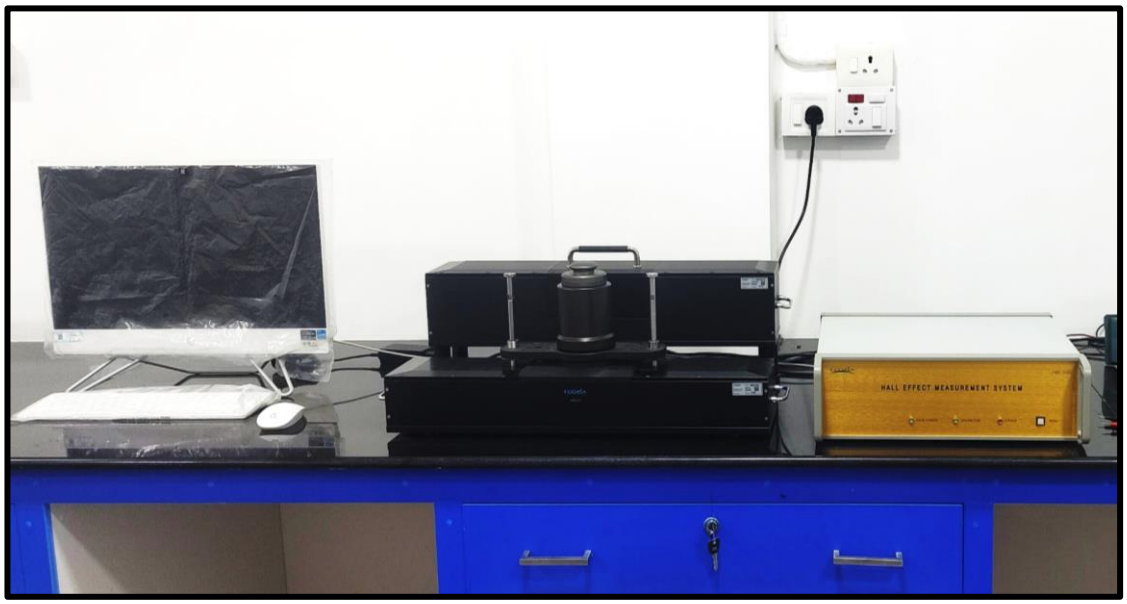

Figure 2- 22 Ecopia HMS-5000 Hall effect measurement system.

concentration, mobility, and scattering mechanisms in semiconductors. In our work we used The Ecopia HMS-5000 Hall effect measurement system represented in Fig. 2-22.

2.4.6 Thermoelectric properties

Thermoelectric properties measurement is a key technique in evaluating a material's ability to convert thermal energy into electrical energy and vice versa. This involves assessing parameters such as the Seebeck coefficient, electrical conductivity, and thermal conductivity, which together determine the material's thermoelectric efficiency, characterized by the dimensionless figure of merit, ZT. Accurate measurements are essential for identifying materials with high thermoelectric performance, enabling advancements in energy harvesting technologies.

2.4.6.1 Electrical conductivity and Seebeck coefficient

The ULVAC ZEM-3M8 is a state-of-the-art instrument designed for the precise measurement of thermoelectric properties in materials. It is widely used in research and development to evaluate the Seebeck coefficient and electrical conductivity, key parameters for assessing a material's thermoelectric efficiency. The ZEM-3M8 is capable of operating over a broad temperature range, allowing for comprehensive analysis of materials under various thermal conditions. This instrument is crucial for identifying and optimizing high-performance thermoelectric materials, which are essential for applications in power generation and cooling technologies [55].

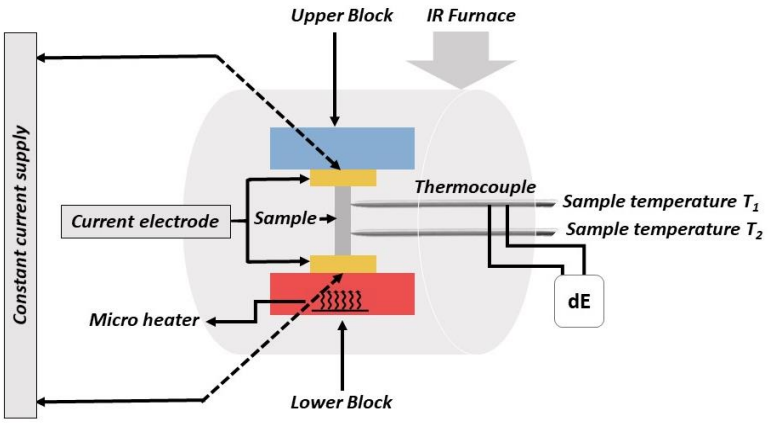

Figure 2- 23 Schematic representation of thermoelectric measurement system.

The system uses a programmable IR furnace to heat the sample up to 900 °C and a micro heater to generate temperature gradient between upper and lower part of the

sample. The measuring chamber should be evacuated to 10^{-3} mbar before the process and is filled with low pressure Helium gas during the whole process. The Seebeck coefficient is measured using static DC method and electrical conductivity is measured using four-probe method. The sample in rectangular bar/ pellet /thin film is placed in contact with the upper and lower blocks across which the temperature gradient is applied. Thermocouples are pushed against the side of the sample to measure the upper and lower temperatures T_1 and T_2, and then the thermal electromotive force dE between the identical wires on one side of the thermocouple is measured to get the Seebeck coefficient using the equation. The micro heater can be programmed, to create temperature gradient of 10, 20 or 30 °C.

To test the specific resistance value and Seebeck coefficient, the sample temperature is stabilized every time. The samples were pre heated for two cycles from room temperature to 900 °C before the measurement was taken using the infrared furnace with filled helium gas at low pressure.

$$S = \frac{dE}{T_2 - T_1} \tag{2.29}$$

Figure 2- 24 UL VAC ZEM-3 TE measurement system.

After sandwiching the sample between top and bottom electrodes two Pt electrodes are pushed towards the sample and four probe contact is achieved. V-I plot measurement is made to judge whether there is a proper contact between the probe and the sample, by applying a constant current I to both ends of the sample, the dc four-terminal technique measures electric resistance and determines the voltage drop dV between the identical wires of the thermocouple by subtracting thermo e.m.f between the leads. The stability of the measurement parameters is indicated by the resistance value that is determined at the end of each heating cycle.

In our work we used ULVAC ZEM 3M8 TE measurement system capable of testing TE parameters from room temperature to 900 °C in helium environment [56,57].

2.4.6.2 Thermal conductivity

Thermal conductivity measurement is fundamental in the study of thermoelectric materials, as it directly impacts the efficiency of converting heat into electricity. In thermoelectricity, materials with low thermal conductivity are desirable to maintain a temperature gradient, essential for generating electrical power. Accurate measurement of thermal conductivity, along with electrical conductivity and the Seebeck coefficient, allows for the calculation of the figure of merit, ZT, a key indicator of a material's thermoelectric performance. Techniques such as the Harman method and the laser flash method are often employed to measure thermal conductivity in these materials. Understanding and optimizing thermal conductivity is crucial for developing high-efficiency thermoelectric devices for power generation and cooling applications.

The divided bar method is a steady-state technique used to measure the thermal conductivity of solid materials, particularly those with low to medium conductivity. It involves creating a steady heat flow through a sample and measuring the temperature difference across it. The method uses a reference material with known thermal conductivity to determine the thermal conductivity of the test sample by comparing temperature gradients in both materials. In the divided bar method, a sample of unknown thermal conductivity is sandwiched between two materials with known thermal

conductivities, often referred to as reference materials. The assembly is placed between a heat source and a heat sink, establishing a steady-state heat flow through the entire setup as indicated in Fig. 2-25. By measuring the temperature differences across the sample and the reference materials, the thermal conductivity of the sample can be calculated [58].

The thermal conductivity (k) is determined using Fourier's law of heat conduction, which relates the heat transfer rate to the temperature gradient across a material:

$$q = -\kappa A \frac{dT}{dx} \tag{2.30}$$

Where q is the heat transfer rate (W), k is the thermal conductivity of the material (W/m·K), A is the cross-sectional area perpendicular to the heat flow (m²), $\frac{dT}{dx}$ is the temperature gradient (K/m).

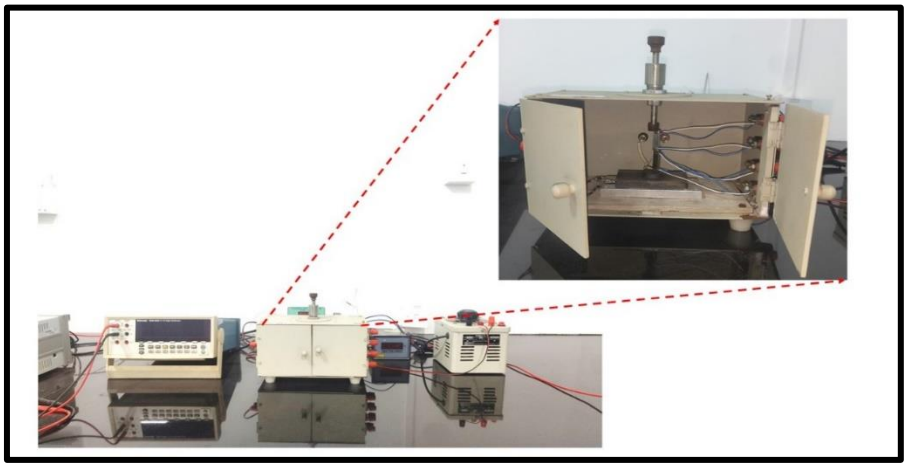

Figure 2- 25 Thermal conductivity Measurement System.

For the reference materials (denoted as 1 and 3) and the sample (denoted as 2), the relationship can be expressed as,

$$q = -\kappa_1 A \frac{dT_1}{dx_1} = -\kappa_2 A \frac{dT_2}{dx_2} = -\kappa_3 A \frac{dT_3}{dx_3} \tag{2.31}$$

Where κ_1, κ_2, κ_3 are the thermal conductivities of the reference materials and the sample, respectively, and dT_1, dT_2 and dT_3 are the temperature differences across the reference

materials and the sample [59]. The thermal conductivity of the sample κ_2, is derived from the known conductivities of the reference materials κ_1 and κ_3, and the measured temperature differences:

$$\kappa_2 = -\kappa_1 \left(\frac{dT_1}{dT_2}\right)\left(\frac{L_2}{L_1}\right) \tag{2.32}$$

L_1 , L_2 and L_3 are the lengths of the reference materials and the sample, respectively.

References:

[1] A. Manikandan, Y. Slimani, A. Dinesh, A. Khan, K. Thanrasu, A. Baykal, S.K. Jaganathan, H. Dzudzevic-Cancar, A.M. Asiri, 8 - Perovskite's potential functionality in a composite structure, in: I. Khan, A. Khan, M.M.A. Khan, S. Khan, F. Verpoort, A. Umar (Eds.), Hybrid Perovskite Composite Materials, Woodhead Publishing, 2021: pp. 181–202. https://doi.org/https://doi.org/10.1016/B978-0-12-819977-0.00008-1.

[2] X. Hao, J. Zhai, L.B. Kong, Z. Xu, A comprehensive review on the progress of lead zirconate-based antiferroelectric materials, Prog Mater Sci 63 (2014) 1–57. https://doi.org/https://doi.org/10.1016/j.pmatsci.2014.01.002.

[3] M. Shah, P.K. Jamshina Sanam, P.P. Pradyumnan, Defect-induced $Sr_{1-x}Pr_xTiO_3$ crystallites by burial sintering and its optoelectronic applications, Journal of Physics and Chemistry of Solids 181 (2023) 111516. https://doi.org/https://doi.org/10.1016/j.jpcs.2023.111516.

[4] D. Ekren, J. Cao, F. Azough, D. Kepaptsoglou, Q. Ramasse, I.A. Kinloch, R. Freer, Controlling the Thermoelectric Behavior of La-Doped $SrTiO_3$ through Processing and Addition of Graphene Oxide, ACS Appl Mater Interfaces 14 (2022) 53711–53723. https://doi.org/10.1021/acsami.2c14408.

[5] M. Ohring, Chapter 3 - Thin-Film Evaporation Processes, in: M. Ohring (Ed.), Materials Science of Thin Films (Second Edition), Academic Press, San Diego, 2002: pp. 95–144. https://doi.org/https://doi.org/10.1016/B978-012524975-1/50006-9.

[6] R.B. Mason Jr., Introduction to Thin Film Deposition Techniques: Key Topics in Materials Science and Engineering, ASM International, 2023. https://doi.org/10.31399/asm.tb.itfdtktmse.9781627084406.

[7] J.A. Venables, Introduction to Surface and Thin Film Processes, Cambridge University Press, Cambridge, 2000. https://doi.org/DOI: 10.1017/CBO9780511755651.

[8] A.H. Simon, 4 - Sputter Processing, in: K. Seshan (Ed.), Handbook of Thin Film Deposition (Third Edition), William Andrew Publishing, Oxford, 2012: pp. 55–88. https://doi.org/https://doi.org/10.1016/B978-1-4377-7873-1.00004-8.

[9] F. Shi, Introductory Chapter: Basic Theory of Magnetron Sputtering, in: Dr.F. Shi (Ed.), Magnetron Sputtering, IntechOpen, Rijeka, 2018: p. Ch. 4. https://doi.org/10.5772/intechopen.80550.

[10] M. Konuma, Physical Vapor Deposition Under Plasma Conditions, in: M. Konuma (Ed.), Film Deposition by Plasma Techniques, Springer Berlin Heidelberg, Berlin, Heidelberg, 1992: pp. 126–148. https://doi.org/10.1007/978-3-642-84511-6_6.

[11] L.W. Martin, Y.-H. Chu, R. Ramesh, Advances in the growth and characterization of magnetic, ferroelectric, and multiferroic oxide thin films, Materials Science and Engineering: R: Reports 68 (2010) 89–133. https://doi.org/https://doi.org/10.1016/j.mser.2010.03.001.

[12] K. Oura, M. Katayama, A. V Zotov, V.G. Lifshits, A.A. Saranin, Growth of Thin Films, in: K. Oura, M. Katayama, A. V Zotov, V.G. Lifshits, A.A. Saranin (Eds.), Surface Science: An Introduction, Springer Berlin Heidelberg, Berlin, Heidelberg, 2003: pp. 357–387. https://doi.org/10.1007/978-3-662-05179-5_14.

[13] M. Kot, In-operando hard X-ray photoelectron spectroscopy study on the resistive switching physics of HfO2-based RRAM, 2014.

[14] T.L. Alford, L.C. Feldman, J.W. Mayer, eds., X-ray Diffraction, in: Fundamentals of Nanoscale Film Analysis, Springer US, Boston, MA, 2007: pp. 129–151. https://doi.org/10.1007/978-0-387-29261-8_7.

[15] N.W. Ashcroft y N. D. Mermin, Solid State Physics, Harcourt College Publishers, 1976.

[16] B. D. CULLITY, Elements of X-RAY DIFFRACTION, Second edition, Addison-Wesley Publishing Company, Inc., 1978.

[17] Diffraction Theory, in: Introduction to X-ray Powder Diffractometry, 1996: pp. 47–95. https://doi.org/https://doi.org/10.1002/9781118520994.ch3.

[18] Qualitative Analysis, in: Introduction to X-ray Powder Diffractometry, 1996: pp. 319–353. https://doi.org/https://doi.org/10.1002/9781118520994.ch12.

[19] J. Rodríguez-Carvajal, Recent advances in magnetic structure determination by neutron powder diffraction, Physica B Condens Matter 192 (1993) 55–69. https://doi.org/https://doi.org/10.1016/0921-4526(93)90108-I.

[20] K. Fujita, Micro-Raman Spectroscopy, in: T.S.S.S. of Japan (Ed.), Compendium of Surface and Interface Analysis, Springer Singapore, Singapore, 2018: pp. 375–379. https://doi.org/10.1007/978-981-10-6156-1_62.

[21] J.A. Koningstein, Laser Raman Spectroscopy, in: H.A. Szymanski (Ed.), Raman Spectroscopy: Theory and Practice, Springer US, Boston, MA, 1967: pp. 82–100. https://doi.org/10.1007/978-1-4684-3024-0_3.

[22] J.R. Ferraro, K. Nakamoto, C.W. Brown, Chapter 1 - Basic Theory, in: J.R. Ferraro, K. Nakamoto, C.W. Brown (Eds.), Introductory Raman Spectroscopy (Second Edition), Academic Press, San Diego, 2003: pp. 1–94. https://doi.org/https://doi.org/10.1016/B978-012254105-6/50004-4.

[23] J.R. Ferraro, K. Nakamoto, C.W. Brown, Introductory Raman Spectroscopy: Second Edition, Introductory Raman Spectroscopy: Second Edition (2003) 1–434.

[24] J.I. Goldstein, D.E. Newbury, J.R. Michael, N.W.M. Ritchie, J.H.J. Scott, D.C. Joy, Scanning Electron Microscope (SEM) Instrumentation, in: J.I. Goldstein, D.E. Newbury, J.R. Michael, N.W.M. Ritchie, J.H.J. Scott, D.C. Joy (Eds.), Scanning Electron Microscopy and X-Ray Microanalysis, Springer New York, New York, NY, 2018: pp. 65–91. https://doi.org/10.1007/978-1-4939-6676-9_5.

[25] A. Ul-Hamid, Imaging with the SEM, in: A. Ul-Hamid (Ed.), A Beginners' Guide to Scanning Electron Microscopy, Springer International Publishing, Cham, 2018: pp. 129–180. https://doi.org/10.1007/978-3-319-98482-7_4.

[26] D. Ananthapadmanaban, Summary of Some Selected Characterization Methods of Geopolymers, in: M. Alshaaer, H.-Y. Jeon (Eds.), Geopolymers and Other Geosynthetics, IntechOpen, Rijeka, 2018: p. Ch. 3. https://doi.org/10.5772/intechopen.82208.

[27] J.I. Goldstein, D.E. Newbury, J.R. Michael, N.W.M. Ritchie, J.H.J. Scott, D.C. Joy, Backscattered Electrons, in: J.I. Goldstein, D.E. Newbury, J.R. Michael, N.W.M. Ritchie, J.H.J. Scott, D.C. Joy (Eds.), Scanning Electron Microscopy and X-Ray Microanalysis, Springer New York, New York, NY, 2018: pp. 15–28. https://doi.org/10.1007/978-1-4939-6676-9_2.

[28] Topographic Imaging, in: Atomic Force Microscopy, 2012: pp. 137–186. https://doi.org/https://doi.org/10.1002/9781118360668.ch4.

[29] Z-Dependent Force Measurements with AFM, in: Atomic Force Microscopy, 2012: pp. 91–136. https://doi.org/https://doi.org/10.1002/9781118360668.ch3.

[30] N.S. Bajaj, R.A. Joshi, Chapter 3 - Energy materials: synthesis and characterization techniques, in: S.J. Dhoble, N.T. Kalyani, B. Vengadaesvaran, A. Kariem Arof (Eds.), Energy Materials, Elsevier, 2021: pp. 61–82. https://doi.org/https://doi.org/10.1016/B978-0-12-823710-6.00019-4.

[31] Overview of AFM, in: Atomic Force Microscopy, 2012: pp. 1–32. https://doi.org/https://doi.org/10.1002/9781118360668.ch1.

[32] M.A.S. Quintanilla, Surface Analysis Using Contact Mode AFM, in: Q.J. Wang, Y.-W. Chung (Eds.), Encyclopedia of Tribology, Springer US, Boston, MA, 2013: pp. 3401–3411. https://doi.org/10.1007/978-0-387-92897-5_323.

[33] Distance-Dependent Interactions, in: Atomic Force Microscopy, 2012: pp. 33–90. https://doi.org/https://doi.org/10.1002/9781118360668.ch2.

[34] J. Zheng, Y. Lyu, B. Wu, S. Wang, Defect engineering of the protection layer for photoelectrochemical devices, Energy Chem 2 (2020) 100039. https://doi.org/https://doi.org/10.1016/j.enchem.2020.100039.

[35] P.M.A. Sherwood, Paul van der Heide: X-ray photoelectron spectroscopy: An introduction to principles and practices, Anal Bioanal Chem 405 (2013) 2415–2416. https://doi.org/10.1007/s00216-012-6667-2.

[36] D. Briggs, Practical surface analysis, Auger and X-Ray Photoelecton Spectroscory 1 (1990) 151–152.

[37] R.L. Johnston, Chapter 1 - Metal Nanoparticles and Nanoalloys, in: R.L. Johnston, J.P. Wilcoxon (Eds.), Frontiers of Nanoscience, Elsevier, 2012: pp. 1–42. https://doi.org/https://doi.org/10.1016/B978-0-08-096357-0.00006-6.

[38] J.E. Penner-Hahn, Handbook of X-ray Spectrometry, 2nd ed., Revised and Expanded Edited by René E. Van Grieken (University of Antwerp) and Andrzej A. Markowicz (Vienna, Austria). Marcel Dekker, Inc: New York and Basel. 2002. xvi + 984 pp. ISBN 0-8247-0600-5., J Am Chem Soc 124 (2002) 12627. https://doi.org/10.1021/ja015389k.

[39] Quantitative Procedures in X-Ray Fluorescence Analysis, in: X-Ray Fluorescence Spectrometry,1999:pp.175–188.https://doi.org/https://doi.org/10.1002/ 9781118521014.ch12.

[40] Considerations in Quantitative X-Ray Fluorescence Analysis, in: X-Ray Fluorescence Spectrometry,1999:pp.161–174.https://doi.org/https://doi.org/10.1002/9781118521014.ch11.

[41] Instrumentation for X-Ray Spectrometry, in: X-Ray Fluorescence Spectrometry, 1999: pp. 89–109. https://doi.org/https://doi.org/10.1002/9781118521014.ch6.

[42] Z.P. Aguilar, Chapter 2 - Types of Nanomaterials and Corresponding Methods of Synthesis, in: Z.P. Aguilar (Ed.), Nanomaterials for Medical Applications, Elsevier, 2013: pp. 33–82. https://doi.org/https://doi.org/10.1016/B978-0-12-385089-8.00002-9.

[43] R. Castaing, Electron Probe Microanalysis, in: L. Marton, C. Marton (Eds.), Advances in Electronics and Electron Physics, Academic Press, 1960: pp. 317–386. https://doi.org/https://doi.org/10.1016/S0065-2539(08)60212-7.

[44] D.C. Bell, A.J. Garratt-Reed, Energy Dispersive X-ray Analysis in the Electron Microscope, Garland Science, 2003. https://doi.org/10.4324/9780203483428.

[45] G. Kortüm, W. Braun, G. Herzog, Principles and Techniques of Diffuse-Reflectance Spectroscopy, Angewandte Chemie International Edition in English 2 (1963) 333–341. https://doi.org/https://doi.org/10.1002/anie.196303331.

[46] A.R.T. SPRINGSTEEN, REFLECTANCE SPECTROSCOPY: AN OVERVIEW OF CLASSIFICATION AND TECHNIQUES, in: J. Workman, A.W. Springsteen (Eds.), Appl Spectrosc, Academic Press, San Diego, 1998: pp. 193–224. https://doi.org/https://doi.org/10.1016/B978-012764070-9/50008-1.

[47] K. Sakoda, Transmission Spectra, in: K. Sakoda (Ed.), Optical Properties of Photonic Crystals, Springer Berlin Heidelberg, Berlin, Heidelberg, 2001: pp. 81–97. https://doi.org/10.1007/978-3-662-14324-7_4.

[48] A. Axelevitch, B. Gorenstein, G. Golan, Investigation of Optical Transmission in Thin Metal Films, Phys Procedia 32 (2012) 1–13. https://doi.org/https://doi.org/10.1016/j.phpro.2012.03.510.

[49] K. Heng, D. Kitzmann, The theory of transmission spectra revisited: a semi-analytical method for interpreting WFC3 data and an unresolved challenge, Mon Not R Astron Soc 470 (2017) 2972–2981. https://doi.org/10.1093/mnras/stx1453.

[50] T.S. Teets, Photoluminescence, American Chemical Society, 2021. https://doi.org/ doi:10.1021/ acsinfocus.7e5014.

[51] C. Kumar, UV-VIS and Photoluminescence Spectroscopy for Nanomaterials Characterization, 2013. https://doi.org/10.1007/978-3-642-27594-4.

[52] Hall Effect Measurements in Materials Characterization, (n.d.).

[53] Charge-Based and Probe Characterization, in: Semiconductor Material and Device Characterization, 2005: pp. 523–562. https://doi.org/https://doi.org/10.1002/0471749095.ch9.

[54] L. Berger, G. Bergmann, The Hall Effect of Ferromagnets, in: C.L. Chien, C.R. Westgate (Eds.), The Hall Effect and Its Applications, Springer US, Boston, MA, 1980: pp. 55–76. https://doi.org/10.1007/978-1-4757-1367-1_2.

[55] B. Beltrán-Pitarch, J. Prado-Gonjal, A. V Powell, F. Martínez-Julián, J. García-Cañadas, Complete Characterization of Thermoelectric Materials by Impedance Spectroscopy, The Journal of Physical Chemistry C 123 (2019) 12608–12613. https://doi.org/10.1021/ acs.jpcc.9b02131.

[56] Seebeck Coefficient/Electric Resistance Measurement System ZEM-3, (n.d.).

[57] D.H. Sung, G.-H. Kang, K. Kong, M. Kim, H.W. Park, Y.-B. Park, Characterization of thermoelectric properties of multifunctional multiscale composites and fiber-reinforced composites for thermal energy harvesting, Compos B Eng 92 (2016) 202–209. https://doi.org/https://doi.org/10.1016/j.compositesb.2016.02.050.

[58] T.M. Tritt, Thermal Conductivity: Theory, Properties, and Applications (Physics of Solids and Liquids), n.d.

[59] Terry M. Tritt, Thermal Conductivity, Springer US, 2004. https://doi.org/10.1007/b136496.

Chapter 3

Optoelectronic properties of Pr substituted strontium titanate crystallites

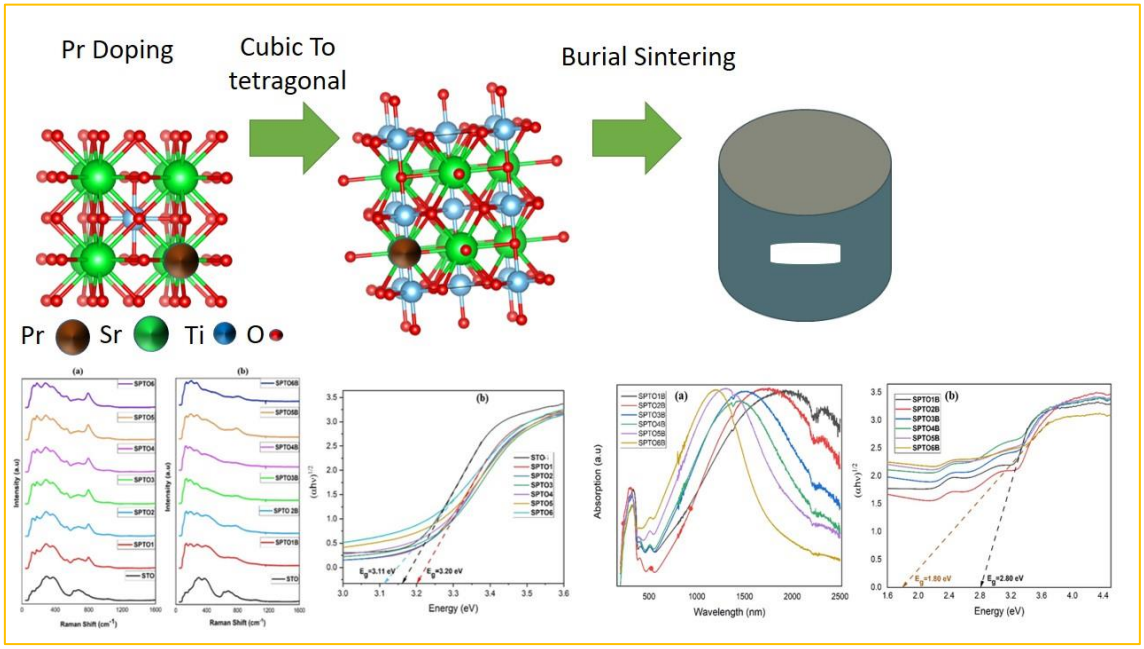

Objectives

This chapter provides a brief outline of electronic band structure alteration of $SrTiO_3$ by introducing Pr^{3+} in the Sr^{2+} site and subsequent graphite burial sintering. The formation of new electronic states observed here offers a novel approach for band gap modification in perovskites for optoelectronic applications.

3.1 Introduction

Strontium titanate (STO) has been extensively studied in its single crystal, bulk ceramic, and thin film forms due to its remarkable physical properties. Alkaline earth titanates with a perovskite structure, such as $BaTiO_3$ and $SrTiO_3$, are utilized in a wide range of electronic and optoelectronic applications. These include sensors, actuators, dielectric components in capacitors, as well as optical devices like modulators, windows, and filters [1–3]. Doped perovskites and delaffosite are also employed in thermoelectric power generation [4–8]. Oxide perovskites, with the general formula ABO_3 (where A and B are cations), exhibit a distinctive structure characterized by BO_6 octahedra that share corners, extending symmetrically in all three dimensions. The A cations occupy the voids formed by eight BO_6 octahedra, resulting in a 12-fold oxygen coordination for A cations and a 6-fold coordination for B cations, as depicted in Fig. 3-1. Doping at the A or B sites with appropriate elements significantly modifies the structural, optical, dielectric, ferroelectric, and thermoelectric properties of STO-based ceramics. Such cation substitution alters the electronic band structure, influencing band curvature and degeneracy, thereby impacting the material's functional properties. The intrinsic structural flexibility of the perovskite lattice enables precise tuning of multifunctional properties through chemical substitution, where subtle octahedral distortions and dopant site occupancy critically govern electron–phonon interactions and thereby modulate the dielectric, optical, and thermoelectric responses of $SrTiO_3$ [9].

Compared to the characteristics of conventional semiconductors, oxide-based semiconductors exhibit a range of unique and fascinating properties. Strontium titanate, a highly promising perovskite oxide material, has a broad spectrum of applications and is widely utilized as a photo catalyst as well as a substrate for the epitaxial growth of various oxide-based thin films [10,11]. It exhibits semiconducting behavior, high dielectric constant, and great thermal stability, resulting in a broad variety of microelectronics applications, making it one of the most promising materials for tunable microwave devices, capacitors, photo catalysts, and light emitters [12]. STO has an optical bandgap

of 3.2 eV and can be varied with appropriate doping, [13–16]. STO exhibits structural characteristics such as the soft bonding of the small Ti^{4+} ion with the surrounding octahedral O^{2-} ions. Its conductivity can be modulated, demonstrating significant low-temperature mobility upon n-type doping, which is commonly achieved through the introduction of oxygen vacancies or by chemical substitution of La^{3+} or Pr^{3+} for Sr^{2+} and Nb^{5+} for Ti^{4+} [17]. While many of these properties are not yet fully understood, they are strongly associated with rare earth element doping and changes in the electronic structure resulting from oxygen vacancies. Impurities and point defects play a significant role in shaping the functional capabilities of the material, and considerable efforts are being made to uncover the underlying mechanisms and their causal relationships. Recent studies have demonstrated that defect-induced electronic states and dopant–vacancy interactions dominate carrier generation and recombination processes in $SrTiO_3$. The coexistence of shallow and deep trap states, originating from oxygen vacancies or aliovalent dopants, plays a pivotal role in defining optical absorption edges and emission behavior. However, the quantitative relationship between defect concentration, local lattice distortion, and optical transition probability remains incompletely understood, motivating detailed spectroscopic and structural investigations.

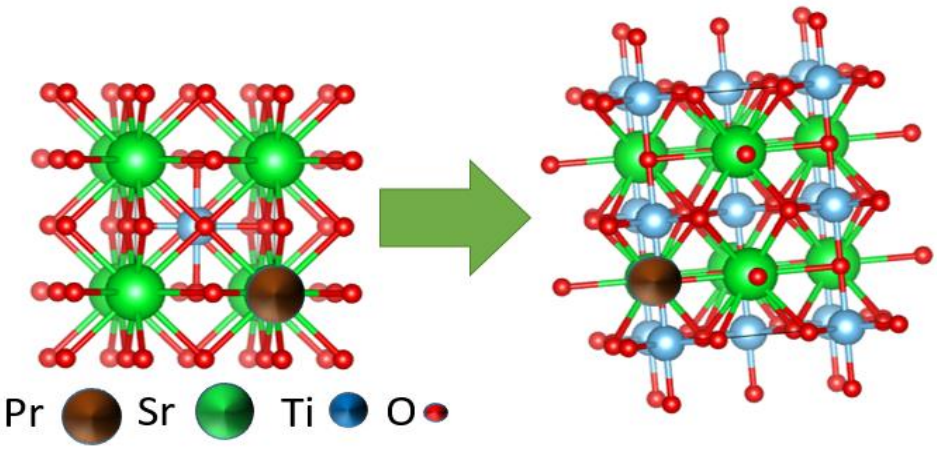

Figure 3- 1 Cubic to tetragonal phase transition of Pr substituted $SrTiO_3$.

Due to its wide band gap, the photocatalytic properties of $SrTiO_3$ are restricted to the UV region of the spectrum. To address this limitation, modifications are being explored to reduce the band gap and enhance the material's light-harvesting capacity across a broader range of the spectrum [18,19]. Sr^{2+}ions lack the complex energy level diagram characteristic of rare earth (RE) ions. As a result, photon management properties can only be achieved through doping with other rare earth ions. Substituting rare earth elements can shift the Fermi level into the conduction band and modify the absorption spectrum by introducing peaks in the 0.1–0.4 eV range [6]. Dopants like Cr, Fe, Eu and Al are widely exploited to change the optical properties of pristine $SrTiO_3$ [3,20–24]. Unlike other RE^{3+}, Pr^{3+} has a unique feature resulting from the close energy separation between the $^1S_0$ level and the lowest edge of the 4f 5d configuration and its emission depends greatly on the position of the 4f 5d configuration, which is extremely influenced by the features of the host. Pr as a dopant is widely used to alter the ferroelectric and thermoelectric properties of STO, but optical modifications are less explored.

In various dielectric crystals, luminescence emission techniques such as photoluminescence, cathodoluminescence, radioluminescence and more recently, ionoluminescence have been employed to study electronic excitations and to create defect centers [25–28]. When exposed to ultraviolet light, STO exhibits photoconductivity, primarily driven by the contributions of both photo generated electrons and holes. The photoluminescence (PL) properties of STO are even more complex and debated than its transport behavior, with self-trapped excitons playing a dominant role in electronic excitations. High-energy electronic excitations, exceeding the band gap, generate free electrons and holes, which rapidly form electron-hole pairs confined within the lattice, creating self-trapped excitons (STE). Pure STO displays greenish luminescence under UV light, peaking at photon energies of 2.2–2.4 eV, corresponding to a wavelength of approximately 500 nm, attributed to the decay of these self-trapped excitons [29–32]. Near the bandgap energy at about 3.2 eV, another band is also observed related to the phonon-assisted transition from the conduction band to the valence band [33].

Ar^+ ion irradiation introduces an additional luminescence band in the blue region at 2.8 eV. Similarly, blue luminescence has been observed in materials with oxygen deficiencies or when doped with Nb donor impurities. [26,34]. The luminescence spectra are influenced by electron doping and the presence of natural oxygen vacancy defects. The use of Pr as a dopant in Sr sites has not been extensively studied for its photoluminescent properties. Typically, Pr-doped titanates exhibit intense red emission under ultraviolet (UV) light excitation [35]. The intensity of red luminescence is typically low, with the position of the emission peak and the full-width at half-maximum (FWHM) playing a crucial role in defining the color gamut. Expanding the color gamut remains a debated topic as it can significantly enhance color vibrancy.

Materials capable of emitting light in narrow spectral bands are essential for achieving a wider gamut. Consequently, high-performance narrow-band emission materials are vital for developing wide-gamut pc-LED backlights [36]. From a photophysical standpoint, Pr^{3+} ions are particularly attractive because their intra-4f–5d transitions are strongly affected by the host crystal field, enabling fine-tuning of emission wavelength and linewidth through host–dopant interactions. Given the sensitivity of Pr emission to lattice symmetry and oxygen coordination, $SrTiO_3$ provides an ideal platform to probe the interplay between local electronic structure, defect states, and radiative recombination mechanisms — aspects that remain relatively underexplored compared to its structural or electrical characteristics.

Most efforts to tune the photoluminescence (PL) properties of $SrTiO_3$ focus on doping at the B-site by substituting Ti^{4+} ions in the lattice. Praseodymium (Pr)-doped luminous materials have shown significant potential in applications such as red phosphors for displays, sensors, and optoelectronic integration. The photoluminescence (PL) performance of Pr-doped ferroelectric ceramics can be greatly improved under the application of an electric field. This enhancement is attributed to the reduction in structural symmetry of the host material following the poling process [37]. Due to their high sensitivity, the emissions of Pr^{3+} have also been used as a structural transition probe

to examine the phase transition of ferroelectric hosts that induces changes in crystal symmetry.

In this study, Praseodymium (Pr) was successfully incorporated into Sr sites within the $SrTiO_3$ matrix. Burial sintered samples of Pr-doped $SrTiO_3$ were prepared using graphite powder, and structural changes were analyzed using X-ray diffraction (XRD) and Raman spectroscopy. Compositional analysis were done by XPS and XRF. The tunability of optical and photoluminescence properties was investigated, and the findings were correlated with the observed structural modifications.

3.2 Experimental methods and techniques

The high-temperature solid-state reaction method was employed to synthesize $Sr_{1-x}Pr_xTiO_3$ with x=0.05, 0.075, 0.10, 0.125, 0.15, 0.20 ceramics. Stoichiometric amounts of $SrCO_3$ (Sigma-Aldrich, 99.9%), TiO_2 (Sigma-Aldrich, 99.9%), and Pr_6O_{11} (Sigma-Aldrich, 99.9%) were mixed and ground in ethanol for 2 hours. Prior to mixing, TiO_2 and Pr_6O_{11} powders were dried at 900 °C for 8 hours, while $SrCO_3$ was dried at 180 °C for 16 hours. The resulting powders were calcined at 1250 °C for 8 hours, followed by further grinding to get uniform crystallites. For the undoped sample, the calcination temperature was optimized to 1200 °C. The samples were labeled as SPTO 1 to SPTO 6, as listed in Table 3-1.

The powders were mixed with a PVA binder and uniaxially pressed into pellets measuring 13 mm in diameter and 2 mm in thickness. The binder was removed by annealing the pellets at 600 °C for 4 hours at a controlled heating rate. These pellets were then buried in graphite powder and subjected to burial sintering at 1450 °C for 4 hours under optimized dwell cycles. The reducing agent CO, generated by the graphite during annealing, created a strong reducing atmosphere. The sintered pellets were ground again, and the resulting powders were labeled as SPTO 1B to SPTO 6B, as shown in Table 3-1.

Table 3-1 Sample labels of $Sr_{1-x}Pr_xTiO_3$ before and after burial sintering.

Concentration of Pr	Before Burial sintering	After Burial sintering
X=0.05	SPTO 1	SPTO 1B
X=0.075	SPTO 2	SPTO 2B
X=0.10	SPTO 3	SPTO 3B
X=0.125	SPTO 4	SPTO 4B
X=0.15	SPTO 5	SPTO 5B
X=0.20	SPTO 6	SPTO 6B

The X-ray diffractometer (Rigaku-MiniFlex 600) with the Cu-K_α radiation of wavelength (λ = 1.5418 Å) was used for structural studies with 2θ values between 20 and 80^o and the obtained data was analyzed using Rietveld refinement method. Raman spectra of the powder were done by Jasco NRS 4100 system (532 nm). XPS measurements were done using Omicron Nanotechnology XPS system. The morphological characterization of the samples was carried out by using a Field emission gun scanning electron microscope (FE-SEM) with EDS and elemental mapping using AMETEC EDAX system. Optical measurements were done by CARY 5000 UV-Vis NIR in wavelength range between 200-2400 nm. PL studies were done between the range 400 and 600 nm.

3.3 Results and discussion

The color of calcined powders changed from white-beige to lemon yellow with increasing Pr content going from x = 0.05 to x = 0.20 in $Sr_{1-x}Pr_xTiO_3$. In burial sintered samples, the color changed to dark grey, indicating the change in the oxidation state of titanium from Ti^{4+} to Ti^{3+} under a strongly reducing atmosphere [38].

3.3.1 Microstructural characterization- XRD – Rietveld refinement, Raman analysis

Fig. 3-2 shows the room temperature XRD patterns of Pr doped STO ceramics Sr_{1-x} Pr_xTiO_3 with different dopant concentrations. Ceramics with higher Pr concentrations undergo a phase transition from the cubic $SrTiO_3$structure to a tetragonal

phase, with no precursor residues remaining after calcination. The reflections obtained align well with the standard database (PDF 00-035-0734), confirming the structural purity. Fig. 3-2a further verifies the successful substitution of Pr^{3+} ions for Sr^{2+} in the $SrTiO_3$ crystal lattice. Due to its smaller ionic radius (0.99 Å) compared to Sr^{2+} (1.26 Å), Pr^{3+} exclusively occupies the A-site (Sr site) in the $SrTiO_3$ lattice [39].

The observation of the asymmetric nature of (310) peaks between 2θ =77-78° is used to investigate the breakdown of cubic symmetry (Pm-3m) and subsequent transformation to tetragonal space group (I4/mcm). The transformation is evident only when the Pr content exceeds x = 0.1, i.e., for the sample SPTO 3, and asymmetry increases with increasing x. Garg et al. Reported tetragonal symmetry from neutron and Raman scattering measurements for x =0.05 compositions, whereas Checchia et al. Reported cubic symmetry from X-ray diffraction measurements up to x=0.075 [40,41].

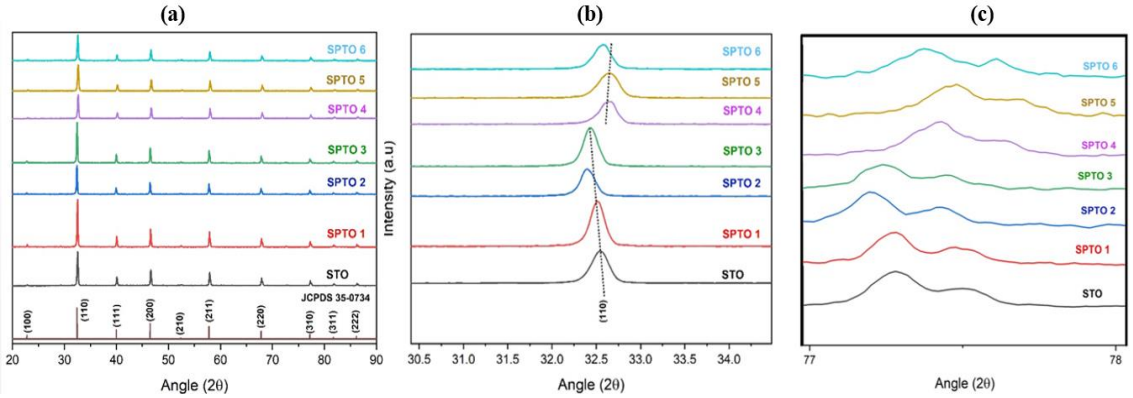

Figure 3- 2 (a) XRD pattern of Pr substituted $SrTiO_3$ **(b)** Shifting of (110) peak **(c)** Asymmetric nature of (310) peaks of samples before burial sintering.

The significant difference in ionic radii between the host Sr^{2+} cations and the dopant Pr^{3+}cations induces tilting of the TiO_6 octahedra, facilitating the observed structural transformation. The crystallite size was estimated using the Scherrer equation, while lattice strain was evaluated using the Williamson-Hall method, as represented by eqn (3.1). The analysis revealed that all samples exhibited a positive slope, indicating tensile strain, which is likely caused by the incorporation of Pr^{3+} into the Sr–Ti–O lattice. Microstrains displayed an irregular trend, and when Pr^{3+} substitutes for Sr^{2+}, free electrons are generated. However, beyond a certain threshold, strontium vacancies are formed,

leading to the generation of oxygen vacancies for electronic compensation [42]. Oxygen vacancies thus generated also contribute to the lattice micro strain, depending on the site preference of Pr^{3+} ions [43].

$$\beta\ cos\theta = \frac{k\lambda}{D} + 4\epsilon\ sin\theta \tag{3.1}$$

All the diffraction peaks were analyzed using the Gaussian function to determine the FWHM and the corresponding 2θ values. The average crystallite size was calculated using the Scherrer equation, based on the five most intense peaks, as detailed in Table 3-2.

The crystallite size decreases with increasing dopant concentration, while the microstrain increases significantly in both cubic and tetragonal systems. Typically, the substitution of dopants with smaller ionic radii results in a shift of XRD peaks to higher angles; however, in the case of lower Pr-doped samples, the peaks shift to lower angles. This unusual behavior suggests that at lower Pr concentrations, more Pr^{3+} ions occupy interstitial sites, causing the lower angle shift. Due to the significant disparity in ionic radii between Ti^{4+} (0.605 Å) and Pr^{3+} in octahedral coordination, Pr incorporation into B-sites is unlikely.

Theoretical studies indicate that in $SrTiO_3$, larger rare earth ions substitute at A-sites via a Sr vacancy mechanism, while smaller rare earth ions may occupy both A- and B-sites, owing to their intermediate ionic radii. Experimental results further support this, showing an abnormal cubic lattice parameter in Pr-doped $SrTiO_3$, indicating possible mixed occupancy of Pr^{3+}at both Sr and Ti sites. The lower angle shift of XRD peaks may result from a combination of grain boundary (GB) and interstitial effects. This aligns with recent theoretical predictions suggesting that Pr-doping at GBs is more beneficial than bulk doping, particularly for dopant concentrations up to 15 mol/L in both dilute and solid solutions [44–46].

Table 3- 2 Average crystallite size and micro strain of $Sr_{1-x}Pr_xTiO_3$ before burial sintering.

Sample label	Crystallite size (nm)	Micro strain (x 10^{-3})
STO	38.8	0.427
SPTO 1	44.4	0.456
SPTO 2	42.0	0.735
SPTO 3	41.2	0.851
SPTO 4	37.9	0.331
SPTO 5	35.8	0.361
SPTO 6	34.9	0.441

A larger strain in SPTO 1, 2, and 3 may be because of this grain boundary substitution. As the Pr content in the sample increases, the (011) XRD peak gradually shifts towards lower diffraction angles, indicating an increase in strain, whereas increasing the Pr content in the sample further releases the strain by creating smaller crystallites and particles, resulting in the XRD peak shifting back to its original position as represented in Fig.3-2 (b).

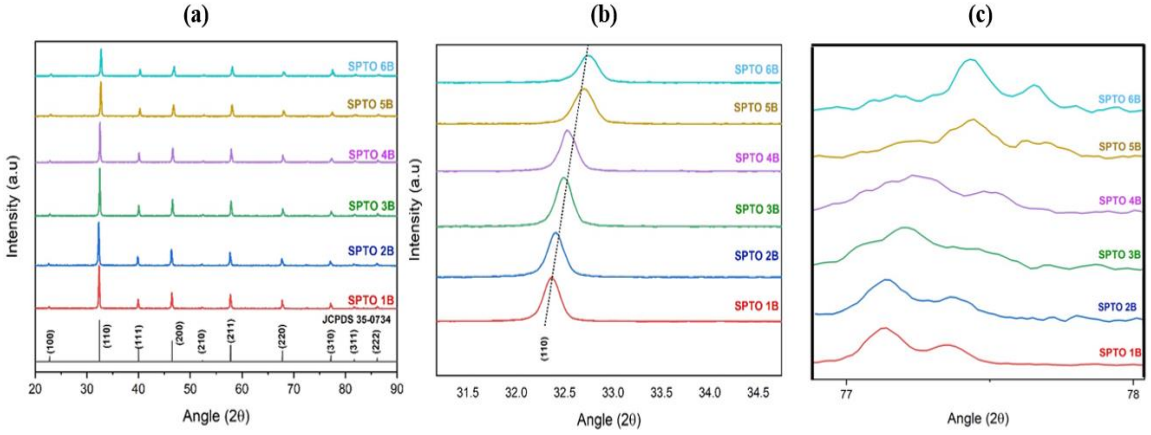

Figure 3- 3 (a) XRD pattern of Pr substituted $SrTiO_3$ **(b)** Shifting of (110) peak **(c)** Asymmetric nature of (310) peaks of samples after burial sintering.

Unlike the conventional sintering process, all burial-sintered samples exhibit an XRD peak shift to higher angles, confirming successful Pr^{3+} doping at the Sr^{2+} site, as shown in Fig.3-3. High-temperature sintering enhances the likelihood of Pr incorporation, and the progressive shift to higher angles highlights the dominance of doping over interstitial occupancy, irrespective of the Pr content in the sample. The Williamson-Hall (W-H) plot represented in Fig.3-4 reveals that all samples, both before and after burial sintering, have a positive slope, indicating tensile strain, as detailed in Table 3-3. Additionally, ceramics with higher Pr concentrations show a phase transition from the cubic $SrTiO_3$ structure to a tetragonal phase, with reflections aligning well with the database. Burial sintering also leads to the reduction of Ti^{4+} ions (0.605 Å) to Ti^{3+} ions (0.67 Å).

The asymmetric nature of (310) peaks in diffraction patterns between 2θ=77-78° is examined, and it is evident only when the Pr content exceeds x = 0.1. Once the system changes to that, all XRD peaks shift towards higher 2θ angles, implying a smaller lattice constant.

Table 3- 3 Average crystallite size and micro strain of $Sr_{1-x}Pr_xTiO_3$ after burial sintering.

Sample label	Crystallite size (nm)	Micro strain (x 10^{-3})
SPTO1B	42.1	0.565
SPTO2B	41.9	1.249
SPTO3B	40.9	1.040
SPTO4B	39.4	0.911
SPTO5B	33.7	0.811
SPTO6B	32.1	1.490

The XRD spectra of the samples, both before and after burial sintering, were thoroughly examined to detect any additional peaks indicative of structural changes. Specific attention was given to peaks associated with anti-phase octahedral tilting, known

as R-point reflections, cation/vacancy ordering referred to as X-point reflections, and in-phase octahedral tilting identified as M-point reflections. To explore these structural features in greater detail, the region near the (200) diffraction peak was magnified. Typically, heavily substituted samples exhibit split peaks in this region, a hallmark of complex structural transformations. However, such split peaks were not observed, even in the highly Pr-rich samples SPTO 6 and SPTO 6B, suggesting a uniform structure despite the high dopant concentration. Further investigation of the spectra for R-point reflections at $2\theta \approx 38°$ also confirmed their absence, even in the samples with the highest levels of Pr doping. This absence of R-point reflections indicates that the $Sr_{1-x}Pr_xTiO_3$ system transitions from a cubic to a tetragonal phase without the presence of additional impurity phases or precursor-related artifacts. This phase transformation is driven solely by Pr substitution and related structural changes.

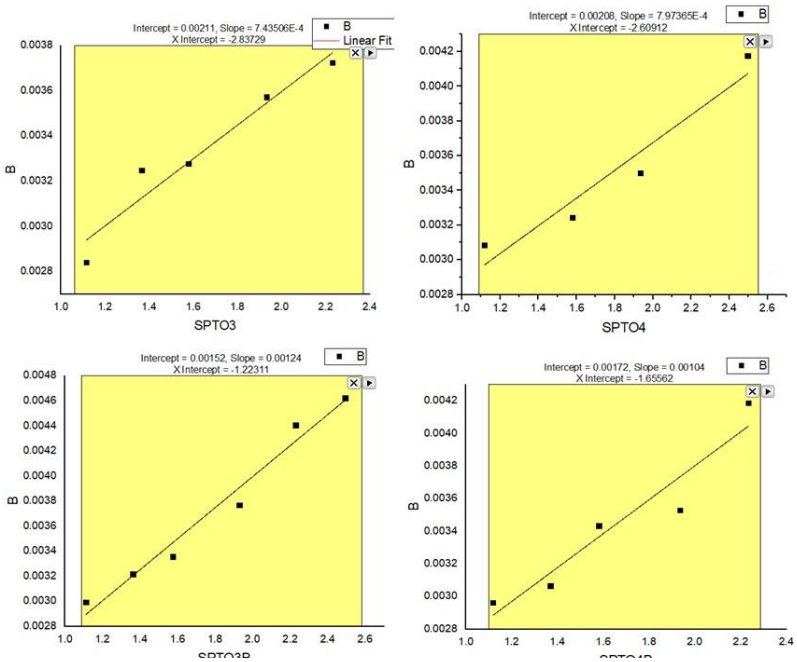

Figure 3- 4 Williamson-Hall plots of SPTO 3, SPTO 3B, SPTO4 and SPTO 4B Ceramics before & after burial sintering

The Rietveld refinement results are represented and tabulated in table 3-4, 3-5 and Fig. 3-5, 3-6 respectively. Since the system shows a transformation from cubic to Tetrag-

onal phase for the $Sr_{1-x}Pr_xTiO_3$ with x≥0.1, for samples with x≥0.1, tetragonal unit cell.parameters were used.

Table 3-4 Structural Parameters of $Sr_{1-x}Pr_xTiO_3$, ceramics before burial sintering.

Sample	**SPTO 1 X=0.05**	**SPTO 2 X=0.075**	**SPTO 3 X=0.10**	**SPTO 4 X=0.125**	**SPTO 5 X=0.15**	**SPTO 6 X=0.2**
Structure	Cubic	Cubic	Tetragonal	Tetragonal	Tetragonal	Tetragonal
Space group	$Pm\bar{3}m$	$Pm\bar{3}m$	$I4/mcm$	$I4/mcm$	$I4/mcm$	$I4/mcm$
Lattice parameter (Å)	$a = 3.9068$ $b = 3.9068$ $c = 3.9068$	$a = 3.9057$ $b = 3.9057$ $c = 3.9057$	$a = 5.5220$ $b = 5.5220$ $c = 7.8087$	$a = 5.5270$ $b = 5.5270$ $c = 7.8096$	$a = 5.5186$ $b = 5.5186$ $c = 7.8145$	$a = 5.5096$ $b = 5.5096$ $c = 7.8097$
Unit cell volume ($Å^3$)	59.631	59.583	238.110	238.573	237.994	237.077
χ^2	1.98	2.04	1.68	2.01	1.74	2.18
GOF index	1.4	1.4	1.3	1.4	1.3	1.5

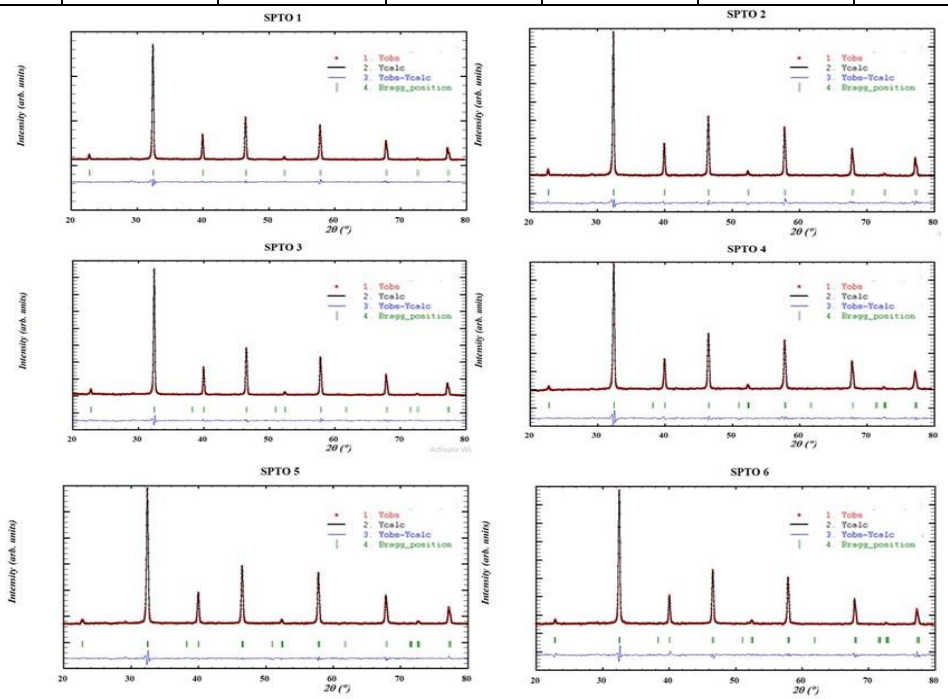

Figure 3- 5 Rietveld refinement of patterns for $Sr_{1-x}Pr_xTiO_3$, ceramics before burial sintering

Table 3-5 Structural Parameters of $Sr_{1-x}Pr_xTiO_3$, ceramics before burial sintering

Sample	**SPTO 1B X=0.05**	**SPTO 2B X=0.075**	**SPTO 3B X=0.10**	**SPTO 4B X=0.125**	**SPTO 5B X=0.15**	**SPTO 6B X=0.2**
Structure	Cubic	Cubic	Tetragonal	Tetragonal	Tetragonal	Tetragonal
Space group	$Pm\bar{3}m$	$Pm\bar{3}m$	$I4/mcm$	$I4/mcm$	$I4/mcm$	$I4/mcm$
Lattice parameters (Å)	$a = 3.9056$ $b = 3.9056$ $c = 3.9056$	$a = 3.9060$ $b = 3.9060$ $c = 3.9060$	$a = 5.5215$ $b = 5.5215$ $c = 7.8150$	$a = 5.5239$ $b = 5.5239$ $c = 7.8144$	$a = 5.5215$ $b = 5.5215$ $c = 7.8245$	$a = 5.5266$ $b = 5.5266$ $c = 7.8309$
Unit cell volume (Å^3)	59.575	59.582	238.259	238.449	238.548	239.185
χ^2	2.06	1.83	1.79	1.82	2.13	2.38
GOF index	1.4	1.4	1.3	1.3	1.5	1.5

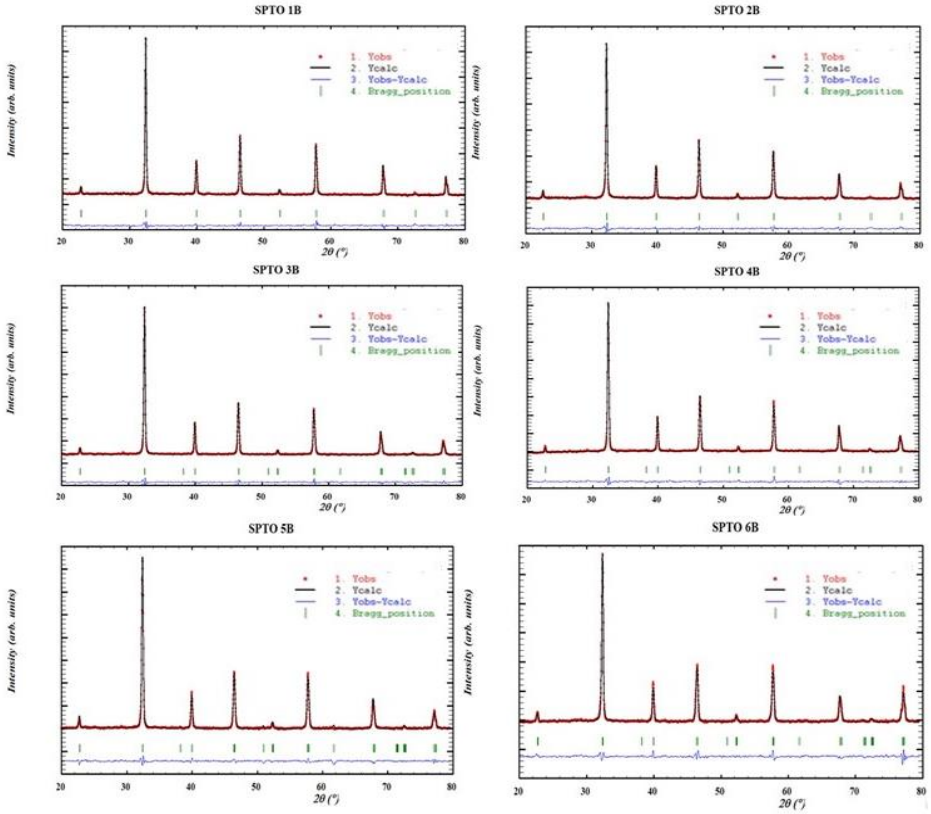

Figure 3- 6 Rietveld refinement of XRD patterns for $Sr_{1-x}Pr_xTiO_3$, ceramics after burial sintering.

Raman spectroscopy studies at room temperature were conducted to further investigate the crystal structure, as shown in Fig. 3-7. Factor group symmetry analysis indicates that all zone-center optical phonons in STO structures have odd symmetry. Consequently, first-order Raman activity is not expected, and the room-temperature spectrum predominantly exhibits second-order scattering. As anticipated, the Raman spectrum within the broad ranges of 200–500 cm^{-1} and 600–800 cm^{-1} corresponds to the second-order Raman active modes of STO. The observed Raman peaks in these ranges align well with previously reported findings [41,42]. Peaks observed at 117-121 and 132-144 cm^{-1} are not permitted by the selection rules in STO perovskites.

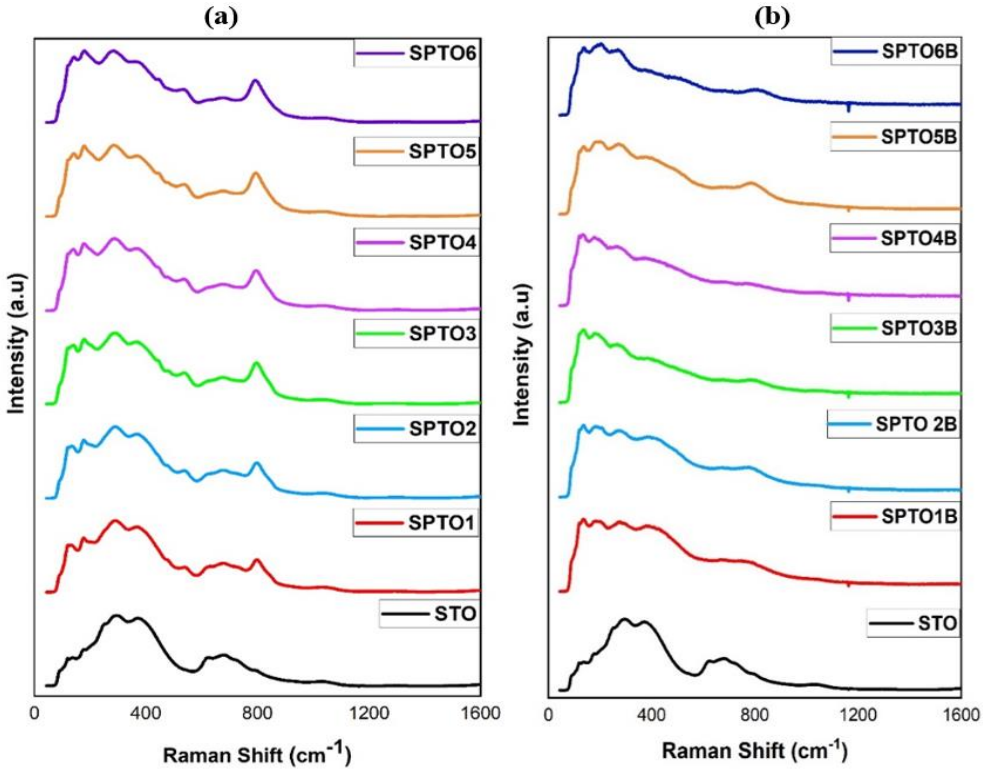

Figure 3- 7 (a) Raman spectra of Pr substituted $SrTiO_3$ before burial sintering **(b)** Raman Spectra of Pr substituted $SrTiO_3$ after burial sintering.

The presence of Raman peaks is attributed to the relaxation of selection rules due to structural defects. The peak at 117 cm^{-1} gradually decreases in intensity and shifts to 121 cm^{-1} as the Pr concentration increases from x=0.05 to x=0.2. Similarly, the peak at 132 cm^{-1} undergoes a blue shift to 144 cm^{-1} with an increase in intensity, indicating a

structural transformation toward tetragonal symmetry. These shifts are caused by lattice stress induced by the incorporation of Pr atoms [47]. The bands observed at 248, 621, 687, and 721 cm^{-1} are additive combinations and overtones. The bands at 293 and 373 cm^{-1} are considered to be different combinations. Here, as shown in Fig.3-6 (a), a weak band centered on 92 cm^{-1} has been recorded. This observation strongly supports the existence of polar micro-regions in $SrTiO_3$ (STO) structures, arising from oxygen vacancies introduced during the synthesis process. Polar micro-regions are typically generated by impurities or structural defects in STO-based materials. Both theoretical and experimental studies provide evidence for the formation of ferroelectric micro-regions (FMR), which are recognized as key indicators of polar disorders. The formation of these micro-regions is believed to be responsible for the emergence of ferroelectricity in $SrTiO_3$, driven by the presence of impurities and defects [48,49]. The presence of polar micro-regions can substantially enhance the functional properties of ferroelectric materials. In STO structures, characteristic peaks were identified at 175, 540 and 795 cm^{-1}, corresponding to the TO_2, TO_4, and LO_4 mode vibrations, respectively. The TO_2 mode is linked to the polar last mode, which involves the motion of A-site cations relative to the BO_6 octahedron. The TO_4 mode corresponds to the polar axe mode, caused by the bending of the oxygen cage within the octahedral structure [50–52]. The polar instability of the STO system is clear from the presence of the TO_2 and TO_4 modes in the Raman spectra [53]. Both TO_2 and TO_4 modes were observed in all Pr-doped samples, whereas pristine $SrTiO_3$ lacks these modes. This strongly indicates that even the smallest Pr concentrations induce polar nanoregions (PNRs) in the system. The incorporation of Pr into the $SrTiO_3$ matrix gives rise to the LO_4 mode, which becomes broader and more intense, reflecting increased disorder within the system due to doping. In addition to these vibrations, a weak mode at 476 cm^{-1}, identified as the LO_3 mode, was observed, consistent with earlier reports. Furthermore, two additional vibration modes were noted at 145 cm^{-1} and 445 cm^{-1} in samples with Pr concentrations $x \geq 0.1$ (SPTO3). These modes correspond to E_g and B_{1g} modes observed in pure $SrTiO_3$ below 105 K. They originate from antiferrodistortive (AFD) behavior in the tetragonal symmetry, caused by the

bending of the octahedron due to the freezing of the triply degenerate R_{25} phonon at the R-point of the first Brillouin zone [41]. Coherent with the XRD results, we may conclude that in the samples with Pr content x≥0.1, the system transforms from cubic symmetry (space group Pm-3m) to tetragonal space symmetry (I4/mcm). A close inspection of the peaks of SPTO 2 reveals a feeble band at 445 cm^{-1} but it becomes evident only for compositions with x=0.1. So we conclude that the exact percentage of Pr content for this symmetry breakdown is between x = 0.075 and x = 0.1. It is observed that as x increases, the intensity of the polar modes TO_2 and TO_4 increases. The inclusion of Pr in the $SrTiO_3$ matrix also affects the line width of TO_4 mode, which shows an increase in dopant concentration because of the reduction in phonon lifetime resulting from A-site disorder. It is also observed that the TO_2 mode shifts to a higher wave number as the composition increases. The substitution of heavier Pr atoms for Sr stiffens the force constant, resulting in an increase in wave number as Pr content increases [54]. The presence of TO modes with high intensity was not observed in other A- site doped titanates, and this is attributed to the tendency of Pr to preserve the ferroelectric distortion [55]. The simulated TO_2 mode vibration is illustrated in Fig. 3-8. Where the ash colored arrows represent the atomic vibrational direction and the Sr/Pr atoms, O atoms, and Ti atoms are represented by blue, red, and grey balls, respectively.

The TO_2 mode displays an asymmetric profile in all Pr-doped samples; however, as the Pr concentration increases, the profile gradually becomes more symmetric. This change indicates the presence of Fano resonance, which arises from strong interference between discrete and continuous vibrational modes [56]. This asymmetric profile can be quantitatively analyzed by introducing the Fano resonance equation (3.2).

$$I(\omega) = I_c \frac{|q+\epsilon|^2}{1+\epsilon^2} + I_b \tag{3.2}$$

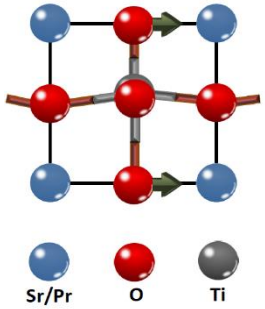

Figure 3- 8 TO_2 mode Raman oscillation in Pr substituted $SrTiO_3$ system.

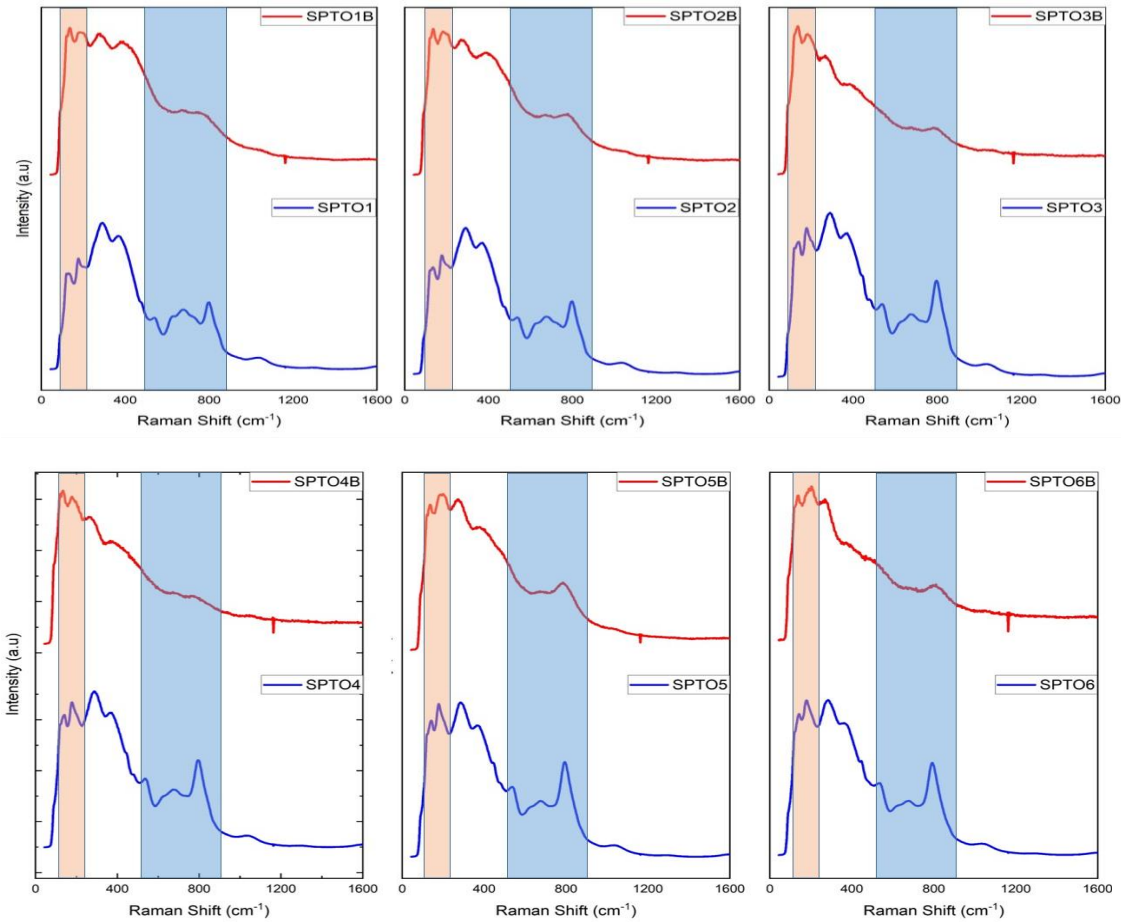

Figure 3- 9 Comparison of suppression modes in Raman spectra of Pr substituted $SrTiO_3$ before and after burial sintering.

$$I_b = A\,(\omega-\omega_p)^3 + B(\omega-\omega_p)^2 + C(\omega-\omega_p) + D \qquad (3.3)$$

A, B, C and D are constants. $\varepsilon = \frac{\omega-\omega_p}{\Gamma}$ is the dimensionless scale for energy reduction. Γ and ω_p are the line width and frequency of the asymmetric Fano resonant mode under consideration. The asymmetry factor q affects the degree of the coupling between the discrete and continuous states, which determines the Fano resonance line shape [57]. Raman spectra of burial sintered samples show peaks in the broad range of 200–500 cm^{-1} and 600–800 cm^{-1} related to the second-order Raman active mode of STO.

Regardless of the doping concentration, the spectra become broader in comparison to the samples before burial sintering. Most of the distinctive peaks are suppressed after the high-temperature sintering process. Fig. 3-9 illustrates the intensity variations between buried sintered and pure samples, scaled to the same Y-axis for direct comparison. Peaks in the red-shaded region (100-280 cm^{-1}) show an increase in intensity, whereas peaks in the blue-shaded region (535-850 cm^{-1}) exhibit a decrease in intensity. The red region includes peaks at 117 cm^{-1} and 134 cm^{-1}, which are forbidden by selection rules in STO perovskites. Their presence is attributed to the relaxation of selection rules caused by structural defects.

The increased intensity of these peaks compared to pure samples indicates increased defects induced in the structure because of the burial sintering process. The blue region includes the peaks at 540 cm^{-1} and 795 cm^{-1}. These peaks were suppressed because of burial sintering except for the samples with high Pr content. The incorporation of Pr into the STO system gives rise to this LO_4 mode that broadens even for low concentrations of Pr, showing increased disorder in the system with doping, which is further enhanced by the sintering process.

3.3.2 Compositional, morphological studies- XRF, XPS, EDX

In order to assess the elemental composition of dopants in the sample XRF data of six samples were analyzed. The fluorescence intensity corresponding to $L_{\beta1}$ and $L_{\beta2}$

emissions of Pr with energies 5.49 KeV, 5.85 KeV increases with Pr content and is presented in the Fig. 3-10 and in the Table 3-6.

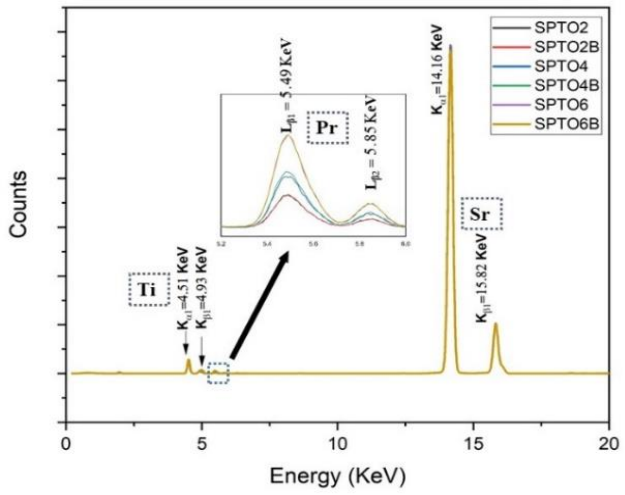

Figure 3- 10 XRF spectra of $Sr_{1-x}Pr_xTiO_3$, ceramics (with x=0.075, 0.15, 0.20).

Table 3- 6 Percentage composition of Pr from XRF spectra of $Sr_{1-x}Pr_xTiO_3$ ceramics.

Sample	Percentage of Pr (%)
SPTO 2	0.153
SPTO 2B	0.157
SPTO 4	0.280
SPTO 4B	0.298
SPTO 6	0.569
SPTO 6B	0.574

To examine the influence of oxidation states and oxygen vacancies on the optoelectronic properties, the samples were analyzed using X-ray photoelectron spectroscopy. Fig. 3-10 presents the survey spectrum and compositional state analysis data of the corresponding elements. Figures 3-11 (a) and (b) specifically display the survey spectrum data for the least doped sample (SPTO 1) and the heavily doped sample (SPTO 6), respectively.

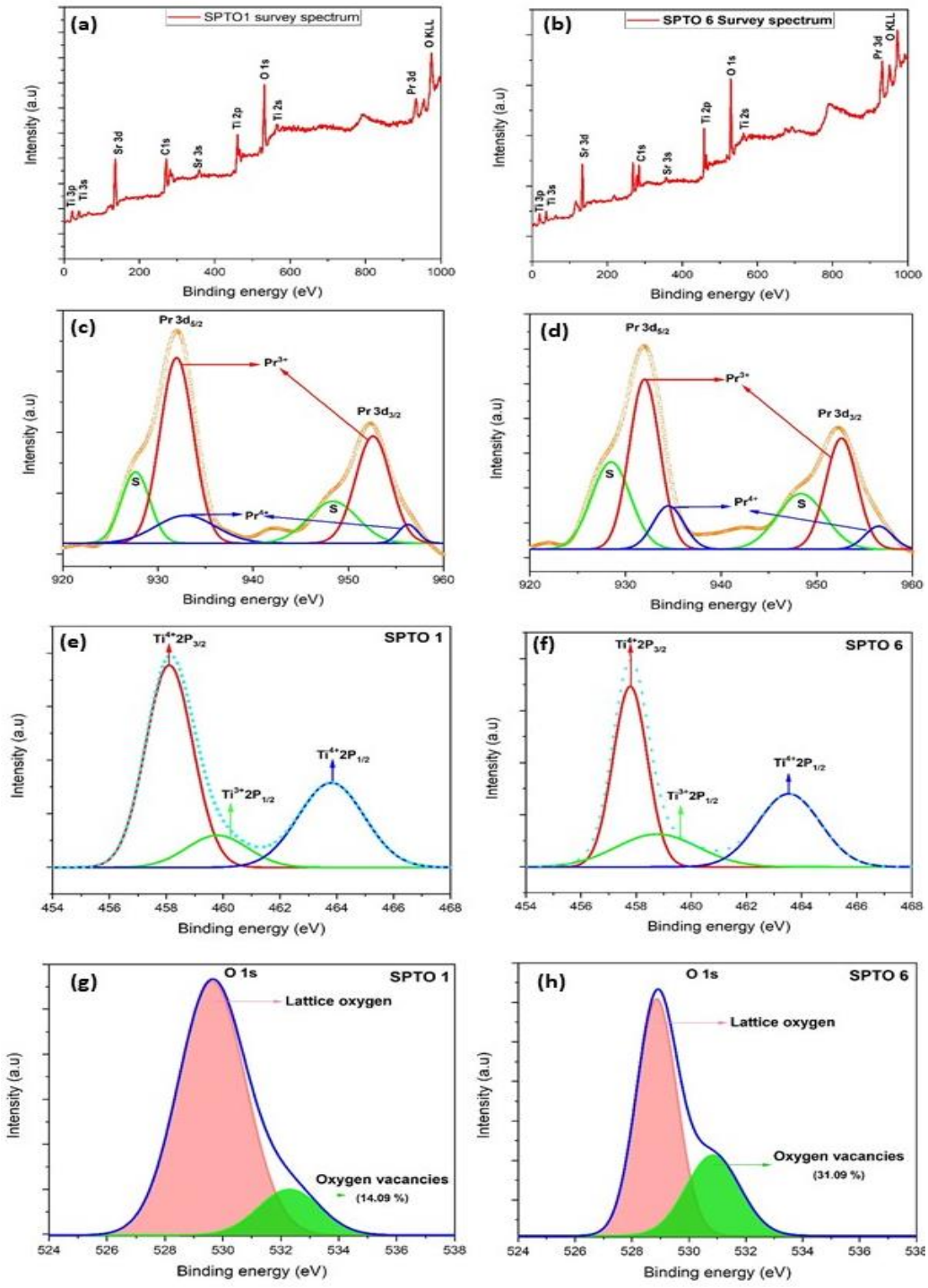

Figure 3- 11 (a) (b) XPS survey spectrum of SPTO 1 and 6 **(c)** deconvoluted Pr 3d levels of SPTO 1**(d)** deconvoluted Pr 3d levels of SPTO 6 **(e)** deconvoluted Ti 2p levels of SPTO 1 **(f)** deconvoluted Ti 2p levels of SPTO 6 **(g)** O 1s levels of SPTO 1**(h)** O 1s levels of SPTO 6.

The spectrum maps all of the elements in the sample, with a higher intensity of dopant Pr shown by Pr 3d peaks in the region 920 to 960 eV as doping concentration increases. Pr 3d exhibits two strong peaks around 933 eV and 953 eV as indicated in the Fig. 3-11 (c) and 3-11 (d) and can be aligned with the Pr $3d_{5/2}$ and Pr $3d_{3/2}$ levels of SPTO 1 and SPTO 6 respectively. Each XPS peak can be deconvoluted into three components corresponding to the oxidation states Pr^{3+} and Pr^{4+}, along with a shake-off satellite peak. The deconvoluted Pr $3d_{5/2}$ peaks at 933 eV and 935 eV correspond to $Pr^{3+}$and Pr^{4+}, respectively, while the satellite peak appears at 929 eV. Similarly, the deconvoluted Pr $3d_{3/2}$ peaks at 953 eV and 957 eV are assigned to Pr^{3+} and Pr^{4+}, respectively, with a satellite peak at 949 eV. The atomic ratio of Pr^{4+} to Pr^{3+} provides insights into the oxygen vacancies in the lattice. For SPTO 1 and SPTO 6, these ratios are 0.1696 and 0.1859, respectively, yielding average valence values for Pr atoms of 3.169 and 3.185. These values are significantly lower than the ideal valence of 3.66 for the dopant compound, indicating the presence of oxygen vacancies in the system.

The XPS spectrum of a doped STO reveals the presence of a Ti doublet originating from the spin-orbit splitting of the Ti 2p levels as shown in Fig. 3-11 (e) and (f). This doublet consists of the Ti $2p_{3/2}$ peak with a binding energy of around 458 eV and the Ti $2p_{1/2}$ peak with a binding energy of 464 eV. The additional peak corresponding to Ti $2p_{1/2}$ (Ti^{3+}) was identified around 459 eV. For the least doped sample $2p_{3/2}$ (Ti^{4+}) doublet peaks are obtained at 458.10 and 463.80 eV and for the heavily doped sample SPTO 6 the same was obtained at 457.78 and 463.48 eV respectively. A 0.32 eV shift in the peak position towards lower binding energies shows that Pr addition has an influence on electronic state of Ti. Some of the Ti ions are most likely replaced by Pr ions. As doping concentration increases from x=0.05 to x=0.20 in lattice, the area of Ti^{3+} peak increased by 19% and that of the peak Ti^{4+} decreased by 13%. Introduction of Pr dopant in lattice reduces the titanium cation partially from $Ti^{4+}$to Ti^{3+} in agreement with the defect chemistry of the rare earth dopants in $SrTiO_3$ [58,59].

The O1s spectrum of doped $SrTiO_3$ is shown in Fig. 3-11 (g) and (h), which is Gaussian fitted with two peaks. The first one at 529 eV was attributed to crystal lattice oxygen and the second one at 531 eV was correlated to non-lattice oxygen. With an increment in the dopant ion concentration from x=0.05 to x=0.20, the two peaks exhibit a slight shift, moving from 529.6 to 529 eV and 532 to 531.1 eV, respectively.

(a)

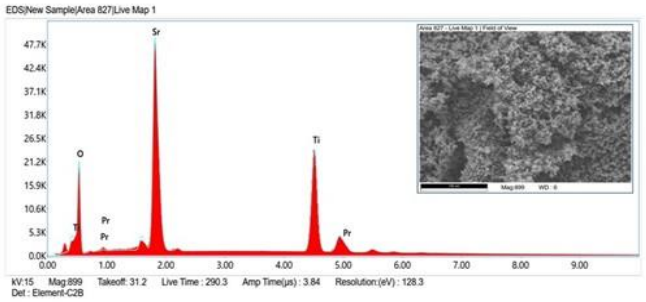

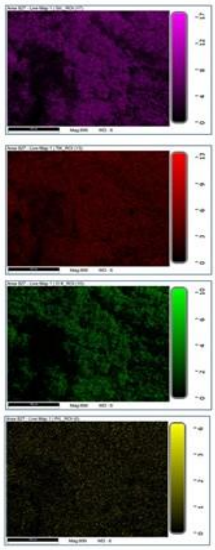

eZAF Quant Result - Analysis Uncertainty: 6.64 %								
Element	Weight %	MDL	Atomic %	Error %	Net Int.	R	A	F
O K	30.2	0.11	64.5	10.6	407.5	0.8300	0.0986	1.0000
Ti K	28.0	0.11	20.0	2.9	964.3	0.9097	0.9200	1.0298
Sr L	36.4	0.08	14.2	4.8	1348.7	0.8698	0.6753	1.0031
Pr L	5.3	0.46	1.3	9.5	54.9	0.9234	0.9088	1.0083

(b)

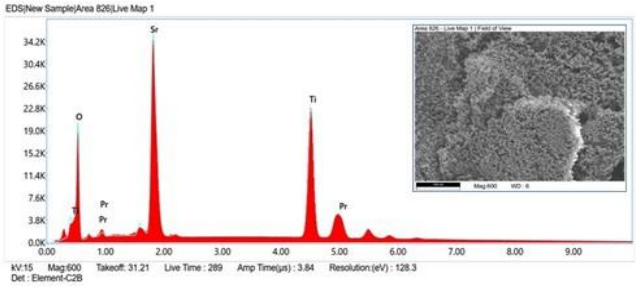

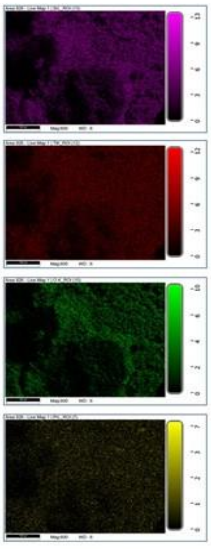

eZAF Quant Result - Analysis Uncertainty: 15.40 %								
Element	Weight %	MDL	Atomic %	Error %	Net Int.	R	A	F
O K	28.9	0.12	64.0	10.5	390.5	0.8226	0.1052	1.0000
Ti K	28.1	0.11	20.7	2.9	914.7	0.9042	0.9215	1.0376
Sr L	29.8	0.09	12.0	5.2	974.2	0.8631	0.6351	1.0032
Pr L	13.2	0.5	3.3	5.1	128.9	0.9185	0.9089	1.0084

Figure 3- 12 EDS spectra and elemental mapping of **(a)** SPTO 1 and (**b)** SPTO 6.

Concurrently, the introduction of doping leads to an increment in the area by non-lattice oxygen, culminating in 31.09 % prevalence of oxygen vacancies in SPTO 6, as opposed to the 14.09 % observed in SPTO 1. The rise in the region of non-lattice oxygen implies the creation of lattice oxygen vacancies. This finding is corroborating the Ti 2p XPS spectrum.

The EDS spectra of the least doped sample SPTO 1 and heavily doped sample SPTO 6 were recorded and are shown in Fig. 3-12 with the corresponding elemental color mapping. The EDS data show that the element peaks corresponding to Sr, Ti, O and Pr make up the samples with increased Pr, and reduced Sr concentration in heavily doped SPTO 6. Bright contrast regions in element mapping coincide with signals of Sr, Ti, O, and Pr.

3.3.3 Morphological studies- FE-SEM

High-resolution FE-SEM micrographs of Pr-doped $SrTiO_3$ ceramics, both before and after the burial sintering process, are presented in Fig. 3-13.

Hard-agglomerated grains were observed in all samples, which were porous and exhibited micro pebble-shaped grains. After burial sintering, the grains became interconnected, growing significantly to sizes between 1–2 μm. This growth is attributed to the thermal energy released during high-temperature sintering, which influences the mass transport mechanism and promotes grain neck growth. In samples before burial sintering, both trans-granular and intergranular fractures are visible. However, after burial sintering, intergranular features dominate, with a significant reduction in trans-granular fractures. Exact cubic granules are not observed; instead, truncated rhombic dodecahedron shapes with {100} facets and hexagonal {110} facets appear in samples with low Pr content. As the Pr content increases, the samples become less compact, resulting in grains with nonuniform features [60]

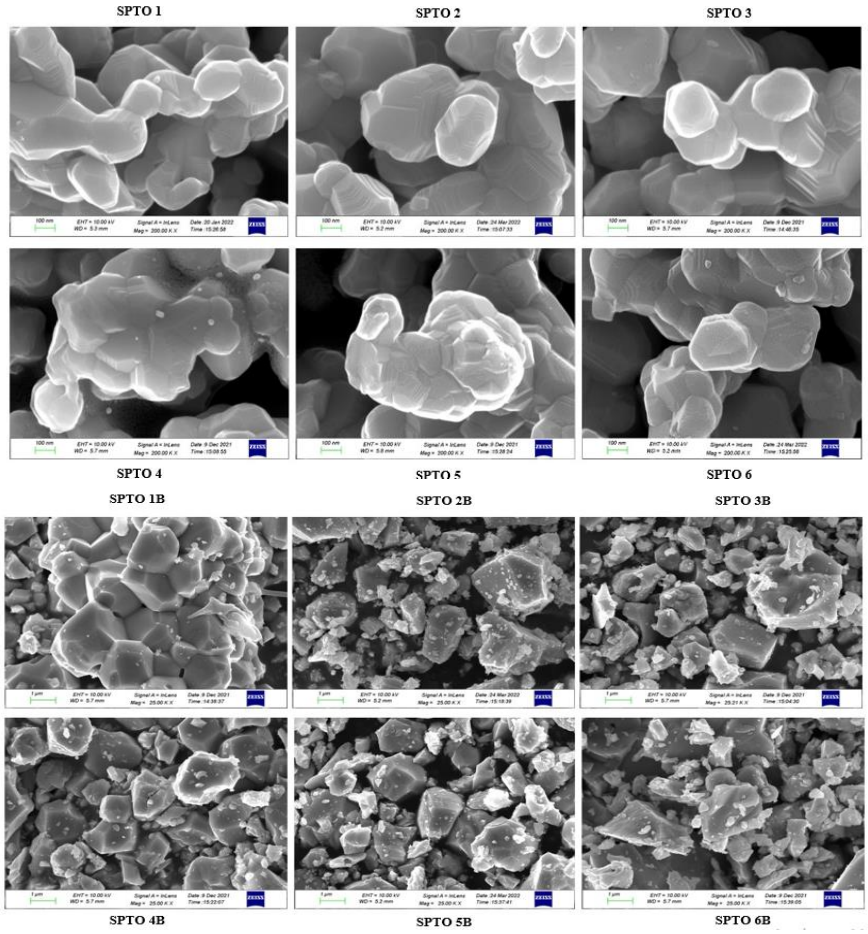

Figure 3- 14 FE-SEM images of Pr substituted $SrTiO_3$ samples before and after burial sintering.

3.3.4 Optical and photoluminescence characterization

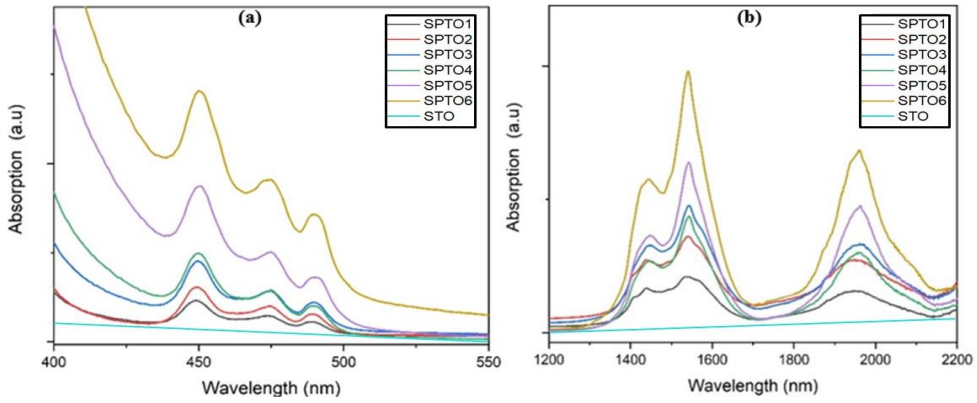

Figure 3- 13 (a) Absorption bands of Pr substituted $SrTiO_3$ in visible region **(b)** in IR region before burial sintering.

The optical properties of the pristine $SrTiO_3$ and Pr doped $SrTiO_3$ before and after burial sintering are investigated by UV-Vis-NIR diffused reflection spectra. The absorption bands of Pr-substituted $SrTiO_3$ in the visible and IR regions before burial sintering are shown in Fig. 3-14, with the corresponding absorption edge represented in Fig. 3-15. The absorption characteristics of pure and doped $SrTiO_3$ indicate a slight variation, as the valence-to-conduction band edge shifts from 388 nm in the least doped sample (x=0.05) to 400 nm in the heavily doped sample (x=0.2). The Tauc plot of photon energy hν versus $(\alpha h\nu)^{1/2}$ for indirect allowed transitions in STO-based semiconductors, shown in Fig. 3-15(b), was used to determine the band gap energy. The band gap of the doped samples decreases from 3.20 eV to 3.11 eV with increasing Pr content. This reduction in the band gap aligns with the reduction in crystallite size observed in the XRD analysis.

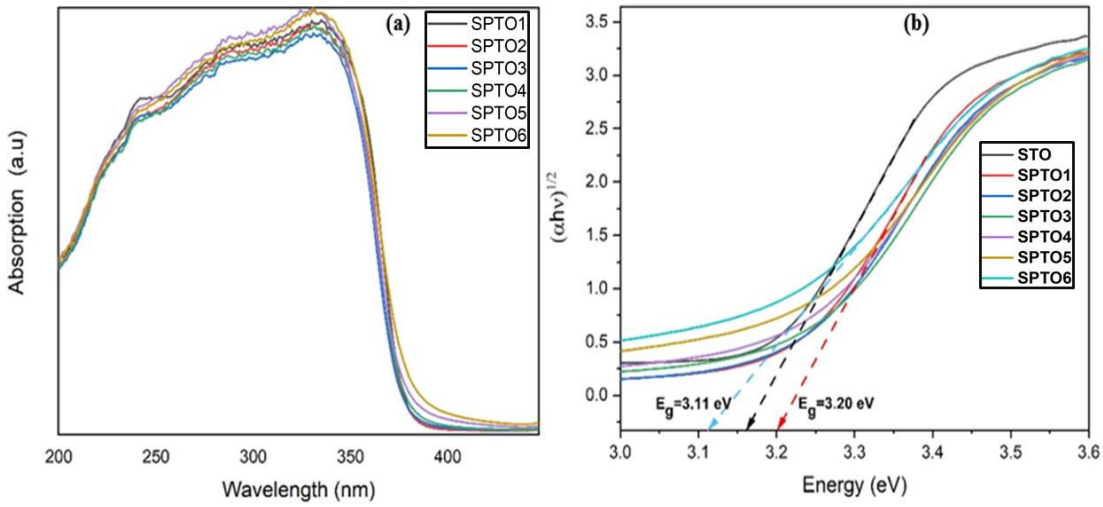

Figure 3- 15 (a) Absorption edge of Pr substituted $SrTiO_3$ **(b)** Tauc plot before burial sintering.

Additionally, a weak absorption tail (Urbach tail) is observed in the visible-light region for all Pr-doped samples, attributed to the formation of mid-gap states caused by the Pr dopant [61,62]. The Urbach tail edges gradually redshift to longer wavelengths with increasing concentrations of dopant. All doped samples indicate eight absorption

peaks corresponding to the transitions from the $^3H_4$ ground state to the various excited states of Pr^{3+} ions. Absorption in the visible region involves peaks at 442 nm, 474 nm, 488 nm, and 600 nm, which correspond to transitions from the ground state to $^3P_2$, $^3P_1$, $^3P_0$, and $^1D_2$. The presence of three distinct absorption bands on the high-energy side (<500 nm) suggests that the sample has favorable UV transmission properties, allowing for a wider range of excitation sources. Absorption at the IR region is centered on 1002 nm, 1442 nm, 1540 nm, and 1960 nm, corresponding to transitions to $^1G_4$, $^3F_4$, $^3F_3$, and $^3F_2$ [63,64]. Absorption peaks corresponding to $^3H_4 \rightarrow {}^3F_4$ and $^3H_4 \rightarrow {}^3F_3$ transitions are found to be fused into one band for lower Pr levels, but it is clear for higher Pr doping concentrations. Among the absorption bands, $^3H_4 \rightarrow {}^3P_2$ and $^3H_4 \rightarrow {}^3F_3$ transitions are found to be more intense because of the change in the local environment around the Pr^{3+} ions and are called hypersensitive transitions (HSTs). These absorption peaks become more intense, indicating increased absorption with Pr content.

The optical absorption coefficient α is related to incident photon energy as in eqn (3.4) [65].

$$\alpha = \alpha_0 \exp\left[\frac{E - E_g}{E_U}\right] \tag{3.4}$$

Where $E = h\nu$ is the incident photon energy, E_g is the optical band gap energy at a specific temperature T, α_0 is a material-dependent coefficient, and the quantity E_U is known as Urbach energy. The optical absorption α has been calculated by converting the diffuse reflectance spectroscopy (DRS) data into the respective absorption spectra by using the Kubelka–Munk relation indicated in eqn (3.5)[66,67].

$$F(R_\infty) = \frac{(1 - R_\infty)^2}{2R_\infty} \tag{3.5}$$

Where $F(R_\infty)$ is the Kubelka–Munk function; $(R_\infty) = R_{sample}/R_{Standard}$, R_{sample} is the diffuse reflectance of the sample, and $R_{standard}$ is that of a standard sample.

Since $F(R_\infty)$ is proportional to the absorption coefficient α, the logarithm of $F(R_\infty)$ can be considered to represent *ln (α)*, and therefore, by rewriting the above equations, we get equation (3.6).

$$\ln \alpha = \ln \alpha_0 + \frac{h\nu - E_g}{E_U} \tag{3.6}$$

The Urbach energy for the Pr-doped series was systematically calculated, as depicted in Fig. 3-16. For the least doped sample (SPTO 1), the Urbach energy is approximately 0.112 eV, which progressively increases with Pr substitution, reaching a maximum value of 0.245 eV at 20% Pr doping. Since all experiments were conducted at room temperature, the thermal contribution to E_U remains constant. Pr substitution at the Sr site introduces both electrical and structural disturbances within the system. These disturbances arise from the disparity in ionic radii between $Pr^{3+}$and Sr^{2+}, as well as the random distribution of Pr ions in the lattice. Such factors lead to potential fluctuations, creating electronic disorder and introducing additional energy levels near the valence band (VB) and conduction band (CB). These effects become more pronounced with increasing Pr concentration. The calculated values of the band gap and Urbach energy for the series of samples are summarized in Table 3-7. A linear relationship is observed between the indirect optical energy gap and the band tail width (Urbach energy), correlating with the ratio of Pr concentration in the matrix.

Table 3- 7 Band gap and Urbach energy of $Sr_{1-x}Pr_xTiO_3$ system

Sample label	**Band gap, E_g (eV)**	**Urbach energy, E_U (eV)**
SPTO 1	3.20	0.112
SPTO 2	3.18	0.123
SPTO 3	3.17	0.145
SPTO 4	3.15	0.164
SPTO 5	3.13	0.219
SPTO 6	3.11	0.245

Burial-sintered samples exhibit significant variations compared to their parent compounds, with a broad absorption spectrum, as shown in Fig. 3-17. The absorption wavelength range can be adjusted based on the Pr content in the samples. For the least doped sample (SPTO 1B), absorption begins in the visible region at 560 nm and extends into the mid-IR range. In contrast, for the heavily doped sample (SPTO 6B), absorption starts at 545 nm and extends up to 2450 nm, demonstrating a blue shift with increased Pr content. The increased oxygen vacancies and changes in the oxidation state of Ti lead to

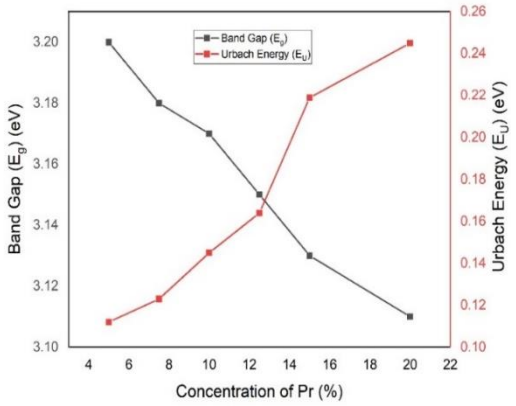

Figure 3- 16 Variation of Urbach energy and band gap with Pr Concentration.

a considerable reduction in the band gap, from 2.80 eV x=0.05 (SPTO 1B) to 1.80 eV for x=0.2 (SPTO 6B). While defect-free STO surfaces exhibit no absorption in the sub-bandgap range (≤ 3.2 eV) the burial-sintered samples display absorption in the sub-bandgap range of 2.7 to 3.1 eV. This observation aligns with findings by Rice et al. and Xie et al., confirming that optical absorption occurs in mid-gap states [68,69]. Apart from these broad IR absorption peaks, all samples indicate an absorption peak near 510 nm (2.43 eV). Its origin may be due to the excitation of an electron trapped at an oxygen vacancy, i.e., an F center. F centers have been reported in $SrTiO_3$ and $BaTiO_3$ [69,70]. The absorption of infrared light is caused by free carriers, which is directly proportional to the concentration of oxygen vacancy and varies with wavelength as λ^n. The absorption band at 2.4 eV is because of a transition from the narrow impurity-type band to the

conduction band. This is formed by oxygen vacancies in the reduced system in the band gap.

All burial-sintered samples, regardless of doping percentage, exhibit a prominent Urbach tail, contributing to sub-bandgap absorption. This tail indicates the presence of structural disorders or defects, such as oxygen vacancies. Compared to pristine materials, oxygen vacancies in $ABO_{3-\delta}$ compounds enhance optical absorption in the visible to near-infrared wavelength region, thereby lowering the onset energy of absorption. Additional absorption peaks between 500 and 2000 nm are attributed to oxygen vacancies, resulting from electron transitions from the occupied defect state energy levels to the conduction band edge.This observation aligns with previous studies, which attribute the spectral tailing to the presence of oxygen vacancies and defects, particularly in the TiO_2 structure. The existence of the Urbach tail in reduced samples further confirms that the reduction process alters the surface structure, creating materials with a high density of defects [71–74].

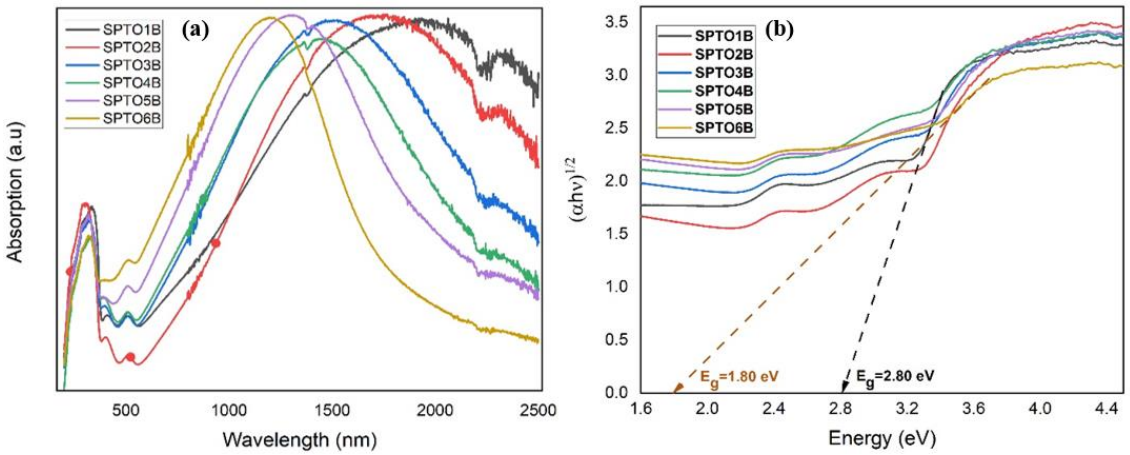

Figure 3- 17 (a) Absorption spectra and **(b)** calculated bandgap of burial sintered $Sr_{1-x}Pr_xTiO_3$ system.

At room temperature, PL measurements were done in order to analyze the electronic transitions and the type of defects in the sample. PL spectra of the $Sr_{1-x}Pr_xTiO_3$ system

were measured under UV excitation of 380 nm and are shown in Fig 3-18 (a). $SrTiO_3$ in its pure form is one of the materials having the lowest emission intensity [75]. When there is Pr^{3+} impurity in a $SrTiO_3$ crystal, Pr^{3+} substitutes Sr^{2+} to form positively charged impurity defect centers, which can suppress the intra-4f electron transitions from $1D^2 \rightarrow 3H^4$ of Pr^{3+} ions. During the sample preparation process, it will generate oxygen vacancies O^{2-} that will be neutralized by the positive charge provided by defect centers. The amount of Ti^{4+} vacancies or Sr^{2+} that may be formed by O^{2-} oxygen vacancies is negligible, therefore the excess positive charge compensation mechanism induced by Pr^{3+} is predominantly compensated by O^{2-} oxygen vacancies; the effect is subtle. Due of these factors, $SrTiO_3$:Pr^{3+} materials have low luminous intensity. One strategy to overcome this is co-doping with ions like Al^{3+} or Mg^{2+}, but that also favors the red emission. But here we adopted heavy Pr doping as a technique to increase PL intensity and that too in blue region 426-430 nm.

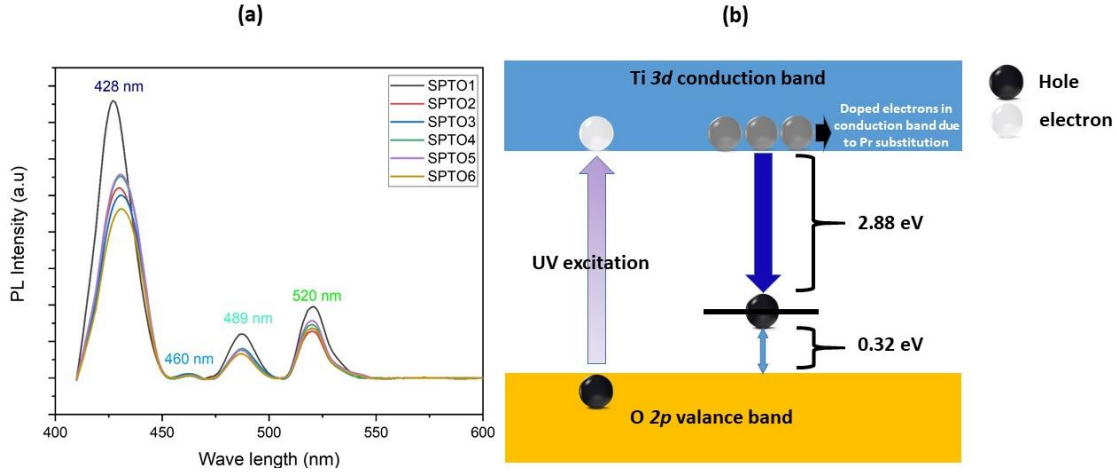

Figure 3- 18 (a) PL emission spectra of the $Sr_{1-x}Pr_xTiO_3$ system under UV excitation of 380 nm **(b)** Band level diagram corresponding to PL emission.

There are previous reports describing about the PL quenching effect in Pr doped $SrTiO_3$. Intensity of PL emission were reported to exhibit abruptly decrease when the Pr^{3+} doping concentration exceeds 0.2%. Previous research suggested that the occurrence of a concentration-quenching effect was likely the cause of the inflection point. The energy transfer between Pr^{3+} ions is the primary cause of the concentration-quenching

effect. The chance of energy transfer between Pr^{3+} rises as the content of Pr^{3+} rises, reducing the distance between Pr^{3+}. Finally, energy transfer among Pr^{3+} results in an increase in energy loss, which results in a reduction in Pr^{3+} transition energy. As a result, when the Pr^{3+} concentration rises beyond a limit, the PL intensity decrease [76,77]. So we deliberately increased the concentration of Pr to quench the emission and at the same time the excess electrons and defect should play a vital role in STO PL emission. The associated band structure is depicted in Fig 3-18 (b).

Photoluminescence peak at 460 nm agrees well with the wavelength of light emitted from Ar^{+} bombarded $SrTiO_3$ and pure STO arising as a result of oxygen vacancies generated during synthesis [29]. Peaks around 460 nm and 520 nm can correspond to trapped charges and oxygen vacancy. Which stems from complex cluster $[TiO_5 \cdot V_0^z]$ and $[SrO_{11} \cdot V_0^z]$, where $V_0^z = V_0^x, V_0^{\cdot}, V_0^{\cdot\cdot}]$ are vacancies identified in disordered $SrTiO_3$. $V_0^x, V_0^{\cdot}, V_0^{\cdot\cdot}$ indicates neutral oxygen vacancy, singly ionized oxygen vacancy and doubly ionized oxygen vacancy respectively. Energy gap are decreased by localized states produced in the band gap. The gap energy increases with the structural order. These observations demonstrate that PL is directly related to the localized states that occur in the band gap and that these localized states are affected by the degree of order-disorder in the lattice. The green emissions reported here is ascribed to shallow defects. The $[TiO_5 \cdot V_0^{\cdot}]$ and $[SrO_{11} \cdot V_0^{\cdot}]$, complex clusters are connected to shallow defects in the band gap and lead to a more energetic PL emission in blue-green region. The presence of oxygen vacancy sites facilitates the trapping of charge carriers, thereby causing a reduction in the recombination of electron-hole pairs. An increase in the concentration of oxygen vacancies corresponds to reduced intensity. As SPTO 6 exhibits a greater abundance of oxygen vacancies compared to SPTO1, the diminished recombination of charge carriers contributes to a reduction in the intensity of photoluminescence spectra, supporting the findings derived from XPS analysis.

A distinct emission peak centered at 430 nm (2.9 eV) was observed, with the peak position shifting slightly depending on the doping concentration. For the least doped

sample (SPTO 1), the peak is at 426 nm, while for all other samples, it remains centered at 430 nm indicating a redshift. The spectral patterns and peak positions closely resemble those of the room-temperature blue light emission observed in oxygen-deficient (STO) following Ar^+ radiation. This intense blue light emission is strongly associated with metallic conduction, which arises from oxygen vacancies and electron doping in STO. These results strongly suggest that the luminescence mechanism in oxygen-deficient metallic STO and Pr-doped STO are identical. The cation substitutions and oxygen vacancies introduce extra electron carriers into the vacant Ti 3*d* conduction bands. These doped electrons recombine with holes in the in-gap states, resulting in blue light emission. However, this blue photoluminescence (PL) is not due to straightforward band-to-band recombination of free electrons and holes, but rather originates from recombination processes involving doped electrons and in-gap hole states [27]. Blue-luminescence intensity is high for low doping concentration and found to decrease for heavy doping, x=.075 onwards and is consistent with behavior of Pr doped STO. Except SPTO 1 all samples of prepared $SrTiO_3$ show nearly equal intensity suggesting a saturation for Pr substitution effect.

The green emission at 489 nm was ascribed to Pr^{3+} - $^3P_0$ to $^3H_4$ emission [30]. It's important to note that neither the green band's location nor its center at 489 nm changes. This phenomena is explained by emission spectrum of Pr^{3+} in STO ceramics being sensitive to local environment. Following polarization, the local electric field surrounding the Pr^{3+} site will manifest itself and align along the direction of the external electric field. As a result, the change in the local electric field would affect the crystallographic field of the Pr^{3+} ions. Therefore, the polarization of the ceramics promotes the formation of peak around 430 nm.

Table 3- 8 The CIE chromaticity coordinates, and color purity of Pr doped $SrTiO_3$.

Sample label	CIE $_x$	CIE $_y$	Correlated color temperature (CCT)-K
SPTO 1	0.1550	0.1054	3202
SPTO 2	0.1572	0.0881	2266
SPTO 3	0.1565	0.0925	2444
SPTO 4	0.1569	0.0864	2216
SPTO 5	0.1571	0.0942	2503
SPTO 6	0.1565	0.0956	2581

The CIE chromaticity coordinates are necessary to evaluate the luminescence properties of phosphors. Fig. 3-19 depicts the CIE chromaticity diagram of Pr doped $SrTiO_3$ crystallites. Table.3-8 includes the CIE parameters correlated color temperature

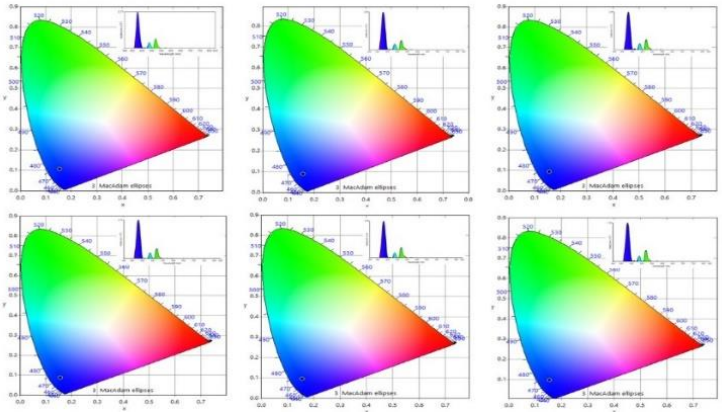

Figure 3- 19 CIE chromaticity diagram and chromaticity coordinates (x, y) of emission from as-grown $Sr_{1-x}Pr_xTiO_3$ samples under UV excitation of 380 nm.

(CCT), and color coordinates, according to the PL spectra, with different Pr concentrations. The sample SPTO 1 is found to exhibit the strongest narrow band emission with FWHM 19.3 nm. Its calculated chromaticity coordinates are (0.1550, 0.1054) and its correlated color temperature (CCT) is 3202 K. The sample SPTO 2 with FWHM of 23.1 nm is having coordinates (0.1572, 0.0881) close to the standard deep blue emission. All other samples shows the CIE_y coordinate less than 0.1 which is a highly desirable parameter.

3.4 Conclusions

Pr atoms were successfully doped into the Sr^{2+} site of the $SrTiO_3$ matrix, with defects and oxygen vacancies introduced using the burial sintering method under a strongly reducing environment. The breakdown of cubic symmetry with Pr doping was confirmed through the asymmetric nature of the (310) peak in XRD analysis and the emergence of Eg and B_{1g} modes in the Raman spectrum. These findings collectively indicate the cubic-to-tetragonal symmetry transformation of the $Sr_{1-x}Pr_xTiO_3$ system for $x \geq 0.1$. The formation of ferroelectric micro-regions, Fano resonance of LO_4 peaks, and forbidden bands in the Raman spectra highlight increasing disorder in the system. Optical studies in the UV-Vis-NIR range revealed a decrease in the band gap from 3.20 eV to 3.11 eV with Pr doping. High infrared absorption and a significant band gap reduction from 2.80 eV to 1.80 eV were achieved due to defects introduced by doping and oxygen vacancies created during burial sintering. Pr doping also affected mid-infrared absorption, making the material adaptable for specific absorption ranges and suitable for mid- to far-infrared sensing applications. Additionally, red photoluminescence (PL) emission from Pr ions was systematically quenched by excess electron doping, tuning the emission characteristics to intense blue light. The material exhibited intense, narrow-band blue emission with full-width at half-maximum (FWHM) in the range of 19–23 nm and CIE_y values below 0.1, validated for display applications. Narrow-band emission enhances the material's color gamut, making it a promising candidate for LED device applications. These properties demonstrate the versatility of Pr-doped $SrTiO_3$ for advanced optoelectronic and sensing applications.

References:

[1] A. Baki, J. Stöver, T. Schulz, T. Markurt, H. Amari, C. Richter, J. Martin, K. Irmscher, M. Albrecht, J. Schwarzkopf, Influence of Sr deficiency on structural and electrical properties of $SrTiO_3$ thin films grown by metal–organic vapor phase epitaxy, Sci Rep 11 (2021) 7497. https://doi.org/10.1038/s41598-021-87007-2.

[2] V. Železný, D. Chvostová, L. Pajasová, M. Jelínek, T. Kocourek, S. Daniš, V. Valvoda, Temperature dependence of the optical properties of $Ba_{0.7}5Sr_{0.25}TiO_3$ thin films, Thin Solid Films 571 (2014) 416–419. https://doi.org/10.1016/j.tsf.2013.11.147.

[3] T.H. Chiang, H. Lyu, T. Hisatomi, Y. Goto, T. Takata, M. Katayama, T. Minegishi, K. Domen, Efficient Photocatalytic Water Splitting Using Al-Doped $SrTiO_3$ Coloaded with Molybdenum Oxide and Rhodium–Chromium Oxide, ACS Catal 8 (2018) 2782–2788. https://doi.org/10.1021/acscatal.7b04264.

[4] P.K. Jamshina Sanam, M. Shah, P.P. Pradyumnan, The enhancement of NIR transparency due to annealing and Mg-doping in $CuCrO_2$ thin films, Mater Lett 330 (2023) 133295. https://doi.org/10.1016/j.matlet.2022.133295.

[5] P.K. Jamshina Sanam, M. Shah, P.P. Pradyumnan, Structure induced modification on thermoelectric and optical properties by Mg doping in $CuCrO_2$ nanocrystals, Solid State Commun 353 (2022) 114855. https://doi.org/10.1016/j.ssc.2022.114855.

[6] P.K.J. Sanam, M. Shah, P.P. Pradyumnan, Raman spectroscopic investigation and thermoelectric studies of defect-induced Mg-doped delafossite thin film, Journal of Materials Science: Materials in Electronics (2022). https://doi.org/10.1007/s10854-022-09013-y.

[7] P.K. Jamshina Sanam, M. Shah, P.P. Pradyumnan, Structure induced modification on thermoelectric and optical properties by Mg doping in $CuCrO_2$ nanocrystals, Solid State Commun 353 (2022) 114855. https://doi.org/10.1016/J.SSC.2022.114855.

[8] M. Shah, Et.al, Magneto thermoelectric effect of nickel thin film synthesized by RF magnetron sputtering, Physica E Low Dimens Syst Nanostruct 147 (2023) 115591. https://doi.org/10.1016/j.physe.2022.115591.

[9] PhysRevB.70.214109, (n.d.).

[10] Z. Li, H. Sun, Z. Xie, Y. Zhao, M. Lu, Modulation of the photoluminescence of $SrTiO_3$(001) by means of fluorhydric acid etching combined with Ar^+ ion bombardment, Nanotechnology 18 (2007) 165703. https://doi.org/10.1088/0957-4484/18/16/165703.

[11] A. Savoia, D. Paparo, P. Perna, Z. Ristic, M. Salluzzo, F. Miletto Granozio, U. Scotti di Uccio, C. Richter, S. Thiel, J. Mannhart, L. Marrucci, Polar catastrophe and electronic reconstructions at the $LaTiO_3/SrTiO_3$ interface: Evidence from optical second harmonic generation, Phys Rev B 80 (2009) 75110. https://doi.org/10.1103/PhysRevB.80.075110.

[12] T. Kanagaraj, S. Thiripuranthagan, Photocatalytic activities of novel $SrTiO_3$ – BiOBr heterojunction catalysts towards the degradation of reactive dyes, Appl Catal B 207 (2017) 218–232. https://doi.org/10.1016/j.apcatb.2017.01.084.

[13] M. Shah, P.K. Jamshina Sanam, P.P. Pradyumnan, Defect-induced $Sr_{1-x}Pr_xTiO_3$ crystallites by burial sintering and its optoelectronic applications, Journal of Physics and Chemistry of Solids 181 (2023) 111516. https://doi.org/10.1016/j.jpcs.2023.111516.

[14] J.S. P.K., M. Shah, P.P. Pradyumnan, Tailoring structure and nanoscale surface topography in Mg–N doped $CuCrO_2$ thin films via post deposition annealing for optothermoelectric application, Opt Mater (Amst) 147 (2024) 114703. https://doi.org/10.1016/j.optmat.2023.114703.

[15] J.S. P.K., M. Shah, P.P. Pradyumnan, Intense narrow band blue emission in CuCrO2 delafossite by Ni^{2+}-Mg^{2+} dual cation doping, Spectrochim Acta A Mol Biomol Spectrosc 305 (2024) 123442. https://doi.org/10.1016/j.saa.2023.123442.

[16] J.S. P.K., M. Shah, P.P. Pradyumnan, Magnetoelectric coupling and thermoelectric behaviors in Ni-doped $CuCrO_2$ crystallites, Chemical Engineering Journal 476 (2023) 146568. https://doi.org/10.1016/j.cej.2023.146568.

[17] D Keroack, Y Lepine, J L Brebner, Drift mobility measurements of small-polaron transport in $SrTiO_3$, Journal of Physics C: Solid State Physics 17 (1984) 833. https://doi.org/10.1088/0022-3719/17/5/013.

[18] X. Ma, Z. Wu, E.J. Roberts, R. Han, G. Rao, Z. Zhao, M. Lamoth, X. Cui, R.D. Britt, F.E. Osterloh, Surface Photovoltage Spectroscopy Observes Sub-Band-Gap Defects in Hydrothermally Synthesized $SrTiO_3$ Nanocrystals, The Journal of Physical Chemistry C 123 (2019) 25081–25090. https://doi.org/10.1021/acs.jpcc.9b06727.

[19] L. Yang, J. Huang, L. Shi, L. Cao, W. Zhou, K. Chang, X. Meng, G. Liu, Y. Jie, J. Ye, Efficient hydrogen evolution over Sb doped SnO_2 photocatalyst sensitized by Eosin Y under visible light irradiation, Nano Energy 36 (2017) 331–340. https://doi.org/10.1016/j.nanoen.2017.04.039.

[20] E. Zhou, J.-M. Raulot, H. Xu, H. Hao, Z. Shen, H. Liu, Structural, electronic, and optical properties of rare-earth-doped $SrTiO_3$ perovskite: A first-principles study, Physica B Condens Matter 643 (2022) 414160. https://doi.org/10.1016/j.physb.2022.414160.

[21] Y. Yu, Z. Lu, Q. Guo, J. Yu, Y. Li, X. Zhang, Y. Cheng, Y. Yao, H. Liu, Enhanced solar-light-driven photocatalytic performance by the synergistic effects of F− doped and Ag loaded $SrTiO_3$ cubic nanoparticles, Chem Phys Lett 692 (2018) 94–101. https://doi.org/10.1016/j.cplett.2017.12.001.

[22] D. Zhou, P. Zhai, G. Hu, J. Yang, Upconversion luminescence and enhanced photocatalytic hydrogen production for Er^{3+} doped $SrTiO_3$ nanopaeticles, Chem Phys Lett 711 (2018) 77–80. https://doi.org/10.1016/j.cplett.2018.09.024.

[23] D. Yang, X. Zhao, X. Zou, Z. Zhou, Z. Jiang, Removing Cr (VI) in water via visible-light photocatalytic reduction over Cr-doped $SrTiO_3$ nanoplates, Chemosphere 215 (2019) 586–595. https://doi.org/10.1016/j.chemosphere.2018.10.068.

[24] Y. Bi, M.F. Ehsan, Y. Huang, J. Jin, T. He, Synthesis of Cr-doped $SrTiO_3$ photocatalyst and its application in visible-light-driven transformation of CO_2 into CH_4, Journal of CO_2 Utilization 12 (2015) 43–48. https://doi.org/10.1016/j.jcou.2015.10.004.

[25] M.L. Crespillo, J.T. Graham, F. Agulló-López, Y. Zhang, W.J. Weber, Non-radiative luminescence decay with self-trapped hole migration in strontium titanate: Interplay between optical and transport properties, Appl Mater Today 23 (2021) 101041. https://doi.org/10.1016/j.apmt.2021.101041.

[26] K.-H. Yang, T.-Y. Chen, N.-J. Ho, H.-Y. Lu, In-Gap States in Wide-Band-Gap $SrTiO_3$ Analyzed by Cathodoluminescence, Journal of the American Ceramic Society 94 (2011) 1811–1816. https://doi.org/10.1111/j.1551-2916.2010.04324.x.

[27] A. Rubano, D. Paparo, F.M. Granozio, U. Scotti di Uccio, L. Marrucci, Blue luminescence of $SrTiO_3$ under intense optical excitation, J Appl Phys 106 (2009) 103515. https://doi.org/10.1063/1.3256140.

[28] Y. Yamada, H. Yasuda, T. Tayagaki, Y. Kanemitsu, Temperature Dependence of Photoluminescence Spectra of Nondoped and Electron-Doped $SrTiO_3$:Crossover from Auger Recombination to Single-Carrier Trapping, Phys Rev Lett 102 (2009) 247401. https://doi.org/10.1103/PhysRevLett.102.247401.

[29] A. Kalabukhov, R. Gunnarsson, J. Börjesson, E. Olsson, T. Claeson, D. Winkler, The role of oxygen vacancies in SrTiO3 at the $LaAlO_3/SrTiO_3$ interface, (2006).

[30] J. Zhang, Y. Hao, M. Bi, G. Dong, X. Liu, K. Bi, Outstanding Photoluminescence in $Pr^{(3+)}$-Doped Perovskite Ceramics., Micromachines (Basel) 9 (2018). https://doi.org/10.3390/mi9090419.

[31] M.L. Crespillo, J.T. Graham, F. Agulló-López, Y. Zhang, W.J. Weber, Recent Advances on Carrier and Exciton Self-Trapping in Strontium Titanate: Understanding the Luminescence Emissions, Crystals (Basel) 9 (2019). https://doi.org/10.3390/cryst9020095.

[32] T. Hasegawa, M. Shirai, K. Tanaka, Localizing nature of photo-excited states in $SrTiO_3$, J Lumin 87–89 (2000) 1217–1219. https://doi.org/10.1016/S0022-2313(99)00520-7.

[33] Y. Yamada, Y. Kanemitsu, Band-to-band photoluminescence in $SrTiO_3$, Phys Rev B 82 (2010) 121103. https://doi.org/10.1103/PhysRevB.82.121103.

[34] D. Kan, T. Terashima, R. Kanda, A. Masuno, K. Tanaka, S. Chu, H. Kan, A. Ishizumi, Y. Kanemitsu, Y. Shimakawa, M. Takano, Blue-light emission at room temperature from Ar+-irradiated $SrTiO_3$, Nat Mater 4 (2005) 816–819. https://doi.org/10.1038/nmat1498.

[35] D. Guo, X. Zhang, J. Yun, Preparation of Compensation Ions Codoped $SrTiO_3:Pr^{3+}$ Red Phosphor with the Sol-Gel Method and Study of Its Luminescence Enhancement Mechanism, Adv Optoelectron 2014 (2014) 674780. https://doi.org/10.1155/2014/674780.

[36] Y. Yao, Z. Wang, L. Cao, M. Zheng, X. Wang, M. Zhang, J. Cui, Z. Yang, W. Ding, P. Li, Achievement of narrow-band blue-emitting phosphors $KScSr_{1-y}Ca_ySi_2O_7:Bi^{3+}$ by the

migration of luminescence centers, RSC Adv 11 (2021) 12568–12577. https://doi.org/10.1039/D1RA01375K.

[37] H. Zou, D. Peng, G. Wu, X. Wang, D. Bao, J. Li, Y. Li, X. Yao, Polarization-induced enhancement of photoluminescence in Pr^{3+} doped ferroelectric diphase $BaTiO_3$-$CaTiO_3$ ceramics, J Appl Phys 114 (2013) 73103. https://doi.org/10.1063/1.4818793.

[38] H. Tan, Z. Zhao, W. Zhu, E.N. Coker, B. Li, M. Zheng, W. Yu, H. Fan, Z. Sun, Oxygen Vacancy Enhanced Photocatalytic Activity of Pervoskite $SrTiO_3$, ACS Appl Mater Interfaces 6 (2014) 19184–19190. https://doi.org/10.1021/am5051907.

[39] R.D. Shannon, Revised effective ionic radii and systematic studies of interatomic distances in halides and chalcogenides, Acta Crystallographica Section A 32 (1976) 751–767. https://doi.org/10.1107/S0567739476001551.

[40] R. Garg, A. Senyshyn, H. Boysen, R. Ranjan, Structure of the noncubic phase in the ferroelectric state of Pr-substituted $SrTiO_3$, Phys Rev B 79 (2009) 144122. https://doi.org/10.1103/PhysRevB.79.144122.

[41] S. Checchia, M. Allieta, M. Coduri, M. Brunelli, M. Scavini, Relaxor ferroeletric behavior in $Sr_{1-x}Pr_xTiO_3$ Cooperation between polar and antiferrodistortive instabilities, Phys Rev B 94 (2016) 104201. https://doi.org/10.1103/PhysRevB.94.104201.

[42] S. Shirasaki, H. Yamamura, H. Haneda, K. Kakegawa, J. Moori, Defect structure and oxygen diffusion in undoped and La-doped polycrystalline barium titanate, J Chem Phys 73 (1980) 4640–4645. https://doi.org/10.1063/1.440654.

[43] K.M. Batoo, R. Verma, A. Chauhan, R. Kumar, M. Hadi, O.M. Aldossary, Y. Al-Douri, Improved room temperature dielectric properties of Gd^{3+} and Nb^{5+} co-doped Barium Titanate ceramics, J Alloys Compd 883 (2021) 160836. https://doi.org/10.1016/j.jallcom.2021.160836.

[44] J.A. Dawson, X. Li, C.L. Freeman, J.H. Harding, D.C. Sinclair, The application of a new potential model to the rare-earth doping of $SrTiO_3$ and $CaTiO_3$, J. Mater. Chem. C 1 (2013) 1574–1582. https://doi.org/10.1039/C2TC00475E.

[45] R. Ranjan, R. Garg, R. Hackl, A. Senyshyn, E. Schmidbauer, D. Trots, H. Boysen, Onset of spontaneous electrostrictive strain below 520 K in Pr-doped $SrTiO_3$, Phys Rev B 78 (2008) 92102. https://doi.org/10.1103/PhysRevB.78.092102.

[46] J.A. Dawson, I. Tanaka, Local Structure and Energetics of Pr- and La-Doped $SrTiO_3$ Grain Boundaries and the Influence on Core–Shell Structure Formation, The Journal of Physical Chemistry C 118 (2014) 25765–25778. https://doi.org/10.1021/jp508444k.

[47] M. Lv, R. Wang, L. Wei, G. Yu, T. Lin, N. Dai, J. Chu, David.J. Lockwood, Strained HgTe plates grown on $SrTiO_3$ investigated by micro-Raman mapping, J Appl Phys 120 (2016) 115304. https://doi.org/10.1063/1.4962852.

[48] Y. Watanabe, Ferroelectricity of stress-free and strained pure $SrTiO_3$ revealed by ab initio calculations with hybrid and density functionals, Phys Rev B 99 (2019) 64107. https://doi.org/10.1103/PhysRevB.99.064107.

[49] S.K. Mishra, R. Ranjan, D. Pandey, R. Ouillon, J.-P. Pinan-Lucarre, P. Ranson, Ph. Pruzan, A Raman scattering study of the antiferroelectric phase transition in $Sr_{0.70}Ca_{0.30})TiO_3$ Phys Rev B 64 (2001) 92302. https://doi.org/10.1103/PhysRevB.64.092302.

[50] C.H. Perry, J.H. Fertel, T.F. McNelly, Temperature Dependence of the Raman Spectrum of $SrTiO_3$ and $KTaO_3$, J Chem Phys 47 (1967) 1619–1625. https://doi.org/10.1063/1.1712142.

[51] U. Balachandran, N.G. Eror, On the defect structure of strontium titanate with excess SrO, J Mater Sci 17 (1982) 2133–2140. https://doi.org/10.1007/BF00540432.

[52] R. Ranjan, R. Hackl, A. Chandra, E. Schmidbauer, D. Trots, H. Boysen, High-temperature relaxor ferroelectric behavior in Pr-doped $SrTiO_3$ Phys Rev B 76 (2007) 224109. https://doi.org/10.1103/PhysRevB.76.224109.

[53] P. DiAntonio, B.E. Vugmeister, J. Toulouse, L.A. Boatner, Polar fluctuations and first-order Raman scattering in highly polarizable $KTaO_3$ crystals with off-center Li and Nb ions, Phys Rev B 47 (1993) 5629–5637. https://doi.org/10.1103/PhysRevB.47.5629.

[54] J. Frantti, V. Lantto, Raman studies between 11 and 300 K of the effects of Nd additive in ferroelectric lead-titanate ceramics, Phys Rev B 54 (1996) 12139–12150. https://doi.org/10.1103/PhysRevB.54.12139.

[55] A.K. Kalyani, R. Garg, R. Ranjan, Tendency to promote ferroelectric distortion in Pr-modified $PbTiO_3$, Appl Phys Lett 95 (2009) 222904. https://doi.org/10.1063/1.3269999.

[56] DiAntonio, Vugmeister, Toulouse, Boatner, Polar fluctuations and first-order Raman scattering in highly polarizable $KTaO_3$ crystals with off-center Li and Nb ions., Phys Rev B Condens Matter 47 10 (1993) 5629–5637.

[57] Y. Wu, F. Liang, X. Wang, J. Wang, H. Yu, H. Zhang, Temperature dependent Raman spectroscopic study of Fano resonance in perovskite ferroelectric $KTa_{1-x}NbxO_3$ single crystal, Opt Mater Express 12 (2022) 247–255. https://doi.org/10.1364/OME.448347.

[58] B. Kamecki, T. Miruszewski, J. Karczewski, Structural and electrical transport properties of Pr-doped $SrTi_{0.93}Co_{0.07}O_{3-\delta}$ a novel SOEC fuel electrode materials, J Electroceram 42 (2019) 31–40. https://doi.org/10.1007/s10832-018-0143-0.

[59] Y.A. Zulueta, J.A. Dawson, P.D. Mune, M. Froeyen, M.T. Nguyen, Oxygen vacancy generation in rare-earth-doped $SrTiO_3$, Physica Status Solidi (b) 253 (2016) 2197–2203. https://doi.org/https://doi.org/10.1002/pssb.201600315.

[60] L. Dong, Q. Luo, K. Cheng, H. Shi, Q. Wang, W. Weng, W.-Q. Han, Facet-Specific Assembly of Proteins on $SrTiO_3$ Polyhedral Nanocrystals, Sci Rep 4 (2014) 5084. https://doi.org/10.1038/srep05084.

[61] J. Ran, T.Y. Ma, G. Gao, X.-W. Du, S.Z. Qiao, Porous P-doped graphitic carbon nitride nanosheets for synergistically enhanced visible-light photocatalytic H_2 production, Energy Environ Sci 8 (2015) 3708–3717. https://doi.org/10.1039/C5EE02650D.

[62] J. Wu, N. Li, H.-B. Fang, X. Li, Y.-Z. Zheng, X. Tao, Nitrogen vacancies modified graphitic carbon nitride: Scalable and one-step fabrication with efficient visible-light-driven hydrogen evolution, Chemical Engineering Journal 358 (2019) 20–29. https://doi.org/10.1016/j.cej.2018.09.208.

[63] A. Herrera, C. Jacinto, A.R. Becerra, P.L. Franzen, N.M. Balzaretti, Multichannel emission from Pr^{3+} doped heavy-metal oxide glass B_2O_3–PbO–GeO_2–Bi_2O_3 for broadband signal amplification, J Lumin 180 (2016) 341–347. https://doi.org/10.1016/j.jlumin.2016.08.019.

[64] V. Naresh, B.S. Ham, Influence of multiphonon and cross relaxations on 3P0 and 1D2 emission levels of Pr3+ doped borosilicate glasses for broad band signal amplification, J Alloys Compd 664 (2016) 321–330. https://doi.org/10.1016/j.jallcom.2015.12.246.

[65] M. Ledinsky, T. Schönfeldová, J. Holovský, E. Aydin, Z. Hájková, L. Landová, N. Neyková, A. Fejfar, S. De Wolf, Temperature Dependence of the Urbach Energy in Lead Iodide Perovskites, J Phys Chem Lett 10 (2019) 1368–1373. https://doi.org/10.1021/acs.jpclett.9b00138.

[66] I. Bonalde, E. Medina, M. Rodríguez, S.M. Wasim, G. Marín, C. Rincón, A. Rincón, C. Torres, Urbach tail, disorder, and localized modes in ternary semiconductors, Phys Rev B 69 (2004) 195201. https://doi.org/10.1103/PhysRevB.69.195201.

[67] M.K. Warshi, A. Kumar, V. Mishra, A. Sati, A. Sagdeo, R. Kumar, P.R. Sagdeo, Effect of self-doping on the charge state of Fe ions and crystal field transitions in $YFeO_3$: Experiments and theory, J Appl Phys 125 (2019) 204101. https://doi.org/10.1063/1.5092736.

[68] W.D. Rice, P. Ambwani, M. Bombeck, J.D. Thompson, G. Haugstad, C. Leighton, S.A. Crooker, Persistent optically induced magnetism in oxygen-deficient strontium titanate, Nat Mater 13 (2014) 481–487. https://doi.org/10.1038/nmat3914.

[69] K. Xie, N. Umezawa, N. Zhang, P. Reunchan, Y. Zhang, J. Ye, Self-doped $SrTiO_{3-\delta}$ photocatalyst with enhanced activity for artificial photosynthesis under visible light, Energy Environ Sci 4 (2011) 4211–4219. https://doi.org/10.1039/C1EE01594J.

[70] W.S. Baer, Free-Carrier Absorption in Reduced $SrTiO_3$ Physical Review 144 (1966) 734–738. https://doi.org/10.1103/PhysRev.144.734.

[71] C.M. Yim, C.L. Pang, G. Thornton, Yim, Pang, and Thornton Reply:, Phys Rev Lett 104 (2010) 259704. https://doi.org/10.1103/PhysRevLett.104.259704.

[72] G. Liu, W. Jaegermann, J. He, V. Sundström, L. Sun, XPS and UPS Characterization of the TiO_2/ZnPcGly Heterointerface: Alignment of Energy Levels, J Phys Chem B 106 (2002) 5814–5819. https://doi.org/10.1021/jp014192b.

[73] X. Mao, X. Lang, Z. Wang, Q. Hao, B. Wen, Z. Ren, D. Dai, C. Zhou, L.-M. Liu, X. Yang, Band-Gap States of TiO_2(110): Major Contribution from Surface Defects, J Phys Chem Lett 4 (2013) 3839–3844. https://doi.org/10.1021/jz402053p.

[74] N. Jain, A. Roy, A. De, Ba-addition induced enhanced surface reducibility of $SrTiO_3$: implications on catalytic aspects, Nanoscale Adv 1 (2019) 4938–4946. https://doi.org/10.1039/C9NA00540D.

[75] R.A.C. Amoresi, V. Teodoro, G.F. Teixeira, M.S. Li, A.Z. Simões, L.A. Perazolli, E. Longo, M.A. Zaghete, Electrosteric colloidal stabilization for obtaining $SrTiO_3$/TiO_2 heterojunction: Microstructural evolution in the interface and photonics properties, J Eur Ceram Soc 38 (2018) 1621–1631. https://doi.org/10.1016/j.jeurceramsoc.2017.10.056.

[76] R.-J. Xie, N. Hirosaki, K. Sakuma, Y. Yamamoto, M. Mitomo, Eu^{2+}-doped Ca-$_\alpha$-SiAlON: A yellow phosphor for white light-emitting diodes, Appl Phys Lett 84 (2004) 5404–5406. https://doi.org/10.1063/1.1767596.

[77] C. Wang, H. Qiu, T. Inoue, Q. Yao, Band gap engineering of SrTiO3 for water splitting under visible light irradiation, Int J Hydrogen Energy 39 (2014) 12507–12514. https://doi.org/10.1016/j.ijhydene.2014.06.059.

Chapter 4

Thermoelectric properties of Pr doped strontium titanate crystallites

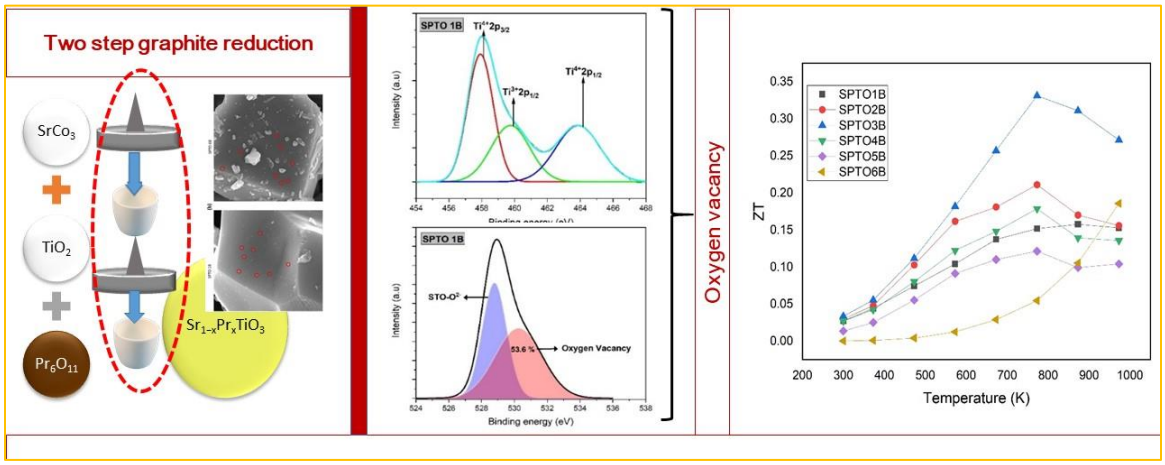

Objectives

This chapter explores the thermoelectric potential of Pr-doped $SrTiO_3$ crystallites, emphasizing how Pr ion incorporation enhances carrier concentration and reduces thermal conductivity, thereby improving thermoelectric performance. The poor carrier mobility and decline in TE output are attributed to the formation of a Double Schottky Barrier (DSB) at the grain boundary, where trapped electrons act as scattering centers, impeding mobility and limiting their contribution to electrical conduction. Controlling the DSB and its associated depletion area is crucial for enhancing the performance of thermoelectric (TE) materials. This chapter also examines the role of graphite sintering in achieving better crystallite densification and grain connectivity, which further optimizes electrical conductivity while mitigating the adverse effects of DSB formation.

4.1 Introduction

Thermoelectric generators have demonstrated their ability to directly convert heat into electricity, even under minimal temperature gradients relative to ambient conditions, making them excellent candidates for capturing waste heat. With no moving parts, minimal maintenance requirements, high conversion efficiency, and exceptional reliability, thermoelectric conversion has become a prominent green energy technology. Advances in thermoelectric (TE) materials have enabled innovative applications across diverse fields, such as recovering waste heat from vehicles, storing thermal energy in building roofs, powering bio-thermal batteries, and enabling localized cooling of electronic components in laser systems, computers, and modern digital devices. TE materials also play a crucial role in satellites and space missions, where efficient energy conversion is essential. Continued research into improving the performance and cost-effectiveness of TE materials is paving the way for broader adoption in both industrial and consumer applications [1–3].

The dimensionless figure of merit, which measures the effectiveness of the thermoelectric energy conversion,

$$ZT = \frac{S^2\sigma}{\kappa}\, T \tag{4.1}$$

Where S is the Seebeck coefficient, σ is the electrical conductivity, κ is the thermal conductivity and T is the absolute temperature. Low thermal conductivity, a high Seebeck coefficient, and high electrical conductivity are necessary for maximizing the thermoelectric figure of merit (ZT) [4–9]. Theoretical investigations using DFT predicts ZT of the range 0.4 to 1.2 for various class of compounds including perovskites [10,11].

Oxide based ceramics like perovskites, delaffosites and ferrites have excellent dielectric properties. Temperature dependent variations of these properties are well explored [12]. Oxide nanocomposites represent a distinct class of materials with remarkable properties, including superior mechanical strength, thermal stability, and electrical conductivity, stemming from the synergistic interactions between their constituent phases. These

materials offer significant advantages in applications such as energy storage, catalysis, and electronics, where their unique nanoscale interactions contribute to notable enhancements in performance [13]. Among these class of oxide ceramics, perovkite oxide Strontium-titanate ($SrTiO_3$) has been used in the optoelectronic, photocatalytic, and dielectric domain by exploring its various physical properties due to its promising structural features [14–19]. STO has a wide range of tunability in its bulk and surface properties, making it suitable for use in basic and applied research. STO displays intrinsically high S and exceptional thermal stability at high temperatures in comparison to other "$ATiO_3$" compounds like $CaTiO_3$ and $BaTiO_3$, which has drawn a lot of interest. Sr substitution with Ba together with A site vacancies has found to be much effective in electromagnetic interference mitigation [20]. Perovskites and delafossites, with appropriate nanostructural modifications, provide a wide range of applications in thermoelectric power generation. The substitution of Sr atoms at the A-site and Ti atoms at the B-site with suitable dopants such as Pr, La, Ta, V, and Nb induces lattice distortions and creates strain fields, ultimately enhancing the phonon scattering mechanism. Additionally, Pr-doping improves thermoelectric performance by promoting the formation of Pr-rich grain boundaries, which contribute to better phonon scattering and enhanced energy conversion efficiency [16,21–26]. Like perovskites, it has been demonstrated that doping manganites with rare earth elements such as Pr, Nd, Sm, Eu, Gd, and Tb may effectively alter their magnetic and electrical characteristics [27]. Ohta et al. reported that the difference in carrier transport between a single crystal and a polycrystalline ceramic is directly related to the polycrystalline grain boundary (GB), as indicated by the temperature-dependent poor carrier mobility in the $SrTiO_3$ film. The poor carrier mobility and declination in TE output was attributed to the formation of a double Schottky barrier (DSB) at the grain boundary [28]. In this double Schottky barrier (DSB) system, electrons become trapped at the grain boundaries, acting as scattering centers that impede electron mobility and prevent them from contributing to electrical conduction. Controlling the DSB and its associated depletion area is crucial for enhancing the performance of thermoelectric (TE) materials. One approach to mitigating

the DSB effect is the incorporation of a two-dimensional conductive second phase, such as graphene. However, the improvement in the power factor (PF) achieved through this method is highly dependent on the quality and dispersion of graphene, which can lead to inconsistencies and poor reproducibility in composite materials. Alternatively, reduction processes can be employed in $SrTiO_3$-based ceramics to effectively address the DSB and enhance their TE performance [29]. The first high-temperature reduction step introduces oxygen vacancies, and the second annealing redistributes these vacancies uniformly, mitigating charge accumulation at grain boundaries. This process effectively flattens the potential profile, suppressing the DSB and enhancing carrier transport critical for thermoelectric performance. The technique was used here to enhance TE performance in Pr substituted STO ceramics. STO prepared by solid state reaction is electrically insulating because the calcination in an oxygen-rich atmosphere leads to the compensation of Sr vacancy rather than electrons to the positively charged dopants. Therefore, additional sintering in reduced atmosphere is essential to reach high electrical conductivity of doped $SrTiO_3$.

Here we report enhancement in thermoelectric performance of $Sr_{1-x}Pr_xTiO_3$ (x=0.05, 0.075, 0.10, 0.125, 0.15, 0.20) system by double reduction process to eliminate DSB and is correlated with structural changes. The alteration of crystal structure by Pr inclusion, oxygen vacancies in synthesis process and subsequent two step reduction of Ti ions by graphite burial sintering were effectively used to manipulate TE performance.

4.2 Experimental methods and techniques

$Sr_{1-x}Pr_xTiO_3$ (x=0.05, 0.075, 0.10, 0.125, 0.15, 0.20) ceramics were synthesized via high-temperature solid-state reaction by mixing stoichiometric amounts of $SrCO_3$, TiO_2, and Pr_6O_{11}, followed by calcination at 1250 °C for 8 hours. Before mixing them, oxide presursers were undergone first step of burial sintering at 1450 °C for 4 hours. The powders were ground, mixed with a PVA binder, and uniaxially pressed into pellets, which were slowly heated to 600 °C to eliminate the binder. A two-step graphite reduction process was employed, where the pellets were buried in a graphite-filled

alumina crucible and sintered at 1450 °C for 4 hours. The process involved creating densely packed system with graphite powder and repeating the sintering to enhance the material properties.

The X-ray Structural analysis was performed using an X-ray diffractometer (PANalytical X'pert 3 Powder) with Cu-K_α radiation (λ = 1.5418 Å) over a 2θ range of 20° to 90°. XPS measurements were conducted with an Omicron Nanotechnology XPS system, while morphological characterization was carried out using a field emission scanning electron microscope (FE-SEM, ZEISS Gemini SEM 300). Seebeck coefficient, electrical conductivity, and power factor were measured in the temperature range of 300 to 973 K using a ULVAC ZEM-3 system, which automates measurements by controlling temperature differences and eliminating dark electromotive forces. Thermal conductivity was determined using a steady-state method with a copper-constantan thermocouple to maintain a constant temperature gradient. Thermal stability was evaluated using an STA 8000 thermogravimetric analyzer in a nitrogen atmosphere, where 9.758 mg of the sample was heated at a rate of 5 °C/min from 30 °C to 800 °C.

4.3 Results and discussion

As a result of reduction of titanium under reducing atmosphere created by graphite powder, the color of the compounds turned to dark grey [16] . Under a reducing environment, oxygen atoms are removed from the $SrTiO_3$ lattice, creating oxygen vacancies. These vacancies often lead to localized electron states that can absorb visible light, giving the material a darker appearance.

4.3.1 Structural, morphological characterization- XRD, XPS and FE-SEM

The XRD patterns of Sr_{1-x} Pr_xTiO_3 ceramics with Pr doping are shown in Fig.4-1(a) for a range of x values, including 0.05, 0.075, 0.10, 0.125, 0.15, and 0.20. Higher doping levels results in cubic symmetry breakdown of the system and shows a change to tetragonal phase, and the peak positions are compatible with the database (PDF 00-035-

0734). As inferred from the XRD peaks of Fig. 4-2(a), the Pr^{3+} ion successfully replaced the Sr^{2+} site in the $SrTiO_3$ crystal lattice.

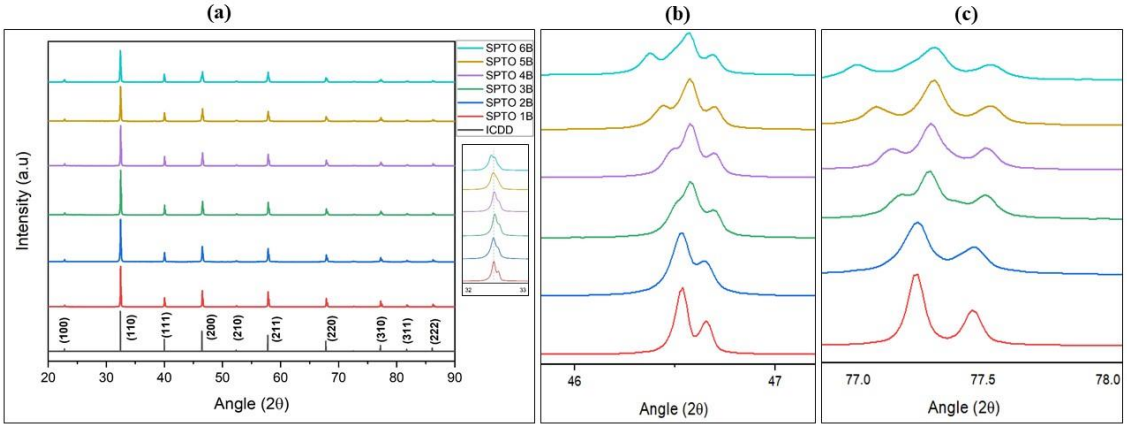

Figure 4-1 (a) XRD pattern of Pr doped $SrTiO_3$ **(b)** Splitting of (200) peak **(c)** Asymmetric nature and splitting of (310) peaks.

The (110) peak in the XRD spectrum shows irregular shifts with Pr content. The shift in the patterns depend on several inter connected factors like the size of dopant atom, strain effects in the lattice, oxygen defects in the structure, electronegativity of the replaced atoms etc. Here for the least doped sample SPTO 1 and highly doped samples SPTO 5 and SPTO 6 lower angle shift is observed as depicted in the inset of Fig. 4-1 (a). But for all in between concentrations higher angle shift is seen. This lower angle shift may be attributed to the lattice expansion resulting from Pr – O repulsion arising from the change in electronegativity between Pr and replaced Sr atoms. The lower angle shift is also an outcome of grain boundary (GB) substitution at lower doping concentration. This supports theoretical predictions that Pr-doping at the GBs is far more favorable than doping in the bulk [23,30].

Peaks corresponding to the perovskite phase were observed across the entire compositional spectrum, but additional features such as asymmetric peaks and peak splitting were noticeable in samples with higher Pr content $x \geq 0.1$. Samples SPTO 1B and SPTO 2B retained a cubic structure, as evidenced by the absence of peak splitting in the (200) reflection and the lack of R-point reflections at $2\theta = 38°$. However, with increasing

Pr content, the system transitions from the cubic Pm-3m space group to the tetragonal I4/mcm space group. Magnified views of the (200) and (310) reflections, shown in Fig. 4.1(b) and (c) for 2θ values in the range, 46-47° and 77-78°, highlight the splitting in SPTO 3B and samples with higher doping percentages. This splitting and the asymmetric nature of the (310) peak from SPTO 3B onwards confirm the tetragonal phase. These findings indicate a cubic-to-tetragonal phase transition for samples with x≥0.1. Previous work on this structural transformation corroborates this conclusion, as the emergence of E_g and B_{1g} modes in Raman spectra at x=0.1 confirms the breakdown of cubic symmetry [17]. Tilting of TiO_6 octahedra due to the significant difference in ionic radii between host Sr^{2+} and dopant Pr^{3+} cations, leads to this structural modification.

The FWHM and the corresponding 2θ value were calculated for each peak using the Gaussian function fitting. Table 4-1 provides the average crystallite size calculated using the Scherrer equation for the five most intense peaks and the strain calculated using the Williamson-Hall method in accordance with equation (4.2).

$$\beta \cos\theta = \frac{k\lambda}{D} + 4\epsilon \sin\theta \tag{4.2}$$

Where β is the FWHM, θ is the angle of diffraction, λ is the X-ray wavelength 1.5418 Å, D is the crystallite size, k is the shape factor (usually around 0.9), and ϵ is the microstrain.

Table 4-1 Average crystallite size and micro strain of Pr doped STO.

Sample label	Crystallite size (nm)	Micro strain (x 10^{-3})
SPTO 1B	45.3± 2.3	1.11
SPTO 2B	41.8±2.1	1.57
SPTO 3B	41.5±2.1	1.64
SPTO 4B	41.4±2.1	1.68
SPTO 5B	40.1±2.0	1.90
SPTO 6B	38.1±1.9	2.12

As the dopant concentration increases, the microstrain on the lattice also increases, while the crystallite size decreases. This trend is observed in both the cubic and tetragonal systems and is attributed to the formation of oxygen vacancies during burial sintering. The data indicate that the presence of Pr^{3+} ions in $SrTiO_3$ reduced the growth of crystal grains. The decrease in crystallite size is due to the compressive strain of crystal lattice and is well understood by the grain growth suppressing effect by Pr-doping. The Pr^{3+} ions may cluster at the grain boundaries or on the surface of STO with the addition of Pr_6O_{11}. As the amount of Pr_6O_{11} increases, $SrTiO_3$-Pr-rich phase segregation forms at the sample's surface and in the grain boundary close to the junctions between STO grains, which will prevent further grain growth. Investigations on the effect of crystallite size on polarization and resultant ferroelectric and thermoelectric properties are of great relevance [31].

XPS measurements were employed to investigate the chemical states of the elements, oxygen vacancies, Ti^{3+} concentration, and the valence state of Pr in doped, burial-sintered $SrTiO_3$. The comprehensive XPS survey spectra of $Sr_{1-x}Pr_xTiO_3$, shown in Fig. 4-2(a), confirm the presence of Pr, Sr, Ti, and O. Fig. 4-2(b) presents the deconvoluted XPS spectra for the praseodymium core level $3d_{5/2}$, showcasing results for three samples with x values of 0.05, 0.10, and 0.20. The $3d_{5/2}$ peak at a binding energy of 932.4 eV correspond to the Pr^{3+} oxidation state of praseodymium in the perovskite structure, while the second peak at 934.1 eV is attributed to Pr^{4+} cations. These observations align with previous studies on the relationship between praseodymium oxidation states and peak positions. The broad shape of the spectrum arises from additional satellite peaks caused by valence orbital hybridization and multiplet coupling effects [32,33]. The amount of Pr^{3+} and Pr^{4+} were also calculated from XPS data and are listed in Table 4-2. The XPS analysis confirmed the mixed valence state of Pr, with Pr^{3+} cations accounting for approximately 65% of the total Pr content. Based on the XPS data, the atomic ratio of Pr^{4+} to Pr^{3+} is about 2:1, giving an average praseodymium valence of approximately 3.35, which is slightly lower than the expected value of 3.66 for Pr_6O_{11}. The analysis did not indicate the presence of praseodymium in the +2 oxidation state.

+

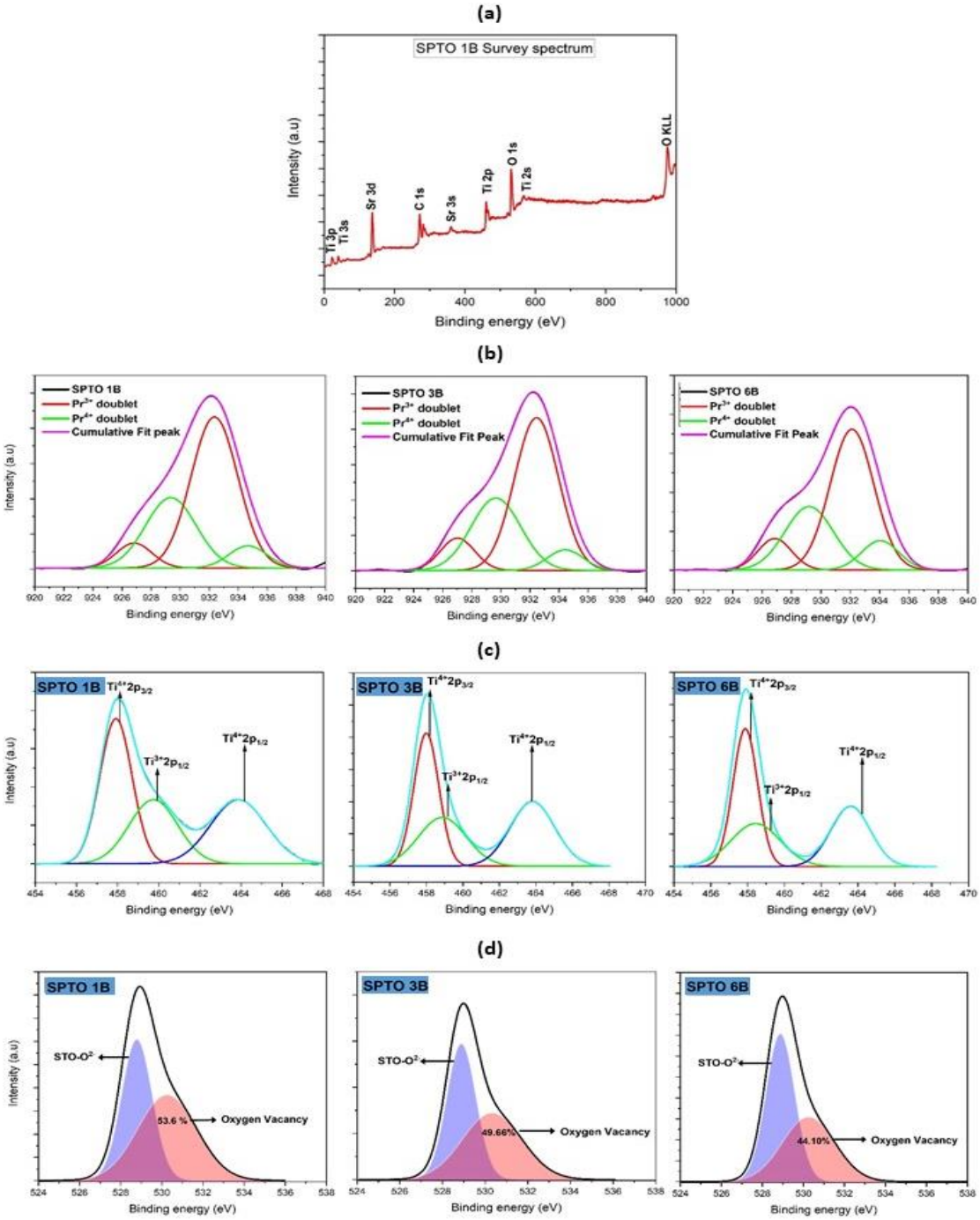

Figure 4- 2 (a) XPS Survey spectrum of SPTO 1B **(b)** deconvolution of high resolution XPS spectra of Pr 3d signal **(c)** Ti 2p signal **(d)** O 1s signal.

The Goldschmidt tolerance factor t can be used to estimate the extent of crystallographic distortions in most perovskites, which are capable of accommodating cations of varying sizes.

For doped $A_{(1-x)}A^{I}{}_{(x)}BX_3$ kind of compounds this can be calculated using equation (4.3)

$$t = \frac{[(1-x)r_A + xr_{A^I} + r_X]}{\sqrt{2}(r_B + r_X)} \tag{4.3}$$

where r_A is the ionic radius of atom A, r_{A^I} is the ionic radius of dopant, r_B is the ionic radius of B site cation and r_X is the ionic radius of O^{2-}. If t deviates from 1, this could suggest the creation of a non-ideal perovskite structure. Tetragonal and hexagonal variations of the perovskite structure are stable if t is greater than 1 as a result of a large A or small B ion. The calculations were carried out with a previously reported ionic radius of Pr^{3+} (1.13 Å) and Pr^{4+} (0.96 Å) for a coordination number (CN) =8. The calculations yield Goldschmidt tolerance factor values of 1.065, 1.053, and 1.041 for the samples SPTO 1B, SPTO 3B, and SPTO 6B, respectively. This indicates that the perovskite structure deviates from its ideal cubic phase, transitioning to a tetragonal structure due to structural distortions induced by Pr doping, as corroborated by XRD analysis.

The oxidation state of titanium ions is crucial in defining the physical properties of the doped system. Burial sintering was employed to introduce Ti^{3+} ions into the lattice by reducing Ti^{4+}. The XPS spectra of titanium were deconvoluted to analyze the oxidation states in the samples SPTO 1B, SPTO 3B, and SPTO 6B. Fig. 4-3(c) presents a comparative analysis of the titanium 2p core levels. The spectral profile aligns well with findings from previous studies [34,35]. Ti doublets arising from spin orbit-splitting having binding energies of 463.9 eV and 458.1 eV exist in all samples. These binding energy values correspond to the $Ti2p_{1/2}$ and $Ti2p_{3/2}$ bands, respectively, which are typical for Ti^{4+}. Another band was identified in a lower binding energy area having binding

energy 460 eV is ascribed to Ti^{3+}. This band was shifted by about 2 eV towards lower binding energies in all samples. After doping with Pr, the high resolution XPS spectrum shows a slight shift in the position along with a variation in the area of the original peaks. The peak positions for the Pr-doped samples, as detailed in Table 4-2, reveal a shift, indicating the influence of Pr addition on the electronic state of the Ti element. Changes in stoichiometry and the Ti^{4+} to Ti^{3+} ratio were determined by analyzing the relative peak areas, as represented in Table 4-2. The praseodymium dopant contributes to the partial reduction of titanium cations, consistent with the defect chemistry typically associated with such dopants in $SrTiO_3$. In the doped samples, the Ti^{3+} peak area increases while the Ti^{4+} peak area decreases compared to the undoped sample. This suggests that the burial sintering process removes oxygen from the lattice, leading to a relative rise in Ti^{3+} concentrations observed in the XPS spectrum.

Table 4- 2 Valence states and oxygen vacancy concentration of Pr doped STO crystallites.

Sample label	$Pr3d_{5/2}$ (±3 %)		Ti 2P (±3 %)				Oxygen vacancy (±3%)
	Pr^{3+}	Pr^{4+}	Ti^{3+}	Position of Ti^{3+} (eV)	Ti^{4+}	Position of Ti^{4+}(eV)	
SPTO 1B	64.51	35.49	31.60	459.81	68.40	458.06	53.60
SPTO 3B	64.12	35.88	27.36	458.95	72.64	458.01	49.66
SPTO 6B	64.05	35.95	26.80	458.46	73.20	457.87	44.10

The high-resolution XPS spectrum of O 1s in STO is shown in Fig. 4-3(d), which can be deconvoluted into two distinct peaks centered on 528.9 eV and 531 eV. The peak at 529 eV is due to O_2, which is primarily derived from the lattice oxygen. The oxygen defects on the surface of STO are responsible for the peak at 531 eV [36]. The peak intensity at a binding energy of 531 eV, associated with the concentration of surface oxygen vacancies in STO, shows a significant increase in the burial-sintered STO samples, indicating a higher concentration of surface oxygen vacancies after the reduction treatment treat. The concentration of oxygen vacancies was determined by calculating

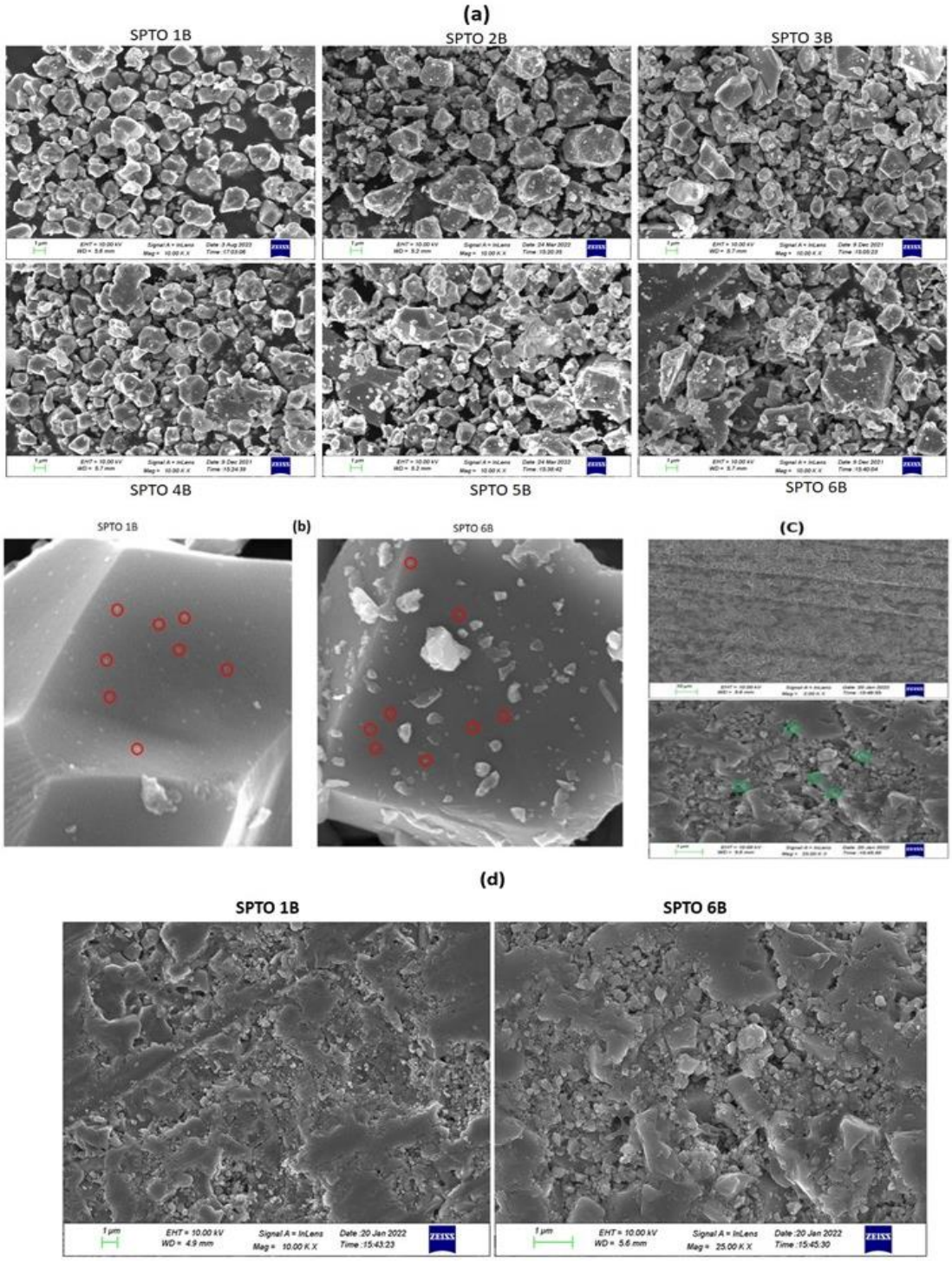

Figure 4- 3 (a) SEM image of Pr substituted $SrTiO_3$ ceramics **(b)** core shell like structures in SPTO 1B and SPTO 6B **(c)** surface scan of pellets showing formation of nanopores **(d)** Porosity difference in least doped and heavily doped samples.

the area under the deconvoluted curve and is presented in Table 4-2. A slight shift in the

oxygen vacancy peak with Pr doping was observed, highlighting the role of Pr in influencing oxygen vacancy formation. The O 1s peak at ≈528.8 eV, characteristic of oxygen in perovskites, shifts slightly to a higher binding energy of 529.93 eV in all the reduced samples, further confirming the effect of the reduction process and Pr doping on the electronic environment [37,38].

SEM analysis was conducted to evaluate the microstructures of the samples after sintering and annealing, as shown in Fig. 4-3(a). The micrographs reveal regular polygon-shaped grains with an average size of 3±0.2 μm, along with smaller grains adhering to larger ones, forming agglomerates that contribute to reduced thermal conductivity. Core-shell grain structures, highlighted by red circles, are observed in all Pr-doped samples, with Fig. 4-3(b) illustrating these features for SPTO 1B and SPTO 6B samples. The sinterability decreases with higher praseodymium content. Samples with lower Pr doping (x=0.05) exhibit relatively dense ceramics, while Pr-rich samples display a more porous structure, significantly impacting their electrical and thermal conductivity. The porosity between particles induces phonon scattering, which helps reduce phonon thermal conductivity. Fig. 4-3(c) shows the smooth surface of polished pellets (using SiC papers of varying grit sizes 400–3000), indicating a compact structure. The SEM image of the SPTO 3B in Fig. 4-3(c) also reveals the presence of nanopores, marked by green circles.

SEM images also reveal that some pores have agglomerated due to the high calcination temperature in the range 1400 to 1500 °C. While the bulk electrical conductivity remains relatively unaffected by the average grain size or its distribution, the grain boundary (GB) conductivity is anticipated to vary depending on the average grain size. This highlights the critical role of microstructural features in determining the thermal and electrical transport properties of the material [39,40]. Graphite sintering atmosphere creating a highly reduced atmosphere further accelerate this effect, as the grain boundary resistance significantly decreased with smaller average grain sizes. This indicates enhanced conductivity along the grain boundaries, leading to the suppression of DSB effects.

4.3.2 Thermal characterization-TGA, DTA and thermal conductivity studies

Differential thermal analysis and thermo gravimetric analysis were used to characterize the thermal properties of Pr substituted $SrTiO_3$ up to 800 °C at a heating rate of 5 °C/min in a nitrogen atmosphere and is represented in Fig. 4-4. The TGA curves were measured in the flowing nitrogen gas rate of 20 ml/min. All samples shows weight gain of 1.2 – 1.5 % during the analysis which is not expected for normal STO, which typically shows a mass loss, which increases monotonically with temperature and is related to the mass loss of chemically adsorbed water molecules.

However, for burial sintered STO samples after post reduction, mass increase can be observed at after 300 °C. We infer that the weight gain of reduced STO sample is due to the adsorption of nitrogen during the analysis. Nitrogen molecules prefer to adsorb on the oxygen vacancies sites that lack of electron through a strong interaction. This adsorption will continue monotonously unless the nitrogen is converted to some other compounds like ammonia in the presence of visible light. The ceramic is treated to be stable during the entire range of TGA cycle with this nominal weight gain. The TGA curves exhibit almost similar oxygen vacancy for all samples. The number of oxygen vacancies increases from the least doped sample SPTO 1B up to SPTO 3B and then decreases with SPTO 6B being the lowest. Recent research by Wang et al. backs up this finding [36]. The amount of nitrogen getting adsorbed in the sample can be quantitatively used to determine the amount of oxygen vacancies. The oxygen deficiency can be found using eqn (4.4). Here δ represents the deviation from stoichiometry — specifically, the amount of oxygen deficiency in the crystal structure.

$$\delta = \frac{(m_A + m_B)\sigma + 48\,\sigma}{16(1+\sigma)} \tag{4.4}$$

Where m_A & m_B are the mass of A site and B site molecules respectively and σ is the relative mass change [41].

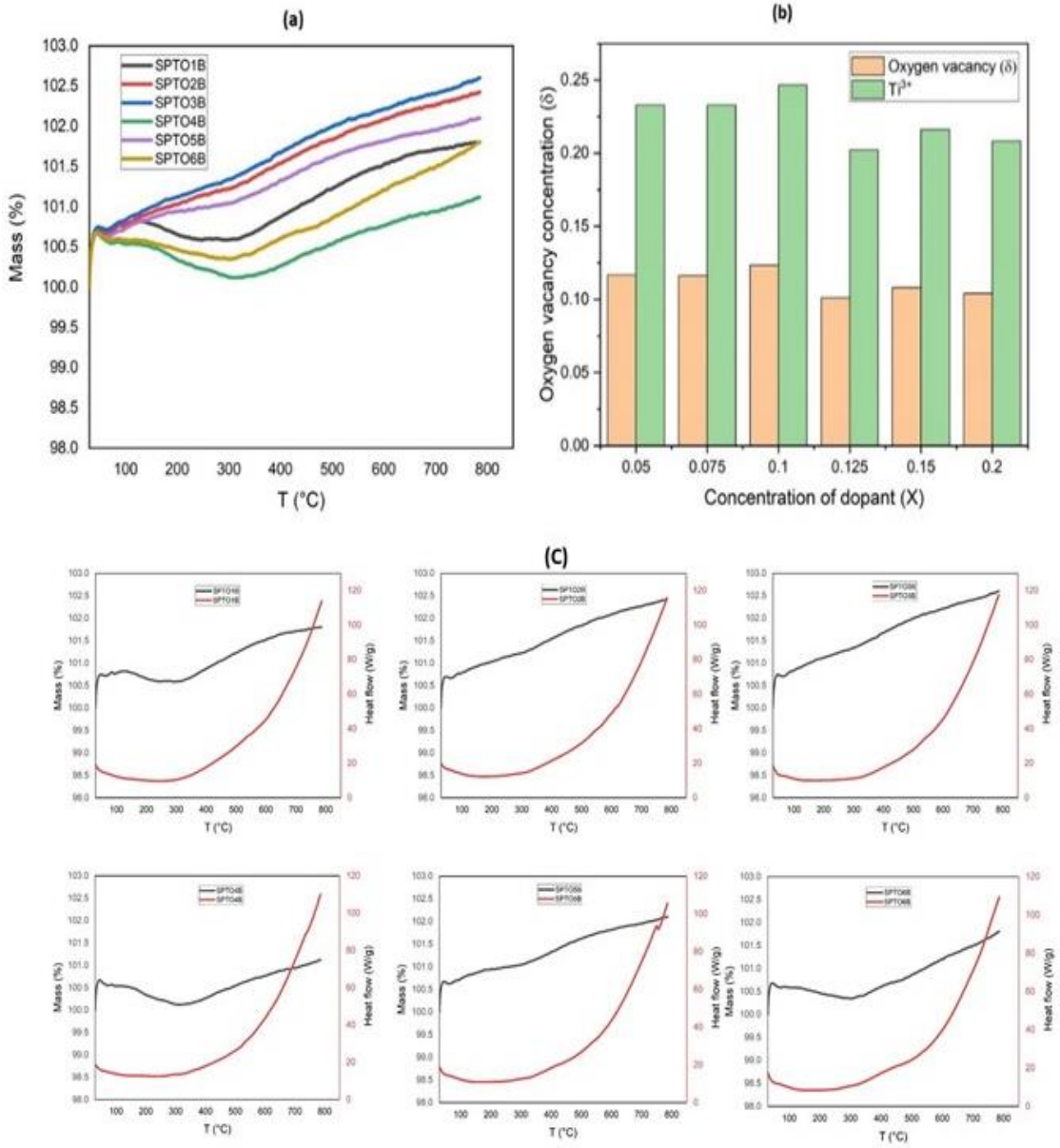

Figure 4- 4 (a) combined TGA plot of Pr substituted $SrTiO_3$ **(b)** oxygen vacancy and corresponding concentration of Ti^{3+} obtained from TGA **(c)** TGA-DTA curves of SPTO 1B to SPTO 6B.

The obtained value of oxygen vacancy and concentration of reduced Ti^{3+} ions are represented in Fig. 4-4 (b). The calculations shows that the sample SPTO 3B is having maximum deficiency with $\delta = 0.123$ and sample SPTO 6B is having minimum oxygen

deficiency with $\delta = 0.103$. Ti^{3+} content is calculated using the stoichiometric representation of the prepared samples $Sr_{1-x}^{2+}Pr_x^{3+}Ti_{2\delta}^{3+}Ti_{1-2\delta}^{4+}O_{3-\delta}^{2-}$.The values varies from 0.247 to 0.208. The oxygen non-stoichiometry can influence a wide range of physical properties of the system including electronic and magnetic properties. Previous works has indicated that changes to oxygen stoichiometry produce only 0.001-0.002 Å change in lattice parameter, which is barely detectable even in bulk samples [42,43]. Even though these structural changes are nominal they can significantly affect the transport properties. The values of oxygen vacancies and Ti^{3+} concentration is found to be higher compared to the H_2-Ar atmosphere sintered samples reported in previous studies [44,45]. The concentration of oxygen vacancies is almost constant with doping since all the samples are prepared under same reducing conditions. This is also backed by XPS studies.

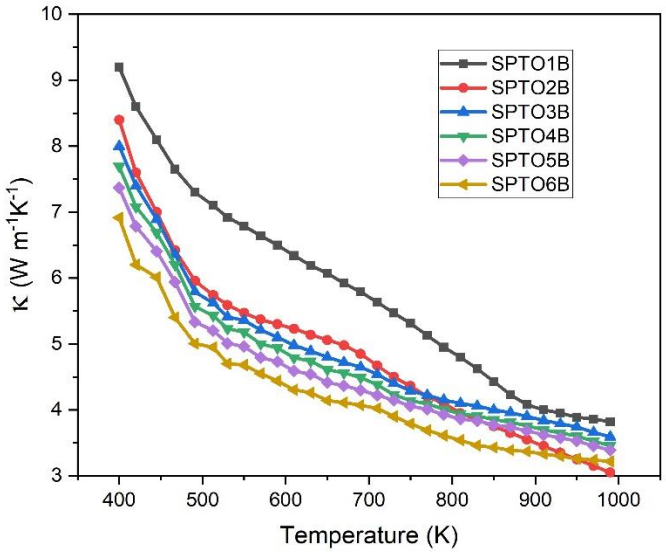

Figure 4- 5 Thermal conductivity variation with temperature in Pr substituted $SrTiO_3$.

Temperature dependent thermal conductivity of prepared samples is shown in Fig. 4-5. The thermal conductivity of all samples in the series $Sr_{1-x}Pr_xTiO_3$ decreases proportionate to T^{-1} with temperature, indicating the dominant role of lattice contribution. Umklapp scattering brought on by phonon-phonon interactions at high

temperatures caused the temperature dependence to be more pronounced for materials with lower Pr content [46]. With increasing Pr content, the dependency gets reduced. κ varied between a maximum of 9 to minimum of 3 W m^{-1} K^{-1} for the samples under study. The creation of point defects as a result of Pr addition is advantageous for better phonon scattering and, results in decreased lattice thermal conductivity with doping. The crystallite size influences thermal conductivity due to the impact of grain boundaries on heat transfer. Smaller crystallites result in materials with lower thermal conductivity.

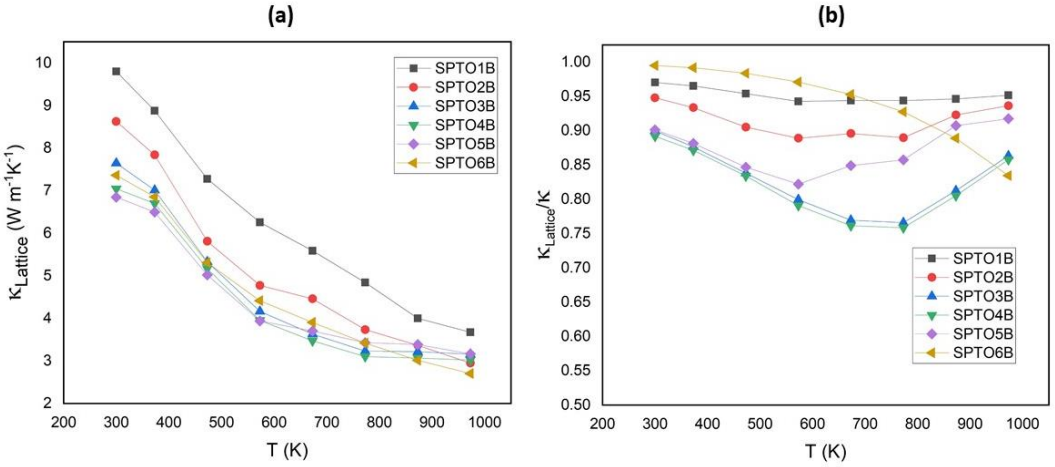

Figure 4- 6 (a) Temperature dependence of lattice thermal conductivity in Pr substituted $SrTiO_3$ ceramics **(b)** Contribution of lattice thermal conductivity to total thermal conductivity.

Lattice thermal conductivity ($\kappa_{Lattice}$) and electronic thermal conductivity ($\kappa_{Electronic}$) contribute to total thermal conductivity of materials as in equation (4.5)

$$\kappa_{Total} = \kappa_{Lattice} + \kappa_{Electronic} \tag{4.5}$$

$\kappa_{Electronic}$ can be expressed using Wiedemann-Franz's law as in equation (4.6)

$$\kappa_{Electronic} = L\sigma T \tag{4.6}$$

Where $L = 2.44 \times 10^{-8} V^2 K^{-2}$. Fig. 4-6 (a) shows the lattice thermal conductivity variation with temperature following a similar trend as total thermal conductivity. In general the electronic part of thermal conductivity is maximum for highly conductive

samples and is in the range 20-25 %. The generation of point defects as a result of Pr addition is advantageous for better phonon scattering and, leads to decreased lattice thermal conductivity. Distortion of lattice with Pr incorporation results in weakening of Ti-O bonds developing a less thermal conductive material. The Pr substitution beyond x=0.125 doesn't significantly affect the total conductivity. The overall reduction of thermal conductivity from bulk value in range 10-12 $Wm^{-1}K^{-1}$ in the prepared samples is also due to the phonon scattering due to oxygen vacancies [47]. The large reduction in thermal conductivity at moderate temperature could be attributed to effective phonon scattering due to the randomly distributed and clustered nature of oxygen vacancies [48]. Furthermore, the size of the clustered oxygen vacancies, a few nanometers, would be comparable to the dominating wavelength of phonons, potentially increasing the efficiency of phonon scattering [49]. All these complex effects determine the total thermal conductivity.

4.3.3 Electrical and thermoelectrical characterization

Doping $SrTiO_3$ with Pr/vacancy at the requisite quantities should not affect Ti oxidation state due to charge neutrality. But the formation of oxygen vacancies leads to reduction of titanium. This reduction procedure is critical in defining the material's thermoelectric properties. Fig.4-7 (a) depicts the relationship between temperature and the overall conductivity of ceramic samples.

Due to an increase in carrier concentration, the conductivity rises with increasing praseodymium content up to SPTO 3B. Defect formation under graphite sintering process aids in this increased conductivity. As the temperature rises, the electrical conductivity falls significantly, indicating degenerate semiconducting behavior in the samples with composition x=0.05 to 0.15 range. The electrical conductivity declined proportionally to T^{-2} at high temperatures over 473 K, suggesting that phonon scattering was the primary cause above that temperature [50]. Pr rich sample SPTO 6B shows a

reverse trend in conductivity indicating a transition to metallic-type behavior with doping, the sample also records least conductivity at room temperature.

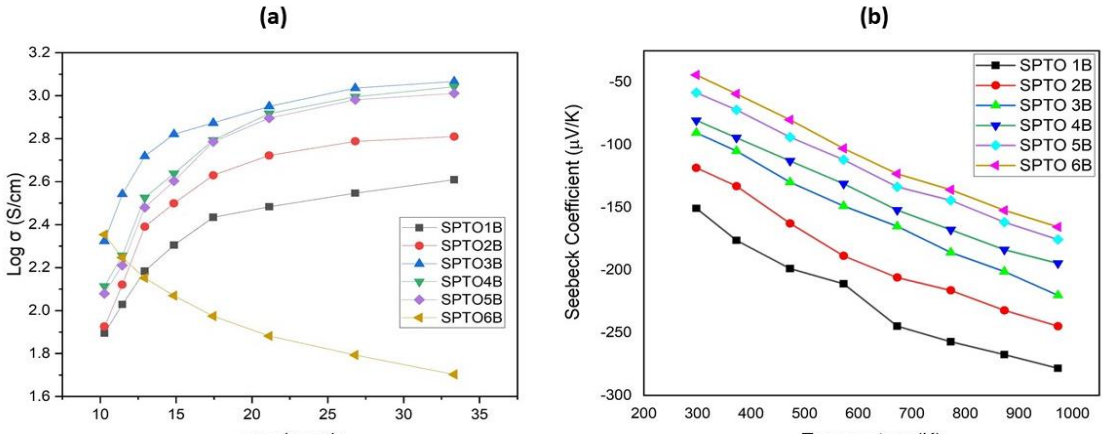

Figure 4- 7 (a) Temperature dependent conductivity variation **(b)** Seebeck coefficient variation in Pr substituted $SrTiO_3$ ceramics.

The decreased conductivity of SPTO 6B is attributed to the less oxygen vacancy and increased defects in the system due to high Pr concentration. Microstructural features like crystallite size and the lattice strain have considerable effect on transport properties. Resistance increases with the decrease of crystallite size due to the growth of insulating grain boundary and the contributions from non collinear surface layers. The grain boundaries in the material act as insulators and significantly resist the flow of electrons. This resistance is caused by the formation of a potential barrier at the grain boundary surfaces. The potential barrier forms due to the trapping of charge carriers at the boundary and the presence of compensating opposite space charges within the grains. Consequently, an increase in the number of grain boundaries in a sample leads to higher resistivity. The smaller crystallite size of the sample SPTO 6B leads to the observed high resistance. The variation in conductivity are affected my multiple factors, so a direct linkage may not hold for all materials. SEM analysis reveals that the grain sizes of SPTO 6B are larger compared to other samples. Smaller grains have a larger specific grain boundary area and a higher concentration of oxygen vacancies [39]. Since the Pr-rich sample SPTO 6B has larger grain sizes, it is expected to have the lowest concentration of oxygen vacancies. Vacancies and Pr atom scattering also cause the drop in conductivity

at higher doping levels. At high doping percentages the mobility of charge carriers tend to reduce steeply as a result of these structural distortions and is responsible for low conductivity near room temperature. It has been reported that doping in the A-site in a perovskite system relaxes oxygen octahedra, which reduces the stability of the ABO_3 perovskite structure [51]. The t_{2g} and e_g orbitals of a Ti^{3+} overlap the Fermi level of doped $SrTiO_3$ at elevated electron concentrations, and as the Pr concentration increases, the resulting structural distortions induce alterations in the Fermi energy level.

Pr substitution reduces lattice volume, allowing for greater overlapping of Ti-3 d orbitals, facilitating electron delocalization and temperature-dependent degenerate semiconductor type conductivity for the samples with $0.05 \leq x \leq 0.15$. Increase in Pr content beyond this level leads to further distortion of the perovskite lattice resulting in change in Ti-O-Ti angle from 180° and enfeebling Ti-O bond. The tilting of TiO_6 octahedra and weakening of bonds significantly affect the electron conduction mechanism. Stress generated in the lattice by Pr incorporation is counteracted by the expansion of the lattice at high temperature and lead to comparable conductivity and even better as observed for SPTO 6B beyond 700 K and is reflected in the power factor calculations.

Fig. 4-7 (b) represents the relationship between temperature and the Seebeck coefficient of ceramic samples. The n-type conductivity of the samples is well understood by the negative sign of Seebeck coefficient. A monotonous increase in the absolute value of *S* with temperature is observed in all samples. A significant reduction in $|S|$ is evident with Pr concentration. This variations can be analyzed by using the degenerated semiconductor model with parabolic band dispersion. Relationship between the Seebeck coefficient and carrier concentration is represented as equation (4.7)

$$S = \gamma - \ln(n) \tag{4.7}$$

with γ being the scattering factor. And *S* can also be expressed as equation (4.8)

$$S = \frac{8\pi^2 {k_B}^2}{3eh^2} m^* T \left(\frac{\pi}{3n}\right)^{2/3} \tag{4.8}$$

where k_B, e, h, n, and m^* are the Boltzmann constant, electron charge, Plank constant, carrier concentration and the density of states effective mass of carriers, respectively. Both these relations suggest that, As the Pr content increases, the increased carrier concentration will lead to the reduction of the Seebeck coefficient. Even then the obtained seebeck coefficient in this work is greater than the previous works [24,44,52]. As a result of scattering the low-energy electrons, the energy filtering effect may take place at grain boundaries and core-shell structure interfaces, increasing the average carrier energy. A greater carrier effective mass might result from a rise in electron localization following Pr addition, which has a significant impact on how electrical conductivity changes with temperature. Due to this influence, a relatively substantial value of $|S|$ may be maintained even for high dopant content, partially offsetting the decrease in the Seebeck coefficient brought on by the increase in carrier concentration.

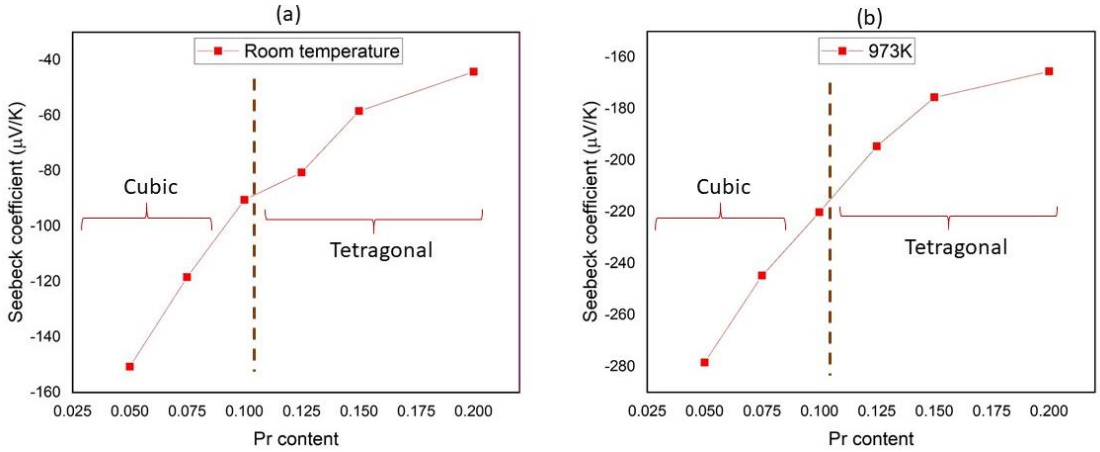

Figure 4- 8 Variation in Seebeck coefficients with doping concentration in cubic and tetragonal Pr substituted $SrTiO_3$ **(a)** in room temperature **(b)** at 973 K.

The shift from a cubic to a tetragonal structure reduces the symmetry of TiO_6 octahedra and it has a bigger impact on $|S|$. It can be seen that the variation in absolute value of Seebeck coefficient with Pr content is more profound for cubic system with $0.05 \leq x \leq 0.10$ as indicated in Fig. 4-8. The difference in slope between cubic and tetragonal system is well understood from the figure. This is because, the Pr/vacancy

concentration has no direct impact on the band structure since the band gap is primarily governed by O 2p and Ti 3d orbitals rather than the distortion of TiO_6 octahedra system, demonstrating the combined effect of electrical conductivity and the Seebeck coefficient on thermoelectric performance.

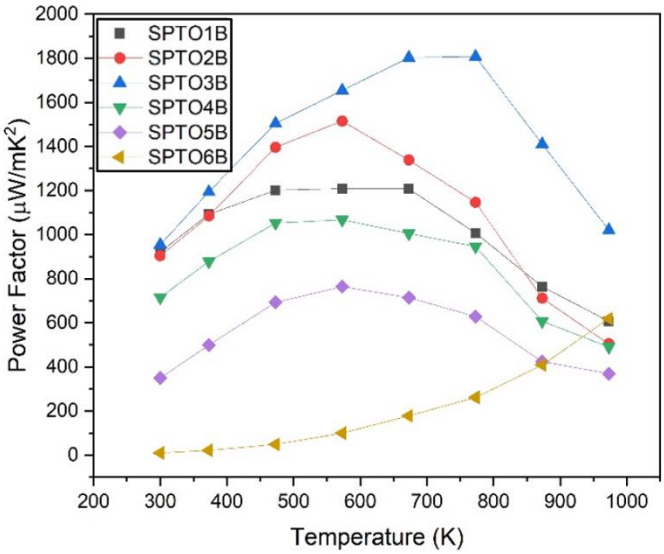

Figure 4- 9 Temperature dependent power factor values Pr substituted $SrTiO_3$ crystallites.

Fig. 4-9 depicts the temperature dependence of the power factor for the Pr substituted. The maximum thermoelectric power factor, σS^2 achieved was 1.8×10^{-3} W m^{-1} K^{-2} at 673 K for sample SPTO 3B, with x=0.1. This is better than La doped STO, La-Dy doped STO, Y doped STO, Nd doped STO and even comparable with A site deficient Pr doped STO, La-Graphite STO [53–59]. The maximum power factor of SPTO3B is due to the rapid rise in conductivity, with a moderately maintained Seebeck coefficient. Power factor declined with increased Pr content beyond x=0.1. For practical applications in mid temperature range power factor values should be maintained over a suitable temperature range. Here we were able to achieve high power factor above 1 x 10^{-3} W m^{-1} K^{-2} in the temperature range of 450-750 K. As a result of improved power factor and relatively low thermal conductivity, high ZT values were obtained for Sr_{1-x} Pr_x TiO_3 ceramics and is depicted in Fig. 4-10.

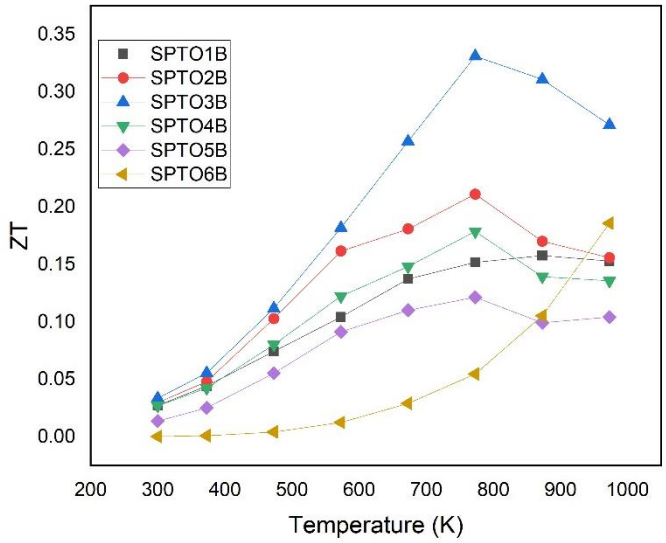

Figure 4- 10 Temperature dependence of the figure of merit ZT of Pr doped $SrTiO_3$.

These values shows an increasing trend with temperature up to 800 K and then stabilizes, except for the highly doped sample which shows a monotonous increment. The maximum ZT of 0.33 was achieved for SPTO 3B with x=0.10. Which is comparable to the best in class n type oxide thermoelectric materials. Pr-doped $SrTiO_3$ polycrystalline samples synthesized with the two step reduction method have significantly higher ZT values throughout the whole temperature range.

4.4 Conclusions

The double reduction technique was successfully applied to improve the TE performance of oxide perovskite in Pr doped STO systems for the first time, The structural transformation from cubic to tetragonal phase was observed for systems with $x \geq 0.10$. Partial substitution of Pr atoms boosted the electrical conductivity of symmetric systems (cubic), whereas the increased distortion in Pr rich systems suppressed the same. The conduction mechanism was aided by the appropriate oxygen deficiency analyzed using XPS. Double Schottky Barrier (DSB), the resistive grain boundaries inhibiting TE performance was eliminated with the two step reduction process resulting in increased

the career mobility. Reduction process also promoted Pr nanoparticle precipitation which act as scattering centers to reduce thermal conductivity. A maximum power factor of 1.8 mW/mK^2 is achieved for x=0.10 system. Along with DSB reduction, the porous structure, Pr defect centers, Oxygen deficiency clusters together reduced the thermal conductivity of the material to achieve a maximum figure of merit of 0.33 at 673K for SPTO 3B (x=0.1) which is comparable to best performing oxide perovskites reported making it an ideal candidate as n type legs in thermoelectric generators to harvest waste heat and thereby to meet sustainable development goals.

References:

[1] J. He, M.G. Kanatzidis, V.P. Dravid, High performance bulk thermoelectrics via a panoscopic approach, Materials Today (2013). https://doi.org/10.1016/j.mattod.2013.05.004.

[2] L.D. Zhao, V.P. Dravid, M.G. Kanatzidis, The panoscopic approach to high performance thermoelectrics, Energy Environ Sci (2014). https://doi.org/10.1039/c3ee43099e.

[3] P.K. Jamshina Sanam, Et.al, Spin chiral interactions modulated Seebeck coefficient and improved optical properties by Zn doping in $CuCrO_2$ crystallites, Mater Chem Phys 308 (2023) 128214. https://doi.org/10.1016/j.matchemphys.2023.128214.

[4] P.K. Jamshina Sanam, M. Shah, P.P. Pradyumnan, Structure induced modification on thermoelectric and optical properties by Mg doping in $CuCrO_2$ nanocrystals, Solid State Commun 353 (2022) 114855. https://doi.org/10.1016/j.ssc.2022.114855.

[5] M. Shah, Et.al, Magneto thermoelectric effect of nickel thin film synthesized by RF magnetron sputtering, Physica E Low Dimens Syst Nanostruct 147 (2023) 115591. https://doi.org/10.1016/j.physe.2022.115591.

[6] P.K.J. Sanam, M. Shah, P.P. Pradyumnan, Raman spectroscopic investigation and thermoelectric studies of defect-induced Mg-doped delafossite thin film, Journal of Materials Science: Materials in Electronics (2022). https://doi.org/10.1007/s10854-022-09013-y.

[7] J.S. P.K., M. Shah, P.P. Pradyumnan, Tailoring structure and nanoscale surface topography in Mg–N doped $CuCrO_2$ thin films via post deposition annealing for optothermoelectric application, Opt Mater (Amst) 147 (2024) 114703. https://doi.org/10.1016/j.optmat.2023.114703.

[8] J.S. P.K., M. Shah, P.P. Pradyumnan, Intense narrow band blue emission in CuCrO2 delafossite by Ni^{2+}-Mg^{2+} dual cation doping, Spectrochim Acta A Mol Biomol Spectrosc 305 (2024) 123442. https://doi.org/10.1016/j.saa.2023.123442.

[9] J.S. P.K., M. Shah, P.P. Pradyumnan, Magnetoelectric coupling and thermoelectric behaviors in Ni-doped $CuCrO_2$ crystallites, Chemical Engineering Journal 476 (2023) 146568. https://doi.org/https://doi.org/10.1016/j.cej.2023.146568.

[10] T.A. Taha, Et.al, Structure, magnetic, opto-electronic and thermoelectric properties of $A_3In_2As_4$ and $A_5In_2As_6$ (A = Sr and Eu) Zintl phase compounds, J Alloys Compd 938 (2023) 168614. https://doi.org/10.1016/j.jallcom.2022.168614.

[11] R.K. Pingak, S. Bouhmaidi, A. Harbi, L. Setti, F. Nitti, M. Moutaabbid, A.Z. Johannes, N.U.J. Hauwali, M.Z. Ndii, A DFT investigation of lead-free $TlSnX_3$ (X = Cl, Br, or I) perovskites for potential applications in solar cells and thermoelectric devices, RSC Adv 13 (2023) 33875–33886. https://doi.org/10.1039/D3RA06685A.

[12] S. V Trukhanov, A. V Trukhanov, L. V Panina, V.G. Kostishyn, V.A. Turchenko, E.L. Trukhanova, An.V. Trukhanov, T.I. Zubar, V.M. Ivanov, D.I. Tishkevich, D.A. Vinnik, S.A. Gudkova, D.S. Klygach, M.G. Vakhitov, P. Thakur, A. Thakur, Y. Yang, Temperature evolution of the structure parameters and exchange interactions in $BaFe_{12-x}In_xO_{19}$, J Magn Magn Mater 466 (2018) 393–405. https://doi.org/10.1016/j.jmmm.2018.07.041.

[13] A. V Trukhanov, M.A. Almessiere, A. Baykal, Y. Slimani, E.L. Trukhanova, A. V Timofeev, V.G. Kostishin, S. V Trukhanov, M. Sertkol, A. Ul-Hamid, Correlation between the composition, structural parameters and magnetic properties of spinel-based functional nanocomposites, Nano-Structures & Nano-Objects 33 (2023) 100941. https://doi.org/10.1016/j.nanoso.2023.100941.

[14] D. Yang, X. Zhao, X. Zou, Z. Zhou, Z. Jiang, Removing Cr (VI) in water via visible-light photocatalytic reduction over Cr-doped $SrTiO_3$ nanoplates, Chemosphere 215 (2019) 586– https://doi.org/10.1016/j.chemosphere.2018.10.068.

[15] Y. Bi, M.F. Ehsan, Y. Huang, J. Jin, T. He, Synthesis of Cr-doped $SrTiO_3$ photocatalyst and its application in visible-light-driven transformation of CO_2 into CH_4, Journal of CO_2 Utilization 12 (2015) 43–48. https://doi.org/10.1016/j.jcou.2015.10.004.

[16] H. Tan, Z. Zhao, W. Zhu, E.N. Coker, B. Li, M. Zheng, W. Yu, H. Fan, Z. Sun, Oxygen Vacancy Enhanced Photocatalytic Activity of Pervoskite $SrTiO_3$, ACS Appl Mater Interfaces 6 (2014) 19184–19190. https://doi.org/10.1021/am5051907.

[17] M. Shah, P.K. Jamshina Sanam, P.P. Pradyumnan, Defect-induced $Sr_{1-x}Pr_xTiO_3$ crystallites by burial sintering and its optoelectronic applications, Journal of Physics and Chemistry of Solids 181 (2023) 111516. https://doi.org/10.1016/j.jpcs.2023.111516.

[18] P.K. Jamshina Sanam, M. Shah, P.P. Pradyumnan, Enhanced thermoelectric properties in dual cation doped $CuCrO_2$ nanocrystals mediated by magnon-carrier drag, Mater Res Bull 164 (2023) 112244. https://doi.org/10.1016/j.materresbull.2023.112244.

[19] P.K. Jamshina Sanam, M. Shah, P.P. Pradyumnan, The enhancement of NIR transparency due to annealing and Mg-doping in $CuCrO_2$ thin films, Mater Lett 330 (2023) 133295. https://doi.org/10.1016/j.matlet.2022.133295.

[20] M.A. Darwish, M.M. Hussein, S.A. Saafan, H.F. Abosheiasha, W. Abd-Elaziem, D.S. Klygach, S. V Trukhanov, T.I. Zubar, A. V Trukhanov, Modulating microwave attributes of $Ba_{1-x}Sr_xTiO_3$ nanoparticles: Insights into strontium concentration, structural intricacies and electromagnetic dynamics, Nano-Structures & Nano-Objects 37 (2024) 101096. https://doi.org/10.1016/j.nanoso.2024.101096.

[21] E. Zhou, J.-M. Raulot, H. Xu, H. Hao, Z. Shen, H. Liu, Structural, electronic, and optical properties of rare-earth-doped $SrTiO_3$ perovskite: A first-principles study, Physica B Condens Matter 643 (2022) 414160. https://doi.org/10.1016/j.physb.2022.414160.

[22] A. Baki, J. Stöver, T. Schulz, T. Markurt, H. Amari, C. Richter, J. Martin, K. Irmscher, M. Albrecht, J. Schwarzkopf, Influence of Sr deficiency on structural and electrical properties of $SrTiO_3$ thin films grown by metal–organic vapor phase epitaxy, Sci Rep 11 (2021) 7497. https://doi.org/10.1038/s41598-021-87007-2.

[23] J.A. Dawson, I. Tanaka, Local Structure and Energetics of Pr- and La-Doped $SrTiO_3$ Grain Boundaries and the Influence on Core–Shell Structure Formation, The Journal of Physical Chemistry C 118 (2014) 25765–25778. https://doi.org/10.1021/jp508444k.

[24] A.M. Dehkordi, S. Bhattacharya, T. Darroudi, H.N. Alshareef, T.M. Tritt, New insights on the synthesis and electronic transport in bulk polycrystalline Pr-doped $SrTiO_{3-\delta}$, J Appl Phys 117 (2015) 55102. https://doi.org/10.1063/1.4905417.

[25] X. Wan, X. Lu, L. Sun, M. Chen, N. Ta, W. Liu, Q. Chen, L. Chen, J. He, P. Jiang, X. Bao, Interface-enhanced thermoelectric output power in $CrN/SrTiO_{3-x}$ heterostructure, Journal of Energy Chemistry 64 (2022) 16–22. https://doi.org/10.1016/j.jechem.2021.04.056.

[26] D. Zhao, A. Würger, X. Crispin, Ionic thermoelectric materials and devices, Journal of Energy Chemistry 61 (2021) 88–103. https://doi.org/10.1016/j.jechem.2021.02.022.

[27] S. V Trukhanov, I.O. Troyanchuk, M. Hervieu, H. Szymczak, K. Bärner, Magnetic and electrical properties of $LBaMn_2O_{6-\gamma}$(L=Pr, Nd, Sm, Eu, Gd, Tb) manganites, Phys Rev B 66 (2002) 184424. https://doi.org/10.1103/PhysRevB.66.184424.

[28] S. OHTA, H. OHTA, K. KOUMOTO, Grain Size Dependence of Thermoelectric Performance of Nb-Doped $SrTiO_3$ Polycrystals, Journal of the Ceramic Society of Japan 114 (2006) 102–105. https://doi.org/10.2109/jcersj.114.102.

[29] J. Huang, P. Yan, Y. Liu, J. Xing, H. Gu, Y. Fan, W. Jiang, Simultaneously Breaking the Double Schottky Barrier and Phonon Transport in $SrTiO_3$-Based Thermoelectric Ceramics via Two-Step Reduction, ACS Appl Mater Interfaces 12 (2020) 52721–52730. https://doi.org/10.1021/acsami.0c16084.

[30] J.A. Dawson, X. Li, C.L. Freeman, J.H. Harding, D.C. Sinclair, The application of a new potential model to the rare-earth doping of $SrTiO_3$ and $CaTiO_3$, J. Mater. Chem. C 1 (2013) 1574–1582. https://doi.org/10.1039/C2TC00475E.

[31] V. Turchenko, A.S. Bondyakov, S. Trukhanov, I. Fina, V. V Korovushkin, M. Balasoiu, S. Polosan, B. Bozzo, N. Lupu, A. Trukhanov, Microscopic mechanism of ferroelectric properties in barium hexaferrites, J Alloys Compd 931 (2023) 167433. https://doi.org/10.1016/j.jallcom.2022.167433.

[32] R.P. Vasquez, $SrTiO_3$ by XPS, Surface Science Spectra 1 (1992) 129–135. https://doi.org/10.1116/1.1247683.

[33] H. Ogasawara, A. Kotani, R. Potze, G.A. Sawatzky, B.T. Thole, Praseodymium 3d- and 4d-core photoemission spectra of Pr_2O_3 Phys Rev B 44 (1991) 5465–5469. https://doi.org/10.1103/PhysRevB.44.5465.

[34] G. Liu, H.G. Yang, X. Wang, L. Cheng, H. Lu, L. Wang, G.Q. (Max) Lu, H.-M. Cheng, Enhanced Photoactivity of Oxygen-Deficient Anatase TiO_2 Sheets with Dominant {001} Facets, The Journal of Physical Chemistry C 113 (2009) 21784–21788. https://doi.org/10.1021/jp907749r.

[35] B. Bharti, S. Kumar, H.-N. Lee, R. Kumar, Formation of oxygen vacancies and Ti3+ state in TiO_2 thin film and enhanced optical properties by air plasma treatment, Sci Rep 6 (2016) 32355. https://doi.org/10.1038/srep32355.

[36] J. Wang, T. Wang, Z. Zhao, R. Wang, C. Wang, F. Zhou, S. Li, L. Zhao, M. Feng, Regulation of oxygen vacancies in $SrTiO_3$ perovskite for efficient photocatalytic nitrogen fixation, J Alloys Compd 902 (2022) 163865. https://doi.org/10.1016/j.jallcom.2022.163865.

[37] M.-C. Hsu, Y.-M. Sun, I.-C. Leu, M.-H. Hon, Microstructural and compositional studies of liquid-phase deposition derived $PbTiO_3$ thin films on LaNiO3 substrates, Appl Surf Sci 253 (2007) 7639–7644. https://doi.org/10.1016/j.apsusc.2007.03.073.

[38] D. Ehre, H. Cohen, V. Lyahovitskaya, I. Lubomirsky, X-ray photoelectron spectroscopy of amorphous and quasiamorphous phases of $BaTiO_3$ and $SrTiO_3$ Phys Rev B 77 (2008) 184106. https://doi.org/10.1103/PhysRevB.77.184106.

[39] A. Tkach, L. Amaral, P.M. Vilarinho, A.M.R. Senos, Oxygen vacancies as a link between the grain growth and grain boundary conductivity anomalies in titanium-rich strontium titanate, J Eur Ceram Soc 38 (2018) 2547–2552. https://doi.org/10.1016/j.jeurceramsoc.2018.01.014.

[40] S. V Trukhanov, A. V Trukhanov, H. Szymczak, R. Szymczak, M. Baran, Thermal stability of A-site ordered $PrBaMn_2O_6$ manganites, Journal of Physics and Chemistry of Solids 67 (2006) 675–681. https://doi.org/10.1016/j.jpcs.2005.09.099.

[41] Q. Tan, J. Li, Determination of the Oxygen Deficiency in Vacuum-Hot-Pressed Ferroelectric Ceramics Using a Thermogravimetric Technique, Journal of the American Ceramic Society 83 (2000) 451–453.https://doi.org/10.1111/j.1151-2916.2000.tb01219.x.

[42] I O Troyanchuk, S V Trukhanov, H Szymczak, K Baerner, Effect of oxygen content on the magnetic and transport properties of $Pr_{0.5}Ba_{0.5}MnO_{3-\gamma}$, Journal of Physics: Condensed Matter 12 (2000) L155. https://doi.org/10.1088/0953-8984/12/7/103.

[43] A. Spinelli, M.A. Torija, C. Liu, C. Jan, C. Leighton, Electronic transport in doped $SrTiO_3$: Conduction mechanisms and potential applications, Phys Rev B 81 (2010) 155110. https://doi.org/10.1103/PhysRevB.81.155110.

[44] D. Ekren, F. Azough, R. Freer, Enhancing the thermoelectric properties of $Sr_{1-x}Pr_{2x/3}\square_{x/3}TiO_{3\pm\delta}$ through control of crystal structure and microstructure, Philosophical Transactions of the Royal Society A: Mathematical, Physical and Engineering Sciences 377 (2019) 20190037. https://doi.org/10.1098/rsta.2019.0037.

[45] A. V Kovalevsky, A.A. Yaremchenko, S. Populoh, A. Weidenkaff, J.R. Frade, Effect of A-Site Cation Deficiency on the Thermoelectric Performance of Donor-Substituted Strontium Titanate, The Journal of Physical Chemistry C 118 (2014) 4596–4606. https://doi.org/10.1021/jp409872e.

[46] T.M. Tritt, Thermal Conductivity: Theory, Properties, and Applications (Physics of Solids and Liquids), n.d.

[47] Y. Miao, Y. Zhao, S. Zhang, R. Shi, T. Zhang, Strain Engineering: A Boosting Strategy for Photocatalysis, Advanced Materials 34 (2022) 2200868. https://doi.org/10.1002/adma.202200868.

[48] C. Yu, M.L. Scullin, M. Huijben, R. Ramesh, A. Majumdar, Thermal conductivity reduction in oxygen-deficient strontium titanates, Appl Phys Lett 92 (2008) 191911. https://doi.org/10.1063/1.2930679.

[49] W. Kim, A. Majumdar, Phonon scattering cross section of polydispersed spherical nanoparticles, J Appl Phys 99 (2006) 084306. https://doi.org/10.1063/1.2188251.

[50] S. Ohta, T. Nomura, H. Ohta, M. Hirano, H. Hosono, K. Koumoto, Large thermoelectric performance of heavily Nb-doped SrTiO3 epitaxial film at high temperature, Appl Phys Lett 87 (2005) 092108. https://doi.org/10.1063/1.2035889.

[51] J.Y. Yi, J.-K. Lee, Stabilized antiferroelectric phase in lanthanum-doped $(Na_{1/2}Bi_{1/2})TiO_3$, J Phys D Appl Phys 44 (2011) 415302. https://doi.org/10.1088/0022-3727/44/41/415302.

[52] A.M. Dehkordi, S. Bhattacharya, J. He, H.N. Alshareef, T.M. Tritt, Significant enhancement in thermoelectric properties of polycrystalline Pr-doped $SrTiO_{3-\delta}$ ceramics

originating from nonuniform distribution of Pr dopants, Appl Phys Lett 104 (2014) 193902. https://doi.org/10.1063/1.4875925.

[53] X.-L. Shi, H. Wu, Q. Liu, W. Zhou, S. Lu, Z. Shao, M. Dargusch, Z.-G. Chen, $SrTiO_3$-based thermoelectrics: Progress and challenges, Nano Energy 78 (2020) 105195. https://doi.org/10.1016/j.nanoen.2020.105195.

[54] Y. Lin, C. Norman, D. Srivastava, F. Azough, L. Wang, M. Robbins, K. Simpson, R. Freer, I.A. Kinloch, Thermoelectric Power Generation from Lanthanum Strontium Titanium Oxide at Room Temperature through the Addition of Graphene, ACS Appl Mater Interfaces 7 (2015) 15898–15908. https://doi.org/10.1021/acsami.5b03522.

[55] D. Liu, Y. Wang, X. Jiang, H. Kang, X. Yang, X. Zhang, T. Wang, Ultrahigh electrical conductivities and low lattice thermal conductivities of La, Dy, and Nb Co-doped $SrTiO_3$ thermoelectric materials with complex structures, J Mater Sci Technol 52 (2020) 172–179. https://doi.org/https://doi.org/10.1016/j.jmst.2020.02.065.

[56] S.R. Popuri, A.J.M. Scott, R.A. Downie, M.A. Hall, E. Suard, R. Decourt, M. Pollet, J.-W.G. Bos, Glass-like thermal conductivity in $SrTiO_3$ thermoelectrics induced by A-site vacancies, RSC Adv 4 (2014) 33720–33723. https://doi.org/10.1039/C4RA06871H.

[57] S. Bhattacharya, A. Mehdizadeh Dehkordi, S. Tennakoon, R. Adebisi, J.R. Gladden, T. Darroudi, H.N. Alshareef, T.M. Tritt, Role of phonon scattering by elastic strain field in thermoelectric $Sr_{1-x}Y_xTiO_{3-\delta}$, J Appl Phys 115 (2014) 223712. https://doi.org/10.1063/1.4882377.

[58] N. Yalini Devi, P. Rajasekaran, K. Vijayakumar, A.S. Alagar Nedunchezhian, D. Sidharth, G. Anbalagan, M. Arivanandhan, R. Jayavel, Enhancement of thermoelectric power factor of hydrothermally synthesised $SrTiO_3$ nanostructures, Mater Res Express 7 (2020) 015094. https://doi.org/10.1088/2053-1591/ab6c96.

[59] K. Park, J.S. Son, S.I. Woo, K. Shin, M.-W. Oh, S.-D. Park, T. Hyeon, Colloidal synthesis and thermoelectric properties of La-doped $SrTiO_3$ nanoparticles, J Mater Chem A Mater 2 (2014) 4217–4224. https://doi.org/10.1039/C3TA14699E.

Chapter 5

Optoelectronic applications of Pr doped $SrTiO_3$ thin films

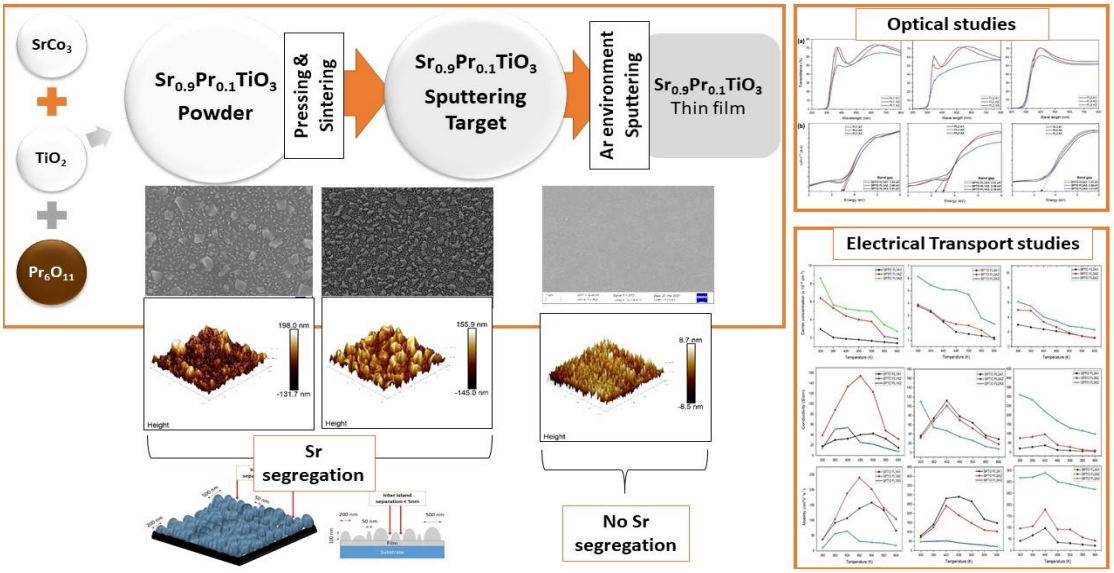

Objectives

This chapter examines the synthesis and characterization of Pr doped $SrTiO_3$ thin films for optoelectronic applications. RF magnetron sputtering in pure Argon atmosphere, followed by post-deposition heat treatment has been utilized for the growth of thin films. The study aims to explore the structural, electrical, and optical properties of the films, including Stranski-Krastanov growth and cation segregation, with a focus on optimizing their electrical transport properties for transparent conducting oxide (TCO) applications. The enhanced carrier mobility and visible light transparency makes these thin films a strong candidate for advanced optoelectronic devices.

5.1 Introduction

Functional oxides have played a pivotal role in advancing technologies across various fields, including wearable devices, sensors, spintronics, photonics, thermoelectrics, and photovoltaics. Their diverse compositional possibilities and phase tunability open up vast potential for developing new functional oxides with a wide range of properties, whether in bulk or thin film forms [1–10]. Thin film materials are employed in a wide range of applications, including anti-reflective coatings, memory devices, piezoelectric and triboelectric systems, energy storage and conversion mechanisms, wearable electronics, and sensing and amplification technologies. Advances in thin film material research and technology have driven significant progress in electronics, yet despite the availability of advanced growth techniques such as molecular beam epitaxy, pulsed laser deposition, RF magnetron sputtering, and atomic layer deposition, challenges remain in pushing performance to new levels. Charge transport in semiconducting oxides is governed by the interaction between cationic and anionic orbitals, making high mobility a key factor in electronic device performance [11,12].

Functional oxides hold great potential for enabling next-generation electronic devices. Among these, perovskite oxides have emerged as a prominent class due to their ability to incorporate nearly all elements from the periodic table into their structures. A significant advantage of perovskites lies in their high static dielectric permittivity, which minimizes electron-charge interactions and facilitates efficient electron transport. In doped perovskite oxides, electron mobility at room temperature is predominantly influenced by electron-phonon interactions rather than ionized impurity scattering, attributed to their strong polarization effects. Strontium titanate, a well-known perovskite oxide, is widely employed in various functional applications, including optoelectronics and photocatalysis. However, its utility in optoelectronics is limited by its wide bandgap of approximately 3.3 eV, which arises from the separation between the dominant O 2p states and the hybridized O2p-Ti3d states (with minor contributions from Ti3d states). To extend the applicability of STO in optoelectronic devices, bandgap modulation

presents a promising approach to achieve enhanced electrical conductivity and optical transparency [13]. Theoretical and experimental attempts have been made to engineer the bandgap, including doping, hetero structure formation and vacancy production [14–16].

Doping $SrTiO_3$ with elements such as Lanthanum, Tantalum, Yttrium, and Niobium is a common approach to enhance its optoelectronic properties. La and Y doped STO show great potential as bottom electrode materials in photovoltaic applications. On the other hand, Nb-doped STO were frequently employed in transparent conducting oxides (TCO) and thermoelectric devices due to its excellent electrical conductivity, high optical transparency, and low thermal conductivity. These modifications expand the functionality of STO, making it a valuable material for various advanced optoelectronic and energy applications.[17,18]. La doped $SrTiO_3$ thin films were previously reported to have good electrical and thermoelectric capabilities with conductivities in the range 10^2-10^4 S/cm but with limited mobility of the order of 10 $cm^2 V^{-1} s^{-1}$ [19–21]. Nb doped films have very high carrier density and conductivity of the order 10^{22}-10^{23} cm^{-3} and 1000 to 3300 S cm^{-1} respectively[22,23]. Pr-doped $SrTiO_3$ (STO) systems have been explored in various applications, including conductive and semiconducting ceramics, photodetectors, solar cells, catalysts, sensors, spintronics, and thermoelectrics. However, most of the research has concentrated on bulk materials. Studies on Pr doping in STO thin films are relatively limited and have mainly focused on their ferroelectric, dielectric, luminescence, and electrical conductivity properties [24–29]. Despite the existing studies on the optoelectronic properties of Pr-doped STO bulk systems, there is a noticeable scarcity of literature on thin film systems, especially compared to La and Nb-doped STO**.** There are previous works that explicitly uses mechanisms like redox chemistry, oxygen vacancy in Pr doped STO systems to manipulate electrical surface properties to get carrier concentration of the order of 10^{20} cm^{-3} [30,31]. Maintaining the optical transparency and metal-like electrical properties of $SrTiO_3$ (STO) is crucial for its effectiveness as a transparent conducting oxide (TCO). Leveraging the potential of STO thin films

necessitates a comprehensive understanding of their optical behavior. Furthermore, analyzing the growth and stabilization processes of doped STO thin films in relation to key synthesis parameters, such as RF sputtering power, gas pressure, dopant concentration, and defect mechanisms, which is critical for their successful implementation in practical applications [32,33]. Heat treatment in perovskite oxide thin films often induces surface restructuring phenomena, leading to the enrichment of A-site cations, particularly Sr, near the surface. This phenomenon is frequently reported and can limit the material's potential in electrochemical and optoelectronic applications.

This study investigates the impact of RF sputtering gas pressure on the electrical and optical properties of Pr-doped STO thin films grown on quartz substrates. A notable enhancement in carrier mobility, resulting in high electrical conductivity, is demonstrated, along with a controlled modulation of the optical bandgap. By employing an oxygen-free synthesis method and optimizing post-deposition annealing to mitigate cation segregation, thin films with minimal cation deficiency were achieved, significantly improving their electrical performance. While surface restructuring and dopant effects have been extensively studied for other elements, the role of Pr in STO remains largely unexplored for electrical and optoelectronic applications. With its partially filled 4f electron shell, Pr can introduce localized electronic states within the bandgap, influencing carrier concentration and conductivity. Additionally, its unique 4f-4f transitions offer sharp, environment-sensitive optical features, making Pr-doped STO a promising candidate for advanced electronic and optoelectronic devices.

5.2 Experimental techniques

Sr_{1-x} Pr_x TiO_3 with x=0.10 sputtering target was prepared through high-temperature solid-state reaction route with suitable precursors having 99.99% purity. The sintered powder was shaped into a 2-inch disk-shaped target. To ensure compositional uniformity, the disk was crushed, pulverized, re-pressed, and re-sintered and used as RF sputtering target. Ultrasonically cleaned and dried quartz substrates were loaded into the deposition chamber, which was evacuated to a base pressure of 5×10^{-6} mbar prior to deposition. Pr

doped STO thin films were deposited on quartz substrates at a substrate temperature of 500 °C, using a sputtering power of 150 W for deposition time of 90 minutes. The sputtering process was carried out in a pure argon atmosphere, with chamber pressures maintained between 1×10^{-2} and 3×10^{-2} mbar. The as-deposited films were annealed in a tubular furnace for 4 hours at temperatures of 600 °C, 700 °C, and 800 °C, and the resulting films were labeled as described in Table 5-1.

Table 5- 1 Sample labels of Pr doped $SrTiO_3$ thin films under different sputtering and annealing conditions

Sputtering pressure (mbar)	**Annealing temperature**		
	600 °C	**700 °C**	**800 °C**
1×10^{-2}	SPTO FL1A1	SPTO FL1A2	SPTO FL1A3
2×10^{-2}	SPTO FL2A1	SPTO FL2A2	SPTO FL2A3
3×10^{-2}	SPTO FL3A1	SPTO FL3A2	SPTO FL3A3

For structural analyses, X-ray diffractometer with Cu-K_α radiation of wavelength (λ= 1.5418 Å) was utilized with 2θ values ranging from 20 to 80°. Raman spectra were obtained using the Jasco NRS 4100 instrument (532 nm). The materials morphology was studied using Field emission gun scanning electron microscope (FE-SEM) and surface characteristics were assessed using a Bruker multimode 8 high-performance atomic force microscope (AFM). Optical spectroscopic measurements were taken between 200 and 800 nm. The Photoluminescence properties of the thin films were investigated using Fluorescence spectrophotometer with Time-correlated single photon counting facility. The electrical transport properties were analyzed using Hall effect measurements performed with the Van der Pauw (VDP) configuration at both room temperature and elevated temperatures.

5.3 Results and discussion

5.3.1 Structural, morphological characterization: XRD, Raman spectroscopic studies, FE-SEM & AFM

The XRD pattern of the sintered Pr-doped STO target is presented in Fig. 5-1(a). The analysis confirmed the presence of a pure STO phase, as the XRD reflections matched the XRD pattern of the sintered Pr-doped STO target is presented in Fig. 5-1(a). The analysis confirmed the presence of a pure STO phase, as the XRD reflections matched the reference pattern in the database (PDF#35-0734).

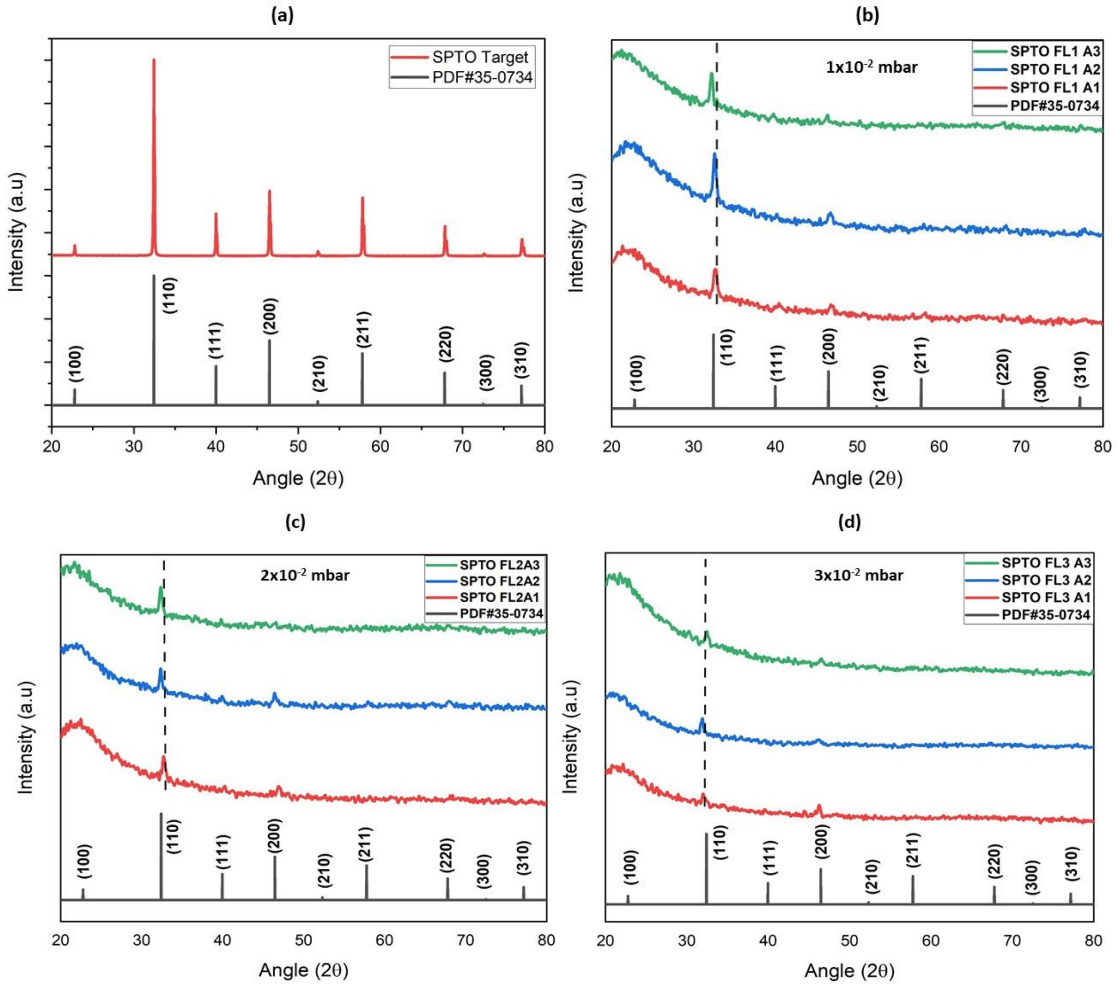

Figure 5- 1 (a) XRD pattern of Pr substituted $SrTiO_3$ sputtering target **(b)** XRD patterns of films deposited at $1x10^{-2}$ mbar **(c)** at $2x10^{-2}$ mbar **(d)** at $3x10^{-2}$ mbar Ar gas pressure and annealed at 600 °C, 700 °C and 800 °C

The as-deposited thin film was initially amorphous and underwent post-deposition annealing at 600 °C, 700 °C, and 800 °C. The diffraction patterns of the annealed thin films, along with the corresponding sputtering gas pressures, are shown in Fig. 5-1(b) (c) and (d). Crystallization was observed in all annealed thin films, with prominent reflections at the (110) plane around 32° and the (200) plane around 46° are shown.

In addition to the primary peaks, thin films deposited at lower gas pressures, such as SPTO FL1 and FL2, exhibit a (111) reflection around 40°. In contrast, thin films grown at higher gas pressures show reduced intensities of dominant peaks, attributed to the shorter mean free path of target particles, which leads to lower deposition rates and reduced crystallinity. At low pressures, electrons with a longer mean free path store more energy before colliding with Ar gas molecules, and these collisions result in active ionizations, leading to increased growth rates. Annealing at higher temperatures between 700 °C and 800 °C significantly enhances the crystallinity of all thin film series compared to those treated at 600 °C. Additionally, the FWHM of all samples decreases with increasing annealing temperature. A shift of the peaks to lower angles, observed in all samples except SPTO FL3A3, indicates an increase in the lattice constant, suggesting lattice expansion. Since the deposition occurs in a pure argon environment, the thin films are oxygen-deficient. Annealing not only improves crystallinity but also helps to compensate the oxygen deficiencies by promoting oxygen incorporation into the lattice. High-temperature annealing around 700 °C in an oxygen-rich environment can fully compensate the oxygen loss and restore stoichiometry [34]. Conversely, annealing at high temperature also promote the loss of oxygen from lattice and the loss intensifies with annealing temperature resulting in oxygen deficient structures [35]. Oxygen loss from the lattice and subsequent oxygen incorporation via oxidation, work in opposition to shape the final structure. The observed lattice expansion, indicated by the shift to lower angles, suggests that the expansion results from increased oxygen loss during annealing. This lattice expansion can be attributed to the lower valence state of the Ti cation, which elongates the Ti-O bond. The strain generated on the grains during deposition and annealing alters the crystal parameters, causing them to deviate from their bulk

counterparts. This increased stress is likely due to changes in the type and concentration of defects, such as the substitution of Pr^{3+} into the Sr^{2+} site and the redistribution of oxygen vacancies. In addition to oxygen defects, factors like thermal stress, deposition rate, and the film thickness under varying gas pressures also contribute to variations in the lattice parameters.

The average crystallite size of the sample was estimated using the Scherrer formula as in eqn (5.1) using the FWHM of two predominant peaks.

$$t = \frac{k\lambda}{\beta \cos\theta} \tag{5.1}$$

Symbols carry their formal significance, and the calculations were performed using k=0.94 under the assumption of a Gaussian peak shape. The results are summarized in Table 5-2. The decrease in FWHM values indicates that the sharpness of the prominent peaks improves with increasing annealing temperature. The estimated crystallite size increased from 13 nm to 20 nm with annealing, attributed to the growth of larger grains driven by enhanced atom migration and mobility. During post-deposition thermal treatment, atoms gain sufficient energy to move toward their equilibrium positions, reducing lattice strain. This enhances grain growth, decreases lattice dislocations, and improves the overall crystallinity of the thin films [36,37]. The microstrain on lattice was calculated using eqn (5.2)

$$\varepsilon = \frac{\beta}{4 \tan\theta} \tag{5.2}$$

As expected with the increase in crystallite size, the microstrain in all series of thin films decreases from approximately 0.009 to 0.005 with annealing. This reduction in microstrain is due to the elimination of lattice defects with the increase of annealing temperature, and reaching its lowest value at 800 °C.

Table 5- 2 Crystallite size and strain of the thin films under various sputtering and annealing conditions

Sample label	A1 600 °C		A2 700 °C		A3 800 °C	
	Crystallite size (nm)	strain ($x10^{-3}$)	Crystallite size (nm)	strain ($x10^{-3}$)	Crystallite size (nm)	strain ($x10^{-3}$)
SPTO FL1	13.2	8.94	15.9	6.64	19.1	5.78
SPTO FL2	16.6	7.84	18.9	5.75	19.5	5.43
SPTO FL3	13.9	8.98	19.2	7.31	20.1	5.81

Raman analysis of various vibrational modes provides crucial insights into the structural changes and phase transitions induced by annealing. Figure 5-2 presents the micro-Raman spectra of Pr-doped STO thin films deposited at different Ar gas pressures and annealed at 600 °C, 700 °C, and 800 °C. The spectra exhibit broad peaks within the ranges of 190–550 cm^{-1} and 680–850 cm^{-1}. STO undergoes an antiferrodistortive phase transition from a cubic structure (space group Pm-3m) to a tetragonal structure (I4/mcm), characterized by the rotation of TiO_6 octahedra. The resulting tetragonal structure is centrosymmetric, suggesting no ferroelectric behavior is expected [38]. From our previous works on Pr doped STO ceramics, it has been observed that when Pr concentration equals or exceeds x=0.10 in $Sr_{1-x}Pr_xTiO_3$ system it transforms from cubic to tetragonal phase [13]. Since the sputtering target we used here was with x=0.10, we presume that thin films will be STO tetragonal.

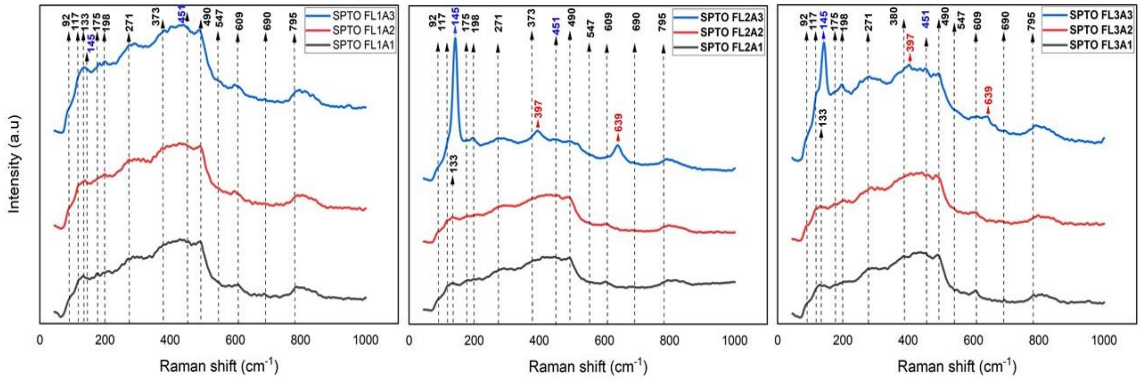

Figure 5- 2 Raman spectra of Pr substituted $SrTiO_3$ thin films deposited at different Ar gas pressure and annealed at 600 °C, 700 °C and 800 °C

In STO-based structures, zone-center optical phonons are Raman inactive, resulting in the spectrum being dominated by second-order vibrations. All 12 optical phonon modes in STO exhibit odd symmetry with respect to inversion, meaning first-order Raman scattering is typically forbidden by phonon momentum selection rules. However, defects introduced through doping, annealing, and oxygen-deficient sputtering conditions relax these rules, making the first-order spectrum observable.

First-order peaks in the Raman spectrum are observed at 175, 271, and 547 cm^{-1}, corresponding to the TO_2, TO_3, and TO_4 phonon modes, while the peaks at 490 and 795 cm^{-1} are attributed to the LO_2 and LO_4 phonon modes, respectively. The appearance of first-order Raman scattering is a result of symmetry breaking caused by factors such as electric fields, strain from lattice mismatch and grain boundaries, and the incorporation of Pr ions into the crystal lattice. The peaks at 175 and 271 cm^{-1} are associated with the (O-Sr-O) bending mode, whereas the peaks at 547 and 795 cm^{-1} are related to the (Ti-O-Ti) bending mode and Ti-O stretching mode, respectively. Additionally, peaks at 117 and 133 cm^{-1} appear in all samples, caused by structural deformation of the lattice, which relaxes the selection rules. A second-order band at 373 cm^{-1} is attributed to the combination of multiple bands such as TO_4-TA, TO_4-TO_1, and $2TO_2$. The band at 690 cm^{-1} is identified as the $2TO_3$ overtone, and the peak at 609 cm^{-1} corresponds to a second-order Raman mode. Notably, prominent peaks at 397 cm^{-1} and 639 cm^{-1} are exclusively observed in samples annealed at 800 °C, corresponding to the $B_{1g(1)}$ and $E_{g(3)}$ modes, respectively [39]. Very strong Raman peak observed at 145 cm^{-1} and a feeble peak at 451 cm^{-1} can be correlated to E_g and B_{2g} modes indicating the tetragonal symmetry. Tetragonal $SrTiO_3$ exhibits seven Raman-active modes, comprising two pairs of degenerate modes $\{E_g, B_{1g}\}$ and a B_{2g} mode. The corresponding Raman bands have been detected within the frequency ranges of 140-150 cm^{-1}, 440-460 cm^{-1}, and 220-260 cm^{-1}. The detected peaks here indicates the tetragonal phase of STO [40–42]. The peaks show higher intensity in the SPTO 2 and SPTO 3 series samples annealed at 800 °C, indicating a more significant tetragonal distortion. Higher annealing temperatures facilitate the formation of larger crystals composed of multiple smaller crystallites, as confirmed by

Table 5- 3 Raman modes observed in Pr doped STO thin films

Peak position (cm^{-1})	**Assignment**	**Phonon mode**	**Mode type**	**Symmetry mode**	**Order**	**Notes**
117	Structural deformation	–	–	–	First	Appears in all samples; relaxes selection rules.
133	Structural deformation	–	–	–	First	Appears in all samples; relaxes selection rules.
145	E_g mode	–	–	E_g	First	Very strong; indicates tetragonal symmetry (140–150 cm^{-1} range).
175	(O-Sr-O) bending	TO_2	TO	–	First	Associated with tetragonal phase.
271	(O-Sr-O) bending	TO_3	TO	–	First	Associated with tetragonal phase.
373	Combination bands	–	–	–	Second	TO_4-TA, TO_4-TO_1, and $2TO_2$.
397	$B_{1g(1)}$ mode	–	–	B_{1g}	First	Exclusively in 800 °C-annealed samples.
451	B_{2g} mode	–	–	B_{2g}	First	Feeble; indicates tetragonal symmetry (440–460 cm^{-1} range).
490	–	LO_2	LO	–	First	–
547	(Ti-O-Ti) bending	TO_4	TO	–	First	–
609	Second-order Raman mode	–	–	–	Second	–
639	$E_{g(3)}$ mode	–	–	E_g	First	Exclusively in 800 °C-annealed samples.
690	$2TO_3$ overtone	–	–	–	Second	–
795	Ti-O stretching	LO_4	LO	–	First	–

XRD analysis. This process leads to a red shift in the Raman frequency and a narrowing of the peak, as observed in the Raman mode at 145 cm^{-1}.

The high-resolution SEM images of the Pr doped STO films are shown in Fig. 5-3, highlighting the significant influence of heat treatments on the film morphology. The observed morphologies vary noticeably across the series of films, depending on the sputtering gas pressure and annealing temperature. In the FL1 series annealed at 600 °C (SPTO FL1A1), fine granular particles are scattered across the surface, forming an island-like pattern. At an annealing temperature of 700 °C (SPTO FL1A2), the islands become slightly more separated, and inter-granular pores begin to appear. When annealed at 800 °C (SPTOFL1A3), distinct changes are observed, with the island-like structures becoming uniformly distributed over the film surface. Large clusters, ranging in size from 300 to 400 nm, are evident, while the smaller inter-cluster granules measure between 50 and 80 nm.

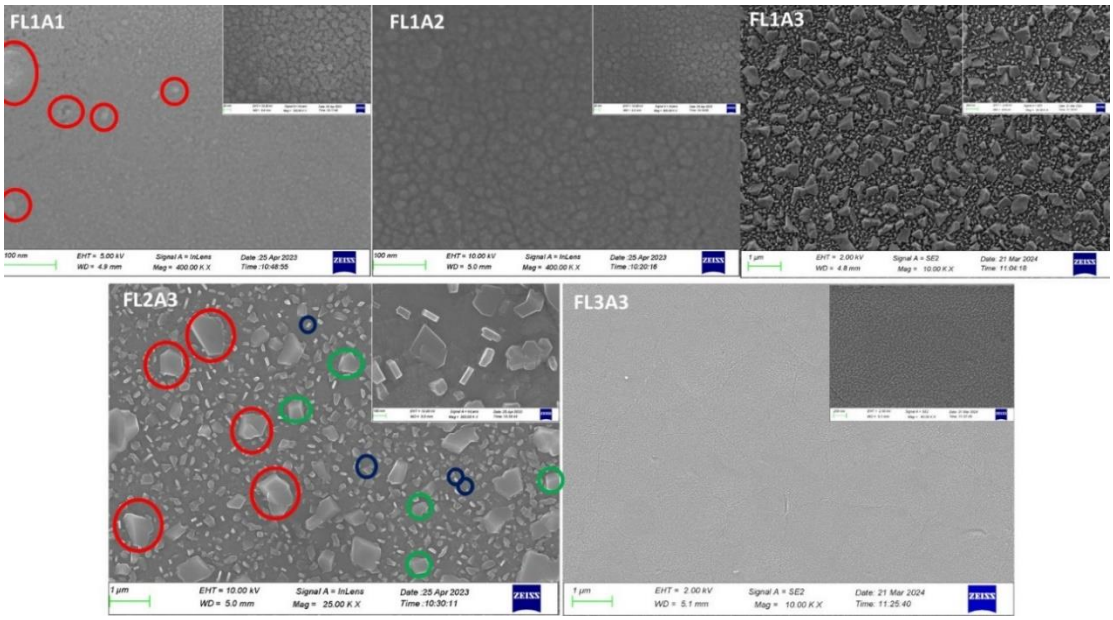

Figure 5- 3 HR SEM images of Pr substituted $SrTiO_3$ films deposited at different Ar gas pressure and annealed at 600 °C, 700 °C and 800 °C

Thin film growth ideally follows the Frank–Van der Merwe (FM) model, which is characterized by layer-by-layer deposition. However, the RF sputtering conditions and subsequent annealing introduce variations in film thickness, causing the growth mode to deviate from the FM model. This deviation leads to the transition towards Stranski–

Krastanov (SK) and Volmer–Weber (VW) growth modes, resulting in thin films that exhibit a combination of island structures and layers, as observed in the samples annealed at 800 °C.

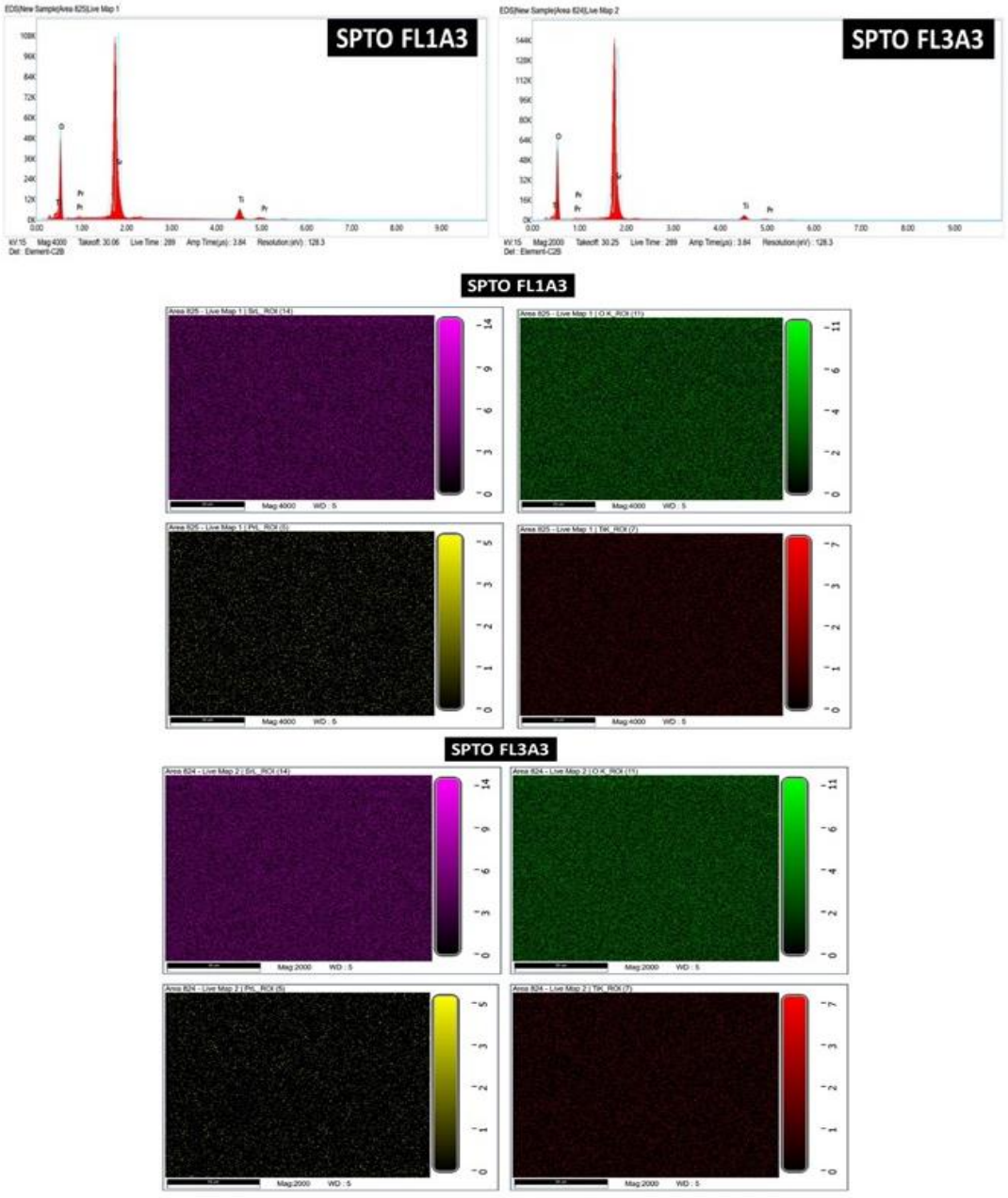

Figure 5- 4 EDS and elemental mapping of Pr substituted $SrTiO_3$ films

The well-established formation of 3D clusters/nano islands has a significant impact on the transport properties of the thin films. This island-like formation is also evident in the SPTO FL2 series of thin films, particularly in those annealed at 800 °C (FL2 A3). In these thin films, the red, green, and blue circled islands have sizes of 500 nm, 200 nm, and 50-80 nm, respectively. Moving on to the FL3 series, thin films annealed at 800 °C show a transformation from island-mode growth to continuous film growth with a high degree of ordering, which is expected to profoundly affect the electrical and thermal transport properties.

Complex oxides commonly undergo symmetry loss at the surface during growth, leading to cation segregation. Gaining insight into these growth mechanisms is essential for identifying appropriate applications for these materials, particularly in fields like photo catalysis, electrochemistry, and thermoelectrics.

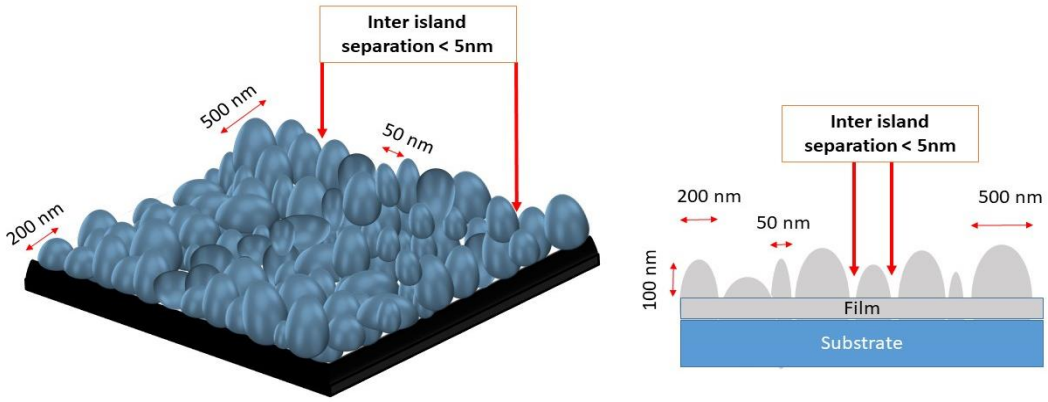

Figure 5- 5 Schematic representation of Stranski–Krastanov growth mechanism in Pr doped $SrTiO_3$ thin films

Annealing in an oxidizing atmosphere promotes Sr segregation at the surface while maintaining the overall perovskite structure. The competition among different cations for the same site, or between A-site and B-site cations, drives atomic rearrangements at the surface, leading to segregation. This effect becomes more pronounced at higher temperatures, where increased ion mobility and faster diffusion dynamics facilitate greater nucleation and segregation [43–45]. Excess Sr segregates at

the thin film surface, appearing as oxide islands. The incorporation of Pr as an A-site dopant and the formation of oxygen vacancies create elastic and electrostatic interactions, both of which influence Sr segregation.

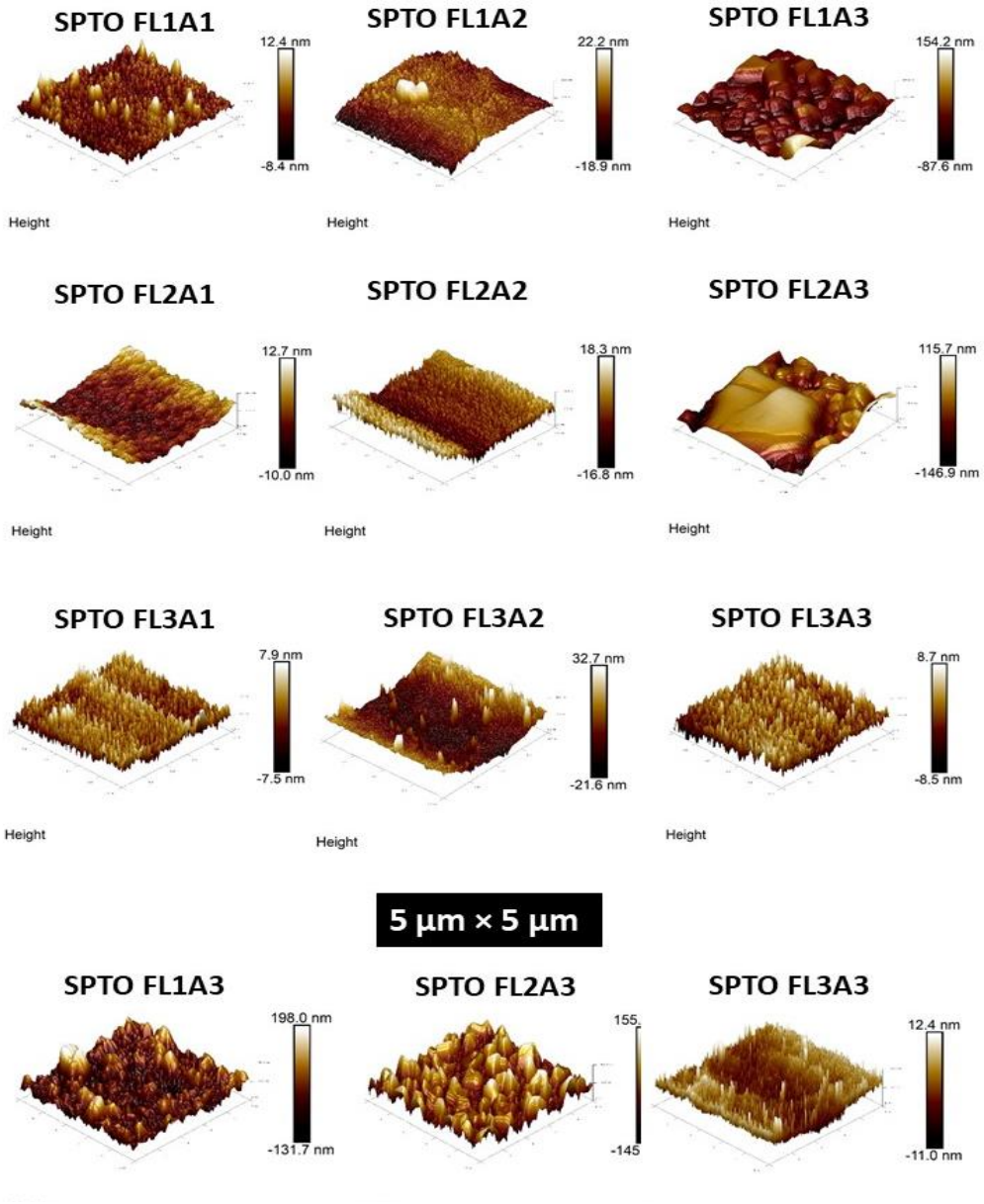

Figure 5- 6 3D AFM images of Pr substituted $SrTiO_3$ thin films

However, disentangling these interconnected phenomena to determine their individual contributions is challenging. The size disparity between the dopant Pr^{3+} (ionic

radius = 1.30 Å) and the host Sr^{2+} (ionic radius = 1.44 Å) generates elastic energy, prompting atomic-scale rearrangements that drive Sr segregation to the surface. Introducing smaller dopants could theoretically mitigate lattice segregation. Applying tensile strain to the system offers an alternative means of reducing segregation. XRD analysis confirms that tensile strain, associated with lattice contraction, is present in the SPTO FL3A3 sample, as indicated by a shift to higher diffraction angles. This tensile strain effectively minimizes Sr segregation.

Figure 5-4 shows the EDS spectra and elemental mapping for thin films SPTO FL1A3 and SPTO FL3A3. The detected peaks correspond to Sr, Ti, O, and Pr, aligning with the composition of the prepared thin films, with no impurity peaks observed. The images also confirm the uniform distribution of all elements, including the dopant, across the surface of the samples.

Fig. 5-5 illustrates the proposed growth mechanism of STO thin films. The surface morphology of the prepared thin films was further examined at room temperature using two-dimensional (2D) and three-dimensional (3D) AFM imaging, with the results displayed in Figure 5-6. The thin films exhibit a uniform, flawless, and crack-free surface morphology. The average surface roughness increases with annealing temperature, leading to highly rough surfaces at 800 °C due to Sr segregation and SK growth. For instance, SPTO FL1A1 shows an RMS roughness of 2.92 nm, which increases to 3.08 nm for SPTO FL1A2 and significantly rises to 37.7 nm for SPTO FL1A3. A similar trend is observed in the SPTO FL2 series. In contrast, SPTO FL3A3 has the smoothest surface morphology within the series, as confirmed by SEM analysis, with an RMS roughness of just 2.11 nm and no evidence of Sr segregation. Across all series, annealing at 800 °C results in high surface roughness, except for SPTO FL3A3.

5.3.2 Optical characterization: UV-Vis Spectroscopy and photoluminescence studies

In order to understand the optoelectronic properties of the prepared thin films, transmission spectra were analyzed in the UV-Vis region (200–800 nm), which covers

the fundamental optical absorption edges of STO-based thin films. The transmission spectra are shown in Fig. 5-7(a), while the bandgap, calculated using the Tauc equation, is presented in Fig. 5-7(b). All samples exhibit significant transmittance in the visible range, ranging from 60% to 70%. With this reasonable transmittance good electrical characteristics is also needed for TCO applications. Thin films subjected to higher annealing temperature exhibited lower transmittance due to the larger grain size, contributing to increased absorption. All thin films have absorption edges that fall between 350 and 390 nm in wavelength. Furthermore, it is seen that, within a given series of thin films, the absorption edge redshifts with increasing annealing temperature, with the exception of SPTO FL3A3, where a blue shift is noted. This behavior can be associated with the concentration of oxygen vacancies, as the dopant concentration is constant within a particular series of thin films.

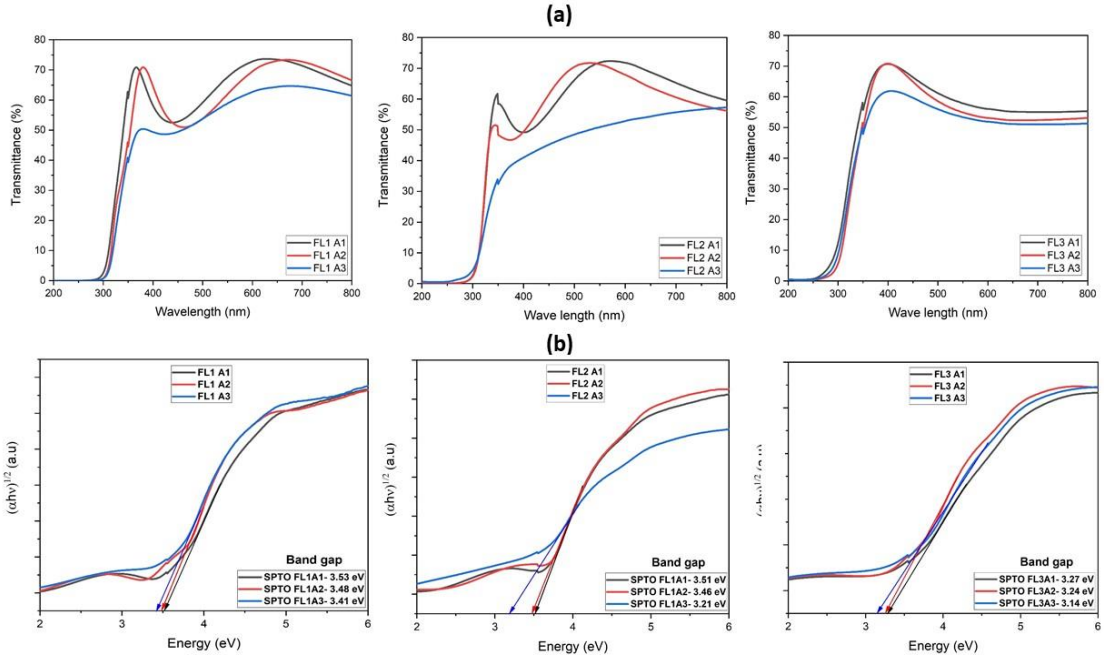

Figure 5- 7 (a) UV-Vis transmission spectra **(b)** Band gap of Pr substituted $SrTiO_3$ thin films deposited at different Ar gas pressure and annealed at 600 °C, 700 °C and 800 °C.

The broadening of the absorption edge can also result from exciton-phonon coupling or dynamic disorder. A similar phenomenon, where oxygen vacancies are linked to a blue shift in the absorption edge, has been reported in previous studies. For

instance, Wei Huang et al. documented a correlation between oxygen vacancies and the observed blue shift in the absorption edge for STO thin films grown under varying oxygen partial pressures during deposition [46]. The blue shift of SPTO FL3A3 is also expected due to the decreased number of oxygen vacancies in the system deduced from XRD analysis.

Absorption coefficient α for thin films is represented as

$$\alpha = \frac{-\ln(T)}{d} \tag{5.3}$$

Where T is the transmittance and d is the thickness of the films. The indirect optical transitions of STO films can be used to determine the band gap as per Tauc relation

$$\alpha E = A(E - E_g)^n \tag{5.4}$$

Using E as the photon energy and A as a function of the refractive index and hole effective masses, n is set to 1/2 or 2 for direct and indirect bandgap materials, respectively. The bandgap values were determined using the linear extrapolation method, as described by eqn (5.4), and are shown in Fig. 5-7(b). The calculated bandgap values are listed in Table 5-3. These values exceed the bulk bandgap of 3.2 eV, which can be attributed to the substitution of Pr at Sr sites, deformation potentials, strain-induced defects from the small crystallite size, and the presence of free carriers [47]. In all three series of films, the bandgap decreases as the annealing temperature increases, with the lowest bandgap observed in the samples annealed at 800 °C, except for SPTO FL3A3. A reduction in bandgap, or a red shift, with increasing temperature suggests that higher temperatures enhance the quality of the STO layer, causing the bandgap to approach the bulk value. This decrease in bandgap can also be linked to the presence of oxygen vacancies in the lattice. As oxygen vacancies increase, the bandgap (E_g) reduces due to the emergence of a new bonding exciton-energy level near the conduction band minimum, narrowing the energy gap. Within a given series of films, the sample with the most left-shifted XRD peaks corresponds to the smallest bandgap, aligning with the relationship between XRD patterns and vacancy-induced disorder.

The Urbach energy of the prepared films may be found following the Urbach relation represented in eqn (5.5) which gives a more comprehensive picture of the band edge characteristics.

$$ln(\alpha) = \frac{1}{E_u} h\upsilon - \frac{E_g}{E_u} + ln(\alpha_0) \quad (5.5)$$

Where α is the absorption coefficient, $h\upsilon$ the energy, E_g is the energy band gap and E_u is the Urbach energy.

Table 5- 4 Bandgap and Urbach energy values of Pr doped $SrTiO_3$ films

Sample label		**Band gap, E_g (eV)**	**Urbach energy, E_u (eV)**
SPTO FL1	A1	3.53	0.360
	A2	3.48	0.377
	A3	3.41	0.401
SPTO FL2	A1	3.51	0.300
	A2	3.46	0.310
	A3	3.16	0.569
SPTO FL3	A1	3.27	0.523
	A2	3.26	0.526
	A3	3.31	0.476

Variations in Urbach-type absorption may reflect static inhomogeneity arising from localized states within the bandgap, which can be assessed by analyzing the steepness of the band edge. In the prepared films, the band edge steepness generally decreases with increasing annealing temperature across all series, except for SPTO FL3A3, where it increases, indicating a reduction in Urbach energy. Higher annealing temperatures lead to an increase in Urbach energy and a decrease in bandgap energy, attributed to film crystallization. An inverse relationship between Urbach energy and

bandgap is observed in all films. The rise in Urbach energy with increasing annealing temperature also correlates with the presence of oxygen vacancies in STO films. As oxygen vacancies increase, a corresponding increase in Urbach energy is expected. This trend aligns with prior research and highlights the role of oxygen vacancies (V_O) in influencing variations in the absorption coefficient. The non-stoichiometric Pr: SrTiO3-δ exhibits a more gradual decrease in absorbance near the absorption edge compared to

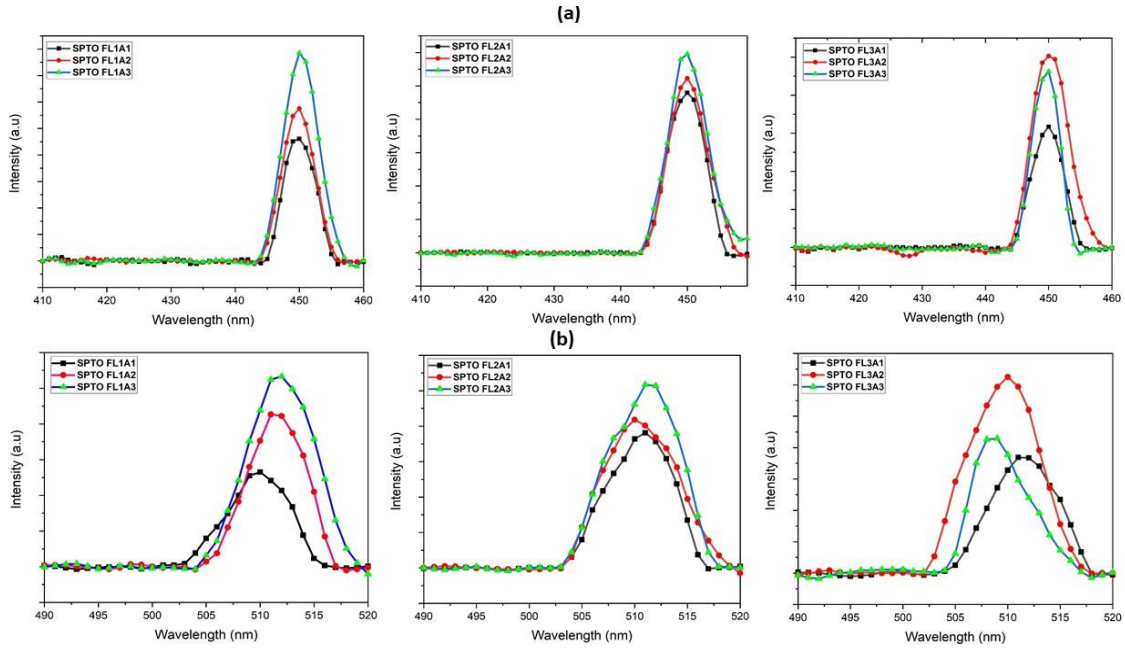

Figure 5- 8 (a) PL emission spectra of Pr substituted $SrTiO_3$ thin films around 450 nm and **(b)** PL emission peaks around 510 nm

the pure STO parent compound due to the presence of a tailing localized state [48–51].

A sharper increase in Urbach energy observed in SPTO FL1A3 and FL2A3 indicates greater distortions and defects in the system caused by surface segregation. Urbach energy, associated with band edge roughness and local potential fluctuations in both the conduction and valence bands, shows a positive correlation with the Stokes shift and an inverse relationship with carrier mobility in semiconductors [52]. In the SPTO FL1 and FL2 series, the thin films annealed at 800 °C (SPTO FL1A3 and SPTO FL2A3) exhibit the highest Urbach energy. These thin films also demonstrate the lowest mobility, confirming the negative correlation between Urbach energy and mobility. Conversely,

in the SPTO FL3 series, the thin film with the lowest Urbach energy, SPTO FL3A3, is likely to exhibit the highest carrier mobility.

Photoluminescence (PL) analysis of $SrTiO_3$ thin films was conducted to investigate emissions potentially caused by oxygen vacancies. Undoped STO typically displays a strong PL peak near 540 nm, along with infrared emission at approximately 800 nm under low-temperature conditions [53]. PL emissions are generally associated with defect states within the bandgap, predominantly arising from impurities and vacancies, particularly oxygen vacancies formed during synthesis, either as isolated entities or in clusters. When excited with UV light at 330 nm, the PL spectra of the samples reveal multiple emission peaks at 450, 467, 510, and 540 nm, with special emphasis on the peaks at 450 nm and 510 nm. Earlier studies on undoped STO subjected to Ar^+ irradiation identified intense blue emission at 430 nm, attributed to oxygen vacancies introduced within 20 nm of the surface under 325 nm excitation. Similarly, research by Rho et al. on STO crystals exposed to 3 MeV proton beam bombardment revealed emission peaks around 420 nm. Blue PL emission has also been observed by various groups using other ion irradiation techniques, such as deuterium and helium [52].

Fig. 5-8 (a) and (b) show emission peaks around 450 nm and 510 nm, which warrant further analysis. These peaks are attributed to the emission characteristics of oxygen vacancies in the system. In each sample series, the intensity of both peaks consistently increases with rising annealing temperature, indicating a corresponding increase in oxygen vacancy concentration, except for SPTO FL3A3. This observation is consistent with previous findings from XRD and UV-Vis analyses. Oxygen vacancies formed during oxygen-free sputtering are only partially compensated during annealing, with the remaining vacancies contributing to the observed blue PL emission.

5.3.3 Electrical properties: temperature dependent Hall studies

Subjecting oxide thin films to high temperature treatment often involves the removal and subsequent replacement of oxygen from the lattice structure. This process can lead to localized inconsistencies, phase alterations, and the creation of interfaces, all

of which can impact the electronic transport properties of typical oxide perovskite systems. To investigate these variations, temperature-dependent Hall measurements were conducted.

An additional electron is introduced, when Pr^{3+} replaces a Sr^{2+} site in the STO lattice, equivalent to one electron per unit cell. Previous studies on bulk Pr-doped STO systems have demonstrated that this increase in carrier concentration significantly enhances n-type conductivity. The carrier concentration in $SrTiO_3$ typically ranges from 10^{14} to 10^{15} cm^{-3}, making it suitable for electronic applications. In addition to n-type doping, managing oxygen defects is also critical for optimizing its performance. Figure 5-9 shows the temperature-dependent variations in carrier concentration, in-plane electron mobility, and conductivity of the thin films, as measured through Hall effect measurements and sheet resistance analysis using the van der Pauw (VDP) geometry.

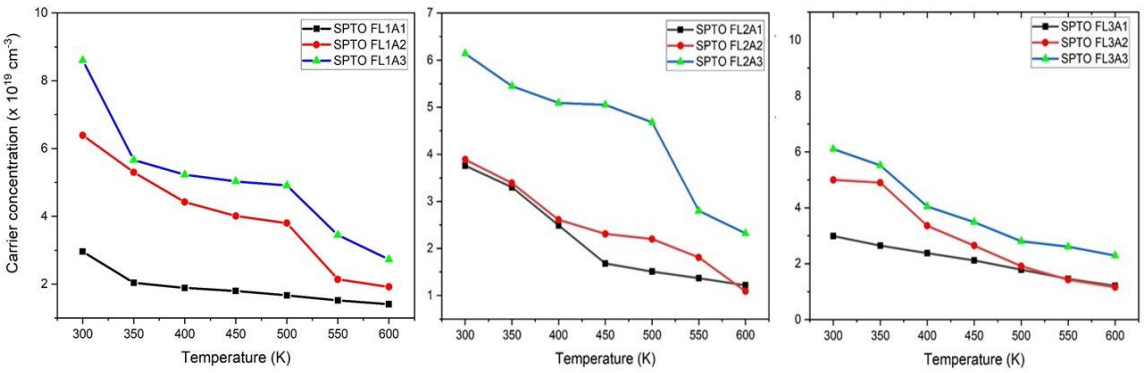

Figure 5- 9 Temperature dependent carrier concentration of Pr substituted $SrTiO_3$ thin films deposited at different Ar gas pressure and annealed at 600 °C, 700 °C and 800 °C

A consistent decrease in carrier concentration with temperature was observed across all series of thin films. For samples annealed at 600 °C, the RT carrier concentration ranged from $3x10^{19}$ cm^{-3} to $4x10^{19}$ cm^{-3}. Similarly, for those annealed at 700 °C, the values ranged from $4x10^{19}$ cm^{-3} to $6x10^{19}$ cm^{-3}, while for those annealed at 800 °C, the values ranged from $6x10^{19}$ cm^{-3} to $8x10^{19}$ cm^{-3} across the series. Samples subjected to higher annealing temperatures exhibit higher carrier concentrations

compared to those annealed at lower temperatures. Additionally, XRD analysis indicates a systematic increase in crystallite size due to annealing, which results in reduced scattering of carriers at grain boundaries, further contributing to the observed increase in carrier concentration. The decline in the concentration of charge carriers is ascribed to either a change in the concentration or a local rearrangement of oxygen vacancies. With increasing temperature, atmospheric oxygen and substrate oxygen tend to infiltrate the host lattice, thereby compensating for the oxygen defects and consequently reducing the carrier concentration. The increased carrier concentration in SPTO FL3A3 may be ascribed to oxygen vacancy clustering [53].

Perovskite oxides commonly form oxygen vacancies, which tend to accumulate on surfaces with low coordination numbers, creating a more positively charged surface that facilitates cation segregation. In this scenario, the substitution of Sr^{2+} with Pr^{3+} introduces an effective charge of -1 relative to the original crystal lattice. As a result, Sr ions diffuse and accumulate on the surface. During this segregation process, Sr atoms consume additional oxygen from both the lattice and the atmosphere to form clusters on the surface, leading to oxygen deficiency in the thin film surface, as described by Equation (5.6).

$$Sr_{Sr}^{X} + O_{O}^{X} \leftrightarrow V_{Sr}^{II} + V_{O}^{\cdot\cdot} + SrO_{Surface} \tag{5.6}$$

The formation of surface SrO can be modeled as a partial Schottky defect reaction. Higher annealing temperatures increase the mobility of Sr vacancies, accelerating the partial Schottky reaction. This process facilitates the creation of Sr vacancies and the transport of Sr to the surface, promoting Sr segregation. This phenomenon is observed in the SPTO FL1A3 and SPTO FL2A3 thin films, as evidenced by the oxygen-deficient systems, high carrier concentrations, and leftward shifts in the XRD patterns. However, the SPTO FL3A3 thin film does not show surface accumulation, indicating an absence of oxygen deficiency caused by Sr segregation. This observation is supported by XRD results for SPTO FL3A3, which display a rightward shift and correspond to less oxygen-deficient systems.

. The Samples annealed at 800 °C demonstrate metallic-degenerate semiconducting behavior, with mobility decreasing as temperature rises. Carrier mobility in oxide perovskites is influenced by multiple factors rather than a single variable. These include the distribution of oxygen vacancies, the incorporation of dopants, scattering mechanisms involving phonons (analyzed through Raman spectroscopy), and the thin film morphology, where island-like growth plays a significant role [54]. The mobility of all thin films shows an increasing trend up to a mid-temperature range of 400–450 K, followed by a decline. The temperature-dependent increase in mobility within the lower range of 300–450 K indicates that room-temperature (RT) mobility is primarily governed by polar optical phonon scattering. At higher temperatures, mobility decreases due to the increased frequency of electron collisions. The decline in mobility beyond this temperature range is observed to be proportionate to T^{-P} (where P ranges from 1 to 2.5), suggesting that acoustic phonons dominate the scattering of charge transport from 450 to 600 K.

The maximum mobility of 33.9 cm^2/V s at 400 K is obtained for thin film deposited at $3x10^{-2}$ mbar pressure and annealed at 800 °C. Although several research groups have reported exceptionally high electron mobility values ranging from 30,000 to 50,000 $cm^2/V{\cdot}s$ in electron-doped $SrTiO_3$ thin films, the utilization of these properties has been confined to extremely low temperatures below 10 K [55,56]. Doped STO thin films produced by methods such as PLD, MBE, and sputtering have been shown to have very low mobility, usually between 1 and 7 $cm^2/V{\cdot}s$ at room temperature. However, despite this low mobility, the thin films exhibit relatively good conductivity due to their high carrier concentration, which exceeds 10^{21} cm^{-3} [57,58]. In this study, the highest reported mobility was achieved by maintaining the carrier concentration within the range of 10^{19} cm^{-3}, which reduced carrier collisions and capitalized on favorable morphological properties. To enhance mobility effectively, it is essential to keep the carrier concentration within an optimal range.

Electron-phonon interactions are a key factor influencing carrier mobility in materials, and Raman spectroscopy provides valuable insights into this relationship. In perovskites like STO, the polarization of LO_1 phonons is relatively weak, with carrier-phonon interactions primarily driven by the strong polarization of LO_2 and LO_4 phonons. Additionally, along with oscillator energy, the polaron coupling constants α_v play a crucial role in determining the relaxation time associated with momentum loss due to carrier scattering from electron-LO phonon interactions, as described by Equation (5.7).

In the provided equation, m_e^* represents the effective mass, $f(\alpha_v)$ is a dimensionless function, m_p denotes the polaron mass describing the increased effective mass of an electron generating local polarization due to Coulombic interaction with the crystal's ions, while k_B and T retain their conventional meanings. This equation holds true for temperatures lower than the Debye temperature. Such temperatures are typically met at room temperature for the considered phonon modes LO_3 and LO_4, with the exception of the soft LO_1 modes, which can be disregarded due to their insignificantly

$$\tau_v = \frac{1}{2\alpha_v \omega_{l_v}} \left(\frac{m_e^*}{m_p}\right)^2 f(\alpha_v) \left[exp\left(\frac{\hbar\omega_{l_v}}{k_B T}\right) - 1\right] \tag{5.7}$$

small polarization.

The effective relaxation time τ_{eff} is related to τ_v and to mobility μ as in eqn (5.8) and eqn (5.9)

$$\tau_{eff} = \sum_v \left(\frac{1}{\tau_v}\right)^{-1} \tag{5.8}$$

$$\mu = \frac{e\tau_{eff}}{m_e^*} \tag{5.9}$$

As evident from eqn (5.8) and (5.9) high electron mobility may be achieved for systems with high effective scattering relaxation time [59,60].

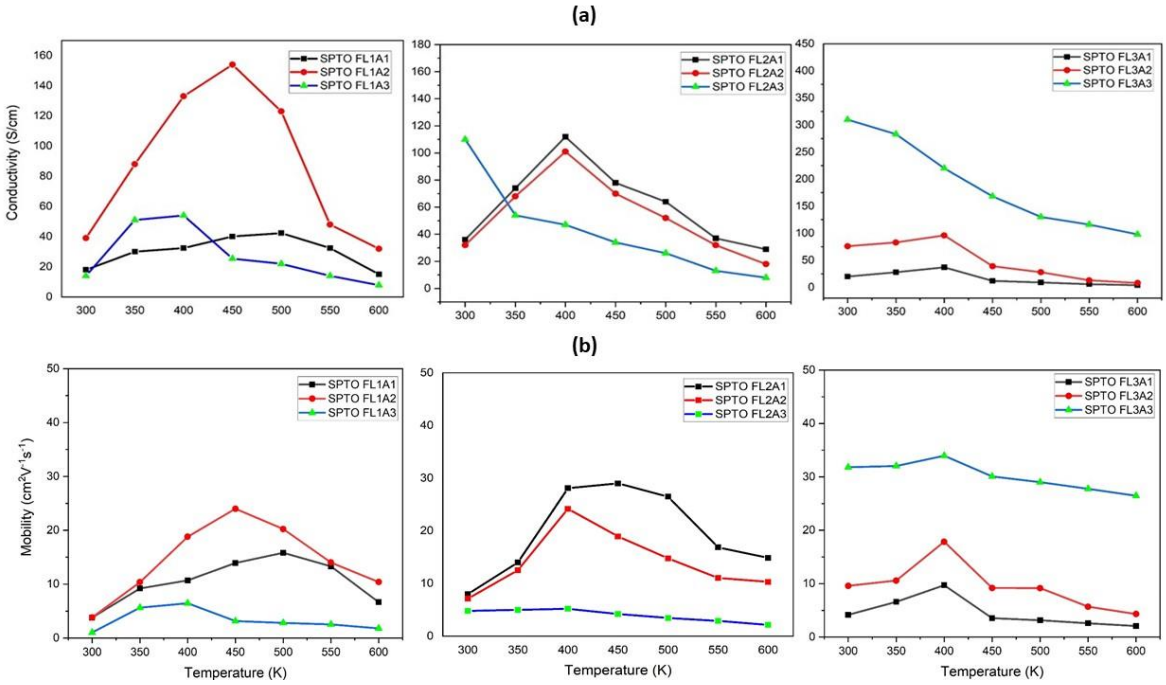

Figure 5- 10 Temperature dependent **(a)** conductivity and **(b)**mobility of Pr substituted $SrTiO_3$ thin films deposited at different Ar gas pressure and annealed at 600 °C, 700 °C and 800 °C

In the SPTO FL1 series, the SPTO FL1A1 and SPTO FL1A2 samples exhibit nearly identical LO oscillator energy and strength, resulting in similar room-temperature mobility. In contrast, the LO_2 and LO_4 peaks for the FL1A3 sample shift to lower energy levels, as indicated by a leftward shift, leading to reduced mobility. Furthermore, the oscillator strength for both peaks in FL1A3 is higher than in the other two thin films, indicating an increased coupling parameter α_v , reduced relaxation time, and consequently, lower mobility. In the SPTO FL2 series, the SPTO FL2A1 and SPTO FL2A2 samples also display nearly identical LO oscillator energy values, yielding similar room-temperature mobility. However, in the FL2A3 sample, while the peaks for both LO modes shift leftward, indicating lower energy, the oscillator strength is significantly reduced. This results in a lower coupling parameter α_v contributing to higher mobility.

For the SPTO FL3 series, both LO oscillators shift rightward in the Raman spectrum, suggesting increasing energy levels in the order SPTO FL3A1, SPTO FL3A2, and SPTO FL3A3. Conversely, the oscillator strength follows the reverse trend, with SPTO FL3A3 showing the least coupling, which indicates the highest mobility at room temperature.

The mobility of thin films is also influenced by their morphological features, as demonstrated by SEM and AFM analyses. The presence of 3D clusters and islands, particularly in thin films annealed at 800 °C, such as SPTO FL1A3 and SPTO FL2A3, indicates regions of dislocation and partial nucleation that act as scattering centers for charge carriers, significantly reducing mobility. This reduction in mobility is evident for these samples in Figure 5-10. Despite the lower mobility, these films maintain reasonable conductivity due to their higher carrier concentration. The conduction mechanism in these thin films, characterized by a layer-island morphology, is governed by a temperature-activated hopping process. During conduction, charge carriers become trapped at these nano islands and clusters, hopping between them via quantum tunneling, resulting in a non-conventional electrical transport mechanism [61–63]. The sharp increase in electrical conductivity and mobility observed in the SPTO FL3A3 thin film can be attributed to its continuous morphology and the reduced presence of defect centers and islands that scatter charge carriers. The FL3A3 film achieves the highest reported room-temperature conductivity of 320 S/cm, demonstrating the potential of Pr-doped STO for use in transparent conducting oxides (TCOs) and thermoelectric applications.

5.4 Conclusions

Praseodymium (Pr)-doped strontium titanate (STO) thin films offer distinct advantages over their bulk counterparts, particularly in tailoring electronic and optical properties for next-generation transparent conducting oxides (TCOs). By leveraging controlled synthesis techniques, thin films enable precise manipulation of oxygen vacancies, strain effects, and cation segregation—factors that are challenging to regulate in bulk materials. Achieving high mobility in transparent conducting oxides (TCOs) at room temperature remains a significant challenge, necessitating meticulous control of

synthesis parameters. This study underscores the critical importance of regulating oxygen vacancies and minimizing Sr segregation on the thin film surface to enhance both electrical and optical performance. Structural characterization through XRD, Raman spectroscopy, and FESEM revealed that the structural integrity of perovskite oxide thin films is intricately linked to their transport and transparency properties. Temperature-dependent electrical transport analyses further emphasized the need for precise oxygen stoichiometry control to achieve the desired balance between conductivity and transparency. Advanced deposition techniques and optimized thermal treatments were instrumental in mitigating cation segregation, particularly Sr segregation, which is a key factor limiting carrier mobility. The successful fabrication of Pr-doped strontium titanate thin films with a mobility of 33.9 $cm^2/V{\cdot}s$ and optical transparency exceeding 60% highlights the potential of these materials for TCO applications. These findings demonstrate the feasibility of producing highly transparent and mobile perovskite oxide thin films that are well-suited for optoelectronic devices such as transparent electrodes, displays, and photovoltaics. Moving forward, further research into controlling surface phenomena and vacancy distributions will be crucial for unlocking the full potential of TCOs in advanced technological applications.

References:

[1] J.S. P.K., M. Shah, P.P. Pradyumnan, Tailoring structure and nanoscale surface topography in Mg–N doped $CuCrO_2$ thin films via post deposition annealing for optothermoelectric application, Opt Mater (Amst) 147 (2024) 114703. https://doi.org/https://doi.org/10.1016/j.optmat.2023.114703.

[2] J.S. P.K., M. Shah, P.P. Pradyumnan, Intense narrow band blue emission in $CuCrO_2$ delafossite by Ni^{2+}-Mg^{2+} dual cation doping, Spectrochim Acta A Mol Biomol Spectrosc 305 (2024) 123442. https://doi.org/https://doi.org/10.1016/j.saa.2023.123442.

[3] J.S. P.K., M. Shah, P.P. Pradyumnan, Magnetoelectric coupling and thermoelectric behaviors in Ni-doped $CuCrO_2$ crystallites, Chemical Engineering Journal 476 (2023) 146568. https://doi.org/https://doi.org/10.1016/j.cej.2023.146568.

[4] P.K. Jamshina Sanam, M. Shah, P.P. Pradyumnan, Enhanced thermoelectric properties in dual cation doped $CuCrO_2$ nanocrystals mediated by magnon-carrier drag, Mater Res Bull 164 (2023) 112244. https://doi.org/https://doi.org/10.1016/j.materresbull.2023.112244.

[5] P.K. Jamshina Sanam, M. Shah, P.P. Pradyumnan, The enhancement of NIR transparency due to annealing and Mg-doping in $CuCrO_2$ thin films, Mater Lett 330 (2023) 133295. https://doi.org/https://doi.org/10.1016/j.matlet.2022.133295.

[6] P.K. Jamshina Sanam, M. Shah, P.P. Pradyumnan, Structure induced modification on thermoelectric and optical properties by Mg doping in $CuCrO_2$ nanocrystals, Solid State Commun 353 (2022) 114855. https://doi.org/https://doi.org/10.1016/j.ssc.2022.114855.

[7] P.K.J. Sanam, M. Shah, P.P. Pradyumnan, Raman spectroscopic investigation and thermoelectric studies of defect-induced Mg-doped delafossite thin film, Journal of Materials Science: Materials in Electronics (2022). https://doi.org/10.1007/s10854-022-09013-y.

[8] P.K. Jamshina Sanam, M. Shah, P.P. Pradyumnan, Structure induced modification on thermoelectric and optical properties by Mg doping in $CuCrO_2$ nanocrystals, Solid State Commun 353 (2022) 114855. https://doi.org/10.1016/J.SSC.2022.114855.

[9] P.K. Jamshina Sanam, K.G. Gopika, P.P. Pradyumnan, Spin chiral interactions modulated Seebeck coefficient and improved optical properties by Zn doping in $CuCrO_2$ crystallites, Mater Chem Phys 308 (2023) 128214. https://doi.org/https://doi.org/10.1016/j.matchemphys.2023.128214.

[10] M. Shah, A.P. Jemshihas, P.K. Jamshina Sanam, P.P. Pradyumnan, Magneto thermoelectric effect of nickel thin film synthesized by RF magnetron sputtering, Physica E Low Dimens Syst Nanostruct 147 (2023) 115591. https://doi.org/https://doi.org/10.1016/j.physe.2022.115591.

[11] A. Nathan, S. Jeon, Oxide electronics: Translating materials science from lab-to-fab, MRS Bull 46 (2021) 1028–1036. https://doi.org/10.1557/s43577-021-00257-3.

[12] H. Fatima, Y. Zhong, H. Wu, Z. Shao, Recent advances in functional oxides for high energy density sodium-ion batteries, Materials Reports: Energy 1 (2021) 100022. https://doi.org/https://doi.org/10.1016/j.matre.2021.100022.

[13] M. Shah, P.K. Jamshina Sanam, P.P. Pradyumnan, Defect-induced $Sr_{1-x}Pr_xTiO_3$ crystallites by burial sintering and its optoelectronic applications, Journal of Physics and Chemistry of Solids 181 (2023) 111516. https://doi.org/https://doi.org/10.1016/j.jpcs.2023.111516.

[14] J. Lim, H. Lim, Y.S. Lee, Ambient dependence of visible emissions in $SrTiO_3$, Current Applied Physics 19 (2019) 1177–1181. https://doi.org/https://doi.org/10.1016/j.cap.2019.07.016.

[15] J. Wang, T. Wang, Z. Zhao, R. Wang, C. Wang, F. Zhou, S. Li, L. Zhao, M. Feng, Regulation of oxygen vacancies in $SrTiO_3$ perovskite for efficient photocatalytic nitrogen fixation, J Alloys Compd 902 (2022) 163865. https://doi.org/10.1016/j.jallcom.2022.163865.

[16] U.S. Shenoy, H. Bantawal, D.K. Bhat, Band Engineering of $SrTiO_3$: Effect of Synthetic Technique and Site Occupancy of Doped Rhodium, The Journal of Physical Chemistry C 122 (2018) 27567–27574. https://doi.org/10.1021/acs.jpcc.8b10083.

[17] M. Markovich, J. Roqueta, J. Santiso, E. Lakin, E. Zolotoyabko, A. Rothschild, Epitaxial growth of Nb-doped $SrTiO_3$ films by pulsed laser deposition, Appl Surf Sci 258 (2012) 9496–9500. https://doi.org/https://doi.org/10.1016/j.apsusc.2012.02.041.

[18] C.-Y. Guo, X. Qi, RF magnetron sputter deposition and electrical properties of La and Y doped $SrTiO_3$ epitaxial films, Mater Des 179 (2019) 107888. https://doi.org/https://doi.org/10.1016/j.matdes.2019.107888.

[19] A. Baki, M. Abdeldayem, C. Morales, J.I. Flege, D. Klimm, O. Bierwagen, J. Schwarzkopf, Potential of La-Doped $SrTiO_3$ Thin Films Grown by Metal–Organic Vapor Phase Epitaxy for Thermoelectric Applications, Cryst Growth Des 23 (2023) 2522–2530. https://doi.org/10.1021/acs.cgd.2c01438.

[20] M. Choi, A.B. Posadas, C.A. Rodriguez, A. O'Hara, H. Seinige, A.J. Kellock, M.M. Frank, M. Tsoi, S. Zollner, V. Narayanan, A.A. Demkov, Structural, optical, and electrical properties of strained La-doped $SrTiO_3$ films, J Appl Phys 116 (2014) 043705. https://doi.org/10.1063/1.4891225.

[21] A. Biswas, N. Li, M.H. Jung, Y.W. Lee, J.S. Kim, Y.H. Jeong, La doped $SrTiO_3$ thin films on $SrLaAlO_4$ (001) as transparent conductor, J Appl Phys 113 (2013) 183711. https://doi.org/10.1063/1.4804664.

[22] F. Aguesse, A.-K. Axelsson, P. Reinhard, V. Tileli, J.L.M. Rupp, N.M. Alford, High-temperature conductivity evaluation of Nb doped $SrTiO_3$ thin films: Influence of strain and growth mechanism, Thin Solid Films 539 (2013) 384–390. https://doi.org/10.1016/j.tsf.2013.05.094.

[23] S.R.S. Kumar, A.Z. Barasheed, H.N. Alshareef, High Temperature Thermoelectric Properties of Strontium Titanate Thin Films with Oxygen Vacancy and Niobium Doping, ACS Appl Mater Interfaces 5 (2013) 7268–7273. https://doi.org/10.1021/am4015956.

[24] X. Wang, X. Lu, Y. Weng, W. Cai, X. Wu, Y. Liu, F. Huang, J. Zhu, Improved electrical properties of Pr-doped $SrTiO_3$ films, Solid State Commun 150 (2010) 267–270. https://doi.org/https://doi.org/10.1016/j.ssc.2009.11.010.

[25] B. Amin, N. Singh, T.M. Tritt, H.N. Alshareef, U. Schwingenschlögl, Major enhancement of the thermoelectric performance in Pr/Nb-doped $SrTiO_3$ under strain, Appl Phys Lett 103 (2013) 031907. https://doi.org/10.1063/1.4815928.

[26] W. Wang, C. Jiang, M. Shen, L. Fang, F. Zheng, X. Wu, J. Shen, Effect of oxygen vacancies on the red emission of $SrTiO_3:Pr^{3+}$ phosphor films, Appl Phys Lett 94 (2009) 081904. https://doi.org/10.1063/1.3089814.

[27] H. Takashima, K. Ueda, M. Itoh, Red photoluminescence in praseodymium-doped titanate perovskite films epitaxially grown by pulsed laser deposition, Appl Phys Lett 89 (2006) 261915. https://doi.org/10.1063/1.2424438.

[28] A. Durán, E. Martínez, J.A. Díaz, J.M. Siqueiros, Ferroelectricity at room temperature in Pr-doped $SrTiO_3$, J Appl Phys 97 (2005) 104109. https://doi.org/10.1063/1.1903100.

[29] H. Takashima, Y. Inaguma, Preparation and luminescence properties of Pr, Al doped $SrTiO_3$ thin films, Ferroelectrics 539 (2019) 153–158. https://doi.org/10.1080/00150193.2019.1570004.

[30] M. Andrä, H. Bluhm, R. Dittmann, C.M. Schneider, R. Waser, D.N. Mueller, F. Gunkel, Chemical control of the electrical surface properties in donor-doped transition metal oxides, Phys Rev Mater 3 (2019) 44604. https://doi.org/10.1103/PhysRevMaterials.3.044604.

[31] E. Zhou, J.-M. Raulot, H. Xu, H. Hao, Z. Shen, H. Liu, Structural, electronic, and optical properties of rare-earth-doped $SrTiO_3$ perovskite: A first-principles study, Physica B Condens Matter 643 (2022) 414160. https://doi.org/10.1016/j.physb.2022.414160.

[32] S. Cook, K. Letchworth-Weaver, I.-C. Tung, T.K. Andersen, H. Hong, L.D. Marks, D.D. Fong, How heteroepitaxy occurs on strontium titanate, Sci Adv 5 (2023) eaav0764. https://doi.org/10.1126/sciadv.aav0764.

[33] H. Wang, X. Luo, K. Peng, Z. Sun, M. Shi, D. Ma, N. Wang, T. Wu, J. Ying, Z. Wang, X. Chen, Magnetic Field-Enhanced Thermoelectric Performance in Dirac Semimetal Cd_3As_2 Crystals with Different Carrier Concentrations, Adv Funct Mater (2019). https://doi.org/10.1002/adfm.201902437.

[34] M.E. Zvanut, S. Jeddy, E. Towett, G.M. Janowski, C. Brooks, D. Schlom, An annealing study of an oxygen vacancy related defect in $SrTiO_3$ substrates, J Appl Phys 104 (2008) 064122. https://doi.org/10.1063/1.2986244.

[35] D. Pasero, S. de Souza, N. Reeves, A.R. West, Oxygen content and electrochemical activity of $LiCoMnO_{4-\delta}$, J Mater Chem 15 (2005) 4435–4440. https://doi.org/10.1039/B508521G.

[36] P. Priyadarshini, S. Das, D. Alagarasan, R. Ganesan, S. Varadharajaperumal, R. Naik, Observation of high nonlinearity in Bi doped $Bi_xIn_{35-x}Se_{65}$ thin films with annealing, Sci Rep 11 (2021) 21518. https://doi.org/10.1038/s41598-021-01134-4.

[37] A. Moustaghfir, E. Tomasella, S. Ben Amor, M. Jacquet, J. Cellier, T. Sauvage, Structural and optical studies of ZnO thin films deposited by r.f. magnetron sputtering: influence of annealing, Surf Coat Technol 174–175 (2003) 193–196. https://doi.org/10.1016/S0257-8972(03)00417-1.

[38] S.A. Hayward, E.K.H. Salje, Cubic-tetragonal phase transition in $SrTiO_3$ revisited: Landau theory and transition mechanism, Phase Transitions 68 (1999) 501–522. https://doi.org/10.1080/01411599908224530.

[39] R.A.C. Amoresi, V. Teodoro, G.F. Teixeira, M.S. Li, A.Z. Simões, L.A. Perazolli, E. Longo, M.A. Zaghete, Electrosteric colloidal stabilization for obtaining $SrTiO_3/TiO_2$ heterojunction: Microstructural evolution in the interface and photonics properties, J Eur Ceram Soc 38 (2018) 1621–1631. https://doi.org/https://doi.org/10.1016/j.jeurceramsoc. 2017.10.056.

[40] C.H. Perry, J.H. Fertel, T.F. McNelly, Temperature Dependence of the Raman Spectrum of SrTiO3 and $KTaO_3$, J Chem Phys 47 (1967) 1619–1625. https://doi.org/10.1063 /1.1712142.

[41] D.J. Gray, T.A. Merz, Y. Hikita, H.Y. Hwang, H. Mabuchi, Orientation-resolved domain mapping in tetragonal $SrTiO_3$ using polarized Raman spectroscopy, Phys Rev B 94 (2016) 214107. https://doi.org/10.1103/PhysRevB.94.214107.

[42] F.A. Rabuffetti, H.-S. Kim, J.A. Enterkin, Y. Wang, C.H. Lanier, L.D. Marks, K.R. Poeppelmeier, P.C. Stair, Synthesis-Dependent First-Order Raman Scattering in $SrTiO_3$ Nanocubes at Room Temperature, Chemistry of Materials 20 (2008) 5628–5635. https://doi.org/10.1021/cm801192t.

[43] H. Chen, C. Lim, T. Tan, M. Zhou, L. Zhang, X. Sun, Z. He, Y. Ye, X. Li, H. Zhang, J.W. Han, C. Yang, Y. Chen, Electronic Activation during Nanoparticle Exsolution for Enhanced Activity at Elevated Temperature, ACS Nano 17 (2023) 10677–10688. https://doi.org/10.1021/acsnano.3c01841.

[44] Y. Chen, H. Téllez, M. Burriel, F. Yang, N. Tsvetkov, Z. Cai, D.W. McComb, J.A. Kilner, B. Yildiz, Segregated Chemistry and Structure on (001) and (100) Surfaces of $(La_{1-x}Sr_x)_2CoO_4$ Override the Crystal Anisotropy in Oxygen Exchange Kinetics, Chemistry of Materials 27 (2015) 5436–5450. https://doi.org/10.1021/acs.chemmater.5b02292.

[45] Y. Yu, K.F. Ludwig, J.C. Woicik, S. Gopalan, U.B. Pal, T.C. Kaspar, S.N. Basu, Effect of Sr Content and Strain on Sr Surface Segregation of $La_{1-x}Sr_xCo_{0.2}Fe_{0.8}O_{3-\delta}$ as Cathode Material for Solid Oxide Fuel Cells, ACS Appl Mater Interfaces 8 (2016) 26704–26711. https://doi.org/10.1021/acsami.6b07118.

[46] W. Huang, R. Nechache, S. Li, M. Chaker, F. Rosei, Electrical and Optical Properties of Transparent Conducting p-Type $SrTiO_3$ Thin Films, Journal of the American Ceramic Society 99 (2016) 226–233. https://doi.org/https://doi.org/10.1111/jace.13949.

[47] A. Janotti, B. Jalan, S. Stemmer, C.G. Van de Walle, Effects of doping on the lattice parameter of SrTiO3, Appl Phys Lett 100 (2012) 262104. https://doi.org/10.1063 /1.4730998.

[48] H. Trabelsi, M. Bejar, E. Dhahri, M.A. Valente, M.P.F. Graça, M. Djermouni, A. Zaoui, Evaluation of the relationship between the magnetism and the optical properties in $SrTiO_{3-}$

$_{\delta}$ defective systems: Experimental and theoretical studies, J Magn Magn Mater 478 (2019) 175–186. https://doi.org/https://doi.org/10.1016/j.jmmm.2019.01.115.

[49] W. Huang, R. Nechache, S. Li, M. Chaker, F. Rosei, Electrical and Optical Properties of Transparent Conducting p-Type $SrTiO_3$ Thin Films, Journal of the American Ceramic Society 99 (2016) 226–233. https://doi.org/https://doi.org/10.1111/jace.13949.

[50] V. Rogé, C. Garlisi, P.L. Popa, K. Menguelti, M. Michel, C. Vergne, E. Wagner, W. Maudez, G. Benvenuti, B.R. Pistillo, E. Barborini, $SrTiO_3$ thin film photoanodes fabricated by combinatorial chemical beam vapour deposition: intricate connection between elemental composition and thin films' properties, J Mater Chem A Mater (2024). https://doi.org/10.1039/D3TA07695D.

[51] T. Supasai, S. Dangtip, P. Learngarunsri, N. Boonyopakorn, A. Wisitsoraat, S.K. Hodak, Influence of temperature annealing on optical properties of $SrTiO_3$/$BaTiO_3$ multilayered films on indium tin oxide, Appl Surf Sci 256 (2010) 4462–4467. https://doi.org/10.1016/j.apsusc.2010.01.072.

[52] K. Eom, E. Choi, M. Choi, S. Han, H. Zhou, J. Lee, Oxygen Vacancy Linear Clustering in a Perovskite Oxide, J Phys Chem Lett 8 (2017) 3500–3505. https://doi.org/10.1021/acs.jpclett.7b01348.

[53] Z. Wei, Z. Li, P. Luo, J. Zhang, J. Luo, Simultaneously increased carrier concentration and mobility in p-type $Bi_{0.5}Sb_{1.5}Te_3$ throng Cd doping, J Alloys Compd 830 (2020) 154625. https://doi.org/https://doi.org/10.1016/j.jallcom.2020.154625.

[54] J. Son, P. Moetakef, B. Jalan, O. Bierwagen, N.J. Wright, R. Engel-Herbert, S. Stemmer, Epitaxial $SrTiO_3$ films with electron mobilities exceeding 30,000 $cm^2 V^{-1} s^{-1}$, Nat Mater 9 (2010) 482–484. https://doi.org/10.1038/nmat2750.

[55] T.A. Cain, A.P. Kajdos, S. Stemmer, La-doped $SrTiO_3$ films with large cryogenic thermoelectric power factors, Appl Phys Lett 102 (2013) 182101. https://doi.org/10.1063/1.4804182.

[56] Y. Kozuka, Y. Hikita, C. Bell, H.Y. Hwang, Dramatic mobility enhancements in doped $SrTiO_3$ thin films by defect management, Appl Phys Lett 97 (2010) 012107. https://doi.org/10.1063/1.3457994.

[57] J. Yue, Y. Ayino, T.K. Truttmann, M.N. Gastiasoro, E. Persky, A. Khanukov, D. Lee, L.R. Thoutam, B. Kalisky, R.M. Fernandes, V.S. Pribiag, B. Jalan, Anomalous transport in high-mobility superconducting $SrTiO_3$ thin films, Sci Adv 8 (2024) eabl5668. https://doi.org/10.1126/sciadv.abl5668.

[58] D.M. Eagles, Polar modes of lattice vibration and polaron coupling constants in rutile (TiO_2), Journal of Physics and Chemistry of Solids 25 (1964) 1243–1251. https://doi.org/https://doi.org/10.1016/0022-3697(64)90022-8.

[59] C.A. Niedermeier, Y. Kumagai, K. Ide, T. Katase, F. Oba, H. Hosono, T. Kamiya, Phonon scattering limited mobility in the representative cubic perovskite semiconductors $SrGeO_3$ $BaSnO_3$, and $SrTiO_3$ Phys Rev B 101 (2020) 125206. https://doi.org/10.1103/PhysRevB.101.125206.

[60] Z.T.Y. Liu, N.J. Podraza, S. V Khare, P. Sarin, Transparency enhancement for $SrVO_3$ by $SrTiO_3$ mixing: A first-principles study, Comput Mater Sci 144 (2018) 139–146. https://doi.org/https://doi.org/10.1016/j.commatsci.2017.12.020.

[61] J. Ravichandran, W. Siemons, H. Heijmerikx, M. Huijben, A. Majumdar, R. Ramesh, An Epitaxial Transparent Conducting Perovskite Oxide: Double-Doped $SrTiO_3$, Chemistry of Materials 22 (2010) 3983–3987. https://doi.org/10.1021/cm1005604.

[62] P. Jood, G. Peleckis, X. Wang, S.X. Dou, Thermoelectric properties of $Ca_3Co_4O_9$ and $Ca_{2.8}Bi_{0.2}Co_4O_9$ thin films in their island formation mode, J Mater Res 28 (2013) 1932–1939. https://api.semanticscholar.org/CorpusID:41413569.

Chapter 6

Thermoelectric properties of Nb doped $SrTiO_3$ thin films

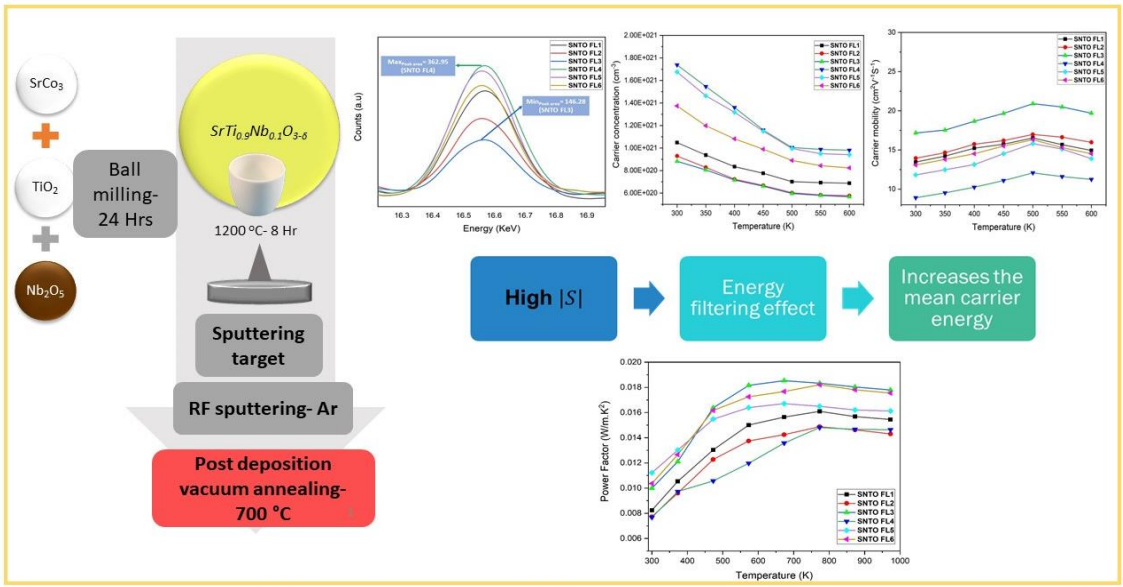

Objectives

This chapter focuses on the synthesis and optimization of Nb doped $SrTiO_3$ thin films to achieve enhanced thermoelectric power factor. It aims to establish a relationship between the structural, compositional, and morphological properties characterized through XRD, XRF, SEM, and EDS and the thermoelectric transport properties determined by Hall and TE measurements. Emphasis is placed on investigating the impact of Nb doping and oxygen vacancies on carrier concentrations and their influence on the conduction mechanism within the framework of a degenerate semiconductor model. The ultimate goal is to identify optimal sputtering conditions that yield high Seebeck coefficients and superior thermoelectric power factors, essential for better TE devices and sensors.

6.1 Introduction

Thermoelectric materials enable the direct conversion of temperature gradient into electrical energy and vice versa, providing a sustainable solution for utilizing waste heat and enhancing energy efficiency. This capability is particularly significant in addressing global energy challenges, as thermoelectric devices can convert waste heat from industrial processes, electronic systems, and automobiles into valuable power. Thin films, in particular, offer unique advantages in thermoelectric applications due to their ability to exhibit enhanced thermoelectric properties through quantum confinement, controlled defect engineering, and precise material composition. This conversion efficiency is represented by the dimensionless figure of merit ZT,

$$ZT = \frac{S^2\sigma}{\kappa}T = \frac{P.F}{\kappa_{lattice(Phonon)} + \kappa_{electronic}}T \quad (6.1)$$

Where S is the Seebeck coefficient, σ is the electrical conductivity and κ is thermal conductivity that can be divided to lattice and electronic parts, and T is the absolute temperature. To maximize the conversion efficiency we need to improve $S^2\sigma$, collectively known as thermoelectric power factor ($P.F$). In this context, oxide perovskite materials, particularly in the form of thin films, have emerged as promising candidates due to their unique combination of properties. Their exceptional thermal stability, inherent low thermal conductivity, and adaptable chemical composition make them ideal for thermoelectric applications. The ability to introduce and manipulate point defects, such as oxygen vacancies, provides an effective mechanism for tailoring electrical transport properties, enhancing the thermoelectric performance of these materials. Thin films offer additional advantages over bulk materials for thermoelectric applications. Their tunable thickness, ability to exhibit quantum confinement effects, and potential for integration into microdevices make them highly suitable for advanced energy harvesting technologies. By controlling deposition techniques and post-processing conditions, thin films of oxide perovskites can achieve optimized carrier concentration, reduced thermal conductivity, and enhanced Seebeck coefficients, thereby improving their ZT values.

Several p-type oxide materials like BiCuSeO, $NaCoO_3$, $CuCrO_2$ and $Ca_3Co_4O_9$ have been reported with ZT between 0.5 and 1, whereas highly efficient n-type counterparts are equally important to realize TE generators [1–12]. $SrTiO_3$-based materials and their derivatives hold significant importance among n-type oxides due to their high Seebeck coefficient and the flexibility to tailor electrical properties through doping at the A-site and B-site. Common approaches to enhance the thermoelectric performance of these materials include nanostructuring, strain engineering, composite formation, nano-inclusions, and defect engineering via oxygen vacancy formation. A-site dopants such as Pr, La, Dy, Nd, and Bi, along with B-site dopants like Nb, Cr, Ta, and Sn, are frequently employed to optimize their properties [13–16]. Among these dopants, Nb serves as a donor dopant by substituting for Ti in the $SrTiO_3$ lattice, introducing additional electrons that substantially enhance carrier concentration and electrical conductivity. A major challenge in developing oxide thermoelectric materials with high ZT values lies in their inherently high lattice thermal conductivity κ_{Phonon} , driven by loosely bound oxygen atoms that promote efficient phonon conduction. While efforts to reduce κ_{Phonon} have seen limited success, the focus must shift toward tailoring oxides to achieve higher power factors for improved thermoelectric performance.

Apart from bulk materials and single crystals, $SrTiO_3$ is extensively used in thin film form for thermoelectric applications especially in micro and nano devices [17,18]. Thin films enable precise tuning of material properties, such as carrier concentration and mobility, by allowing meticulous control over composition and structure. Advanced deposition techniques like pulsed laser deposition (PLD), molecular beam epitaxy (MBE), and sputtering facilitate the creation of high-quality thin films with controlled thickness and tailored nanostructures. Niobium (Nb) doping in $SrTiO_3$ thin films significantly influences their electrical properties by introducing additional charge carriers and modifying the material's electronic structure. As the Nb concentration increases, the electrical conductivity of Nb-doped $SrTiO_3$ thin films exhibits a semiconducting behavior, with conductivity increasing exponentially with temperature due to enhanced thermal carrier excitation. Additionally, the thermoelectric performance

of STO thin films improves upon 2% Nb-doping. However, in epitaxial Nb-doped $SrTiO_3$ thin films, a gradual decrease in electrical conductivity is observed as the film thickness decreases, indicating that thickness plays a role in the electrical properties. Furthermore, the electrical transport across Au/Nb:$SrTiO_3$ Schottky interfaces varies with different Nb doping densities, with thermionic emission dominating transport in low-doped substrates, while deviations occur in highly doped substrates. These findings highlight the critical role of Nb doping in tailoring the electrical properties of $SrTiO_3$ thin films for various electronic applications [19–21]. Notably, Ohta et al. reported an exceptional power factor of 1.48 W/mK² by heavily doping Nb in $SrTiO_3$ thin films, while Sarath Kumar et al. achieved power factors exceeding 1 W/mK² in Nb-doped $SrTiO_3$ films by strategically manipulating oxygen vacancies [22–24].

In this study, we adopted a comprehensive approach to achieve a high power factor in the $SrTiO_3$ (STO) system. Key strategies included optimal Nb doping to enhance carrier concentration, oxygen-free RF sputtering to induce oxygen deficiencies, and vacuum annealing to further increase charge carriers [25,26]. Silicon was chosen as the substrate for thin film growth due to its similar thermal expansion coefficient to $SrTiO_3$, minimizing thermal stress and mechanical failure during high-temperature annealing. These methods, combined with optimized sputtering parameters, resulted in high electrical conductivity and an enhanced Seebeck coefficient, culminating in a record-breaking power factor of 0.0185 W/mK² for oxide thin films.

6.2 Experimental methods and techniques

$SrTi_{0.9}Nb_{0.1}O_{3-\delta}$ sputtering target was prepared via high-temperature solid-state reaction method with stoichiometric amounts of $SrCO_3$ (Sigma-Aldrich 99.9%), TiO_2 (Sigma-Aldrich 99.9%), and Nb_2O_5 (Sigma-Aldrich 99.9%). The obtained powder was sintered and formed into a 2-inch disk-shaped target. To ensure compositional uniformity, the disk was crushed, pulverized, repressed, and re-sintered and used as sputtering target. Ultrasonically cleaned Si substrates were then placed in the sputtering chamber, which was evacuated to 5×10^{-6} mbar prior to deposition. Nb-doped thin films

were grown on the Si substrates at a temperature of 500 °C with a sputtering power of 120 W and 150 W for a duration of 90 minutes. Sputtering occurred in a pure argon atmosphere with chamber pressures ranging from 1×10^{-2} to 3×10^{-2} mbar. The deposited thin films were then annealed in a vacuum furnace at 700 °C for 1 hour, and the resulting films were labeled as shown in Table 6-1.

The structural, morphological, and surface characterizations were carried out using the same techniques detailed in previous chapters, including XRD, XRF, FE-SEM with EDS and elemental mapping, and AFM. Similarly, the electrical transport and thermoelectric properties, such as the Seebeck coefficient, electrical conductivity, and power factor, were evaluated using Hall effect measurements and the ULVAC ZEM-3 system.

6.3 Result and discussion

6.3.1 Structural, morphological characterization: XRD, XRF, FE-SEM-EDS

The XRD pattern of $SrTi_{0.9}Nb_{0.1}O_{3-\delta}$ sputtering target is shown in Fig. 6-1(a). XRD reflections matched the reference pattern in the database (PDF#35-0734), revealed that the target contains the pure phase of STO. The as deposited thin films were found as

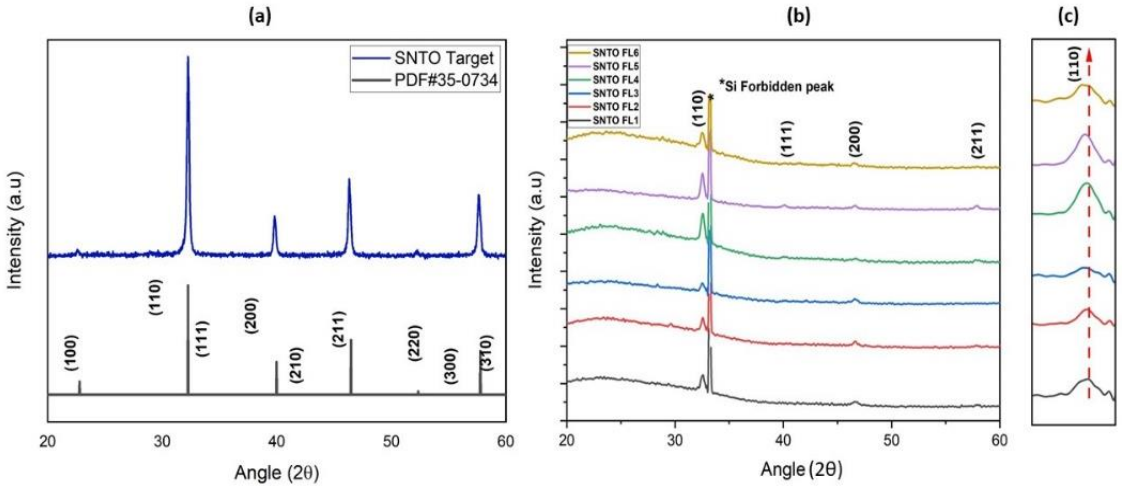

Figure 6- 1 (a) XRD pattern of $SrTi_{0.9}Nb_{0.1}O_{3-\delta}$ sputtering target **(b)** XRD patterns of films deposited at different Ar gas pressure **(c)** shift in (111) peak

amorphous and subjected to post deposition vacuum annealing at 700 °C. The diffraction patterns of annealed films along with sputtering gas pressure is represented in Fig. 6-1(b) and the shifting of (111) plane is indicated in Fig. 6-1(c). The crystallization effect was observed for all thin films after annealing, where reflections corresponding to (110), (111), (200) and (211) peak were visible.

The peak intensities is found to be more for thin films deposited at higher sputtering power due to the increased sputtering rates. The reduction in the intensity of XRD peaks with increased sputtering gas pressure, while maintaining constant power, can be attributed to several factors related to the deposition process and the resulting thin film quality. At higher sputtering gas pressures, the mean free path of the sputtered atoms is reduced due to more frequent collisions with gas molecules. This can lead to a decrease in the energy of the atoms when they reach the substrate, resulting in a less dense and more amorphous film. Higher sputtering pressures can lead to a reduction in the surface mobility of adatoms. Lower mobility results in less effective nucleation and growth of crystallites, leading to poor crystallinity and a decrease in the XRD peak intensity.

The (110) peak around 32° shows a shift to lower angle with increasing gas pressure. The average crystallite size of the sample was estimated using the Scherrer formula as in eqn (6.1) using the FWHM of predominant peaks.

$$t = \frac{k\lambda}{\beta \cos\theta} \tag{6.1}$$

the results are summarized in Table 6-1. The microstrain on lattice was deliberated using eqn (6.2)

$$\varepsilon = \frac{\beta}{4 \tan\theta} \tag{6.2}$$

In each series, the thin film deposited at an Ar pressure of $2x10^{-2}$ mbar exhibited the largest crystallite size, with significantly lower strain compared to other films in the series. At this optimal pressure, the sputtered atoms achieve a balance of energy and

mobility, enabling them to diffuse efficiently across the substrate surface and promote the growth of larger crystallites.

In contrast, at a lower pressure of $1x10^{-2}$ mbar, the atoms possess excessive kinetic energy, leading to high mobility but potentially unstable nucleation, resulting in smaller crystallites. Conversely, at a higher pressure of $3x10^{-2}$ mbar, the increased gas pressure causes more frequent collisions between sputtered atoms and gas molecules, reducing their energy and mobility, which also leads to smaller crystallite sizes. Additionally, the conditions at $2x10^{-2}$ mbar may favor the formation of fewer nucleation sites, allowing existing crystallites to grow larger. In comparison, both lower and higher pressures might result in a greater number of nucleation sites, leading to the development of smaller crystallites [27–29]. The forbidden peak in silicon around 33° in X-ray diffraction (XRD) patterns is an anomalous reflection that arises due to the symmetry and structure of the silicon crystal lattice that appear due to the dynamic scattering effects, thermal vibrations, doping and defects and residual strain.

Table 6- 1 Sample labels, crystallite size and strain of Nb doped $SrTiO_3$ thin films

Sputtering Power (W)	Sputtering pressure (mbar)	Sample label	Crystallite size (nm)	Micro strain
120	1×10^{-2}	SNTO FL1	22.1	0.00558
	2×10^{-2}	SNTO FL2	26.2	0.00471
	3×10^{-2}	SNTO FL3	23.6	0.00523
150	1×10^{-2}	SNTO FL4	22.8	0.00541
	2×10^{-2}	SNTO FL5	24.2	0.00510
	3×10^{-2}	SNTO FL6	23.7	0.00521

The texture coefficient (TC) is an important parameter in characterizing the crystallographic orientation of thin films. It provides insight into the preferred orientation

of crystallites in the film, which can significantly impact the material properties. To get a better understanding of thin film orientation TC was calculated using Harris formula as in eqn (6.3) for the peaks (110), (111) and (200) and are tabulated in Table 6-2.

Table 6- 2 Texture Coefficient of Nb doped $SrTiO_{3-\delta}$ thin films

Sample label	**Texture Coefficient (TC)**		
	(110)	**(111)**	**(200)**
SNTO FL1	0.94	1.27	0.79
SNTO FL2	0.90	1.26	0.83
SNTO FL3	0.88	1.29	0.86
SNTO FL4	1.05	1.24	0.69
SNTO FL5	1.17	1.15	0.66
SNTO FL6	0.96	1.29	0.78

$$TC^{hkl} = n\frac{I^{hkl}/I_0^{hkl}}{\sum I^{hkl}/I_0^{hkl}} \tag{6.3}$$

Where I^{hkl} is the measured intensity of the (hkl) reflection, I_0^{hkl} is the standard intensity from the powder diffraction file, and n is the number of reflections considered. Even though, in all the XRD patterns the (110) reflection is dominant its TC is found to be low when compared to (111) plane. TC for (110) is also found to increase with sputtering power. In both series of films, (200) texturing is very weak indicated by low TC values. The low TC for the (110) plane, despite its dominant reflection, indicates that the thin film has a relatively strong preferred orientation along the (111) plane. The (111) plane has a lower absolute intensity but contributes more significantly relative to its expected intensity in the standard, its TC can be higher.

X-ray fluorescence (XRF) analysis has been done on prepared thin films, since it is proven to be a powerful tool allowing for precise quantification of elemental composition and dopant distribution and is represented in Fig. 6-2. This provides critical insights into the uniformity and incorporation of niobium within the $SrTiO_3$ matrix, which are essential for understanding the material's electronic and structural properties. Sr, Ti, and Nb were detected in the XRF spectra of all samples, each at their respective concentrations. The peaks at 4.51 and 4.93 KeV correspond to the $K_{\alpha 1}$ and $K_{\beta 1}$ signals of titanium, while the peaks at 14.16 and 15.82 KeV are associated with the $K_{\alpha 1}$ and $K_{\beta 1}$ signals of strontium, and the 16.6 KeV peak corresponds to the dopant niobium. XRF analysis was specifically conducted to determine the dopant concentration in each film, given that the sputtering target composition remained constant. This analysis helps to reveal how sputtering conditions influenced the Nb content across the series.

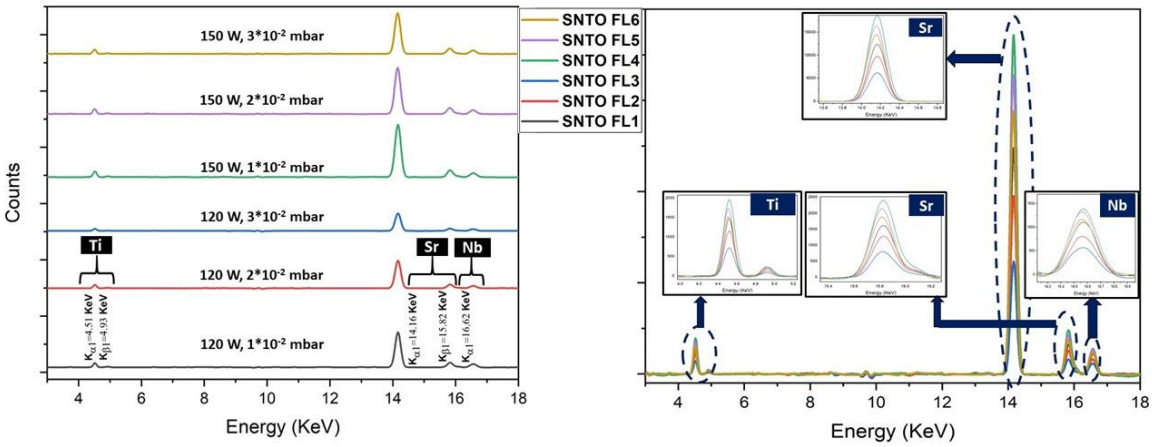

Figure 6- 2 XRF Spectra of $SrTi_{0.9}Nb_{0.1}O_{3-\delta}$ thin films with various sputtering conditions

The cumulative peak area under the Nb- K_α peak was thoroughly examined, yielding values of 233.96, 192.33, 146.28, 362.95, 343.21, and 290.81 for the thin films in the series SNTO FL1 to SNTO FL6 as indicated in Fig. 6-3. X-ray net intensities were obtained by integrating the regions of interest and subtracting the background using the trapezoid rule as given in equation (6.4) [30].

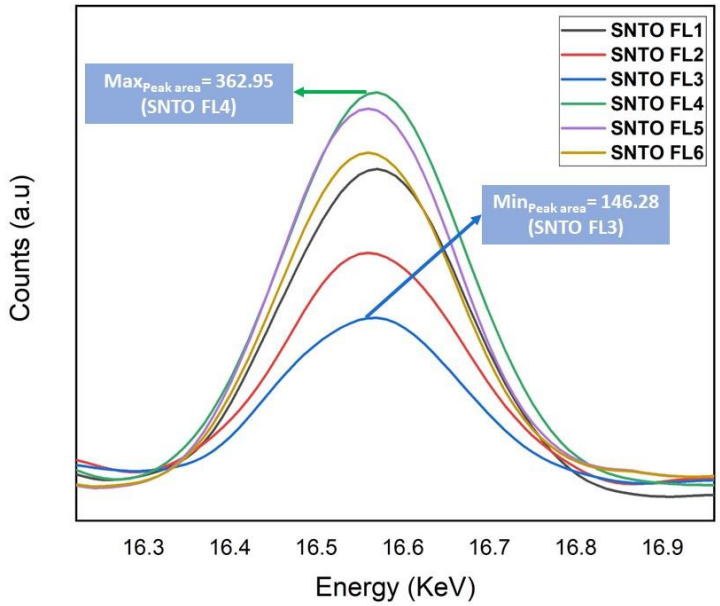

Figure 6- 3 Nb concentration revealed by XRF analysis of $SrTi_{0.9}Nb_{0.1}O_{3-\delta}$ thin films

$$Net\ counts = \sum_{i=ch\ 1}^{ch\ 2} Spect_i - \frac{(Spect_{ch1} + Spect_{ch2})(ch\ 2 - ch\ 1)}{2} \qquad (6.4)$$

Where, $Spect_i$ represents the spectrum (counts in channel (i), while $ch\ 1$ and $ch\ 2$ denote the first and last channels of the region of interest for the X-ray line being analyzed. With a constant sputtering power, increasing the Ar pressure resulted in a reduction of Nb content in the thin films.

Additionally, as the sputtering power increased, there was a noticeable rise in Nb concentration, with SNTO FL4 having the highest and SNTO FL3 the lowest Nb content. As the Nb content is found to be very high in SNTO FL4 and FL5 it is anticipated that the carrier concentration will also follow the order. Higher sputtering pressure increases the density of Ar gas molecules in the chamber, leading to more collisions between the sputtered Nb atoms and the gas molecules. This scattering effect reduces the energy and

directionality of Nb atoms, causing fewer of them to reach the substrate and incorporate into the growing film, thus lowering the dopant concentration.

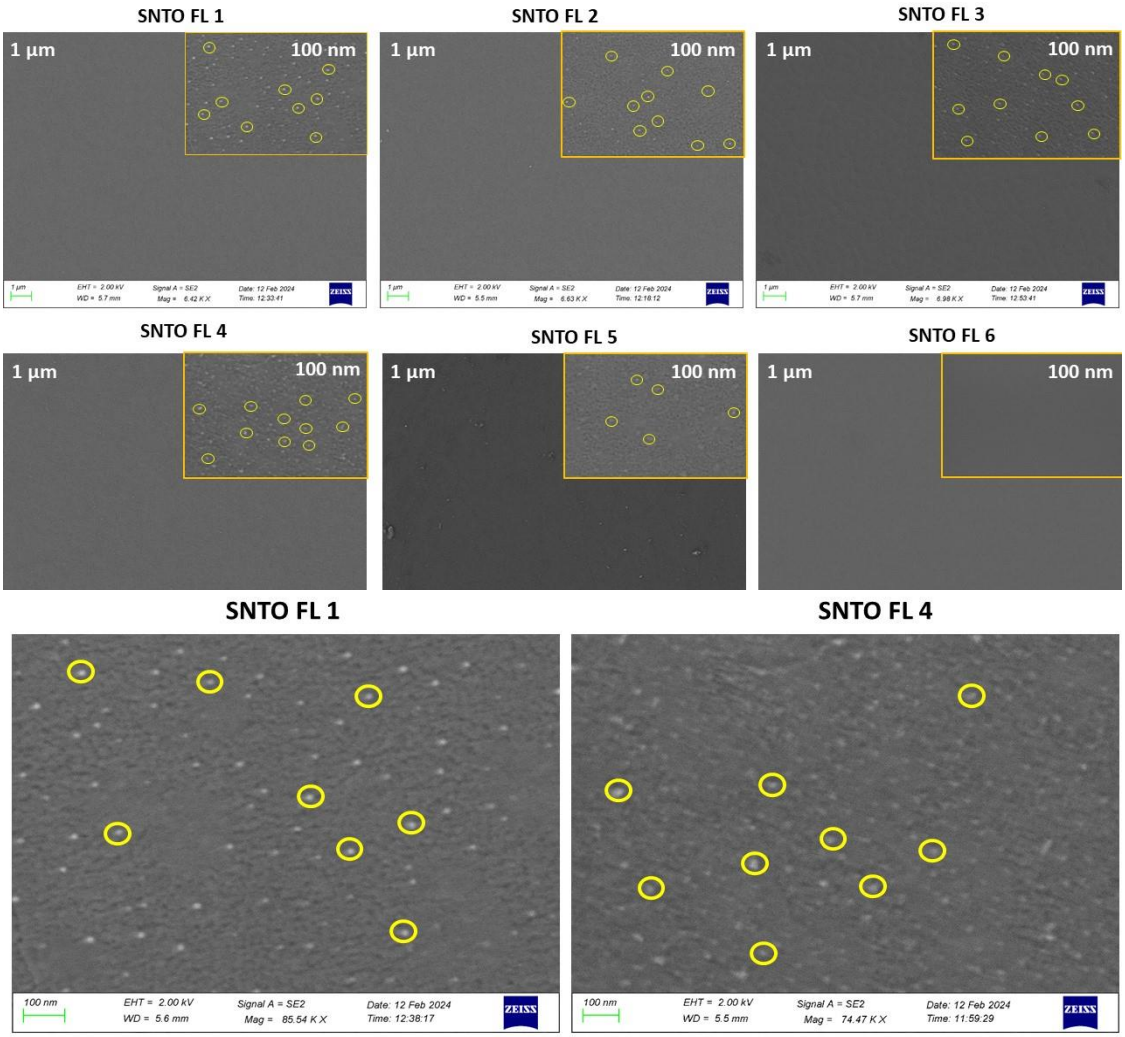

Figure 6- 4 SEM images of $SrTi_{0.9}Nb_{0.1}O_{3-\delta}$ thin films highlighting the Sr segregation

SEM images of Nb doped $SrTiO_3$ thin films indicated in Fig. 6-4 revealed that the relatively smooth surface, with a fine texture across the image. This indicates a uniform deposition process, which is critical for the thin film's functionality. SEM images of all samples except SNTO FL6 reveals the presence of bright spots with size ranging from 10 to 20 nm, scattered across the surface indicated by yellow circles. The presence of bright spots corresponds to Sr segregation driven by the thermodynamics and kinetics of the material system, particularly in the context of oxygen vacancies and the film's

interaction with the substrate and atmosphere. The degree of segregation is too low since the annealing is under vacuum and duration is minimal. Doping B site cation with Nb, formation of oxygen vacancies induce elastic and electrostatic interactions that have a role in determining the Sr segregation and is often very difficult to decouple these interlinked phenomena to find which one have considerable role. The size and distribution of segregates vary with sputtering power and gas pressure. At 150 W, the higher sputtering power provides more energetic adatoms and increased surface mobility, promoting the formation and aggregation of Sr into clusters; however, their density decreases with increasing gas pressure due to reduced kinetic energy and limited migration of Sr atoms. In contrast, films sputtered at 120 W exhibit less pronounced segregation owing to the lower energy and mobility of adatoms, further influenced by the pressure-dependent reduction in cluster formation [31,32].

During the process strontium (Sr) atoms migrate from the bulk of the material to the surface or grain boundaries and form small island like structures. During vacuum annealing at high temperatures the system seeks to minimize its overall energy, and one way to achieve this is by rearranging the atoms to more energetically favorable positions. Sr atoms, with their relatively lower bonding energy in the lattice compared to Ti, may

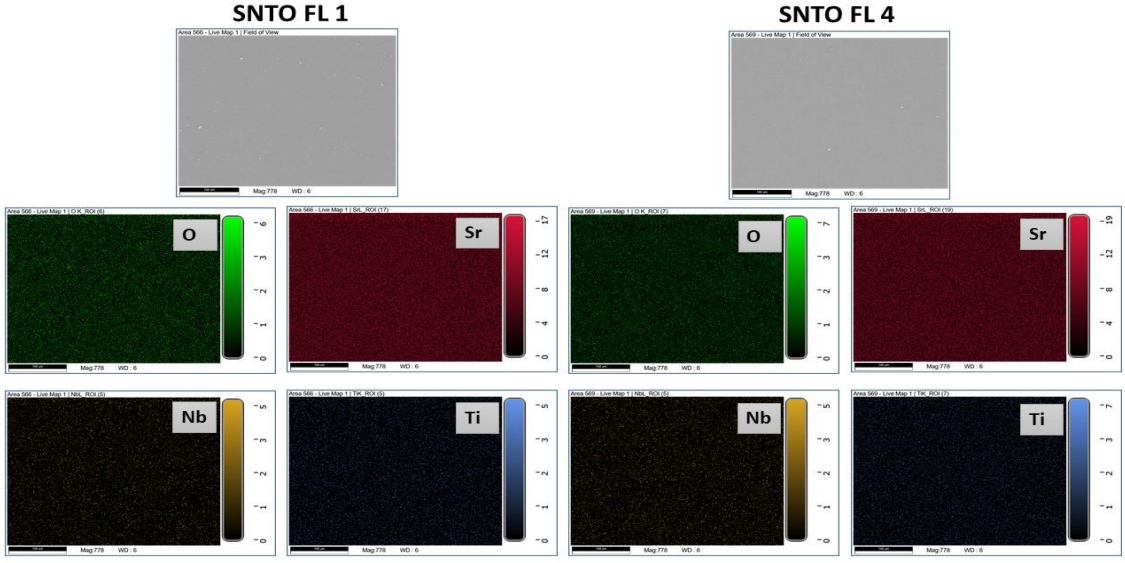

Figure 6- 5 EDS elemental mapping of $SrTi_{0.9}Nb_{0.1}O_{3-\delta}$ thin films

migrate to the surface where they are more stable. In vacuum conditions, oxygen atoms are more likely to leave the strontium titanate lattice, creating oxygen vacancies. These oxygen vacancies act as pathways for Strontium diffusion. Sr atoms can migrate along these vacancies toward the surface or grain boundaries, where the concentration of oxygen vacancies is lower.

The size of the Sr segregates is too small when compared to the earlier reported values which reaches up to few micrometers including our work on Pr doped $SrTiO_3$ thin films [33,34]. Vacuum annealing can reduce the size of Sr segregation in $SrTiO_3$ thin films by facilitating the diffusion of Sr atoms back into the bulk material or enabling a more even redistribution across the film. The enhanced atomic mobility helps break down larger segregated regions of Sr, resulting in a more uniform composition and minimizing the extent of Sr segregation at the surface. More over the temperature above 700 °C usually result in excessive Sr segregation. So this is prevented by limiting the annealing temperature under vacuum environment.

Fig. 6-5 shows the EDS elemental mapping images show the distribution of elements (O, Sr, Nb, Ti) in Nb-doped $SrTiO_3$ thin films for two samples: SNTO FL1 and SNTO FL4. The Oxygen maps for both SNTO FL1 and SNTO FL4 show a uniform distribution of the element throughout the thin films, indicating that the oxygen content is fairly consistent across both samples. The Strontium mapping shows the presence of Sr across the films, but the intensity seems slightly different between the two samples. For both SNTO FL1 and SNTO FL4, the Sr distribution appears fairly uniform, with a few scattered bright spots. These bright spots likely indicate regions of Sr segregation. The Nb distribution shows a relatively uniform presence of Nb across the thin films suggesting consistent doping of Nb in both samples. Similar to Nb, Ti is also evenly distributed across both films, with no significant variations or clusters.

6.3.2 Electrical characterization

To get insights into their charge carrier dynamics and transport properties, Hall effect studies were conducted on Nb-doped $SrTiO_3$ thin films across a wide temperature range

from 300 K to 600 K and is represented in Fig. 6-6. These measurements help to quantify key parameters such as carrier concentration, mobility, and the nature of charge carriers in the system. In addition to pentavalent impurity incorporation, sputtering Nb-doped $SrTiO_3$ in an oxygen-free environment followed by vacuum annealing can lead to the formation of oxygen-deficient thin films. These vacancies act as n-type dopants by releasing additional free electrons, thereby increasing the carrier concentration in the material. Previous ab-initio studies predicted that introducing small oxygen vacancies would lead to the formation of an additional donor band approximately 0.3–0.4 eV below the conduction band minimum [35,36]. As a result, increasing the concentration of oxygen vacancies would correspond to a rise in carrier density. Irrespective of the sputtering power and gas pressure all thin films shows a decrease in carrier concentration with temperature. The room temperature carrier concentration of the films sputtered at 120 W ranges from 8.82×10^{21} to 1.04×10^{22} cm^{-3}, whereas for the thin films sputtered at 150 W the change is from 1.37×10^{22} to 1.74×10^{22} cm^{-3}. The decreased carrier density for the films sputtered at 120 W is attributed to the low concentration of Nb in the thin films. The increased concertation of Nb in 150 W sputtered films resulted in carrier concentration of the order of 10^{22}. As the temperature increases, thermal excitation of electrons from the conduction band back to defect levels (such as Nb donor levels or

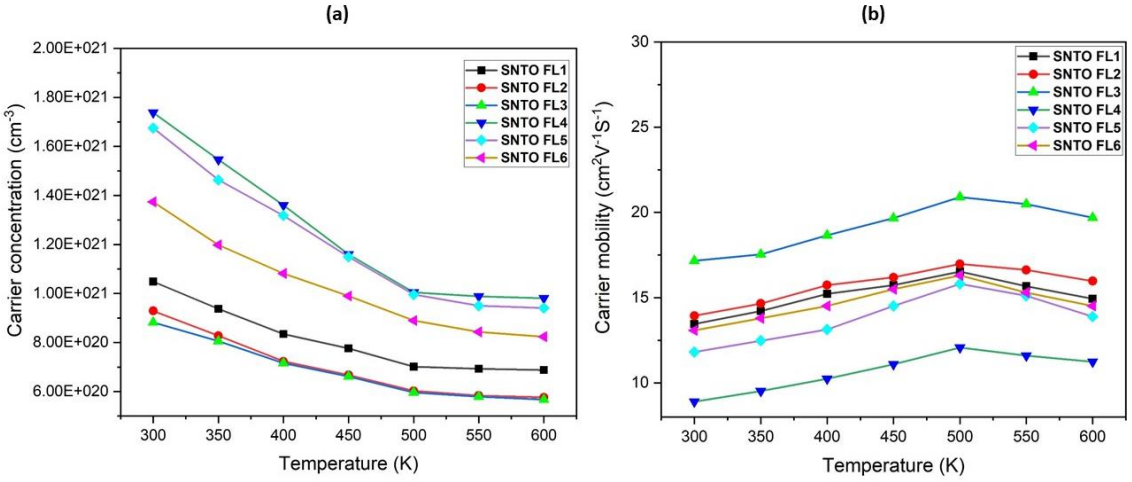

Figure 6-6 Temperature dependent **(a)** carrier concentration **(b)** mobility of $SrTi_{0.9}Nb_{0.1}O_{3-\delta}$ thin films

oxygen vacancy levels) can occur. At higher temperatures, carriers can more easily be thermally activated into traps or recombine, leading to a reduction in the effective free carrier concentration. At elevated temperatures, oxygen vacancies can be replenished by oxygen diffusion from the environment, thus reducing the vacancy concentration and thereby decreasing the number of electrons contributing to conduction.

The partial density of states (DOS) for Ti and O undergoes significant changes when Nb dopant is introduced. The valence band of Nb-doped $SrTiO_3$ is primarily composed of O 2p states with some contributions from Ti 3d and Nb 4d states, while the conduction band is mainly formed by Ti 3d and Nb 4d states with O 2p admixtures. While the conduction band experiences significant changes due to Nb doping, the valence band remains largely dominated by O 2p states. Therefore, the overall DOS shape remains similar because the fundamental structure of the valence band remains unchanged [37]. As the Nb concentration increases, the overall electronic energy levels of the system shift downward due to the increased electron density in the conduction band, while the overall shape of the DOS remains similar but moves to lower energy levels resulting in availability of more carriers.

The increased carrier concentration is attributed to multiple factors. Apart from the donor doping, oxygen vacancy formation, Ti^{4+} reduction to Ti^{3+}, Sr vacancy formation and 2D electron gas formation between $SrTiO_3/SiO_2$ interfaces amplifies the carrier density. When grown in an argon (Ar) atmosphere, oxygen vacancies are more likely to form, creating a donor band near the conduction band edge. Each oxygen vacancy donates two electrons to the conduction band, which leads to an increase in carrier density. Based on thermodynamic conditions, neutral oxygen on regular sites may leave the lattice, leaving behind oxygen vacancies as per eqn (6.5). At high temperatures, oxygen vacancies tend to lose electrons more easily. When this happens, the vacancy becomes positively ionized, and the released electrons are injected into the conduction band of the material.

$$O_o^X \leftrightarrow V_{\ddot{O}} + 2e^l + \frac{1}{2}O_2 \tag{6.5}$$

The mass action law can be expressed as in eqn (6.6)

$$[V_{\ddot{O}}]n^2 P(O_2)^{\frac{1}{2}} = K_{V_{\ddot{O}}}(T) \tag{6.6}$$

In eqn (6.6) $K_{V_{\ddot{O}}}(T)$ represents the temperature-dependent formation constant of oxygen vacancies that are doubly ionized. Formation of singly ionized oxygen vacancies, $V_{\dot{O}}$ is not favorable at temperatures above 600 °C [38]. Oxygen free sputtering environment and low partial pressure environment will lead to formation of oxygen vacancies resulting in overall carrier concentration indicated by eqn (6.7).

$$n \approx 2[V_{\ddot{O}}] + [Nb_{\dot{Ti}}] \tag{6.7}$$

Where $[Nb_{\dot{Ti}}]$, is the Nb^{5+} replacing Ti^{4+}. It has been shown by Blennow et.al that at very low oxygen partial pressure the conductivity of Nb doped $SrTiO_3$ ceramics can be represented as eqn (6.8), which shows $P(O_2)^{-1/6}$ dependence [39]. Since the sputtering was done at extremely low oxygen partial pressure, we may expect a surge in electrical conductivity.

$$\sigma_n \approx K_1(T)eP(O_2)^{-1/6}\mu_n(T) \tag{6.8}$$

The carrier mobility of the thin films in Fig. 6-6 increases with temperature up to 500 K, after which it decreases. At lower temperatures, ionized impurity scattering from dopant atoms and defects like oxygen vacancies limits mobility. As temperature rises, the thermal energy reduces the impact of impurity scattering, allowing mobility to improve. However, above 500 K, phonon scattering, caused by lattice vibrations, becomes the dominant mechanism, reducing electron mobility. The shift from impurity to phonon scattering is reflected in the mobility's temperature dependence, with a $T^{1.5}$ increase below 500 K and a $T^{-1.5}$decrease beyond that point.

The films with low carrier concentrations SNTO FL3 and SNTO FL6 among 120 W and 150 W deposited series, shows high motilitiy due to reduced scattering of charge

carriers. The enhanced mobility of SNTO FL6 among 150 W sputtered films is also attributed to the smooth surface texture reveled by SEM images. The increased mobility of the order of 10^2 $cm^2v^{-1}s^{-1}$ for all thin films can be attributed to the strain developed, when films are grown on mismatched substrates like silicon. $SrTiO_3$ has a perovskite structure with a lattice constant that doesn't match with the silicon lattice, causing epitaxial strain in the $SrTiO_3$ layer. Since the substrate has a larger lattice parameter than the thin film it develops tensile strain to reduce the bandgap, potentially leading to improved carrier mobility by facilitating electron transport across a narrower bandgap. This strain engineering has already been in use to enhance mobility for La doped STO systems [40]. Sr vacancy clusters can form during vacuum annealing, creating regions of tensile lattice strain around the clusters and compressive lattice strain between them. These strain variations act as efficient transport channels for electrons, potentially resulting in enhanced electron mobility [41].

6.3.3 Thermoelectrical properties: Temperature dependent Seebeck coefficient and power factor

Thermoelectric studies were conducted to investigate the temperature-dependent electrical conductivity and Seebeck coefficient of Nb doped $SrTiO_3$ thin films over the temperature range of 300 K to 973 K and results are represented in Fig. 6-7.

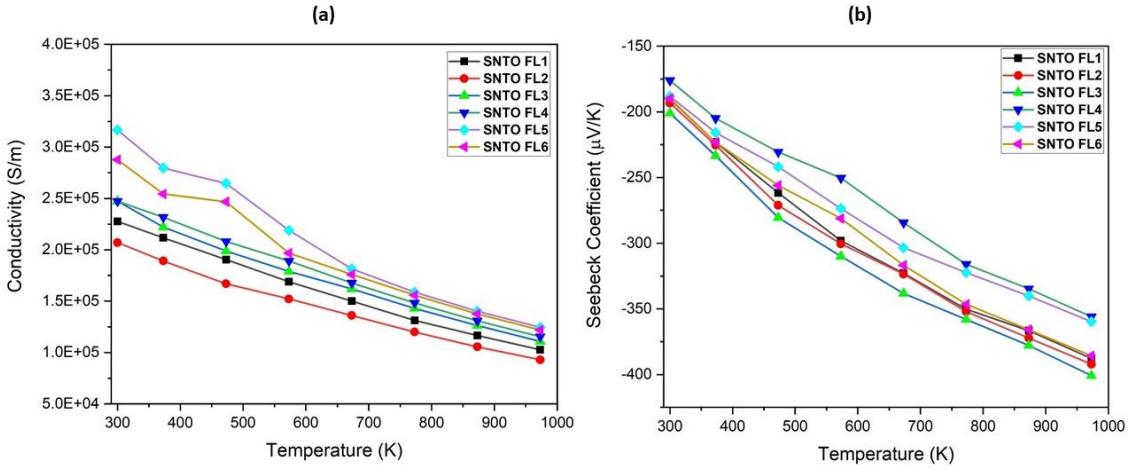

Figure 6-7 (a) Temperature dependent conductivity **(b)** Seebeck coefficient of $SrTi_{0.9}Nb_{0.1}O_{3-\delta}$ thin films

The electrical conductivity of all samples shown in Fig. 6-7(a) shows a decreasing trend with temperature. This shows a degenerate semiconductor behavior due to the high concentration of doped carriers, which places the Fermi level inside the conduction band resulting in metallic behavior. The carrier concentration studies revealed the Nb^{5+} donors have already created an environment surpassing the critical density for metallic type of conduction. The decrease in conductivity follows T^{-2} for all thin films, indicating that phonon scattering was the dominant mechanism [42–44]. The negative sign of Seebeck effect indicate the n type conductivity in samples. To compensate the excessive charge of Nb^{5+} in substitution to Ti^{4+}, one Ti cation vacancy may be created per four Nb introduced or the stoichiometric reduction of Ti^{4+} to Ti^{3+} per Nb introduced may happen depending on the processing conditions, which introduces shallow donor levels below the CB edge and increases the metallic character.

The absolute value of Seebeck coefficient, $|S|$ is found to increase with temperature showing a positive correlation. $|S|$ is found to be lowest for the sample SNTO FL4 and highest for SNTO FL3 following the trend of Nb content in thin films. In degenerate semiconductors, the Fermi level is close to or within the conduction band. As temperature increases, the difference between the energy of high-energy and low-energy carriers increases, enhancing the Seebeck coefficient. Since the conduction mechanism remains metallic-like, this leads to a steady increase in $|S|$. Heikes formula predicts a limit for the Seebeck coefficient in strongly correlated materials, particularly at high temperatures, when the entropy contribution to the Seebeck coefficient dominates. Even though direct Heikes limit was not observed for the whole range indicating the presence of additional complexities in the material, such as defects, impurities, or energy filtering, a tendency to Heike like limit is observed at high temperatures. At high carrier concentrations Seebeck coefficient can be represented by Pisarenko relation as in eqn (6.9) [45,46].

$$S = \frac{8\pi^2 k_B^2 T}{3eh^2} m^* \left(\frac{\pi}{3n}\right)^{2/3} \tag{6.9}$$

where, k_B, e, h, m^*, n are the Boltzmann constant, electron charge, Planck's constant, effective mass and carrier concentration respectively. As evident from the equation Seebeck coefficient has an inverse relationship with carrier concentration. The sample with higher Nb content and higher carrier concentration is SNTO FL4 and is having the lowest value of $|S|$, and the converse is hold for SNTO FL3.The value of Seebeck coefficient is higher when compared to previous research at the same doping level. It means that energy filtering effect, variation in effective mass have a role in defining S. By blocking low-energy carriers, energy filtering increases the mean carrier energy, which leads to an increase in the Seebeck coefficient without significantly reducing the electrical conductivity. This is particularly relevant in degenerate semiconductors, where the carrier concentration is high but the Seebeck coefficient tends to be low. Energy filtering can help break this trend by enhancing S while maintaining or only slightly reducing electrical conductivity [47,48]. The normalized effective mass - (m^*/m_0) of all samples were calculated and tabulated in Table 6-3.

Table 6- 3 Normalized effective mass of $SrTi_{0.9}Nb_{0.1}O_{3-\delta}$ thin films at room temperature

Sample	Seebeck coefficient (μV/K)	Carrier concentration (cm^{-3})	Normalized effective mass (m^*/m_0)
SNTO FL1	190.22	1.07 E+21	9.90
SNTO FL2	194.22	9.32 E+20	9.22
SNTO FL3	196.06	8.76 E+20	8.93
SNTO FL4	176.10	1.71 E+21	12.57
SNTO FL5	188.20	1.55 E+21	12.47
SNTO FL6	192.80	1.39 E+21	11.97

The values of normalized effective mass is comparatively high when compared to those obtained by Ohta *et al.*, but it is higher than other oxide materials [49,50],

comparable to the theoretical and experimental results obtained by Fumega1*et al.* and Kumar *et al.*[51,52].

The overall value of $|S|$ depend on carrier concentration values too, so may not depend on electron effective mass trend. Thin films sputtered with 120 W power is found to have less effective mass when compared to those at 150 W. The high effective mass in the series for SNTO FL4, SNTO FL5 and SNTO FL6 results in decreased mobility.

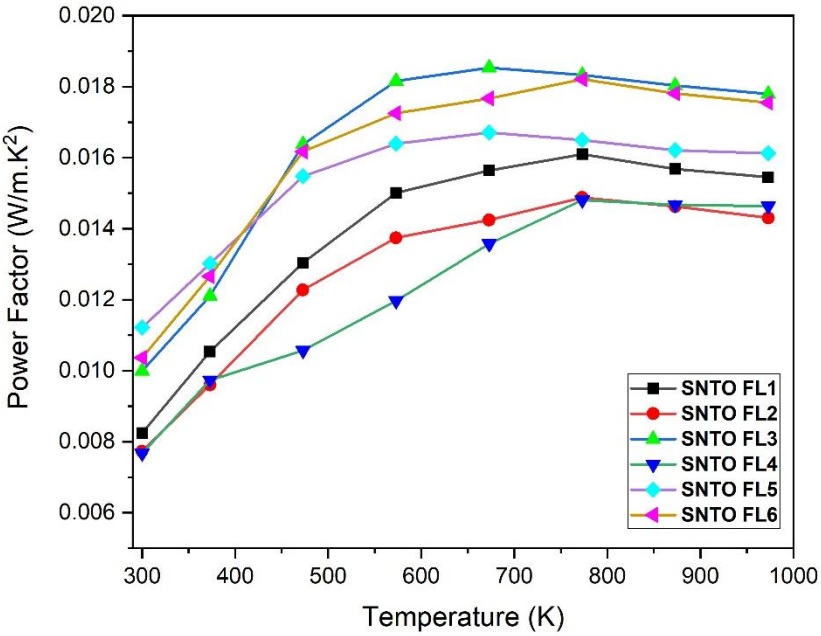

Figure 6- 8 Temperature dependent power factor of $SrTi_{0.9}Nb_{0.1}O_{3-\delta}$ thin films

Another aspect that is to be considered here is the energy filtering and strain effect on relatively large Seebeck coefficient. Lattice mismatch introduces strain that distorts the crystal lattice of the Nb-doped $SrTiO_3$ thin film. This strain can lead to band structure modifications, such as band flattening or splitting of degenerate bands, which increases the density of states near the Fermi level. A higher density of states enhances the Seebeck coefficient by increasing the energy dependence of carrier transport. Strain and interface effects can localize carriers and introduce selective scattering, which suppresses low-energy carriers and promotes energy filtering. This allows high-energy carriers to contribute more effectively, boosting the Seebeck coefficient [53,54].

Accounting for the spin degeneracy and t_{2g} degeneracy, Seebeck coefficient may be expressed as,

$$S_{T\to\infty} = \frac{-k_B}{e} log\left[2f_{t2g}\frac{1-\eta}{\eta}\right] \tag{6.10}$$

Where f_{t2g} represents a function the weights the t_{2g} degeneracy. In the unstrained case, all the t_{2g} bands are energetically degenerate, leading to a triple orbital degeneracy. However, under tensile (or compressive) strain, the energy levels shift such that the d_{xy} band drops lower for tensile strain, or the d_{xz} and d_{yz} bands drop lower for compressive strain. This results in a single or double degeneracy depending on the type of strain applied. As per the calculations based on this model by Fumega1*et al*, for low doping levels, the three possible cases of degeneracy are observed: in the unstrained situation, there is threefold degeneracy, while applying compressive or tensile strain reduces the system to a twofold degenerate state. As doping levels rise, the t_{2g} bands become more filled, making the influence of band splitting less significant. Once doping exceeds 5%, the degeneracy factor approaches 3 and becomes almost unaffected by the applied strain [52]. The strain dependence of S is expected here due to the low doping levels and the obtained values are matching with theoretical predictions.

To achieve an enhanced power factor, it is crucial to optimize physical quantities such as the Seebeck coefficient and electrical conductivity. Proper tuning of these parameters ensures a balance between carrier transport efficiency and energy conversion, which is vital for improving thermoelectric performance. The P.F values obtained represented in Fig. 6-8, indicate the highest value of 0.0185 W/mK^2 for SNTO FL3 at 673 K due to higher Seebeck coefficient.

6.4 Conclusions

$SrTi_{0.9}Nb_{0.1}O_{3-\delta}$ thin films were synthesized via RF sputtering under pure Argon atmosphere, followed by post-deposition vacuum annealing. This approach effectively

limited Sr segregation and induced a high concentration of oxygen vacancies, enhancing carrier concentration to the order of 10^{21}-10^{22} cm^{-3}. The resulting combination of high carrier concentration and improved mobility led to significantly enhanced electrical conductivity, possibly supported by two-dimensional electron gas (2DEG) formation at the $SrTiO_3/SiO_2$ interface. Thermoelectric performance was further boosted by strain-induced effects and energy filtering mechanisms, which enhanced the Seebeck coefficient without compromising conductivity. Optimal doping, lattice mismatch-induced strain, and modulation of the effective mass contributed to favorable band structure tuning and mobility enhancement. Collectively, these strategies yielded a record-high thermoelectric power factor of 0.0185 W/mK^2, establishing Nb doped $SrTiO_3$ as a highly efficient thermoelectric material.

References:

[1] X. Zhang, Y. Zhang, L. Wu, A. Tsuruta, M. Mikami, H.J. Cho, H. Ohta, $Ba_{1/3}CoO_2$: A Thermoelectric Oxide Showing a Reliable ZT of ∼0.55 at 600 °C in Air, ACS Appl Mater Interfaces 14 (2022) 33355–33360. https://doi.org/10.1021/acsami.2c08555.

[2] Z. Liu, X. Guo, R. Li, J. Qin, H. Li, X. Chen, X. Zhou, Band structure manipulated by high pressure-assisted Te doping realizing improvement in thermoelectric performance of BiCuSeO system, Journal of Materiomics 5 (2019) 649–656. https://doi.org/10.1016/j.jmat.2019.06.002.

[3] J. Yu, R. Freer, Calcium cobaltite, a promising oxide for energy harvesting: effective strategies toward enhanced thermoelectric performance, Journal of Physics: Energy 4 (2022) 022001. https://doi.org/10.1088/2515-7655/ac5172.

[4] J.S. P.K., M. Shah, P.P. Pradyumnan, Tailoring structure and nanoscale surface topography in Mg–N doped $CuCrO_2$ thin films via post deposition annealing for optothermoelectric application, Opt Mater (Amst) 147 (2024) 114703. https://doi.org/https://doi.org/10.1016/j.optmat.2023.114703.

[5] J.S. P.K., M. Shah, P.P. Pradyumnan, Intense narrow band blue emission in CuCrO2 delafossite by Ni^{2+}-Mg^{2+} dual cation doping, Spectrochim Acta A Mol Biomol Spectrosc 305 (2024) 123442. https://doi.org/10.1016/j.saa.2023.123442.

[6] J.S. P.K., M. Shah, P.P. Pradyumnan, Magnetoelectric coupling and thermoelectric behaviors in Ni-doped $CuCrO_2$ crystallites, Chemical Engineering Journal 476 (2023) 146568. https://doi.org/https://doi.org/10.1016/j.cej.2023.146568.

[7] P.K. Jamshina Sanam, M. Shah, P.P. Pradyumnan, Enhanced thermoelectric properties in dual cation doped $CuCrO_2$ nanocrystals mediated by magnon-carrier drag, Mater Res Bull 164 (2023) 112244.https://doi.org/10.1016/j.materresbull.2023.112244.

[8] P.K. Jamshina Sanam, M. Shah, P.P. Pradyumnan, The enhancement of NIR transparency due to annealing and Mg-doping in CuCrO2 thin films, Mater Lett 330 (2023) 133295. https://doi.org/https://doi.org/10.1016/j.matlet.2022.133295.

[9] P.K. Jamshina Sanam, M. Shah, P.P. Pradyumnan, Structure induced modification on thermoelectric and optical properties by Mg doping in $CuCrO_2$ nanocrystals, Solid State Commun 353 (2022) 114855. https://doi.org/10.1016/j.ssc.2022.114855.

[10] P.K.J. Sanam, M. Shah, P.P. Pradyumnan, Raman spectroscopic investigation and thermoelectric studies of defect-induced Mg-doped delafossite thin film, Journal of Materials Science: Materials in Electronics (2022). https://doi.org/10.1007/s10854-022-09013-y.

[11] P.K. Jamshina Sanam, M. Shah, P.P. Pradyumnan, Structure induced modification on thermoelectric and optical properties by Mg doping in $CuCrO_2$ nanocrystals, Solid State Commun 353 (2022) 114855. https://doi.org/10.1016/J.SSC.2022.114855.

[12] P.K. Jamshina Sanam, Et.al, Spin chiral interactions modulated Seebeck coefficient and improved optical properties by Zn doping in $CuCrO_2$ crystallites, Mater Chem Phys 308 (2023) 128214. https://doi.org/10.1016/j.matchemphys.2023.128214.

[13] M. Shah, P.K. Jamshina Sanam, P.P. Pradyumnan, Defect-induced $Sr_{1-x}Pr_xTiO_3$ crystallites by burial sintering and its optoelectronic applications, Journal of Physics and Chemistry of Solids 181 (2023) 111516. https://doi.org/10.1016/j.jpcs.2023.111516.

[14] M. Shah, A.P. Jemshihas, P.K. Jamshina Sanam, P.P. Pradyumnan, Magneto thermoelectric effect of nickel thin film synthesized by RF magnetron sputtering, Physica E Low Dimens Syst Nanostruct 147 (2023) 115591. https://doi.org/10.1016/j.physe.2022.115591.

[15] M. Shah, P.K.J. Sanam, P.P. Pradyumnan, Tuning of photoluminescence properties: Impact of Pr-doping in $SrTiO_3$ crystallites, Mater Today Commun 39 (2024) 109323. https://doi.org/https://doi.org/10.1016/j.mtcomm.2024.109323.

[16] X.-L. Shi, H. Wu, Q. Liu, W. Zhou, S. Lu, Z. Shao, M. Dargusch, Z.-G. Chen, SrTiO3-based thermoelectrics: Progress and challenges, Nano Energy 78 (2020) 105195. https://doi.org/10.1016/j.nanoen.2020.105195.

[17] C.H. Suen, L. Zhang, K. Yang, M.Q. He, Y.S. Chai, K. Zhou, H. Wang, X.Y. Zhou, J.-Y. Dai, High thermoelectric performance of ZrTe2/$SrTiO_3$ heterostructure, Journal of Materiomics 8 (2022) 570–576. https://doi.org/10.1016/j.jmat.2021.12.004.

[18] X. Wan, X. Lu, L. Sun, M. Chen, N. Ta, W. Liu, Q. Chen, L. Chen, J. He, P. Jiang, X. Bao, Interface-enhanced thermoelectric output power in CrN/$SrTiO_{3-x}$ heterostructure,

Journal of Energy Chemistry 64 (2022) 16–22. https://doi.org/10.1016/j.jechem.2021.04.056.

[19] A. Chatterjee, Z. Lan, D.V. Christensen, F. Bauitti, A. Morata, E. Chavez-Angel, S. Sanna, I.E. Castelli, Y. Chen, A. Tarancon, N. Pryds, On the thermoelectric properties of Nb-doped $SrTiO_3$ epitaxial thin films, Physical Chemistry Chemical Physics 24 (2022) 3741–3748. https://doi.org/10.1039/D1CP03679C.

[20] F. Aguesse, A.-K. Axelsson, P. Reinhard, V. Tileli, J.L.M. Rupp, N.M. Alford, High-temperature conductivity evaluation of Nb doped $SrTiO_3$ thin films: Influence of strain and growth mechanism, Thin Solid Films 539 (2013) 384–390. https://doi.org/https://doi.org/10.1016/j.tsf.2013.05.094.

[21] J. Kim, L.T. Duy, S.Y. Lee, M. Ko, H. Seo, Thermoelectric properties of Nb-doped $SrTiO_3$ films prepared by co-sputtering, Journal of Asian Ceramic Societies 8 (2020) 1135–1146. https://doi.org/10.1080/21870764.2020.1824325.

[22] S.R.S. Kumar, A.Z. Barasheed, H.N. Alshareef, High Temperature Thermoelectric Properties of Strontium Titanate Thin Films with Oxygen Vacancy and Niobium Doping, ACS Appl Mater Interfaces 5 (2013) 7268–7273. https://doi.org/10.1021/am4015956.

[23] S.R.S. Kumar, A.Z. Barasheed, H.N. Alshareef, High Temperature Thermoelectric Properties of Strontium Titanate Thin Films with Oxygen Vacancy and Niobium Doping, ACS Appl Mater Interfaces 5 (2013) 7268–7273. https://doi.org/10.1021/am4015956.

[24] A.I. Abutaha, S.R.S. Kumar, K. Li, A.M. Dehkordi, T.M. Tritt, H.N. Alshareef, Enhanced Thermoelectric Figure-of-Merit in Thermally Robust, Nanostructured Superlattices Based on $SrTiO_3$, Chemistry of Materials 27 (2015) 2165–2171. https://doi.org/10.1021/acs.chemmater.5b00144.

[25] PhysRevB.63.113104, (n.d.).

[26] H. Ohta, S. Kim, Y. Mune, T. Mizoguchi, K. Nomura, S. Ohta, T. Nomura, Y. Nakanishi, Y. Ikuhara, M. Hirano, H. Hosono, K. Koumoto, Giant thermoelectric Seebeck coefficient of a two-dimensional electron gas in $SrTiO_3$, Nat Mater 6 (2007) 129–134. https://doi.org/10.1038/nmat1821.

[27] L. Zhao, C. Zhao, J. Liu, Z. Liu, Y. Chen, Effect of sputtering pressure on the structure and properties of SiO2 films prepared by magnetron sputtering, Micro Nano Lett 15 (2020) 872–876. https://doi.org/10.1049/mnl.2020.0222.

[28] A. Büttner, A.-C. Probst, F. Emmerich, C. Damm, B. Rellinghaus, T. Döhring, M. Stollenwerk, Influence of sputtering pressure on microstructure and layer properties of iridium thin films, Thin Solid Films 662 (2018) 41–46. https://doi.org/10.1016/j.tsf.2018.06.056.

[29] S. Yu, W. Xu, H. Zhu, W. Qiu, Q. Fu, L. Kong, Effect of sputtering power on structure and properties of ZTO films, J Alloys Compd 883 (2021) 160622. https://doi.org/https://doi.org/10.1016/j.jallcom.2021.160622.

[30] G. Gottardi, R. Pandiyan, V. Micheli, G. Pepponi, S. Gennaro, R. Bartali, N. Laidani, Effect of Nd3+ incorporation on the microstructure and chemical structure of RF sputtered ZnO thin films, Materials Science and Engineering: B 178 (2013) 609–616. https://doi.org/https://doi.org/10.1016/j.mseb.2012.12.013.

[31] J.E. Kleibeuker, G. Koster, W. Siemons, D. Dubbink, B. Kuiper, J.L. Blok, C.-H. Yang, J. Ravichandran, R. Ramesh, J.E. ten Elshof, D.H.A. Blank, G. Rijnders, Atomically Defined Rare-Earth Scandate Crystal Surfaces, Adv Funct Mater 20 (2010) 3490–3496. https://doi.org/10.1002/adfm.201000889.

[32] T. Ohnishi, K. Shibuya, T. Yamamoto, M. Lippmaa, Defects and transport in complex oxide thin films, J Appl Phys 103 (2008) 103703. https://doi.org/10.1063/1.2921972.

[33] Y. Yu, K.F. Ludwig, J.C. Woicik, S. Gopalan, U.B. Pal, T.C. Kaspar, S.N. Basu, Effect of Sr Content and Strain on Sr Surface Segregation of $La_{1-x}Sr_xCo_{0.2}Fe_{0.8}O_{3-\delta}$ as Cathode Material for Solid Oxide Fuel Cells, ACS Appl Mater Interfaces 8 (2016) 26704–26711. https://doi.org/10.1021/acsami.6b07118.

[34] B. Koo, K. Kim, J.K. Kim, H. Kwon, J.W. Han, W. Jung, Sr Segregation in Perovskite Oxides: Why It Happens and How It Exists, Joule 2 (2018) 1476–1499. /https://doi.org/10.1016/j.joule.2018.07.016.

[35] J. Ravichandran, W. Siemons, M.L. Scullin, S. Mukerjee, M. Huijben, J.E. Moore, A. Majumdar, R. Ramesh, Tuning the electronic effective mass in double-doped $SrTiO_3$:Phys Rev B 83 (2011) 35101. https://doi.org/10.1103/PhysRevB.83.035101.

[36] W. Wunderlich, H. Ohta, K. Koumoto, Enhanced effective mass in doped $SrTiO_3$ and related perovskites, Physica B Condens Matter 404 (2009) 2202–2212. https://doi.org/10.1016/j.physb.2009.04.012.

[37] K. Ozdogan, M. Upadhyay Kahaly, S.R. Sarath Kumar, H.N. Alshareef, U. Schwingenschlögl, Enhanced carrier density in Nb-doped $SrTiO_3$ thermoelectrics, J Appl Phys 111 (2012) 054313. https://doi.org/10.1063/1.3692057.

[38] R. Moos, K.H. Hardtl, Defect Chemistry of Donor-Doped and Undoped Strontium Titanate Ceramics between 1000° and 1400°C, Journal of the American Ceramic Society 80 (1997) 2549–2562. https://doi.org/10.1111/j.1151-2916.1997.tb03157.x.

[39] P. Blennow, A. Hagen, K.K. Hansen, L.R. Wallenberg, M. Mogensen, Defect and electrical transport properties of Nb-doped $SrTiO_3$, Solid State Ion 179 (2008) 2047–2058. https://doi.org/10.1016/j.ssi.2008.06.023.

[40] B. Jalan, S.J. Allen, G.E. Beltz, P. Moetakef, S. Stemmer, Enhancing the electron mobility of $SrTiO_3$ with strain, Appl Phys Lett 98 (2011) 132102. https://doi.org/10.1063/1.3571447.

[41] S. Kobayashi, Y. Mizumukai, T. Ohnishi, N. Shibata, Y. Ikuhara, T. Yamamoto, High Electron Mobility of Nb-Doped $SrTiO_3$ Films Stemming from Rod-Type Sr Vacancy Clusters, ACS Nano 9 (2015) 10769–10777. https://doi.org/10.1021/acsnano.5b05720.

[42] S. Ohta, T. Nomura, H. Ohta, K. Koumoto, High-temperature carrier transport and thermoelectric properties of heavily La- or Nb-doped $SrTiO_3$ single crystals, J Appl Phys 97 (2005) 034106. https://doi.org/10.1063/1.1847723.

[43] K. Park, J.S. Son, S.I. Woo, K. Shin, M.-W. Oh, S.-D. Park, T. Hyeon, Colloidal synthesis and thermoelectric properties of La-doped $SrTiO_3$ nanoparticles, J Mater Chem A Mater 2 (2014) 4217–4224. https://doi.org/10.1039/C3TA14699E.

[44] D. Liu, Y. Zhang, H. Kang, J. Li, Z. Chen, T. Wang, Direct preparation of La-doped $SrTiO_3$ thermoelectric materials by mechanical alloying with carbon burial sintering, J Eur Ceram Soc 38 (2018) 807–811. https://doi.org/10.1016/j.jeurceramsoc.2017.09.022.

[45] P. Dey, S.S. Jana, F. Anjum, T. Bhattacharya, T. Maiti, Effect of semiconductor to metal transition on thermoelectric performance in oxide nanocomposites of SrTi0.85Nb0.15O3 with graphene oxide, Appl Mater Today 21 (2020) 100869. https://doi.org/10.1016/j.apmt.2020.100869.

[46] G.J. Snyder, E.S. Toberer, Complex thermoelectric materials, Nat Mater 7 (2008) 105–114. https://doi.org/10.1038/nmat2090.

[47] D. Li, D. Wang, X. Zhang, L.-D. Zhao, Synergistically enhanced electrical transport properties of $SrTiO_3$ via Fermi level regulation and modulation doping, J Mater Chem C Mater 10 (2022) 13851–13859. https://doi.org/10.1039/D2TC00719C.

[48] J.M.O. Zide, D. Vashaee, Z.X. Bian, G. Zeng, J.E. Bowers, A. Shakouri, A.C. Gossard, Demonstration of electron filtering to increase the Seebeck coefficient in $In_{0.53}Ga_{0.47}As/In_{0.53}Ga_{0.28}Al_{0.19}As$ superlattices, Phys Rev B 74 (2006) 205335. https://doi.org/10.1103/PhysRevB.74.205335.

[49] S. OHTA, H. OHTA, K. KOUMOTO, Grain Size Dependence of Thermoelectric Performance of Nb-Doped $SrTiO_3$ Polycrystals, Journal of the Ceramic Society of Japan 114 (2006) 102–105. https://doi.org/10.2109/jcersj.114.102.

[50] K. Fujita, T. Mochida, K. Nakamura, High-Temperature Thermoelectric Properties of $NaxCoO_{2-\delta}$ Single Crystals, Jpn J Appl Phys 40 (2001) 4644. https://doi.org/10.1143/JJAP.40.4644.

[51] S.R.S. Kumar, A.Z. Barasheed, H.N. Alshareef, High Temperature Thermoelectric Properties of Strontium Titanate Thin Films with Oxygen Vacancy and Niobium Doping, ACS Appl Mater Interfaces 5 (2013) 7268–7273. https://doi.org/10.1021/am4015956.

[52] A.O. Fumega, V. Pardo, Ab initio study of the strain dependence of thermopower in electron-doped $SrTiO_3$, Journal of Physics: Condensed Matter 29 (2017) 065501. https://doi.org/10.1088/1361-648X/29/6/065501.

[53] K. Berland, X. Song, P.A. Carvalho, C. Persson, T.G. Finstad, O.M. Løvvik, Enhancement of thermoelectric properties by energy filtering: Theoretical potential and experimental reality in nanostructured ZnSb, J Appl Phys 119 (2016) 125103. https://doi.org/10.1063/1.4944716.

Chapter 7

Magneto thermoelectric effect

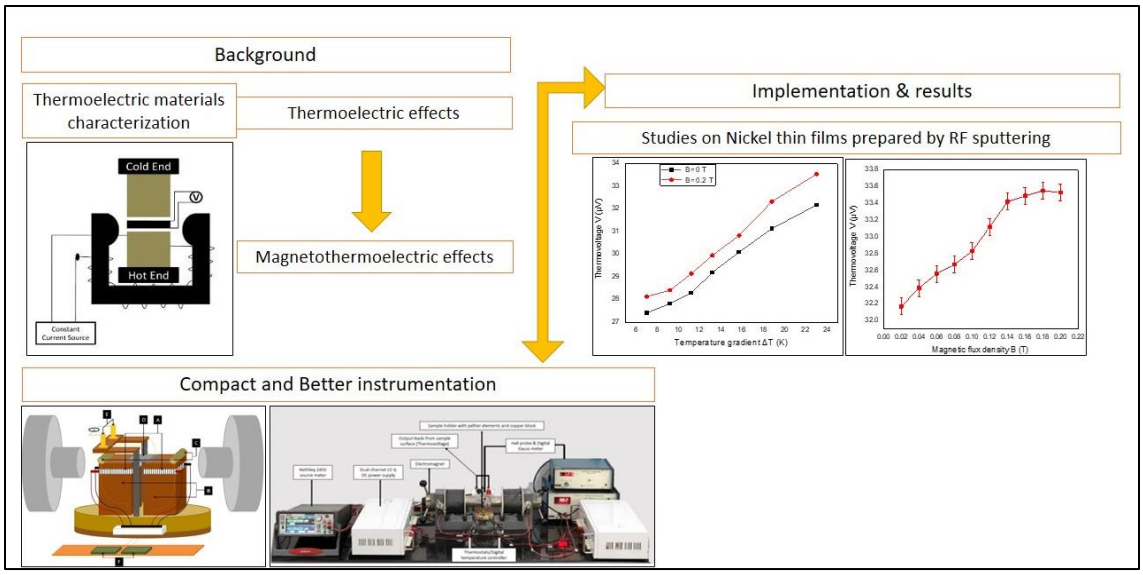

Objectives

This chapter explores the magneto-thermoelectric effect, with a focus on the influence of magnetic inclusions on the thermoelectric properties of materials. An experimental setup was designed to systematically study the impact of external magnetic fields on thermoelectric performance, using nickel thin films as a model system. The investigation explores how the application of magnetic fields alters charge carrier dynamics, particularly through mechanisms such as spin-dependent scattering, which contributes to enhancements in the Seebeck coefficient and power factor. These techniques can be expanded for utilizing them in technological applications like magnetic, temperature sensors and magneto TE generators.

7.1 Introduction

Thermoelectric and photovoltaic systems enable the conversion of environmental energy into usable electricity, offering versatile applications across industries. They are widely utilized in the automotive sector, biomedical devices, portable electronics, and communication systems. Specifically, thermoelectric materials excel at converting heat energy into electrical energy and vice versa, making them invaluable for energy harvesting and thermal management solutions [1]. Thermoelectric conversion has achieved a distinct position among green energy technologies due to its advantages, including the absence of moving parts, low maintenance requirements, high conversion efficiency, and exceptional reliability [2,3]. Recent advances in thermoelectric (TE) materials are driving the development of next-generation energy conversion technologies across diverse sectors. Beyond conventional applications like waste heat recovery in automotive exhaust systems and industrial processes, emerging innovations are enabling efficient thermal energy harvesting from urban infrastructure, such as building facades and wearable electronics. Novel TE devices are being integrated into microelectronic systems for on-chip cooling, thermal logic circuits, and autonomous sensor networks powered by body heat or ambient temperature gradients. In aerospace and deep-space missions, radioisotope thermoelectric generators (RTGs) continue to provide long-term, maintenance-free power, while new materials aim to enhance efficiency under extreme conditions. These advancements are supported by breakthroughs in low-dimensional systems, nanostructuring, and band engineering, which offer unprecedented control over carrier transport and phonon scattering, paving the way for high-performance, scalable thermoelectric technologies [4–7]

The efficiency of the thermoelectric energy conversion is expressed by the dimensionless figure of merit as in eqn (7.1),

$$ZT = \frac{S^2\sigma}{\kappa}\,T \tag{7.1}$$

Where, σ is the electrical conductivity, S is the Seebeck coefficient, T is the temperature, and κ is the thermal conductivity. Maximizing the thermoelectric figure of merit (ZT) necessitates achieving a combination of low thermal conductivity, high Seebeck coefficient, and high electrical conductivity. This balance is crucial for enhancing the efficiency of thermoelectric materials in energy conversion applications [8,9]. Differential methods are widely employed to characterize the Seebeck coefficient of thermoelectric (TE) materials, with flexibility in equipment configurations to accommodate different sample types. Various experimental setups have been developed, each specifically designed to suit the characteristics and forms of the samples being studied. These tailored configurations ensure accurate measurement of the Seebeck coefficient across a range of materials and conditions [10–14]. The thermoelectric characterization of prepared samples, both in bulk and thin film form, is commonly done with advanced instruments like ULVAC-ZEM series or Linseis LSR series in an inert gas atmosphere. The temperature ranges can also be varied between -100 °C to 1500 °C. While characterizing materials at temperatures below room temperature and at very high temperatures is essential for understanding the underlying physics of their properties. Sharath Chandra et al. developed simple yet precise thermoelectric power measurement setups that can effectively analyze materials across a wide range of temperatures and environmental conditions. These setups offer an efficient way to evaluate thermoelectric materials under practical operating conditions [15]. Setups with coil and pencil type heating elements are reported by Ashish Kumar et al., and Chun Sum Brian Pang et al., but Peltier elements with accurate digital temperature controllers to study fine temperature variations up to 0.1 K, is not yet reported to the best of our knowledge [16,17]. The majority of materials and TE generators will be utilized at temperatures close to room temperature, often below 100 °C and under ambient conditions.

The generated thermovoltage varies with both the magnitude and direction of an applied external magnetic field. Studies examining the dependence of the Seebeck coefficient on the magnetic field provide valuable insights into the material's microscopic electric and magnetic properties. Magneto-thermoelectricity explores this interplay

between thermal and electrical transport in materials under the influence of a magnetic field, enabling novel control over heat-to-electricity conversion. The applied magnetic field modifies charge carrier dynamics, influencing thermopower, carrier mobility, and energy harvesting efficiency. Recent advances highlight the potential of magneto-thermoelectric materials in next-generation energy applications, leveraging spin and charge interactions for enhanced performance [18]. To explore this field-dependent thermoelectric behavior, practical devices must incorporate sample stages that allow for the rotation of the sample or magnets. In most cases, thermovoltage increases with the magnetic field, as demonstrated in studies on indium antimonide (InSb), where thermovoltage shows a monotonic increase with the magnetic field. Additionally, applying the magnetic field along different crystallographic axes yields intriguing results, revealing the complex interactions between the material and the magnetic fields [19].Since the sample we used here is polycrystalline nickel film, such direction dependant variations are not expected.

Topological Dirac and Weyl semimetals are an interesting class of materials where the applied field strongly affects thermal and electronic transport properties. As an example, Cd_3As_2 is expected to be great potential for high thermoelectric performance because of the ultrahigh electron mobility (10^4– 10^6 cm^2 V^{-1} s^{-1}) leading to a large value of power factor. Applying an external field along an appropriate direction can significantly enhance the thermoelectric performance. This approach enables the coupling of magnetic and thermoelectric parameters, allowing for the measurement of the magneto-thermoelectric figure of merit for such materials. This combined analysis provides deeper insights into the material's performance under both magnetic and thermal influences, offering potential for advanced applications [20]. The magnetic field greatly reduces the electronic thermal conductivity and improves thermoelectric power, which eventually leads to an increase in ZT.

In this work, we developed a simple and compact setup for both standard thermoelectric (TE) measurements and field-dependent TE measurements. Accurate characterization of field-dependent thermoelectricity and spin-dependent thermoelectric

effects necessitates careful design and effective signal extraction methods to ensure reliable results. Several experimental setups like physical property measurement system (PPMS) and VersaLab are commonly used for these measurements. However, most setups used for field-dependent thermoelectric measurements are complex and costly due to their cryogenic capabilities and superconducting magnets, which create the necessary experimental conditions. The majority of studies rely on thermocouples or other direct temperature sensors to measure temperature differences. Some systems utilize integrated Neodymium permanent magnets (NdPMs) to apply a fixed magnetic field, but these are not ideal for studying field-dependent thermoelectricity. In many cases, the saturation field of the materials under investigation exceeds the strength of these fixed magnets, preventing the achievement of a hysteresis loop. The design by Wongjom et al. is compact, but the use of conventional heaters can lead to temperature fluctuations, affecting measurement accuracy [21,22]. In this study, we employed Peltier heaters controlled by thermostats to maintain a stable temperature, offering better control over temperature variations. PT 100 sensors were attached to the blocks using heat sink compound to ensure accurate temperature measurements. While low-temperature studies are essential, our investigations primarily focus on near room-temperature applications. We designed an experimental setup that can measure both conventional thermoelectric and magneto-thermoelectric effects, and it is also capable of studying spin-thermoelectric effects. The traditional method for studying these effects is depicted in Fig. 7-1.

The following measurements can be conducted using this setup.

1. The dependence of thermovoltage on the direction of the applied external magnetic field relative to the crystallographic axes (for single crystals).
2. The dependence of thermovoltage on the direction of the applied external magnetic field concerning the orientation of thin films (grown on preferred oriented substrates).
3. Study the efficient use of the external magnetic field to change the thermovoltage and obtain a substantial increase in TE properties.

4. Studies on samples with magnetic anisotropy.

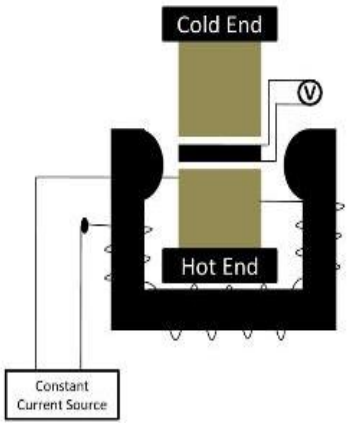

Figure 7- 1 Schematic representation of conventional setup used to measure field dependent thermoelectric effects.

7.2 Experimental methods and techniques

We used the setup to measure the thermoelectric parameters of thin films grown by RF magnetron sputtering, specifically nickel thin films. Nickel thin films with a thickness of 20 nm were deposited on clean glass and sapphire (Al_2O_3) substrates using an RF magnetron sputtering technique, with a Ni target (99.99% purity, Alfa Aeser) having a diameter of 50 mm and thickness of 3 mm. Ar (99.99% purity) gas was employed as the sputtering gas. The sputtering chamber was evacuated to get an ultimate pressure of 9×10^{-6} mbar by diffusion pump. During sputtering, the working pressure and RF power were set to 2×10^{-2} mbar and 150 W, respectively. The film thickness during deposition was monitored with a quartz crystal thickness monitor. The sputtering rate was maintained at 0.8 Å/Sec. Before deposition, the nickel target was pre-sputtered in an Ar atmosphere for 10 minutes to remove any oxide layers. Additionally, the glass and sapphire substrates were cleaned in an ultrasonic bath with distilled water for 30 minutes, followed by drying with air. Thin films were then deposited on the substrates at room temperature. These thin films were used for field-dependent thermoelectric studies. The X-ray diffractometer (Rigaku-MiniFlex 600) with the Cu-K_α radiation of wavelength

(λ = 1.5418 Å) was used for structural studies. MFM images were taken using Bruker-MultiMode 8.

7.2.1 Experimental setup to measure magneto thermoelectric effect

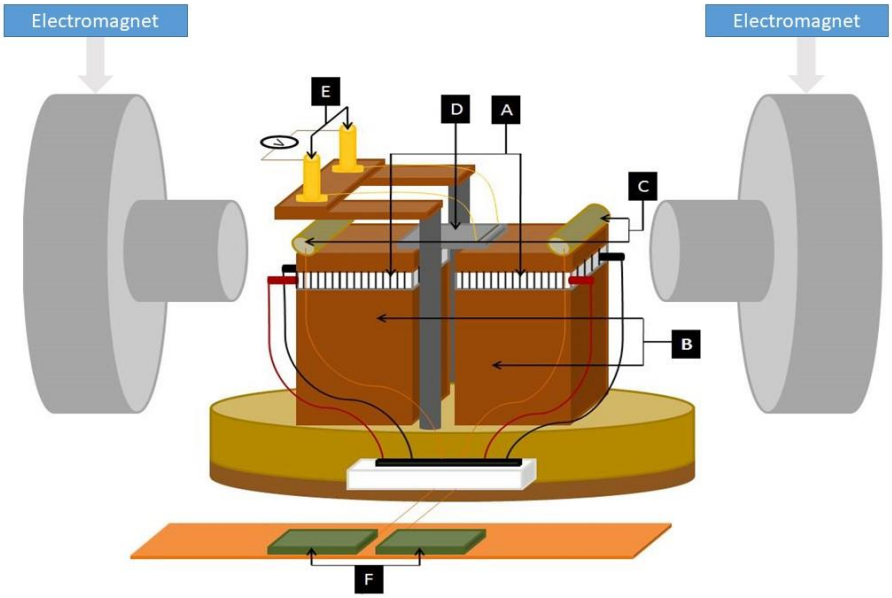

Figure 7- 2 Schematic diagram of experimental set up to measure Seebeck effect, field dependent Seebeck effect effects.

The experimental setup we present here in Fig. 7-2 can be used to measure the Seebeck Coefficient, field-dependent variation of the Seebeck coefficient, and can be extended to spin Seebeck in the transverse configuration. The major parts of the experimental setup are,

A. **Peltier elements**: They are operated according to the Peltier effect. A voltage is applied across joined conductors to create an electric current. When the current flows through the junctions of the two conductors, heat is removed from one junction and is deposited at the other junction. They can be used to either heat or cool the sample surface. The Peltier elements we used were standard 3 cm x 3 cm.

B. **Copper blocks**: Two identical copper blocks attached to the bottom Peltier elements serve as heat sinks. The copper blocks fixed above the Peltier elements distribute heat evenly on the surfaces of the contact specimen. The size of the lower blocks was 3 cm x 3 cm x 5 cm (L x B x H).

C. **Pt 100 - Temperature sensor:** This is a resistance temperature detector used for accurate measurement of temperature. Two such sensors are used to measure the temperatures of two copper blocks. We used 4 channel Pt 100 sensors (-50 °C to 200 °C) from RS PRO. The sensors were attached to the surfaces using highly conductive thermal pastes with thermal conductivity of 0.65W/mK.

D. **Sample and sample holder:** Thin film sample is used for measurement and was fixed on the copper block using a heat sink compound. This part consisting of two copper blocks acts as a sample holder. Seebeck effect and field-dependent Seebeck effect doesn't depend on the size of the sample. So we can use samples of different dimensions adjusted to the distance between movable copper blocks. The standard measurement size is 1 cm x 1 cm.

E. **Gold screws:** Two gold screws were used as output leads. Gold wires attached to the sample surface using silver paste are taken and joined to this terminal because of its high electrical conductivity and corrosion resistance nature. They are in turn connected to Keithley 2450 source meter in its voltage measurement mode, to measure the output voltage in any configurations.

F. **Thermostats:** We used Selec TC-344-AX Digital temperature controller for accurately setting the temperature of Peltier elements and measuring the temperature of upper peltier connected copper blocks via connected Pt 100 sensors.

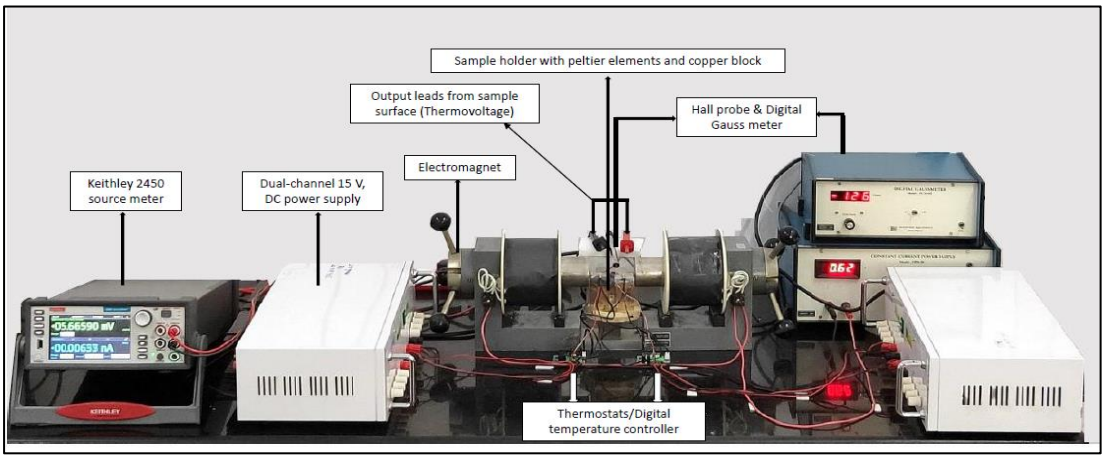

Figure 7- 3 Experimental setup to measure Seebeck effect, field dependent seebeck effect.

7.2.2 Measurement of thermovoltage, field dependent thermovoltage

In order to measure the field dependent thermovoltage, two dual-channel 15 V, DC power supplies were used as sources for Peltier coolers and temperature controllers. One Peltier is connected in a reverse manner to the power supply so that the heating element comes in contact with the sample. The other Peltier is connected in standard configuration so that the cooling surface comes into contact with the specimen. The thermostats can be programmed to set various temperatures from -20 °C to 70 °C. By properly programming thermostats within the temperature range -20 °C to 70 °C, a maximum of 90 °C temperature gradient can be created across the sample surface. Thermovoltage generated by temperature gradient can be varied by an applied magnetic field. All the measurements were taken after the system get stabilized. The final values we present here represent the average of ten successive readings to maximise the measurement accuracy and minimise errors.

To determine the Seebeck coefficient and field-dependent variation of the same, output has to be taken across the hot and cold ends of the sample surface. The external magnetic field is applied along the sample surface as indicated in Fig. 2 using an electromagnet, to get a maximum flux density of 2T at a 10 mm air gap. The field strength near the sample surface is measured by an InAs Hall probe (indium arsenide

crystal with four soldered contacts mounted on a PCB strip and covered with a protective layer) connected to a digital Gauss meter. The two output terminals from sample ends are connected to Keithley 2450 source meter through gold screws to read the output voltage. To study spin Seebeck effect output has to be taken as indicated in Fig. 7-2.

When we apply a transverse temperature gradient across ferromagnetic metals and semiconductors, out-of-plane thermal gradients develop, a transverse thermopower, planar Nernst effect (PNE) may affect the original TE signals. But this effect may be neglected because the magnitude of PNE is of the order of nanovolts in most of the FM substances. In the case of nickel thin films, it is of the order of 80-100 nV [23]. If we want to separate PNE contribution, angle-dependent measurements of TE voltage may be taken using the same apparatus we designed, since it's on a rotational stage. Unintended out-of-plane temperature gradients due to heat flux into the surrounding region may cause anomalous Nernst effect (ANE). Since the film's thickness is only 20 nm, there won't be an appreciable temperature gradient between the bottom and top of the sample surface.

7.3 Results and discussion

Nickel thin films:

Fig. 7-4 shows the XRD patterns of prepared nickel thin films. The diffraction peaks at 44.5° correspond well with the intense peaks (111) of the face-centered cubic

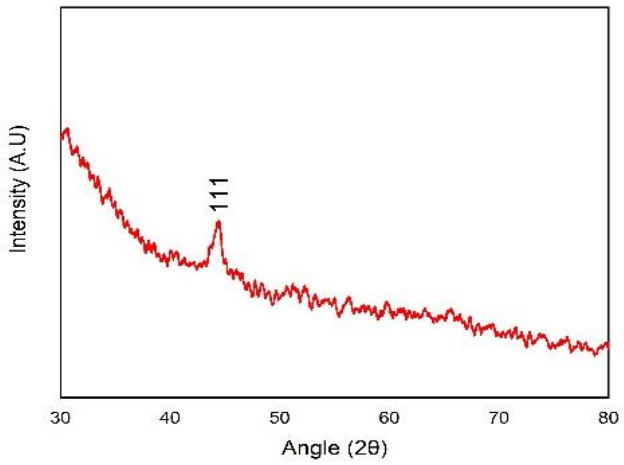

Figure 7- 4 XRD pattern of RF sputtered nickel thin film.

(FCC) metallic nickel (JCPDS Card No 01-087-0712). The thin film shows a preferred orientation along (111) direction.

Magnetic force microscopy (MFM) images of nickel thin films given in Fig. 7-5 show the formation of magnetic domains. Very distinctive domain structures are visible only if the thickness of film is greater than 100 nm. Here we deposited thin films of thickness 20 nm to avoid parasitic TE signals.

This thin film was used to study the variation of thermovoltage in presence of the external magnetic field. Variation of Seebeck coefficient of nickel thin films is studied in two aspects. The first one, keeping the temperature gradient a constant and varying the magnetic flux density from 0 T to 0.20 T. Second one by keeping the magnetic flux density B, constant at 0.20 T and varying the temperature of the Peltier from room temperature to 65 °C so that temperature gradients ranging from 7 ^{0}C to 23 ^{0}C can be achieved across the nickel thin film. The results of the first set are summarized in Table 7-1 and that of the second set is in Table 7-2 and graphically represented in Fig. 7-6 (a) and Fig. 7-6 (b) respectively.

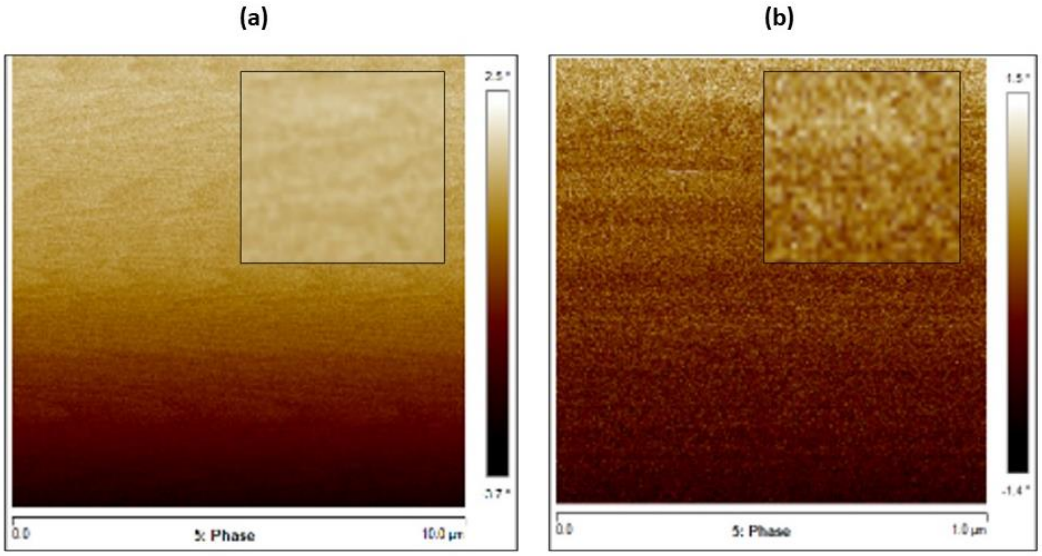

Figure 7- 5 MFM phase image of sputtered nickel thin films deposited on **(a)** sapphire **(b)** glass substrate.

Table 7- 1 Thermovoltage in Ni thin films with constant temperature gradient of 23 K

Magnetic flux density B (Tesla)	Thermo voltage (V) (μV)	Seebeck coefficient S (μV/K)
0.02	32.17	1.398
0.04	32.39	1.408
0.06	32.56	1.415
0.08	32.67	1.420
0.10	32.83	1.427
0.12	33.12	1.440
0.14	33.42	1.453
0.16	33.49	1.456
0.18	33.55	1.458
0.20	33.53	1.457

Table 7- 2 Thermovoltage in nickel thin films with constant magnetic field of 0.2 T

Effective temperature difference ΔT (^{0}C)	Thermovoltage (V) (B=0 T) (μV)	Thermovoltage (V) (B=0.2 T) (μV)
7.0	27.41	28.13
9.2	27.82	28.41
11.2	28.29	29.14
13.2	29.2	29.95
15.7	30.09	30.82
18.8	31.13	32.32
23.0	32.17	33.53

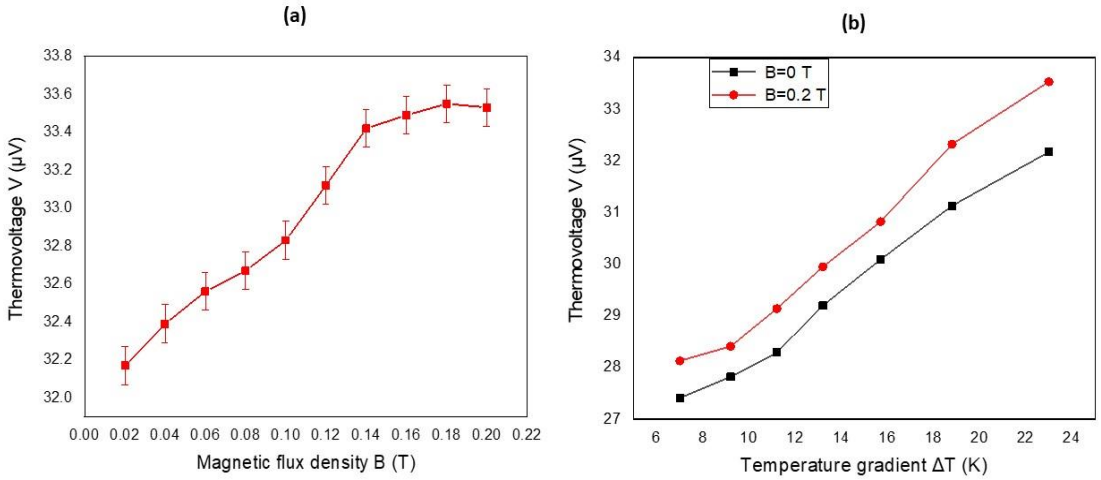

Figure 7- 6 (a) Variation of thermovoltage in nickel thin films with constant temperature gradient **(b)** Variation of thermovoltage in nickel thin films with constant magnetic field

We observe a linear increase of V with ΔT as expected. The actual values of generated thermovoltage and Seebeck coefficient bear a negative sign since electrons are the charge carriers in nickel. But here we take only the magnitude of these parameters. The magnitude of the Seebeck coefficient tends to zero as the temperature is decreased. The temperature range under consideration for this experiment is greater than 300 K we do not expect any phonon drag effect since its only visible for temperatures less than 100 K. Here we observe a diffusion-limited behaviour similar to the bulk Ni. The smaller absolute values of the Seebeck coefficient of the thin films as compared to bulk values can be justified using Tellier's model [24].

If B is increased in the range between 0 to 0.2 T, thermovoltage increases by nearly 5%. The increase in thermovoltage with B is related to an increase of S with applied magnetic field, as a first approximation

$$S = S_0 + \frac{\partial S}{\partial B} B \tag{7.2}$$

It is significant to note that no effect of B on thermovoltage is seen when ΔT = 0. Consequently, we do in fact detect a magneto-thermoelectric effect. The absence of any effect at ΔT = 0 confirms that the observed influence of the magnetic field on thermovoltage is genuinely a magneto-thermoelectric effect and not due to any direct electrical or magnetic interference, but due to the coupling of thermal gradients with magnetic fields.

The variation of thermovoltage in presence of an external magnetic field shows the same trend as obtained in previous works on nickel nanowires. The variation of ΔS with B can be expressed in terms of the carrier lifetime τ and the carrier concentration n.

$$\Delta S = \frac{\partial S}{\partial r} S_0 \Delta r = -\frac{\partial S}{\partial r} S_0 \frac{d\sigma(B)}{\sigma(B)} = -\frac{\partial S}{\partial r} S_0 \left[\frac{\partial \tau}{\tau} + \frac{dn}{n} \right] \quad (7.3)$$

Hence, the change of S with the magnetic field is due to a change in the mobility of charge carriers. The possible intensities of the applied field are consistent with the works on thickness-dependent magnetic properties of polycrystalline nickel thin films.

At B = 0 T and T = 30 ^{0}C, the thermopower value is lower when compared to bulk materials. As the thickness of film reduces the greater impact of surface scattering with smaller size comes in to picture and lowers the absolute value. The Seebeck coefficient depends on l_o/d, where l_o is the electronic mean free path and d is the grain diameter. As observed in the case of nickel nanowires there may be an optimum thickness for the thin film, where the surface effect has little impact on thermopower [25].

As the temperature drops, the magnitude of S decreases to zero. S must be zero at 0 K because it is also the entropy per electric charge. The variation of thermovoltage also shows a linear behaviour concerning temperature gradient across thin film surfaces. But as the applied field crosses 0.20 T, thermovoltage doesn't show much variation with B. The value of magnetic flux density above 0.20 T matches with the range of saturation magnetization of 20 nm thick nickel thin films [26,27]. This indicates a saturation point for field-dependent variation of the Seebeck coefficient for magnetic nickel thin films. All thermoelectric data reported here are compared with the measurements done using

ULVAC – ZEM 3 and are found within a variation limit of 3 to 4 % that is due to the Helium characterization environment, in ULVAC-ZEM 3.

7.4 Conclusion

We built an experimental setup to systematically investigate magneto-thermoelectric effects, specifically in nickel thin films. The setup enabled precise control of temperature gradients, achieving stability within ±0.1 °C using a standard power source regulated by a PID controller or thermostat, eliminating the need for bulky and expensive constant current sources typically required in conventional systems. This allowed for steady-state and highly stabilized thermoelectric measurements. The measurements revealed that the thermovoltage increased with the applied magnetic field and saturated at approximately 0.2 T. This saturation behavior provides an indirect yet effective method to probe the magnetization characteristics of thin films. The setup also offers potential for studying thermoelectric materials with magnetic nano-inclusions, which are known to exhibit significant field-dependent variations in their thermoelectric properties. The experimental platform we developed demonstrates excellent utility for exploring and characterizing magneto-thermoelectric phenomena in a wide range of thermoelectric materials.

References:

[1] M.G. Kanatzidis, Nanostructured thermoelectrics: The new paradigm?, Chemistry of Materials (2010). https://doi.org/10.1021/cm902195j.

[2] A. Paulson, N.A. Muhammed Sabeer, P.P. Pradyumnan, Enhancement of optical and thermoelectric properties in dysprosium doped ZnO thin films as an impact of non-parabolic band structure, Mater Sci Eng B Solid State Mater Adv Technol (2020). https://doi.org/10.1016/j.mseb.2020.114745.

[3] S.B. Riffat, X. Ma, Thermoelectrics: A review of present and potential applications, Appl Therm Eng (2003). https://doi.org/10.1016/S1359-4311(03)00012-7.

[4] P.K. Jamshina Sanam, M. Shah, P.P. Pradyumnan, Structure induced modification on thermoelectric and optical properties by Mg doping in $CuCrO_2$ nanocrystals, Solid State Commun 353 (2022) 114855. https://doi.org/https://doi.org/10.1016/j.ssc.2022.114855.

[5] P.K.J. Sanam, M. Shah, P.P. Pradyumnan, Raman spectroscopic investigation and thermoelectric studies of defect-induced Mg-doped delafossite thin film, Journal of

Materials Science: Materials in Electronics (2022). https://doi.org/10.1007/s10854-022-09013-y.

[6] D. Zabek, F. Morini, Solid state generators and energy harvesters for waste heat recovery and thermal energy harvesting, Thermal Science and Engineering Progress (2019). https://doi.org/10.1016/j.tsep.2018.11.011.

[7] P.P. Murmu, A. Shettigar, S. V Chong, Z. Liu, D. Goodacre, V. Jovic, T. Mori, K.E. Smith, J. Kennedy, Role of phase separation in nanocomposite indium-tin-oxide films for transparent thermoelectric applications, Journal of Materiomics 7 (2021) 612–620. https://doi.org/https://doi.org/10.1016/j.jmat.2020.10.015.

[8] J.He,M.G.Kanatzidis, V.P.Dravid, High performance bulkthermoelectrics via a panoscopic approach, Materials Today (2013).https://doi.org/10.1016/j.mattod.2013.05.004.

[9] L.D. Zhao, V.P. Dravid, M.G. Kanatzidis, The panoscopic approach to high performance thermoelectrics, Energy Environ Sci (2014). https://doi.org/10.1039/c3ee43099e.

[10] J. García-Cañadas, G. Min, Multifunctional probes for high-throughput measurement of Seebeck coefficient and electrical conductivity at room temperature, Review of Scientific Instruments (2014). https://doi.org/10.1063/1.4871553.

[11] H.J. Goldsmid, A simple technique for determining the Seebeck coefficient of thermoelectric materials, J Phys E (1986). https://doi.org/10.1088/0022-3735/19/11/008.

[12] R.L. Kallaher, C.A. Latham, F. Sharifi, An apparatus for concurrent measurement of thermoelectric material parameters, Review of Scientific Instruments (2013). https://doi.org/10.1063/1.4789311.

[13] A. Mishra, S. Bhattacharjee, S. Anwar, Simple apparatus to measure Seebeck coefficient up to 900 K, Measurement (Lond) (2015). https://doi.org/10.1016/j.measurement.2015.03.005.

[14] O. Boffoú, A. Jacquot, A. Dauscher, B. Lenoir, M. Stölzer, Experimental setup for the measurement of the electrical resistivity and thermopower of thin films and bulk materials, Review of Scientific Instruments (2005). https://doi.org/10.1063/1.1912820.

[15] L.S. Sharath Chandra, A. Lakhani, D. Jain, S. Pandya, P.N. Vishwakarma, M. Gangrade, V. Ganesan, Simple and precise thermoelectric power measurement setup for different environments, in: Review of Scientific Instruments, 2008. https://doi.org/10.1063/1.3002426.

[16] A. Kumar, A. Patel, S. Singh, A. Kandasami, D. Kanjilal, Apparatus for Seebeck coefficient measurement of wire, thin film, and bulk materials in the wide temperature range (80-650 K), Review of Scientific Instruments (2019). https://doi.org/10.1063/1.5116186.

[17] C.S.B. Pang, W. Ng, J. Liang, Q. Qu, H.T.M. Chau, M. Niu, M.K. Cheng, I.K. Sou, A Simple Thermoelectric Effect Setup for Determining the Conductivity Type of Thin Film Materials, IEEE Trans Instrum Meas (2021). https://doi.org/10.1109/TIM.2020.3046922.

[18] Y. Pan, B. He, X. Feng, F. Li, D. Chen, U. Burkhardt, C. Felser, A magneto-thermoelectric with a high figure of merit in topological insulator $Bi_{88}Sb_{12}$, Nat Mater 24 (2025) 76–82. https://doi.org/10.1038/s41563-024-02059-9.

[19] V.& W. Карапетян, Геворк & Dneprovski, Influence of Magnetic Field on Thermoelectric Coefficient Value and Peltier Factor in InSb, in: Advanced Materials: Physics, Mechanics and Applications, 2014: pp. 127–133.

[20] H. Wang, X. Luo, K. Peng, Z. Sun, M. Shi, D. Ma, N. Wang, T. Wu, J. Ying, Z. Wang, X. Chen, Magnetic Field-Enhanced Thermoelectric Performance in Dirac Semimetal Cd_3As_2 Crystals with Different Carrier Concentrations, Adv Funct Mater (2019). https://doi.org/10.1002/adfm.201902437.

[21] P. Wongjom, W. Thongsamrit, H. Ramamoorthy, S. Chinwong, R. Somphonsane, C. Ruttanapun, Cost-Effective Experimental Setup for Studies of Spin Seebeck Effect and Electrical Transport in Thermoelectric Materials, IEEE Trans Instrum Meas (2020). https://doi.org/10.1109/TIM.2019.2935597.

[22] A. Sola, V. Basso, M. Kuepferling, M. Pasquale, D.C. Ne Meier, G. Reiss, T. Kuschel, T. Kikkawa, K.I. Uchida, E. Saitoh, H. Jin, S.J. Watzman, S. Boona, J. Heremans, M.B. Jungfleisch, W. Zhang, J.E. Pearson, A. Hoffmann, H.W. Schumacher, Spincaloritronic Measurements: A Round Robin Comparison of the Longitudinal Spin Seebeck Effect, IEEE Trans Instrum Meas (2019). https://doi.org/10.1109/TIM.2018.2882930.

[23] A.D. Avery, M.R. Pufall, B.L. Zink, Observation of the planar nernst effect in permalloy and Nickel thin films with in-plane thermal gradients, Phys Rev Lett (2012). https://doi.org/10.1103/PhysRevLett.109.196602.

[24] C.R. Pichard, C.R. Tellier, A.J. Tosser, Thermoelectric power of thin polycrystalline metal films in an effective mean free path model, Journal of Physics F: Metal Physics (1980). https://doi.org/10.1088/0305-4608/10/9/016.

[25] E. Shapira, A. Tsukernik, Y. Selzer, Thermopower measurements on individual 30 nm nickel nanowires, Nanotechnology (2007). https://doi.org/10.1088/0957-4484/18/48/485703.

[26] U. Parlak, M.E. Aköz, S. Tokdemir Öztürk, M. Erkovan, Thickness dependent magnetic properties of polycrystalline nickel thin films, in: Acta Phys Pol A, 2015. https://doi.org/10.12693/APhysPolA.127.995.

[27] R. Mitdank, M. Handwerg, C. Steinweg, W. Töllner, M. Daub, K. Nielsch, S.F. Fischer, Enhanced magneto-thermoelectric power factor of a 70 nm Ni-nanowire, in: J Appl Phys, 2012. https://doi.org/10.1063/1.4721896.

Chapter 8

General summary

Objectives

The objective of this thesis is to explore the structural, optoelectronic, and thermoelectric properties of Pr and Nb doped $SrTiO_3$ crystallites and thin films, focusing on their potential applications in energy harvesting and optoelectronic devices. By systematically studying doping-induced band structure modifications, carrier transport mechanisms, and defect engineering, this work aims to enhance the material's electronic and thermoelectric performance. The impact of synthesis techniques, such as graphite burial sintering and RF magnetron sputtering, on crystallite densification, phase transformation, and carrier mobility is critically analyzed. Special emphasis is placed on optimizing thermoelectric power factors and transparent conducting properties through controlled defect engineering, strain effects, and energy filtering mechanisms. Furthermore, the study explores the emerging field of magneto-thermoelectric effects, investigating how magnetic field influence thermoelectric performance, thereby broadening the applicability of $SrTiO_3$ based materials for next-generation energy and sensing technologies.

8.1 Introduction

The field of optoelectronics relies on precise control of material properties to optimize light absorption, emission, and electrical transport. This thesis explores the optoelectronic properties of Pr doped $SrTiO_3$ crystallites and thin films, focusing on band structure engineering, defect modulation, and optical tuning. The incorporation of Pr into the $SrTiO_3$ matrix induces structural transformations, modifies electronic states, and enhances optical responses, making it a promising material for advanced optoelectronic applications. Investigations into photoluminescence, infrared absorption, and visible light transparency demonstrate the potential of these materials in light-emitting devices, infrared sensors, and transparent electronics. Through controlled synthesis and post-processing techniques, this work establishes a pathway for developing high-performance perovskite-based optoelectronic materials.

Thermoelectric (TE) materials have garnered considerable interest in recent years due to their capability to convert waste heat into electrical energy, providing a sustainable solution for energy recovery. The performance of these materials is primarily governed by the thermoelectric power factor, which depends on optimizing the Seebeck coefficient, electrical conductivity, and minimizing thermal conductivity to achieve higher efficiency. While traditional thermoelectric materials like bismuth telluride have demonstrated promising ZT values, they are often constrained by issues such as limited thermal stability and environmental concerns. In contrast, oxide-based materials, particularly $SrTiO_3$, have shown great potential for thermoelectric applications owing to their inherent thermal stability, environment friendly nature, and robustness at high temperatures. Doping the A-site and B-site of $SrTiO_3$ with elements like Praseodymium (Pr) and Niobium (Nb) induces substantial modifications to its electronic structure, enhancing carrier mobility, and consequently boosting the power factor. These dopants influence the Seebeck coefficient through mechanisms such as energy filtering and effective mass modulation, further enhancing the thermoelectric efficiency. Moreover, the introduction of dopant-

induced states within the band gap significantly improves light absorption and emission, thereby enhancing the material's optoelectronic properties [1–5].

This summary chapter consolidates the findings of the thesis, which explores the effects of Pr and Nb doping on the thermoelectric and optoelectronic properties of $SrTiO_3$ nanostructures. By examining the interplay between doping, carrier dynamics, and structural modifications, the work presents insights into the mechanisms driving improved thermoelectric performance in oxide materials. Additionally, it highlights the potential of these doped oxide nanostructures for high-efficiency device applications across a range of temperature conditions.

8.2 Summary of the thesis

This thesis explores the transformation of perovskite oxide material $SrTiO_3$ into a high-performance n-type material for optoelectronic and thermoelectric applications. Various strategies, including modulation doping, burial sintering, quantum confinement, and nanostructuring, were employed to achieve these objectives. $SrTiO_3$ offers significant tunability for doping at both the A and B sites of its lattice, with Pr identified as a suitable A-site dopant and Nb as a B-site dopant, based on factors such as ionic radius compatibility, valence state, and the influence on carrier concentration and band structure. The synthesis conditions of $SrTiO_3$ powder was optimized through solid-state reaction methods followed by graphite burial sintering. High-performing Pr doped $SrTiO_3$ with enhanced optical and thermoelectric properties was achieved by eliminating the double Schottky barrier (DSB) through two-step sintering.

RF magnetron sputtering parameters were fine-tuned to limit Sr segregation, leading to the creation of a highly mobile and transparent conducting oxides. Nb doped thin films with elevated charge carrier concentrations were realized by oxygen-free sputtering and vacuum annealing, resulting in energy filtering and strain engineered films with record-breaking thermoelectric power factors. The role of oxygen vacancies in defining both the optoelectronic and thermoelectric performance of $SrTiO_3$ was critically

analyzed and optimized in the thin films. Finally, an experimental setup was developed to study the impact of magnetic fields on thermoelectric performance, verified using nickel thin films, with potential applications for studying magnetic nano-inclusions in thermoelectric materials.

8.2.1 Investigations on optoelectronic properties of strontium titanate bulk ceramics- Praseodymium doping

- Praseodymium (Pr^{3+}) was substituted at the Sr^{2+} site in $SrTiO_3$, and graphite burial sintering was employed to alter the band structure of the material.
- X-ray diffraction (XRD) analysis revealed an asymmetric (310) peak, and Raman spectroscopy identified the emergence of E_g and B_{1g} modes, indicating a phase transition from cubic to tetragonal for $Sr_{1-x}Pr_xTiO_3$ when $x \geq 0.1$.
- The forbidden first-order Raman peaks and new spectral features were attributed to local vibrational modes associated with oxygen vacancies in the crystal lattice.
- Williamson-Hall (W-H) plots were used to investigate structural variations and lattice strain, while high-resolution field emission scanning electron microscopy (FE-SEM) was used to analyze morphological changes.
- Optical studies showed high infrared absorption in UV-Vis-NIR spectra, with the band gap reduced from 2.8 eV to 1.8 eV, driven by increased lattice disorder and Ti^{4+} reduction.
- The absorption spectra exhibited a blue shift with increased Pr concentration, which can be exploited for tuning the absorption range in sensing applications.
- New electronic states formed by Pr doping provide a pathway for band gap engineering in perovskites, offering potential in photocatalytic and photovoltaic applications. The combination of Pr doping and oxygen vacancy creation via burial sintering enables the material to absorb mid- to far-infrared radiation, making it suitable for infrared sensing technologies

- The combination of Pr doping and oxygen vacancy creation via burial sintering enables the material to absorb mid- to far-infrared radiation, making it suitable for infrared sensing technologies.
- Praseodymium (Pr^{3+}) was incorporated into the Sr^{2+} site of $Sr_{1-x}Pr_xTiO_3$ (x = 0.05–0.20) to tune the photoluminescence (PL) emission from red to blue with excess electrons.
- The emission mechanism was influenced by oxygen vacancies, as revealed by X-ray photoelectron spectroscopy (XPS), and morphological analysis via high-resolution FE-SEM showed the formation of micro-pebble-like grains.
- Under 380 nm UV illumination, a narrow-band blue emission peak with a full width at half maximum (FWHM) of 19.3 nm at 428 nm was observed for the sample with x = 0.05.
- Chromaticity coordinates (CIE) analysis demonstrated that the blue emission had CIEy values less than 0.1, making the material ideal for applications in lighting and display technologies.
- The narrow-band blue emission and reduced FWHM in the range of 19–23 nm enhance the material's color gamut, making it suitable for light-emitting diode (LED) applications.

8.2.2 Investigations on optoelectronic properties of strontium titanate – Praseodymium doping and quantum confinement

- Strontium titanate-based thin films exhibit unique properties such as unsaturated bonds, dimension restrictions, oxygen vacancies, and point defects, making them ideal for optoelectronic applications.

- Praseodymium doped $SrTiO_3$ thin films were synthesized via RF magnetron sputtering in a pure argon environment, followed by heat treatment to enhance structural and electrical properties.

- X-ray diffraction (XRD) and Raman spectroscopy were employed to analyze structural parameters, which were correlated with electrical transport properties, revealing critical insights into conduction mechanisms.
- Morphological features such as Stranski–Krastanov (SK) growth and cation segregation, observed through field emission scanning electron microscopy (FE-SEM) and atomic force microscopy (AFM), provided deeper understanding of film conductivity.
- Optical studies demonstrated significant transparency in the visible spectrum, making the films suitable for optoelectronic applications, while photoluminescence (PL) emission studies highlighted the role of oxygen vacancies.
- By optimizing sputtering parameters and annealing conditions, Pr-doped $SrTiO_3$ thin films achieved the highest reported carrier mobility of 33.9 cm^2/V s, with transparency exceeding 60%, positioning them as promising transparent conducting oxides (TCOs).
- Effective control of oxygen vacancies and cation segregation was crucial to enhance carrier mobility and transparency, making the films suitable for a broad range of optoelectronic applications.

8.2.3 Investigations on thermoelectric properties of strontium titanate - Praseodymium, Niobium doping and quantum confinement

- Praseodymium (Pr^{3+}) was introduced into the Sr^{2+} site of $Sr_{1-x}Pr_xTiO_3$ (x = 0.05–0.20) via a two-step graphite burial sintering process, which enhanced carrier concentration and minimized the double Schottky barrier (DSB) at grain boundaries.

- X-ray diffraction (XRD) analysis showed peak splitting and asymmetry at $x \geq 0.10$, indicating a structural phase transition from cubic to tetragonal, driven by Pr doping.
- X-ray photoelectron spectroscopy (XPS) confirmed the formation of oxygen vacancies and the reduction of Ti^{4+} to Ti^{3+}, induced by the burial sintering process, contributing to an increase in carrier concentration.
- The $Sr_{0.9}Pr_{0.1}TiO_3$ sample achieved a maximum power factor of 1.8 mW/mK^2 at 673 K, aided by the reduction of the DSB, which enhanced electrical conductivity.
- Porous structures, Pr defect centers, and oxygen vacancy clusters collectively reduced the thermal conductivity, leading to a maximum figure of merit (ZT) of 0.33 at 673 K, making the material suitable for thermoelectric applications.
- The double reduction technique promoted the precipitation of Pr nanoparticles, which acted as scattering centers, further reducing thermal conductivity and improving thermoelectric performance.
- This approach positions $Sr_{0.9}Pr_{0.1}TiO_3$ as a promising candidate for n-type legs in thermoelectric generators, offering a pathway to harvest waste heat and contribute to sustainable energy solutions.
- A record high thermoelectric power factor of 1.85 W/mK^2 was achieved in $SrTi_{0.9}Nb_{0.1}O_{3-\delta}$ thin films synthesized via RF magnetron sputtering, offering potential for efficient heat-to-electricity conversion in thermoelectric devices.
- Structural, compositional, and morphological characteristics were analyzed using X-ray diffraction (XRD), X-ray fluorescence (XRF), scanning electron microscopy (SEM), and energy-dispersive X-ray spectroscopy (EDS), and correlated with electrical and thermoelectric transport properties.
- High carrier concentrations in the range of 10^{21}–10^{22} cm^{-3} were obtained due to Nb doping and oxygen vacancies introduced during sputtering in an Argon environment followed by vacuum annealing.

- The conduction mechanism follows a degenerate semiconductor model, approximated by a parabolic band structure, contributing to enhanced electrical conductivity and thermoelectric performance.
- Seebeck coefficients ranging from 200 to 400 μV/K were attributed to energy filtering, effective mass modulation, and strain-induced band degeneracy, achieved without sacrificing electrical conductivity.
- Optimized sputtering conditions, including careful doping and post-deposition treatments, were essential for achieving high carrier mobility and maximizing the power factor.
- The combination of high Seebeck coefficients, enhanced mobility, and formation of a two-dimensional electron gas (2DEG) at the $SrTiO_3/SiO_2$ interface positions $SrTi_{0.9}Nb_{0.1}O_{3-\delta}$ as a promising material for advanced thermoelectric converters.

8.2.4 Investigations on magnetothermoelectric effect-Experimental setup and verification

- Thin films of nickel were deposited using the RF magnetron sputtering technique, and Magnetic Force Microscopy (MFM) revealed the formation of magnetic domains, with X-ray diffraction (XRD) confirming a preferred (111) crystal orientation.
- The thermoelectric and magneto-thermoelectric effects of the nickel thin films were systematically investigated using a custom-built experimental setup incorporating Peltier elements, thermostats, and proportional-integral-derivative (PID) controllers for precise temperature regulation.
- Seebeck coefficient measurements under an applied external magnetic field showed an increase in thermovoltage from 32.17 μV to 33.53 μV, saturating at a field strength of 0.2 T, indicating the interaction of charge carriers with the magnetic field.

- The saturation behavior of thermovoltage at 0.2 T provides a method to indirectly investigate the magnetization properties of magnetic thin films, offering insights into their magnetic nature.
- The experimental setup enables precise temperature control up to 0.1 °C, improving measurement stability and overcoming limitations of conventional setups, which rely on costly and space-intensive constant current sources.
- This setup can be used to systematically study the field-dependent thermoelectric properties of TE materials containing magnetic nano-inclusions, allowing for detailed investigation of their magneto-thermoelectric effects.

References:

[1] M. Shah, P.K.J. Sanam, P.P. Pradyumnan, Tuning of photoluminescence properties: Impact of Pr-doping in $SrTiO_3$ crystallites, Mater Today Commun 39 (2024) 109323. https://doi.org/10.1016/j.mtcomm.2024.109323.

[2] M. Shah, P.K. Jamshina Sanam, P.P. Pradyumnan, Defect-induced $Sr_{1-x}Pr_xTiO_3$ crystallites by burial sintering and its optoelectronic applications, Journal of Physics and Chemistry of Solids 181 (2023) 111516. https://doi.org/10.1016/j.jpcs.2023.111516.

[3] M. Shah, A.P. Jemshihas, P.K. Jamshina Sanam, P.P. Pradyumnan, Magneto thermoelectric effect of nickel thin film synthesized by RF magnetron sputtering, Physica E Low Dimens Syst Nanostruct 147 (2023) 115591. https://doi.org/10.1016/j.physe.2022.115591.

[4] M. Shah, J. Sanam P.K, P.P. Pradyumnan, Graphite sintered strontium praseodymium titanate perovskite for thermoelectric applications, Mater Chem Phys 327 (2024) 129866. https://doi.org/10.1016/j.matchemphys.2024.129866.

[5] M. Shah, S.P.K. Jamshina, P.P. Pradyumnan, Optimization of carrier mobility in Pr-doped $SrTiO_3$ thin films through controlled Sr-segregation for optoelectronic applications, Surfaces and Interfaces 55 (2024) 105331. https://doi.org/10.1016/j.surfin.2024.105331.

Chapter 9

Recommendation for future research

Objectives

This chapter aims to outline future research directions for enhancing the optoelectronic and thermoelectric properties of $SrTiO_3$-based materials. Investigating controlled A-site (Sr) or B-site (Ti) vacancies could optimize carrier concentration and energy filtering while reducing thermal conductivity for improved performance. The incorporation of metallic or magnetic nano-inclusions may further enable tunable thermoelectric and magneto-thermoelectric applications by influencing charge transport and phonon scattering mechanisms. Additionally, designing superlattice structures and p-n junction thermoelectric generators could unlock new pathways for improving Seebeck coefficient, electrical conductivity, and energy conversion efficiency in oxide-based thermoelectric devices.

9.1 Outlook and future perspectives

- We have successfully achieved enhanced optoelectronic and thermoelectric properties in $SrTiO_3$ based materials through Pr and Nb doping, quantum confinement, oxygen vacancy engineering, and advanced synthesis techniques such as RF magnetron sputtering and burial sintering. However, there remain unexplored areas such as interface-controlled transport phenomena, and the role of magnetic nano-inclusions, which offer significant potential for future investigation.
- Structuaral properties could be modified by A-site (Sr) or B-site (Ti) vacancies in $SrTiO_3$ to enhance its optoelectronic and thermoelectric performance. By tuning these vacancies, it may be possible to optimize carrier concentration, improve energy filtering mechanisms, and reduce thermal conductivity, thereby advancing the material's efficiency in thermoelectric and optoelectronic applications.
- It is possible investigate the role of metallic inclusions, such as silver or copper, in enhancing the optoelectronic and thermoelectric performance of $SrTiO_3$. These metallic inclusions may act as effective scattering centers to reduce thermal conductivity while simultaneously boosting electrical conductivity, thereby improving the overall efficiency of $SrTiO_3$ in thermoelectric and optoelectronic applications.
- Explore the incorporation of magnetic nano inclusions like Fe, Co and Ni in $SrTiO_3$ to investigate their influence on field-dependent thermoelectric and magneto-thermoelectric properties. By studying the interaction between magnetic fields and charge carriers, this approach may reveal new pathways to enhance the material's thermoelectric efficiency and enable tunable magneto-thermoelectric applications.
- Forming superlattices of Praseodymium (Pr) and Niobium (Nb) doped alternate layers in $SrTiO_3$ offers a promising avenue for enhancing

thermoelectric (TE) properties. The superlattice structure can introduce quantum confinement effects, strain modulation, and interface engineering, potentially leading to significant improvements in the Seebeck coefficient and electrical conductivity. Additionally, exploring the interplay between dopant concentrations, layer thickness, and annealing conditions could provide deeper insights into optimizing the TE performance of these materials for energy harvesting applications.

- Developing a p-n junction thermoelectric generator using $SrTiO_3$ as the n-type material and suitable p-type counterparts, such as doped $LaCoO_3$ or NiO, could lead to efficient thermoelectric energy conversion. The junction formation may enhance the Seebeck effect and improve power generation by optimizing charge carrier separation and reducing thermal losses. Investigating the compatibility of these materials, including their interface stability, carrier mobility, and thermal conductivity, could yield significant advancements in the performance of oxide-based thermoelectric devices.
- The advancements in optoelectronic and thermoelectric properties of Pr and Nb doped $SrTiO_3$ demonstrated in this thesis pave the way for the development of temperature sensors. By leveraging the strong temperature-dependent electrical and optical responses, these materials can be integrated into infrared sensors and thermoelectric temperature detectors with high sensitivity.
- Realization of such sensors can be achieved by optimizing dopant concentration and defect engineering to enhance the temperature coefficient of resistance (TCR) and thermovoltage response, enabling precise temperature monitoring in industrial and environmental applications [1–5].
- Spin-dependent thermoelectricity: Explore magneto-thermoelectric and spin Seebeck effects in $SrTiO_3$ with magnetic dopants (Fe, Co, Ni) to enable spin-caloritronic applications and field-tunable energy conversion.

References:

[1] D. Srivastava, C. Norman, F. Azough, M.C. Schäfer, E. Guilmeau, D. Kepaptsoglou, Q.M. Ramasse, G. Nicotra, R. Freer, Tuning the thermoelectric properties of A-site deficient $SrTiO_3$ ceramics by vacancies and carrier concentration, Physical Chemistry Chemical Physics 18 (2016) 26475–26486. https://doi.org/10.1039/C6CP05523K.

[2] D. Srivastava, C. Norman, F. Azough, M.C. Schäfer, E. Guilmeau, R. Freer, Improving the thermoelectric properties of $SrTiO_3$-based ceramics with metallic inclusions, J Alloys Compd 731 (2018) 723–730. https://doi.org/10.1016/j.jallcom.2017.10.033.

[3] Z. Lu, H. Zhang, W. Lei, D.C. Sinclair, I.M. Reaney, High-Figure-of-Merit Thermoelectric La-Doped A-Site-Deficient $SrTiO_3$ Ceramics, Chemistry of Materials 28 (2016) 925–935. https://doi.org/10.1021/acs.chemmater.5b04616.

[4] X.-L. Shi, H. Wu, Q. Liu, W. Zhou, S. Lu, Z. Shao, M. Dargusch, Z.-G. Chen, SrTiO3-based thermoelectrics: Progress and challenges, Nano Energy 78 (2020) 105195. https://doi.org/10.1016/j.nanoen.2020.105195.

[5] T. Liao, Z. Ye, J. Chen, Spin-Seebeck Temperature Sensors, IEEE Trans Electron Devices 64 (2017) 2655–2658. https://doi.org/10.1109/TED.2017.2691762.

Journal of Physics and Chemistry of Solids 181 (2023) 111516

Contents lists available at ScienceDirect

Journal of Physics and Chemistry of Solids

journal homepage: www.elsevier.com/locate/jpcs

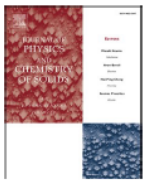

Defect-induced $Sr_{1-x}Pr_xTiO_3$ crystallites by burial sintering and its optoelectronic applications

Midhun Shah [a,b], Jamshina Sanam P.K. [a], P.P. Pradyumnan [a,*]

[a] Department of Physics, University of Calicut, Malappuram, India
[b] Department of Physics, Farook College, Kozhikode, India

ARTICLE INFO

Keywords:
Burial sintering
Raman spectroscopy
Structure transformation
Oxygen vacancy
Band gap reduction
IR absorption

ABSTRACT

The band structure of $SrTiO_3$ was altered by introducing Pr^{3+} in the Sr^{2+} site and subsequent graphite burial sintering. The asymmetric nature of the (310) peak in XRD and the emergence of E_g and B_{1g} modes in the Raman spectrum suggest the transformation from cubic to tetragonal phase for the $Sr_{1-x}Pr_xTiO_3$ system with $x \geq 0.1$. The development of the forbidden first-order Raman peaks and novel spectral properties are attributed to the local vibrational modes linked to oxygen vacancies. Structural variations in terms of lattice strain were investigated using a W–H plot, and morphological changes were analyzed by high-resolution FE-SEM. High infrared absorption in UV–Vis–NIR spectra and a significant reduction in band gap from 2.8 eV to 1.8 eV were accomplished through increased disorder in the lattice and the reduction of Ti^{4+}. The blue shift in absorption spectra with Pr concentration can be used to tune the absorption range for sensing purposes. The formation of new electronic states observed here offers a novel approach for band gap modification in perovskites for photocatalytic and photovoltaic applications.

1. Introduction

Due to its intriguing physical characteristics strontium titanate (STO) has been widely explored in single crystal, bulk ceramics, and thin film forms. Perovskite-type alkaline earth titanates, such as $BaTiO_3$ and $SrTiO_3$, have several electronic and optoelectronic applications, including sensors, actuators, dielectric layers in capacitors, optical modulators, optical windows, and optical filters [1–3]. Doped perovskites and delaffosite are also employed in thermoelectric power generation [4–7]. Oxide perovskites have the general structural formula ABO_3 (where A and B are cations). The structure comprises the BO_6 octahedra sharing corners infinitely in all 3 dimensions, making a symmetric structure. The A cations occupy every hole which is created by eight BO_6 octahedra, resulting in 12-fold oxygen coordination for A cations and 6-fold oxygen coordination for B cations as indicated in Fig. 1. Chemical doping in A and B site using suitable elements alter the structural, optical, dielectric, ferroelectric, and thermoelectric properties of STO-based ceramics [8]. Cation substitution transforms the electronic band structure, which reflects in the band curvature thus band degeneracy.

STO is a wide band gap insulator ($E_g \sim 3.2$ eV) at room temperature. Because of this wide band gap, its photocatalytic properties are limited to the UV region of the spectrum. Therefore, improvisations to $SrTiO_3$ are attempted to shorten the band gap and thus broaden the light-harvesting capacity of the material [9,10]. Sr^{4+} ions do not have the rich energy level diagram that defines the rare earth (RE) ions. Therefore, the photon management properties can only be produced by doping with other rare earth ions. Rare earth element substitutions can shift the Fermi-level into the conduction band and change the absorption spectrum by adding peaks at 0.1–0.4 eV [5]. Dopants like Cr, Fe, Eu and Al are widely exploited to change the optical properties of pristine $SrTiO_3$ [3,11–15]. Unlike other RE^{3+}, Pr^{3+} has a unique feature resulting from the close energy separation between the $^1S_0$ level and the lowest edge of the 4f 5d configuration and its emission depends greatly on the position of the 4f 5d configuration, which is extremely influenced by the features of the host. Pr as a dopant is widely used to alter the ferroelectric and thermoelectric properties of STO, but optical modifications are less explored.

In the present study, we successfully incorporated Pr in Sr sites of the $SrTiO_3$ matrix. The burial sintered samples of Pr doped $SrTiO_3$ were also prepared using graphite powder and the structural changes were investigated with XRD and Raman spectroscopy. The tunability of the

* Corresponding author.
E-mail address: ppp@uoc.ac.in (P.P. Pradyumnan).

https://doi.org/10.1016/j.jpcs.2023.111516
Received 27 March 2023; Received in revised form 12 May 2023; Accepted 14 June 2023
Available online 15 June 2023

Materials Today Communications 39 (2024) 109323

Contents lists available at ScienceDirect

Materials Today Communications

journal homepage: www.elsevier.com/locate/mtcomm

Tuning of photoluminescence properties: Impact of Pr-doping in $SrTiO_3$ crystallites

Midhun Shah [a,b], P.K. Jamshina Sanam [a], P.P. Pradyumnan [a,*]

[a] Department of Physics, University of Calicut, Malappuram, India
[b] Department of Physics, Farook College, Kozhikode, India

ARTICLE INFO

Keywords:
XRD analysis
Rietveld refinement
Phase change
Photoluminescence
XPS
Oxygen vacancy
Narrow band emission
CIE plot

ABSTRACT

Materials having deep blue emission characteristics with a CIEy chromaticity value less than 0.1 are highly desired. Here we incorporated Pr^{3+} into the Sr^{2+} site of the $Sr_{1-x}Pr_xTiO_3$ (x=0.05, 0.075, 0.10, 0.125, 0.15, 0.20) to quench the typical red photoluminescence (PL) emission in Pr-doped compounds and tune it to a blue-emitting system. XRD analysis and structural refinement demonstrate transition from cubic to tetragonal symmetry at Pr concentrations of, x≥0.1. The contribution of oxygen vacancies in emission mechanism was investigated through XPS analysis. High-resolution FE-SEM analysis of morphological features revealed the creation of tiny grains with the appearance of micro pebbles. Under 380 nm UV illumination a narrow-band blue emission peak FWHM of 19.3 nm was obtained at 428 nm for x=0.05. CIE plots were used to examine the quality of emission peaks and samples show CIEy less than 0.1. This blue emission is crucial for lighting and display applications.

1. Introduction

Strontium titanate ($SrTiO_3$) has been intensively explored due to its fascinating physical features, in single crystal, bulk ceramics, and thin film forms. It has paraelectric and piezoelectric characteristics, and polarization may be generated by applying an electric field, even without a permanent electric dipole [1,2]. Doped perovskites and delaffosite are also employed in thermoelectric and photovoltaic power generation [3–8]. In contrast to the characteristics of traditional semiconductors, oxide-based semiconductors provide a number of interesting features. Strontium titanate (STO) is one such promising perovskite oxide material with a wide range of applications and has been employed as a photo catalyst and as a substrate for the epitaxial growth of various oxide-based films [9,10]. It exhibits semiconducting behavior, high dielectric constant, and great thermal stability, resulting in a broad variety of microelectronics applications, making it one of the most promising materials for tunable microwave devices, capacitors, photo catalysts, and light emitters [11]. STO has an optical bandgap of 3.2 eV and can be tuned with appropriate doping, which accounts for catalysis efficacy of the material under UV–visible illumination [12–15].

Structural features of STO include soft bonding of the small Ti^{4+} ion to the neighboring octahedral O^{2-}. Its conductivity can be modified with sizable low-temperature mobility after n-type doping, which is typically achieved either by introducing oxygen vacancies or by chemical substitution by La^{3+}, Pr^{3+} for Sr^{2+}, or Nb^{5+} for Ti^{4+} [16]. Even though many of these features are still poorly understood, they are inextricably linked to doping with rare earth elements, and alteration of electronic structure by the introduction of oxygen vacancies. There is a great role of impurities and point defects in determining its functional capabilities, and much effort is being made to identify the underlying mechanisms and their causal relationships.

In a variety of dielectric crystals, luminescence emission experiments including photoluminescence, cathodoluminescence, radio luminescence, and more recently ionoluminescence have been utilized to characterize the electronic excitations and generate defect centers [17–20]. When STO is exposed to ultraviolet light, it appears that both photo generated electrons and holes contribute to the material's photoconductivity. The photoluminescence (PL) characteristics of STO is even more perplexing and contentious than their transport properties. Role of self-trapped excitons in all kinds of electronic excitations is dominant. Free electrons and holes are produced by electronic excitations that have energies exceeding the band gap. These free carriers bind into e-h pairs that are confined in the lattice extremely quickly, creating a self-trapped exciton (STE). Pure STO shows a greenish luminescence when exposed to UV light, with a maximum of 2.2–2.4 eV of photon energy centered on wavelength 500 nm due to the decay of these

* Corresponding author.
E-mail address: ppp@uoc.ac.in (P.P. Pradyumnan).

https://doi.org/10.1016/j.mtcomm.2024.109323
Received 28 March 2024; Received in revised form 17 May 2024; Accepted 20 May 2024
Available online 21 May 2024

Materials Chemistry and Physics 327 (2024) 129866

Contents lists available at ScienceDirect

Materials Chemistry and Physics

journal homepage: www.elsevier.com/locate/matchemphys

Graphite sintered strontium praseodymium titanate perovskite for thermoelectric applications

Midhun Shah [a,b], Jamshina Sanam P.K [a], P.P. Pradyumnan [a,*]

[a] Department of Physics, University of Calicut, Malappuram, India
[b] Department of Physics, Farook College, Kozhikode, India

HIGHLIGHTS

- The cubic symmetry of $Sr_{1-x}Pr_xTiO_3$ was broken by and transformed it to Tetragonal system.
- Double Schottky Barrier, inhibiting TE performance was eliminated with the two step graphite reduction.
- A maximum TE power factor of 1.8 mW/mK^2 is achieved for x = 0.10.
- Porous structure, Pr defect centers, Oxygen vacancies along with reduced thermal conductivity lead to maximum ZT of 0.33.

GRAPHICAL ABSTRACT

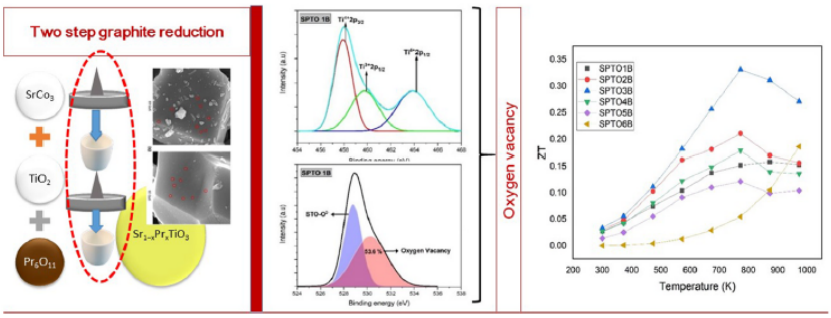

ARTICLE INFO

Keywords:
Burial sintering
Double Schottky barrier
XPS analysis
Oxygen vacancy
Seebeck coefficient
Thermoelectric figure of merit

ABSTRACT

Here Pr^{3+} was introduced in the Sr^{2+} site in Sr_{1-x} Pr_xTiO_3 (x = 0.05, 0.075, 0.10, 0.125, 0.15, 0.20) system followed by two step graphite burial sintering. Powder reduction helps to increase the carrier concentration and the doped sample pellet reduction minimizes Double Schottky Barrier generated by strontium and oxygen vacancies at grain boundary by regulating the point defects. Samples with $x \geq 0.10$ shows splitting and asymmetry of (200) and (310) peak in XRD indicating structural transformation from cubic to tetragonal phase. XPS spectra of the samples confirmed the formation of oxygen vacancies and reduction of Ti^{4+} to Ti^{3+} induced by graphite burial sintering resulting in enhanced carrier concentration. A maximum power factor of 1.8 mW/mK^2 was obtained for $Sr_{0.9}$ $Pr_{0.1}TiO_3$ samples at 673 K. Reduced thermal conductivity due to porous structure, Pr defect centers, oxygen vacancy clusters together with enhanced power factor lead to a maximum figure of merit 0.33, making this an ideal candidate as n type legs in thermoelectric generators.

1. Introduction

Rising energy use has resulted in global warming and environmental deterioration. To mitigate these consequences, scientists are working to improve energy harvesting-based power producers. Thermoelectric generators have proved their capacity to directly convert heat energy in to electricity. The ability of thermoelectric materials to convert heat into electricity even at very slight temperature gradients compared to their

* Corresponding author.
E-mail address: ppp@uoc.ac.in (P.P. Pradyumnan).

https://doi.org/10.1016/j.matchemphys.2024.129866
Received 1 April 2024; Received in revised form 9 August 2024; Accepted 16 August 2024
Available online 17 August 2024

Surfaces and Interfaces 55 (2024) 105331

Contents lists available at ScienceDirect

Surfaces and Interfaces

journal homepage: www.sciencedirect.com/journal/surfaces-and-interfaces

Optimization of carrier mobility in Pr-doped $SrTiO_3$ thin films through controlled Sr-segregation for optoelectronic applications

Midhun Shah [a,b], Sanam P.K. Jamshina [a], P.P. Pradyumnan [a,*]

[a] Department of Physics, University of Calicut, Malappuram, India
[b] Department of Physics, Farook College, Kozhikode, India

ARTICLE INFO

Keywords:
Thin films
Cation segregation
SK growth
Carrier mobility
Urbach energy
Hall effect measurements

ABSTRACT

Functional oxides employed in electronic components hold significant promise for future electronic devices. Strontium titanate based thin films have several emergent features due to unsaturated bonds, dimension restriction, production of oxygen vacancies and point defects that make them attractive for optoelectronic applications. Here we prepared Pr-doped strontium titanate thin films via RF magnetron sputtering in a pure Argon environment at various gas pressures followed by heat treatment. The structural parameters, analyzed via XRD and Raman spectroscopy, were correlated with the electrical transport properties. Intriguing morphological features such as Stranski–Krastanov (SK) growth and cation segregation observed by FESEM and AFM analysis were further examined to elucidate the conduction mechanism in the films. The optical studies unveiled significant transparency in the visible spectrum. Photoluminescence emission studies at specific wavelengths shed light on the involvement of oxygen vacancies. By carefully controlling annealing conditions and optimizing sputtering parameters, thin films devoid of Sr segregation with highest reported carrier mobility of 33.9 $cm^2/V\,s$ were prepared. The high mobility leading to enhanced conductivity render the films suitable for a wide range of optoelectronic applications.

1. Introduction

Functional oxides have been at the core of a number of remarkable technological progress in wearable devices, sensors, spintronics, photonics, thermoelectrics and photovoltaics. Numerous compositional options and phase tunability provide extensive opportunities for creating new functional oxides with a variety of characteristics in both bulk and thin film forms [1–10]. Materials in thin film forms are utilized in a variety of applications including anti-reflective coatings, memory devices, piezoelectric and triboelectric devices, mechanisms for energy storage and conversion, wearable electronic systems, sensing and amplification. Advances in thin film material research and technology have fueled a slew of new advancements in electronics. Even though cutting edge techniques for thin film growth such as molecular beam epitaxy, pulsed laser deposition, RF Magnetron sputtering and atomic layer deposition are available for thin film growth, the quest to increase performance to new heights still faces obstacles. High mobility in the semiconducting oxide, where transport is governed by the overlap of the cationic and anionic orbitals, is a crucial performance characteristic in electronic devices [11,12].

Functional oxides employed in electronic components hold significant promise for future optoelectronic devices [55]. Perovskite oxides have received a lot of attention among functional oxides because of their propensity to create compounds with practically every element in the periodic table. The advantageous property of perovskites is their relatively high static dielectric permittivity, which effectively screens electron-charge interaction and facilitates electron transport. Because of the strong polarization effect, electron-phonon interactions rather than ionized impurity scattering dominate the electron mobility in doped perovskite oxides at ambient temperature. One commonly utilized material as a functional oxides is perovskite strontium titanate ($SrTiO_3$ or STO). It also offers diverse applications in optoelectronics and photo catalysis. However its uses in optoelectronics field is limited by wide band gap of the range 3.3 eV The bandgap results from the separation of the dominating O 2p states and the hybridized O 2p-Ti 3d states (with small contribution from Ti 3d states). Band gap modulation to get good electrical conductivity and transparency should be a suitable strategy to make STO a functional oxide material for optoelectronic applications [13]. Theoretical and experimental attempts have been made to engineer the bandgap, including doping, hetero structure formation and

* Corresponding author.
E-mail address: ppp@uoc.ac.in (P.P. Pradyumnan).

https://doi.org/10.1016/j.surfin.2024.105331
Received 9 July 2024; Received in revised form 1 October 2024; Accepted 23 October 2024
Available online 24 October 2024

Physica E 147 (2023) 115591

Contents lists available at ScienceDirect

Physica E: Low-dimensional Systems and Nanostructures

journal homepage: www.elsevier.com/locate/physe

Magneto thermoelectric effect of nickel thin film synthesized by RF magnetron sputtering

Midhun Shah [a,b], A.P. Jemshihas [c], P.K. Jamshina Sanam [a], P.P. Pradyumnan [a,*]

[a] Department of Physics, University of Calicut, Malappuram, India
[b] Department of Physics, Farook College, Kozhikode, India
[c] AKNM Govt Polytechnic College, Thiroorangadi P.O, Malapuram, India

ARTICLE INFO

Keywords:
Thin films
Magneto thermoelectric effects
Seebeck coefficient
Thermoelectricity
Instrumentation and measurement

ABSTRACT

External magnetic fields can effectively alter the thermoelectric performance of materials, particularly magnetic thin films and nanostructures. Here, we used the RF magnetron sputtering technique to deposit thin films of nickel. Magnetic force microscopy (MFM) imaging revealed the formation of magnetic domains. XRD patterns showed the preferred orientation of nickel films in [111] plane. Thermoelectric and magneto-thermoelectric effects of the sputtered thin films were investigated using an experimental setup designed by the authors. Peltier elements, thermostats, and PIDs were employed to regulate the sample's temperature, and examined variations in the Seebeck coefficient with the applied magnetic field. Interaction of external field with charge carriers resulted in an increase of thermovoltage from 32.17 μV to 33.53 μV and saturated at 0.2 T. Saturation behaviour of thermoelectricity can be used to investigate the magnetic nature of materials.

1. Introduction

Environmental energy of various forms may be converted to useful electricity with the aid of thermoelectric and photovoltaic systems. They have a wide variety of applications in the automobile industry, biomedical industry, portable electronics, communication systems, etc. Thermoelectric materials can convert heat energy into electrical energy and vice versa [1]. Among the green energy mechanisms, thermoelectric conversion has attained a unique status because of the lack of moving parts, low maintenance, high conversion efficiency, and high reliability [2,3]. Research in the field of thermoelectric (TE) materials across the globe emerge with creative solutions and applications like waste heat recovery of automobiles, thermal energy trapped on the roof of buildings, bio thermal batteries, localized cooling for electronic components in LASER sources, computers, and modern digital gadgets. Radioisotope thermoelectric generators (RTG) are extensively used as power sources of satellites and space probes, where electricity is generated by converting heat energy released by the decay of radioactive material by the Seebeck effect [4–7].

The efficiency of the thermoelectric energy conversion is expressed by the dimensionless figure of merit,

$$ZT = \frac{S^2\sigma}{\kappa} T \quad (1)$$

Where, σ is the electrical conductivity, S is the Seebeck coefficient, T is the temperature, and κ is the thermal conductivity. Maximization of the thermoelectric figure of merit (ZT) requires a low thermal conductivity along with a high Seebeck coefficient and high electrical conductivity [8,9]. Differential methods are commonly used to characterize the Seebeck coefficient TE materials, and they can support a variety of equipment configurations depending on the nature of the samples. Various experimental settings are already in use, each one tailored to certain forms of samples [10–14]. The thermoelectric characterization of prepared samples, both in bulk and thin film form, is commonly done with advanced instruments like ULVAC-ZEM™ series or Linseis LSR™ series in an inert gas atmosphere. The temperature ranges can also be varied between −100 °C and 1500 °C. Although characterization of materials below room temperature and at very high temperatures is vital for understanding the physics underlying their properties, it may not be necessary for practical applications. Sharath Chandra et al. devised simple and precise thermoelectric power measurement setups that can be used to analyze the materials for different environments and at wide temperature ranges [15]. Setups with coil and pencil type heating elements are reported by Ashish Kumar et al. and Chun Sum Brian Pang

* Corresponding author.
E-mail address: ppp@uoc.ac.in (P.P. Pradyumnan).

https://doi.org/10.1016/j.physe.2022.115591
Received 29 October 2022; Received in revised form 25 November 2022; Accepted 27 November 2022
Available online 7 December 2022